A Ph.D. Dissertation on

Time-Frequency Based Signal Processing for Modal Parametric System Identification

submitted by

Swarup Mahato

(136104010)

under the supervision of

Dr. Arunasis Chakraborty

DEPARTMENT OF CIVIL ENGINEERING

INDIAN INSTITUTE OF TECHNOLOGY GUWAHATI

August, 2019

Certificate

It is certified that the work contained in the dissertation entitled **"Time-Frequency Based Signal Processing for Modal Parametric System Identification"**, by **Swarup Mahato (136104010)** for the partial fulfillment of the requirements for the award of the *Doctor of Philosophy (Ph.D.)* in *Civil Engineering* with the specialization in *Structural Engineering* at the *Indian Institute of Technology Guwahati, India* is an authentic work. This work has been carried out under my sole supervision and it has not been submitted elsewhere for the award of a degree.

Dr. Arunasis Chakraborty
Associate Professor
Department of Civil Engineering
Indian Institute of Technology Guwahati
Guwahati - 781039, India

Date: September, 2019

Acknowledgements

This thesis is an outcome of analytical and experimental studies carried out during my Ph.D. tenure. On completion of this, first and foremost, I would like to express my sincere thanks and gratitude to my supervisor *Dr. Arunasis Chakraborty*. He has a pivotal role in my research work with his unconditional support and effortless motivation. He has not only helped me to develop the theoretical background but also provided necessary facilities to conduct the experiments. Working with him gives great pleasure and lifelong lessons as a professional.

My sincere thanks to chairmen of Doctoral Committee *Prof. Anjan Dutta* for all his technical help and encouragement during my tenure. I like to thank my Doctoral Committee members *Dr. Sandip Das*, *Dr. Prithwijit Guha* and *Dr. V. Vijaya Saradhi* for their constructive feedback during my research work. Again, I would like to acknowledge the help received from *Prof. Anjan Dutta*, *Prof. Sajal K. Deb* and *Prof. Sudip Talukdar* for carrying out tests and developing the models of test structure. I wish to convey my thanks to *Mr. Biswajit Debnath* for helping me to conduct various experiments. I like to thank Civil Engineering Department of IIT Guwahati for providing all necessary help to carry out this work.

I also thank my colleague *Mr. Amit K Rathi* for the critical suggestions, *Mr. Meda V Teja*, *Mr. Sajeer M.* and *Mr. Pranjal Tamuly* for their helping hand in the experiments. Finally, I would like to thank my family (parent and sisters) for their continuous moral support which proved to be crucial during this tenure.

Swarup Mahato
(136104010)
Department of Civil Engineering
Indian Institute of Technology Guwahati
Guwahati - 781039, India

Date: September, 2019

Abstract

Time-frequency based signal processing is a popular technique for output only operational modal analysis (OMA). It is easy to implement and demands no prior knowledge of the structural parameters. These techniques are mostly based on either Hilbert transform (HT) or wavelet transform (WT) beside other time-frequency tools which are less popular among the researcher and engineers. Different Hilbert transform based techniques are empirical mode decomposition (EMD) or Hilbert-Huang transform (HHT), ensemble empirical mode decomposition (EEMD), analytic mode decomposition (AMD) and multi-variate mode decomposition (MEMD). The major drawback of these tools are their lack of strong mathematical background in the light of modal vibration and their susceptibility to generate spurious modes. Moreover, these techniques have a prerequisite for free vibration response for modal identification which are either directly obtained or digitally processed using other techniques available in the literature [e.g. random decrement technique (RDT) or natural excitation technique (NExT)]. This prerequisite poses serious threat to apply them on civil infrastructure as free vibrations are difficult to obtain directly. Also, their digital generation from forced response demands strong intermittency which is often heuristic in nature. Besides these hurdles, there is a constant need to evolve these methods for their application on forced response (in particular seismic response). The reason behind this need is to assess and certify the infrastructures immediately after the seismic event when further application of external loads to generate response (either harmonic or broad banded input) is not recommended. This motivates the current study to investigate the improvements of HHT based algorithm for their use on forced response directly. The improved algorithm should have the ability to minimize the generation of spurious mode and to differentiate between the modal and the forcing frequencies. To address the first issue, an adaptive filtering technique is proposed prior to apply HHT based identification techniques. This is followed by a phase comparison which separates out input frequencies present in the response. It compares two decomposed responses belonging to the same mode extracted from two different sensors. This modification over the conventional HHT, allow the extraction of modal frequencies

accurately from an array of sensors. However, the efficiency of this proposal depends on the quality of the band-pass filters. The proposed methodology can extract modal frequencies from the forced vibration without any user intervention. Here, two different filters are used i.e. Butterworth filter and wavelet filter where modified Littlewood-Palley (MLP) basis function is used. The compact support of MLP basis works better as it has zero energy leakage compared to Butterworth filter. This adoption enables the tracking algorithm to trace frequencies accurately from the non-stationary response of the structure which itself is a major advantage as compared to other similar methods available in the literature.

With the successful implementation of improvised HHT for OMA using forced vibration response, the study continued to investigate further for more accurate and efficient time-frequency analysis. It is observed that wavelet based pre-filtering works efficiently which makes the EMD operation redundant. Hence, a combined WT-HT based algorithm is further developed that can avoid the spurious mode generation. Finally, the potential of wavelet transform in the light of non-stationary structural response is investigated. Traditional approach of wavelet based OMA has two major drawbacks - i) it demands large number of scales for workable resolution and ii) the ridge-skeleton based approach requires user intervention to extract modal frequencies. The problem is more complex in presence of contiguous modal or forcing frequencies which are clubbed over different regions in the scalogram. To address these issue, two major modifications are proposed in this study - i) use recently developed synchrosqueezed transform that offers better resolution with the same number of scales and ii) use machine learning algorithm to bypass ad-hoc intermittency which are practically difficult to implement in forced response based OMA. The synchrosqueezed transform used in this study offers better energy spectrum in a workable precision. It is followed by k-means clustering based unsupervised learning to avoid intermittency and to achieve automated identification of energy segregation. Together these two modification offers a high fidelity identification algorithm for forced response based OMA. The quality of the results are impressive as the estimation errors are consistently well within the allowable limits for all practical purpose. This technique is then applied on random eigen value problems to identify the mean modal frequencies. It is observed that detectability of modal frequencies are largely affected by sensor locations. Each proposal presented in this study is validated using simulated numerical examples as well as he field tests on real structure e.g. full scale building, concrete road bridge and thin beam laboratory model. In general, the improvised HT and WT based OMA algorithms presented in this thesis offer promising performance in the light of non-stationary forced response and hence, adopted for identification and health monitoring of infrastructures.

List of Publications

Journal Articles:

1. S. Mahato, M. V. Teja and A. Chakraborty, Adaptive HHT (AHHT) based modal parameter estimation from limited measurements of an RC-framed building under multicomponent earthquake excitations, *Structural Control and Health Monitoring*, 2015, 22(7), 984-1001.

2. S. Mahato, M. V. Teja and A. Chakraborty, Combined wavelet-Hilbert transform-based modal identification of road bridge using vehicular excitation, *Journal of Civil Structural Health Monitoring*, 2017, 7 (1), 29-44.

3. S. Mahato, and A. Chakraborty, Sequential clustering of synchrosqueezed wavelet transform coefficients for efficient modal identification, *Journal of Civil Structural Health Monitoring*, 2019, 9 (2), 271-291.

Conference Proceedings:

1. M. Teja, S. Mahato and A. Chakraborty, Modal Parameter Estimation of LTI System Using Hilbert-Huang Transform of Wireless Sensor Data, The Second Australasia and South-East Asia Structural Engineering and Construction Conference ASEA-SEC-2, Bangkok, Thailand, 3-7 November, 2014

2. S. Mahato and A. Chakraborty, Performance of Adaptive Hilbert Transform and Its Variants in Modal Identification of RC Bridge, ISSS National Conference on MEMS, Smart Materials, Structures and Systems, Kanpur, India, 28-30 September, 2016

Contents

List of Figures

List of Tables

List of Major Symbols and Abbreviations

Symbols	Meaning
$\mathbf{M}$	Mass matrix
$\mathbf{K}$	Stiffness matrix
$\mathbf{C}$	Damping matrix
ω	frequency
ω_n	natural frequency
t	time
η	modal damping ratio
Δt	time resolution
$\Delta\omega$	frequency resolution
$\mathscr{H}[\cdot]$	Hilbert transformation
$W_\psi(\cdot)$	Wavelet co-efficient
$\psi(\cdot)$	Wavelet basis function
$\mathbf{U}$	Displacement
$\dot{\mathbf{U}}$	velocity
$\ddot{\mathbf{U}}$	Acceleration
Φ	Mode shape
$\boldsymbol{\iota}$	Influence vector
f	frequency
λ	cluster weight

Abbreviations

AMD	Analytic mode decomposition
EMD	Empirical mode decomposition
EEMD	Ensembled mode decomposition
ERA	Eigen realization algorithm
HT	Hilbert transformation
IMF	Intrinsic modal function
MEMD	Multivariate mode decomposition
MLP	Modified Littlewood-Paley
NExT	Naturally excitation technique
OMA	Operational modal analysis
RDT	Random decrement technique
STFT	Short time fourier transformation
SST	Synchrosqueezed Transformation

Chapter 1

Introduction

Structural systems are large, often spatially distributed whose performance gradually deteriorate with time and hence need continuous maintenance. Considering their invaluable societal functionality, long-term health management of civil infrastructure systems is as important as their design and construction. In this context, rapid socio-economic development in the recent past has forced the infrastructures to perform under extreme conditions, pushing their operational envelope to meet the ever-increasing demand. It requires continuous performance evaluation to maintain the optimal output without any interruption. For this reason, structural health monitoring (SHM) is of great concern to the engineers and scientists for uninterrupted and efficient performance during the entire service life. SHM also helps to ensure reliability and safety of the structure besides minimizing the operational and life-cycle cost. Early detection of structural parameters is critical for the decision making on repair and maintenance in order to guarantee the specified structural and operational reliability. It not only evaluates in-situ condition to decide necessary maintenance required for smooth operation, but also provides advance warning to avoid any catastrophic failure in future. In this process, deteriorations of material and/or geometric properties and boundary conditions over the time are evaluated [1–3]. Various methods are available in the literature for inverse problem in structural health monitoring (SHM). Image processing [4], motion capturing technique [5], acoustic emission [6] are a few among many others. Compared to other methods, vibration based SHM techniques are widely used [7, 8] in civil engineering as it has distinct advantage over others. Doebling et al [9] presented a review of the vibration based parameter estimation and damage detection. These methods are broadly classified into two categories - input-output based methods and output only methods. To implement the techniques in the first category, user needs to know the structural details, input excitation and the response while in the second category, only the recorded responses are required for system identification. Stochastic Subspace Identification (SSI) [10, 11], Wavelet Transformation (WT) [12–14], Hilbert-Huang Transformation (HHT) [15–17] and Blind Source Separation (BSS) [18–20] are widely used techniques among other output only

methods. These techniques are easy and fast to implement for structural vibration control [21–23], retrofitting/restrengthening of structures [24–26] and other decision making processes. Moreover, it can be easily adopted for continuous monitoring even on real time basis. Due to this reason, system identification using the measured vibration signals has received considerable attention in the recent past. In this context, challenges in system identification are plenty - limited knowledge of geometric and material properties, noise in measurements, incomplete description of structural behavior in their numerical models etc. Vibration based identification are classified into three major paradigms - frequency domain analysis, time domain analysis and time-frequency domain analysis.

The main goal of vibration based linear system identification is to evaluate the modal parameters (i.e. natural frequencies, mode shapes and modal damping ratios) from the measurements. These parameters can quantify in-situ conditions and their anticipated behavior in future. Identification algorithms based on vibration records due to unknown operational loads are popularly known as Operational Modal Analysis (OMA). Significant amount of literatures are available on OMA [27–30] where identification strategies are mainly classified into three categories as mentioned above. Cimellaro et. al. [29] compared three different output only identification techniques applied on an ancient masonry structure - frequency domain decomposition (FDD) [31], random decrement technique (RDT) [32] with eigen realization algorithm (ERA) and natural excitation technique (NExT) with ERA [33]. Their study showed that all three methods gave satisfactory results. Time domain techniques like autoregressive moving average (ARMA) [34], stochastic subspace identification (SSI) [30, 35], natural excitation technique (NExT) [36] are commonly used for OMA. In the recent past, researchers have used principle component analysis (PCA) or independent component analysis (ICA) based blind source separation (BSS) techniques to extract the modal features [37–40] where the underlying theory is singular value decomposition. BSS based identification have shown promising results for various structural systems and input excitations.

On the other hand, frequency domain decomposition (FDD) [41], fourier spectra [42] and peak picking method [43] are in frequency domain. In these methods, recorded responses are considered as a stationary process. However, structural systems are often subjected to non-stationary excitations like earthquake, gust, vehicular traffic with random change in speed. In this context, both time and frequency domain techniques have their inherent limitations to identify the instantaneous amplitude and phase of a non-stationary signal. Therefore, there is a constant need for developing OMA techniques that can address non-stationary characteristics of the recorded signal. For this purpose, time-frequency analysis (e.g. Short-time Fourier transform, Wigner-Ville transform, Hilbert-Huang transform, Wavelet transform etc.) have gained popularity among the scientists and engineers in the last few decades.

1.1 Time-Frequency Analysis

Among all these techniques mentioned above, time-frequency based approach is popular for its efficient implementation to identify system parameters without any prior knowledge of the input force. This output-only modal identification has shown excellent capabilities in health monitoring of large civil infrastructure. Several time-frequency domain algorithms have been studied extensively, and the wealth of literature on this topic is vast [44–49]. More recently, powerful signal processing methods including empirical mode decomposition (EMD) [50] and Hilbert-Huang transform [51, 52] have been investigated in numerous structural health monitoring applications. Various time-frequency domain techniques are reported in the literatures of OMA. Some of these methods are short time fourier transform (STFT) [53, 54], wavelet transform (WT) [55–58] and Hilbert-Huang transform (HHT) [50, 59, 60]. Each method has its own merits and demerits depending on their applications. Short time Fourier transform (STFT) is one of the first time-frequency based signal processing technique in SHM [61, 62]. In STFT, time-frequency spectrum of a transient signal is obtained by multiplying a sliding window function in time domain. Nagarajaiah & Varadarajan [61] and Narasimhan & Nagarajaiah [62] used STFT to identify the model parameters of two ASCE benchmark buildings and used these parameters for vibration control. However, STFT has poor time resolution due to its fixed window width. A wider window has better frequency resolution but poor time resolution and vice-versa. To overcome the fixed resolution of STFT, wavelet transform is developed [63] which has flexibility in window length selection. Wavelet transform of a transient signal reveals time localized frequency details in multiple scales. Kijewski and Kareem [64] used Continuous Wavelet Transform (CWT) to analyze ambient response of a bridge, where the modal parameters were obtained from the wavelet coefficients by extracting its ridges and skeleton. They also identified damping ratios from the free decay of the recorded ambient response using Random Decrement Technique (RDT). In this context, different basis functions (e.g. Morlet, Complex Morlet, Cauchy, Harmonic, MLP) were used by previous researchers to identify the modal parameters [63–65]. This, in turn, indicates that the use of CWT for system identification is not restrictive to the selection of the mother wavelet. However, performance of different basis functions vary in different applications and restrict their generalization. Inspite of its wider appeal, wavelet transform is inherently non-adaptive and its performance is also dependent on the selection of the mother wavelet. Here, the term adaptiveness is used to mean the ability of the frequency scaling to zoom in for the modal frequency where they are localized. Adaptiveness in signal processing is different and hence should not be mixed with the meaning referred in this section. These shortcomings affect the accuracy of the identification scheme, if it is applied as a blackbox.

Parallel to the development of wavelet transform, Hilbert transform (HT) based time-frequency analysis has also gained lot of attention from the researchers and engineers working in various fields over the last two decades. Hilbert transform was first used by Feldman [49] to evaluate the parameters of a non-linear system from its mono-component free and forced vibration responses.

However, HT can extract instantaneous frequency and phase of the mono-component signals only. Thus, its application is restricted in vibration based modal analysis of real life structures whose responses are often multi-component in nature. To overcome this limitation of HT, Huang et. al. [50] introduced empirical mode decomposition (EMD) of multi-component signals prior to HT. The idea behind this approach is to decomposed the signal into its intrinsic mode functions (IMF). Each IMF corresponds to a mono-component signal which paves the way for HT to extract the time localized information of frequency content and phase. One can trace back the original signal by adding the IMFs and the residue left after the empirical mode decomposition [50, 66]. These two together (*i.e.* EMD and subsequent HT of each IMF to extract frequency and phase information of a signal) is commonly called HHT in signal processing. Yang *et al.* [60] and Min & Fan [67] used HHT to identify the modal parameters of linear time invariant systems. In these studies, simulated free vibration response of the structures are used for numerical analysis. The results presented in these research works show that HHT can identify modal parameters (*i.e.* natural frequency, modal damping) with considerable accuracy. In another work, Yang *et al.* [68] simulates ambient response of a twenty story building and convert it into free vibration response using random decrement technique (RDT). Once the free vibration is obtained, HT is used to extract the modal parameters. The HHT based method is further extended to identify modal parameters from the response due to known sinusoid and sine sweep excitations [69–72]. It has excellent frequency resolution to evaluate the natural frequencies. Therefore, as a natural consequence it is also able to detect the changes in them (*i.e.* damage). Hence, HHT is used to locate and quantify damage using measured vibration responses [73–76]. In these studies, ASCE benchmark structure for both undamage and damage cases are modeled in FE framework whose damage is assumed to affect the element stiffness only. Therefore, different failure patterns are studied by reducing appropriate element stiffness and the effectiveness of HHT based identification strategies from ambient vibration responses are presented.

Besides application in civil infrastructures, HHT based signal processing has gained popularity among the researchers and engineers in other fields like electrical engineering [70, 77], mechanical operations [78, 79], oceanography [80] etc. Wu *et al.* [81] and Yan & Gao [79] used HHT to identify the performance of a rotary machine during its operation. Peng *et al.* [82, 83] used pre-filtering of the signals to identify frequency localization prior to HHT. It helps to avoid mode mixing in case of multi-degrees of freedom (MDOF) systems.

SSI, HHT and BSS have been extensively used for system identification in the recent past. While HHT becomes more popular for its simplicity to implement and data independence, it lacks strong mathematical foundation. In many cases, it is observed to provide spurious information, mode-mixing [84] and demands strong user interface, often heuristic in nature. Other methods (e.g. SSI and BSS) are based on either singular value decomposition or eigen value decomposition. These mathematical frameworks help to segregate the components of any signal very fast. The main

drawback of these methods is the little control over the decomposition level. These techniques often provide only strong components present in the signal and fails to detect frequencies that have lower energy contents.

1.2 EMD & Its Variants for Modal Identification

Empirical mode decomposition is a powerful signal decomposition tool for nonlinear and nonstationary signals. An IMF generated for this purpose must satisfy the following two conditions – (1) the number of extrema and the number of zero-crossings must be either equal or differ at most by one, and (2) at any point, the mean value of the envelope defined by local maxima and minima is zero. The sifting process is implemented by identifying local extrema in the data ($y(t)$) between successive pairs of zero crossings and connecting them by a cubic spline line to create the envelope. If the envelope mean is e_1, the difference $y(t) - e_1 = I_1$ is the first IMF, provided it satisfies the necessary conditions. If not, the sifting process is repeated by treating I_1 as the original data until an IMF is obtained. The IMF is then subtracted from the original signal, and the sifting is continued to decompose the data into multiple IMFs [50]. Yang et. al. [85] applied HHT on the recorded free vibrations to identify the modal parameters. Chen et. al. [86] used HHT to analyze the typhoon induced vibration of Tsing-Ma suspension bridge where responses were processed through EMD to obtain the IMFs. Finally, RDT was applied to derive free decay of the structure, which were used to evaluate the modal parameters. He et. al. [87] used a combination of EMD and RDT to identify the modal parameters from the non-stationary responses of a railway bridge. Unlike any other time-frequency decomposition tools, EMD is capable of dealing with the nonlinear and nonstationary signals using an adaptive transformation and therefore has gained significant popularity in the field of structural condition assessment. In fact, EMD utilizes a single sensor for vibration measurement to extract a subset of modal information [51]. Because of its self-adaptive nature without requiring the use of basis function, EMD method has garnered much attention in the field of time-frequency decomposition. IMFs can identify modal frequencies that match well with those obtained using traditional peak-picking methods and finite element analysis. Yu and Ren [88] proposed EMD based stochastic subspace identification of civil infrastructure for operational modal analysis where measurements were first decomposed into modal responses using EMD with intermittency criteria. Stochastic subspace identification technique was then applied on the IMFs to evaluate the modal parameters. Yan and Miyamoto [89] compared the performance of HHT and WT using three different examples viz. numerically simulated response of a damped system with two closely spaced modes, impact test results from an experimental setup with three well separated modes and ambient vibration test of a benchmark bridge. Results showed that both WT and HHT performed well and one could not be preferred over the other. Although, HHT is a promising tool for feature extraction of non-stationary signals, it faces several challenges in system

identification due to the generation of spurious modes along with mode-mixing [84]. This problem is more prominent for systems with closely spaced modes and for modes with low energy content. Peng *et. al.* [82] used wavelet packet transformation to decompose a general signal into a set of narrow banded signals with single frequency component so that IMFs for each of them could be derived. Due to successive interpolation operation in the sifting process, IMFs obtained by the EMD are sensitive to noise and results in mode-mixing [90].

Recently, EMD has been successfully employed for modal identification of structural systems in conjunction with Hilbert Transform (e.g. Hilbert-Huang Tranform) [82, 83], where the mode-mixing is alleviated using band-pass filtering. EMD is also integrated with BSS [91, 92] and random decrement technique (RDT) [93] to perform modal identification using partial measurements. However, significant user intervention in the form of intermittency criteria based on band-pass filtering is a prerequisite in these methods. To alleviate this problem, different adaptive filtering schemes were developed by the previous researchers [82, 83, 94] to improve the performance of the traditional EMD scheme.

1.2.1 Multi-variate EMD (MEMD)

Standard EMD method primarily works only for a single real valued signal. While dealing with the measurements of multiple sensors, it faces two problems [95] – (a) there is no guarantee that the decomposed IMFs from multiple channels of measurements will match in terms of number or their frequency values and (b) joint information between multiple sensors are not exploited as the signals from multiple sensors are treated individually. Traditionally, EMD is based on the computation of local mean by averaging the envelopes. However, for multivariate signals, the local extrema may not be well defined. Moreover, the concept of modes in IMFs are not obvious for multivariate signals. To address these issues, multiple envelopes constructed by projecting the signal along different directions in a $n-$dimensional space as proposed by Rehman and Mandic [96, 97]. The envelop obtained from different projections are then averaged to obtain the local mean. Mapping a multivariate signal into many real-valued projected signals to generate the multi-dimensional envelopes, is a generalization of the bivariate and trivariate [98] extensions of the singular EMD algorithm.

Rehman and Mandic [96] have shown that trivariate EMD generate more points with greater concentration near the poles which they improve by a low-discrepancy Hammersley sampling [95]. They have also studied the performance of their multivariate EMD using ECG signals and have demonstrated its superiority over the traditional EMD techniques. The MEMD method has been successfully used to separate the source signals of multi-channels measurements of bio-medical applications [99] and mechanical systems [100]. However, mode mixing is still an issue [100] as in the standard EMD; although in much lesser proportion.

1.2.2 Other EMD Like Techniques

Besides conventional and multivariate EMD techniques, other proposals are available in the literature which use additional noise or *sinusoide* to mask the original signal. Wu and Huang [84] proposed an improvement (called Ensemble EMD or EEMD) over the conventional EMD to overcome the mode-mixing. They have shown that, mode-mixing occurs due to the presence of noise in the actual signal or response. As per their recommendations, addition of ensemble white noise can cancel out the noise present in the original signal. Wang *et. al.* [101] compared the performance of EMD and EEMD using geological data to evaluate the seismic profiles. In their study, they demonstrated significant improvement in EEMD. In another work, Yang *et. al.* [102] proposed an improvement of the numerical procedure to evaluate the envelope of maxima and minima of the signal. In the conventional EMD, after finding out the maxima/minima, a cubic spline was fitted to find out the two extreme envelopes of any signal. As per the new recommendation of Yang *et. al.* [102] a piecewise monotone polynomial function is used to evaluate the envelopes. With the help of synthetic signals, they demonstrated its performance and concluded that their proposal should provide smoother envelop for a signal with a sudden jump or unnatural peaks. Though this improvement did not address the major drawback of conventional EMD (i.e. mode-mixing or spurious mode in OMA), it offered a new way to find out smoother envelopes for better IMFs. On further improving this technique, Chen and Wang [103–105] developed Analytical Mode Decomposition (AMD) based on Bedrosian identity by masking the original signal with a known signal. According to this property (i.e. Bedrosian identity) HT of a fast varying signal masked by a slowly varying signal, acts over the fast varying component only. Thus, if a *sinusoide* with varying frequency component is used for masking the original signals, the original signal can be separated into two parts of lower and higher frequency components. Chen and Wang [103, 104] proved the potential of their proposal using synthetic response of discrete system vibrating due to initial condition only (i.e. free vibration).

1.3 WT and Its Advanced Version

Among all these methods, WT enjoys popularity for its robustness and better control over its parameters to get object oriented results. The main parameter in WT is the scale that decides the number of components into which the main signal is to be decomposed. With the increase of scale, an user can get finer details of the frequency contents. Thus, to decompose a signal containing very high frequency, the number of scale in this integral transformation also needs to be very high. In this context, relation between the scale and frequency is given by

$$a = \frac{f_c}{f_{ps}} \frac{1}{\Delta_f} \tag{1.1}$$

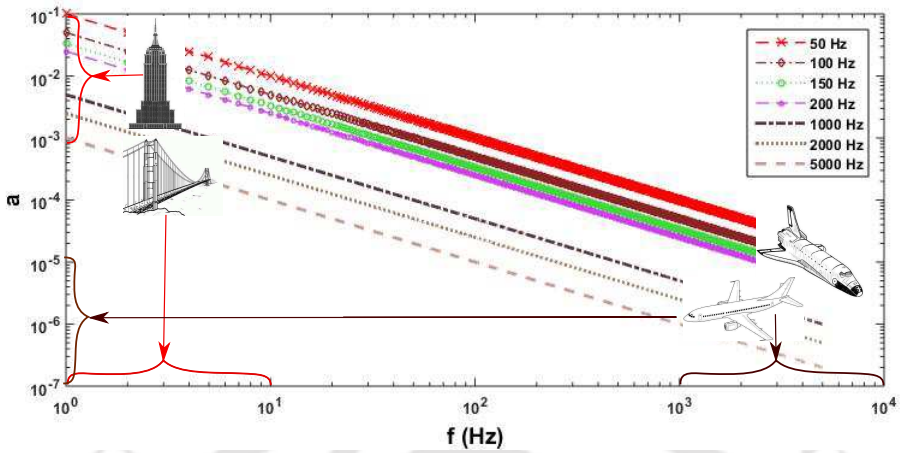

Figure 1.1: Scales for different frequency resolution

In the above relation, a, f_c, f_{ps} and Δ_f represent scale, central frequency, pseudo frequency and sampling rate, respectively. It clearly shows the typical dominant structural frequencies and their respective scales. For example, a cable stayed bridge can have higher modes excited during its operation that demands a different set of scales besides its regular structural modes which are much lower. Besides f_{ps}, the sampling rate Δ_f is also a deciding factor in the wavelet transformation which remains unchanged during an experiment. Thus, to get a higher level of accuracy, an user needs to go for the higher number of scales which, in turn, invokes more computational time. Though, computational time alone is not an issue in the inverse problem based health monitoring but an equal division of frequency scale in the area where frequencies are well apart produces a large amount of redundant data. Moreover, the participation of modal frequency may change depending upon many factors. Therefore, frequency tracking over a large range is a major challenge. It is also a major hurdle in case of real-time decision making and incorporating the result in close loop vibration control. This problem of frequency tracking over wider range also demands better resolution than the original wavelet transformation for a data with a prefixed sampling rate.

Recently, synchrosqueezed transformation (SST) [106, 107] is introduced over WT. This new technique is capable to enhance the resolution between two scales. Thus, it offers better clarity in the frequency localization. Due to this property, researchers have [108–114] adopted it for different applications i.e. separate out frequencies from a noisy signal, damage identification, frequency tracking etc. Yang [110] and Thakur *et. al.* [112] studied the efficiency of SST using a signal that contained different harmonic frequencies. They found that SST based algorithm can identify low frequency components due to its enhance resolution. In another study by Li and Liang [114], SST was used to identify the harmonic components of gearbox vibrations and damage, if any, by detecting the sifted harmonic components. In all these studies, SST showed impressive performance, though these applications were not very critical to solve using WT, as finer scales could perform the same task. Wu *et. al.* [107] showed mathematically that in spite of the improvement in resolution,

SST failed to identify closely spaced frequencies if it was not designed with proper judgment. Their study showed that if the difference in frequency of the two closely spaced modes were below the sampling rate, SST also failed to separate them and demanded finer sampling rate of the original signal. Besides sampling rate, frequency tracking itself offered several challenges as the response of a vibrating body contained dominant modes that might evolve with time, apart from the frequency content of the input excitation. In this context, it may be noted that spurious modes present in the transformed data also impose difficulty in modal identification.

1.4 Objectives

In view of the above discussion on the importance and necessity of the time-frequency based modal identification, following objectives are set for this thesis -

1. Develop an output only Hilbert-Huang transformation (HHT) based algorithm which can evaluate the modal parameters from the response of any linear time invariant (LTI) structure subjected to multi-component non-stationary ground motions. This has practical implication, as applying known force (e.g. impulse or sinusoid) to access structural health immediately after any seismic event is not recommended. Therefore, developing identification scheme based on earthquake response helps in decision making immediately after the event. Validate the proposed algorithm using synthetic experiment where the system behavior are defined in advance.

2. Implement the proposed Hilbert-Huang transformation based strategy to identify the modal parameters of a reinforced concrete framed building subjected to multi-component earthquake ground motions. In this context, limited measurements are used as measuring responses at all degrees of freedom (dof) has practical difficulties due to inaccessibility and limited availability of sensors.

3. Utilize the combined benefits of wavelet transformation and Hilbert transformation where continuous wavelet is proposed to be used as a leakage free bandpass filter while Hilbert transformation (not HHT) helps to evaluate the amplitude and phase modulation for modal identification. This efficient use of WT and HT bypass heuristic evaluation of intrinsic modes through empirical mode decomposition that often leads to spurious modes and mode mixing.

4. Develop an efficient modal identification strategy using synchrosqueezed wavelet transformation (SST). The main contribution, in this context, is to apply this signal processing tool to extract large number of frequencies with significant accuracy. Here, the major challenge is to separate the modal frequencies from other frequencies (e.g. excitation frequencies and

spurious modes) which are relatively difficult using conventional wavelet transform. Its performance is proposed to be demonstrated using both synthetic and experimental data.

5. Study the advantages and disadvantages of synchrosqueezed transformation based signal processing in the light of modal identification. Here, two main aspects are – (a) effects of resolution on the frequency tracking and (b) choice of basis function on the quality of the end results.

6. Develop an automated strategy by combining the synchrosqueezed transformation based signal processing with unsupervised machine learning to avoid user intermittency. In this context, it may be noted that wavelet transformation based modal identification needs significant intermittency in its popular approach using ridge and skeleton. To avoid this issue to make the modal identification strategy intelligent and self reliant, unsupervised machine learning is adopted to identify mode localization. This is proposed to be followed by phase spectrum analysis to detect modal frequency from an array of frequencies that contaminated with input frequencies and spurious modes, if any.

7. Once the algorithm is automated, it is further adopted to estimate uncertainty associated with the natural frequencies of a structure whose system matrices are random. These random eigen values are planned to be estimated from the measured responses applying the proposed identification strategy. Once the parameters are identified, the uncertainty associated with the natural frequencies are quantified in the probabilistic framework. This SST based automated modal identification strategy for stochastic eigen value problem is proposed to be validated using experimental results.

1.5 Organization of Thesis

The main objective of this thesis is to improve the efficiency of the time-frequency techniques (in particular HHT and WT) to apply them for OMA using forced response. The work carried out to meet the above objectives in this thesis are organized as follows -

- In Chapter 1, the literature review on different time-frequency analyses proposed in the published works are presented. Major emphasis is given on short time Fourier transformation, Hilbert transformation and its variants and wavelet transformation. The state of the art presented in this section clearly shows the scope of work to further improve these methods for OMA using forced response. With this in view, objectives are set to meet this goal. Section 1.4 outlines these objectives in detail followed by description on the organization of this thesis.

- Chapter 2 provides an overview of the available time-frequency analysis in literature. The development of these methodologies with their mathematical background are discussed here. This is followed by numerical implementation of these techniques for modal identification.

- Improvisation of the available time-frequency analyses are discussed in Chapter 3. The main contribution of this thesis is the adaptive use of time-frequency analysis where drawbacks of traditional techniques are addressed by tuning them for OMA using forced responses. First, pre-filtering is used where Butterworth filters are used adaptively for EMD analysis to avoid spurious modes and mode mixing. Next, the benefits of MEMD are utilized to improve the performance of EMD in the same adaptive framework. This idea is further developed by combining the wavelet and Hilbert transformation (not EMD). Here, continuous wavelet transformation is used as a pre-filter followed by Hilbert transformation. This helps to bypass unnecessary and time consuming empirical mode decomposition. This study motivates to revisit the wavelet transformation where an advanced version (i.e. synchrosqueez transformation) can be adopted for OMA. All these algorithms are discussed and the simulated example cases are presented in this chapter.

- The real life application of the proposed methods are presented in Chapter 4. The forced response of building and bridge structures are considered for their modal parameter estimation. For this purpose, a full scale building and bridge in IIT Guwahati campus are used as the test setup whose seismic responses are used to verify the accuracy of the proposed methodologies. Finite element modal updating is used here in conjunction with the time-frequency analysis for mode shape estimation as field implementation restricts the number of sensors to estimate the mode shape directly from the measurements. The effectiveness of the proposed methods are compared with other conventional methods.

- Chapter 5 addresses the use of the proposed operational modal analysis for uncertainty quantification associated with random eigen value problems. In this concept, random frequencies are detected from the measured response automatically without any user intervention. This strategy is repeated for an ensemble of experiments to develop the underlying probability distribution associated with the identified modal frequencies. The outcomes of this experimental investigation are compared with the predefined probabilistic features of the random eigen values to quantify the reliability of the identified modes in mean sense.

- Finally, Chapter 6 concludes the major contribution of this thesis towards operational modal analysis in time-frequency domain. This is followed by a discussion on the possible avenues of future research to extend these methods for other challenging problems.

Chapter 2

Time-Frequency Analysis

Amon all the signal processing techniques, time-frequency analysis stands different for its ability to provide information on both temporal (i.e. time) and frequency domain. To perform signal processing using this technique requires least information about the system as it purely based on the recorded signals only. This advantage gives it more popularity to apply them for physical dynamic problems. The changes in physical systems are reflected in the response and by applying time-frequency analysis, these changes can be detected. In the domain of civil infrastructure, these changes are very slow in nature and it takes decades to make any observable variation. Thus, it require periodic monitoring of the structure which comes under paradigm of parametric system identification or inverse problem.

In this chapter, the non-adaptive time-frequency methods available in the literature are discussed. The term 'non-adaptive' used here is purely based on the structural dynamic response. This term used for methods which could not eschew the problem faced in vibration based signal processing (mode-mixing, source separation are few problems among all others). The first technique discussed here is Fourier transformation which is a frequency domain analysis. However, Fourier transformation is discussed here as it is the foundation for development of many time-frequency methods. This is followed by windowed Fourier transformation (i.e. Short-time Fourier transformation), Hilbert-Huang transformation with its variants and wavelet transformation which are popular time-frequency analysis tools.

2.1 Fourier transformation

Fourier transform falls under the category of frequency domain method where a time function $x(t)$ is transformed into frequency domain as follow

$$X(\omega) = \frac{1}{\sqrt{2\pi}} \int_{-\infty}^{\infty} x(t) e^{-\mathrm{j}\omega t} dt \tag{2.1}$$

In the above equation, $\mathrm{j} = \sqrt{-1}$ and $e^{-\mathrm{j}\omega t}$ is the kernal or basis function used in this transformation. The inverse Fourier transform takes the following form to get back the original time function $x(t)$

$$x(t) = \frac{1}{\sqrt{2\pi}} \int_{-\infty}^{\infty} X(\omega) e^{\mathrm{j}\omega t} d\omega \tag{2.2}$$

In this context, it may be noted that energy of the signal in both time and frequency domain remains same (i.e. Perseval Identity conserved) which indicates that

$$\int_{-\infty}^{\infty} |x(t)|^2 dt = \frac{1}{2\pi} \int_{-\infty}^{\infty} |X(\omega)|^2 d\omega \tag{2.3}$$

Here, the time signal must satisfy the following criterion for this transform

- $\int_{-\infty}^{\infty} |x(t)| dt$ exist (i.e. signal should have finite energy content)
- The time function $x(t)$ should have finite number of discontinuity
- The signal should have bounded variation

Once the signal used in forward transformation (i.e. Eq. 2.1), it can be reconstructed point wise by Eq. (2.2). Fourier transformation is applicable to both continuous and discrete functions i.e.

$$x(t) = \begin{cases} \int_{-\infty}^{\infty} e^{j\omega t} \left[\int_{-\infty}^{\infty} x(t) e^{-j\omega t} dt \right] d\omega & \text{for } x(t) \text{ continuous at } t \\ \frac{1}{2} \left[x(t_+) + x(t_-) \right] & \text{for } x(t) \text{ discontinuous at } t \end{cases} \tag{2.4}$$

Let us consider a signal $x(t)$ contaminated with noise which takes the following form

$$x(t) = 12 \cos(2\pi 4t) + 15 \sin(2 * \pi 9t) + \epsilon_{noise} \tag{2.5}$$

The signal is shown in Fig. 2.1(a) and its Fourier transform as in Eq. (2.1) is invoked to identify the frequencies. Fourier amplitude spectrum is presented in Fig. 2.1(b). From this Fourier spectrum, the two contributing frequencies are clearly visible. Here, it needs to be mentioned that for demonstration purpose, a harmonic signal is chosen with added zero mean Gaussian white noise to

replicate the real measurements. From these plots, it can be observed that though Fourier spectrum is able to locate the contributing frequencies, but it may not be always conclusive due to the presence of noise. The contribution of noise is observed in Fig. 2.1(b). There are oscillations around mean component of the signal. In practical applications, if the contribution of noise is high then it may be difficult to identify the peaks from Fourier spectrum, even for signals that are represented by additive sinusoid as in Eq. (2.5). Now, let us consider a signal which has sinusoids

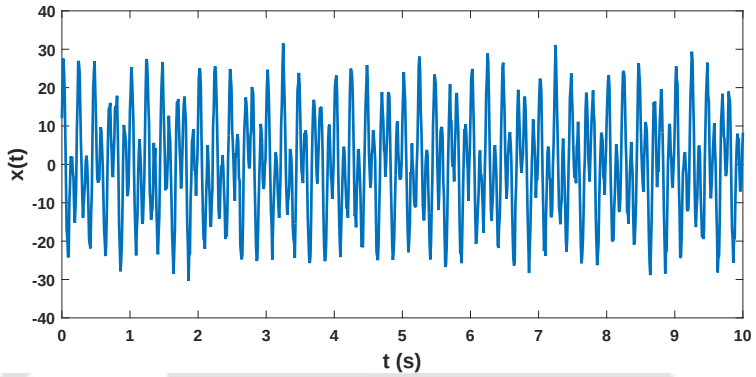

(a)

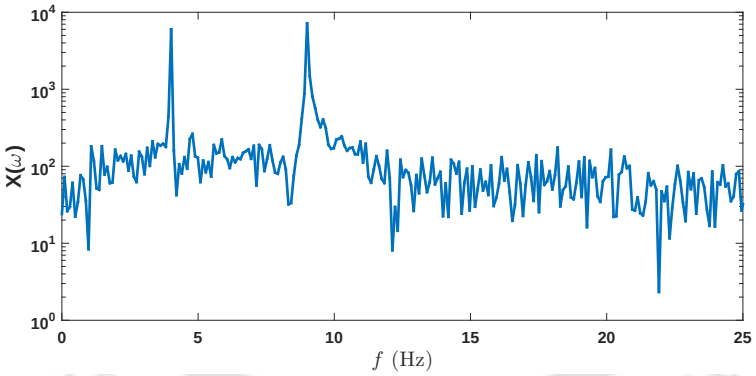

(b)

Figure 2.1: Noise contaminated signal $x(t)$ (a) Time history and (b) Fourier amplitude spectrum

in the product form. The Fourier transformation of these type of modulation is given by

$$\begin{aligned} F_t\left[\cos(2\pi\omega_0 t)x(t)\right](\omega) &\equiv \frac{1}{\sqrt{2\pi}}\int_{-\infty}^{\infty} x(t)\cos(2\pi\omega_0 t)e^{-j\omega t}dt \\ &= \frac{1}{2}\left[X(\omega-\omega_0)+X(\omega+\omega_0)\right] \end{aligned} \tag{2.6}$$

Above equation shows that if multiple *sine/cosine* signals are present in the product form, modulated frequencies are obtained from Fourier transformation instead of the component frequencies. To elaborate it further, using the components of the signal in Eq. (2.5) a new signal is constructed

as follows

$$x(t) = \{12\cos(2\pi 4t)\}\{15\sin(2\pi 9t)\} + \epsilon_{noise} \tag{2.7}$$

It is shown in Fig. 2.2(a) whereas its Fourier amplitude spectrum is shown in Fig. 2.2 which shows frequencies near 5 and 13 Hz. From this analysis, it can be concluded that Fourier transform fails

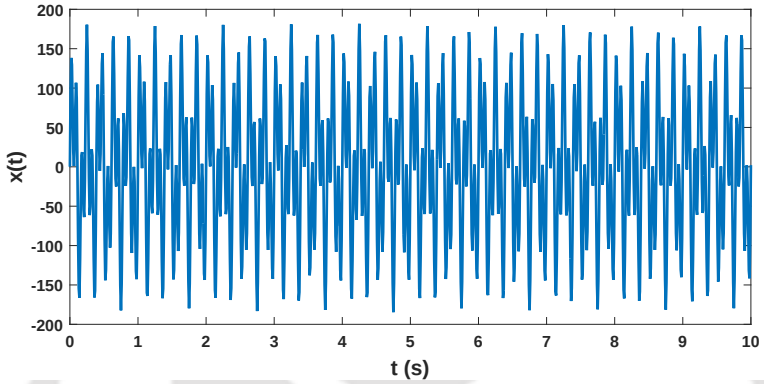

(a)

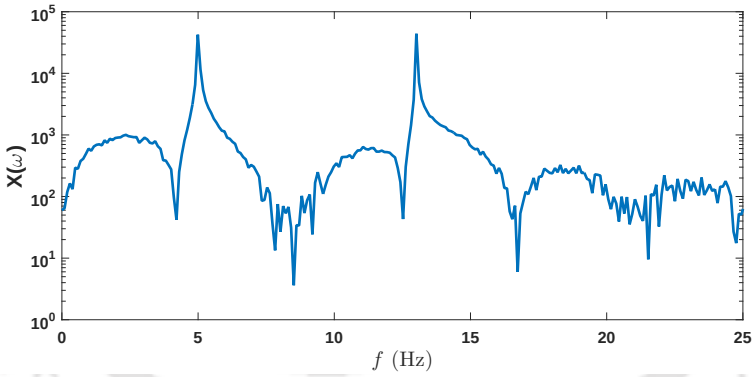

(b)

Figure 2.2: Fourier transformation of modulated signal - (a) Time history and (b) Fourier amplitude spectrum

to distinguish the two frequencies of the signal which are modulated as shown in Eq. (2.7) and Fig. (2.2). Finally, a sineswipe is considered whose amplitude is unity and the frequency changes quadratically from 0 to 5Hz in 0 to 5sec as shown in Fig. 2.3(a). Fig. 2.3(b) shows its Fourier spectrum, where the evolution of the underlying frequencies are not detected and the frequency signature in Fig. 2.3(b) shows the amplitude spectrum which does not corresponds to the physical problem. This, in tern, demands a more powerful signal processing tool for frequency tracking and hence, the time-frequency analysis comes to reality.

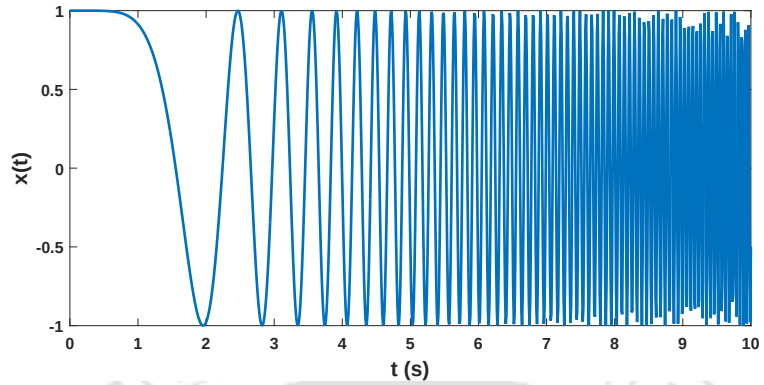

(a)

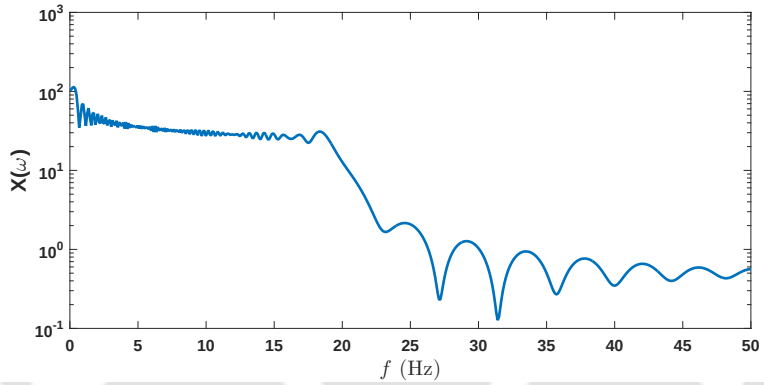

(b)

Figure 2.3: Fourier transformation of a frequency modulated signal (a) Time history and (b) Fourier amplitude spectrum

2.1.1 Short Time Fourier Transform

As discussed in the previous subsection, Fourier transformation is unable to detect the change in frequency content over time. To overcome this issue, Fourier transformation is modified with a window function which divides the signal into parts and perform the Fourier transformation over that window which is popularly called short-time Fourier transform (STFT). So, short time Fourier transformation is given as [115]

$$F_{STFT}(t,\omega) = \frac{1}{\sqrt{2\pi}} \int_{-\infty}^{\infty} x(t) h^*(t-u) e^{-\mathrm{j}\omega t} dt \tag{2.8}$$

In the above equation, $h(u)$ is the window function. Different functions are proposed in the literature [115] as the time window for this modified Fourier transform e.g. rectangular, Gaussian, Hann etc. The spectral power of the STFT is calculated by taking square of the modulus of the transformation

i.e.

$$SP(t,\omega) = \left| \frac{1}{\sqrt{2\pi}} \int_{-\infty}^{\infty} x(t) h^*(t-u) e^{-\mathrm{j}\omega t} dt \right|^2 \tag{2.9}$$

In general, graphical representation of the spectral power is refereed as the spectrogram. The rationale behind the selection of a window is the assumption that within the time window, spectral power will not change. Hence, a longer window can not capture the rapid change in power of the signal. On other side, if window is too short then it smudges the time-frequency distribution. If a monocomponent signal with constant amplitude is considered, then the optimal window duration will be guided by the change in instantaneous frequency ($\omega(t)$). For a rectangular type of window it can be shown that the duration δt of the window is given by [116]

$$\delta t = \sqrt{2} \left| \frac{d}{dt} \omega(t) \right|^{-1/2} \tag{2.10}$$

The STFT discussed above is applied on the signal shown in Fig. 2.3(a). Fig. 2.4(a), shows the scalogram of the signal with three different window lengths. It can be observed that with the frequency information, it gives the time instances of corresponding frequencies also. In this case, it shows very good localization time but in corresponding frequency is not so good. If the width of the window is reduce to 0.10sec then the frequency localization is improved as shown in Fig. 2.4(b). Finally, window width is reduced to 0.02sec and the scalogram is shown in Fig. 2.4(c). Though spectrogram provides information regarding time and frequency simultaneously but it is a compromise between them. The energy density in time is dependent on $|x(t)|^2$ whereas $|X(\omega)|^2$ represents frequency domain energy. In time-frequency analysis, these two parameters are related by the uncertainty principle as given follow [117, 118]

$$\Delta t . \Delta \omega \geq \frac{1}{2} \tag{2.11}$$

Here, Δt and $\Delta \omega$ represents the time and frequency resolutions respectively. From this relation, it is clear that if the time resolution is increased the frequency resolution will narrow down and vice-versa.

2.2 Hilbert Transformation

Let us consider, an integral in the complex z-plane of the form $\oint_\Gamma \frac{q(t)}{t-a} dt$ which is commonly referred as Cauchy integral [49]. If $q(t)$ is an analytic signal and Γ is a piecewise smooth close-contour in

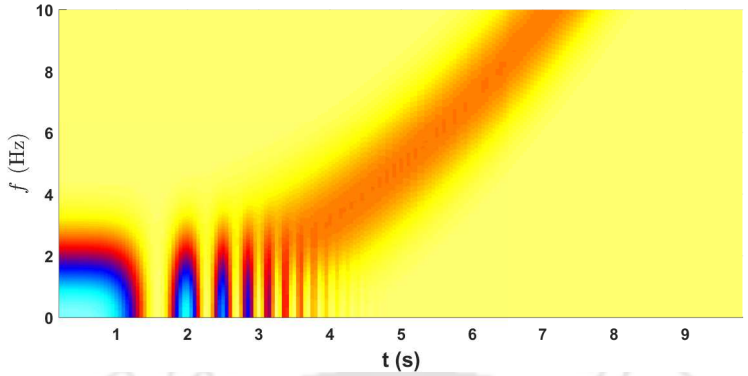

(a)

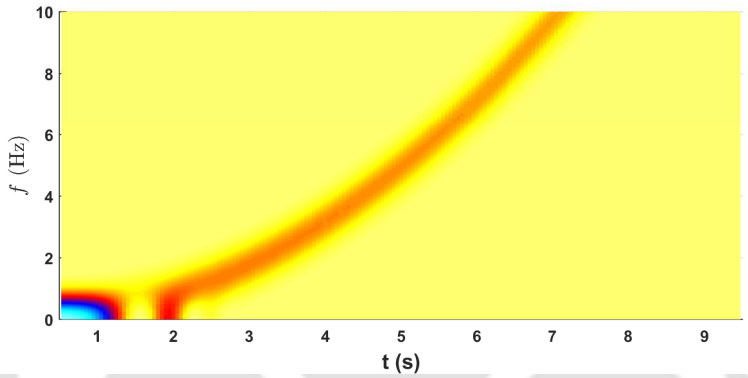

(b)

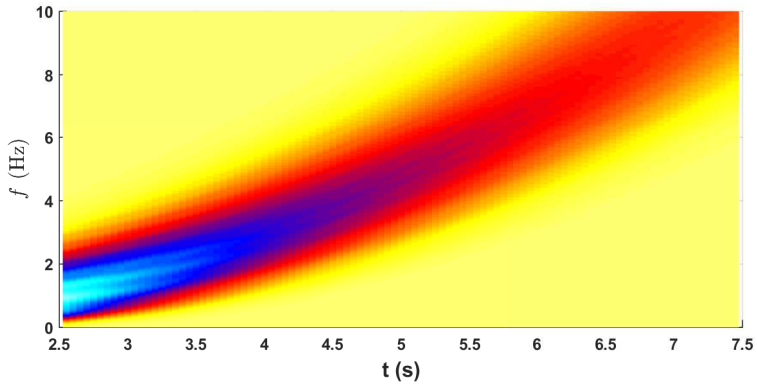

(c)

Figure 2.4: Short time Fourier transformation with (a) 0.33sec window, (b) 0.10sec window and (c) 0.02sec window

an open domain as shown in Fig. 2.5(a), then the Cauchy integral theorem is applicable as follows

$$\begin{aligned} \oint_{\Gamma} \frac{q(t)}{t-a} dt &= 2\pi j q(a) \quad \text{if } a \text{ is inside } \Gamma \\ &= 0 \quad \text{if } a \text{ is outside } \Gamma \end{aligned} \tag{2.12}$$

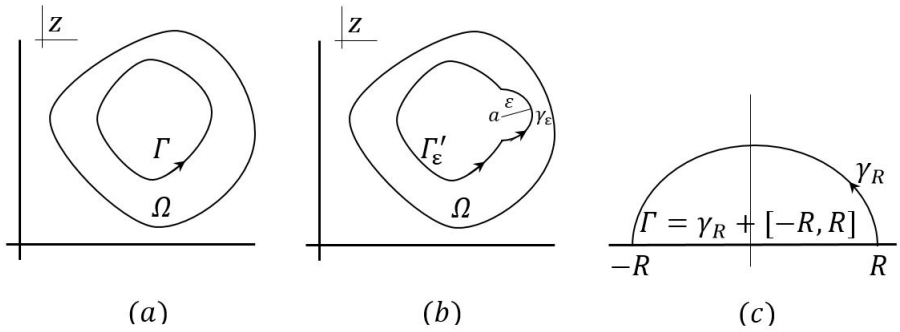

Figure 2.5: Piecewise smooth close-contour for (a) Γ in open domain, (b) Γ'_ε in open domain and (c) Limit of Γ

To find the result when a lies on Γ, a new contour Γ'_ε is created as in Fig. 2.5(b) where

$$\oint_{\Gamma'_\varepsilon} \frac{q(t)}{t-a} dt = 2\pi j q(a) \tag{2.13}$$

If the radius ε of the semicircle γ_ε tends to zero, the contribution from the semicircle γ_ε to the integral along Γ'_ε approaches $\pi j q(a)$ as shown by Saff and Snider [119]. So, the integral of the Cauchy principle value is

$$P\int_{\Gamma} \frac{q(t)}{t-a} dt = \lim_{\varepsilon\to 0} \int_{\Gamma'_\varepsilon} \frac{q(t)}{t-a} dt = \pi j q(a) \tag{2.14}$$

A particularly useful identity arises when the contour Γ as shown in Fig. 2.5(c) is closed by the semicircle γ_R and the real x-axis. If $q(t)$ is a function that is analytic in an open region that contains the upper half-plane and tends to zero at infinity in such a rate that the contribution from the semicircle γ_R vanishes as $R \to \infty$, then we have

$$P\int_{\infty}^{\infty} \frac{q(\tau)}{\tau - x} d\tau = \pi j q(x) \tag{2.15}$$

This forms the backbone of Hilbert transformation based time-frequency analysis. Unlike the other transformation (e.g. Fourier transformation, Laplace transformation), Hilbert transformation (HT) does not change the domain of signal (i.e. from time to frequency). It alternates the signal in between real and imaginary field by shifting the phase of the original signal. Hilbert transform gained popularity in the science and engineering [120] when researcher faced the need to represent a random signal as a product of an envelope (i.e. amplitude modulation) and a phase function. The first use of HT in engineering application was done by Lee [121] on electrical network. The Hilbert transform of signal $q(t)$ having finite energy in $L^2(\mathbb{R})$ space is given by [49]

$$\tilde{q}(t) = \mathscr{H}[q(t)] = \int_{-\infty}^{\infty} q(\tau) L(t-\tau) d\tau \tag{2.16}$$

If a signal is represented as a product of a slow varying and fast varying functions, HT of the signal acts on the fast varying component only, keeping slow varying component unaffected i.e.

$$\mathscr{H}[\{n_{slow}(t) + n_{fast}(t)\}x(t)] = n_{slow}(t)\tilde{x}(t) + \tilde{n}_{fast}(t)x(t) \tag{2.17}$$

The above expression is known as Bedrosian Identity [122]. In system identification, first HT was applied by Simon and Tomlinson [123, 124] to detect any change in the frequency response function. The parameters of a single degrees of freedom system was identified by Feldman [125, 126] using HT.

In general, it is applied to form the analytic signal which has two dimension with real and imaginary components as given here

$$\mathbf{Q}(t) = q(t) + j\tilde{q}(t) = \mathbf{Q}_a(t)e^{\mathrm{j}\mathbf{Q}_\lambda(t)} \tag{2.18}$$

Here, $\mathbf{Q}_a$ is the instantaneous amplitude and $\mathbf{Q}_\lambda$ is the instantaneous phase angle of the analytic signal which are given by

$$\mathbf{Q}_a = [q^2(t) + \tilde{q}^2(t)]^{1/2} \tag{2.19}$$

and

$$\mathbf{Q}_\lambda = \tan^{-1}\left[\frac{\tilde{q}(t)}{q(t)}\right] = 2\pi\omega t \tag{2.20}$$

On differentiating both sides of the above equation, it can be shown that the instantaneous angular frequency of the original signal $q(t)$ is

$$\omega = \frac{1}{2\pi}\frac{d\mathbf{Q}_\lambda}{dt} \tag{2.21}$$

In Fig. 2.6, projection of Hilbert transformation and the formation of the analytic signal are shown for the following signal

$$x(t) = e^{-0.2t}\cos(2\pi t) \tag{2.22}$$

Hilbert transformation of the above signal is given by

$$\tilde{x}(t) = \mathscr{H}[x(t)] = e^{-0.2t}\sin(2\pi t) \tag{2.23}$$

According to Eq. (2.18), the analytic signal takes the following form

$$X(t) = x(t) + j\tilde{x}(t) = e^{-0.2t}\cos(2\pi t) + \mathrm{j}e^{-0.2t}\sin(2\pi t) = e^{-0.2t}e^{\mathrm{j}2\pi t} = x_a(t)e^{\mathrm{j}x_\lambda(t)} \tag{2.24}$$

Thus, the instantaneous amplitude of the signal is $x_a(t)$ and instantaneous phase is $x_\lambda(t)$. From this expression, instantaneous frequency can be calculated as follow

$$\omega_{inst} = \frac{dx_\lambda(t)}{dt} \tag{2.25}$$

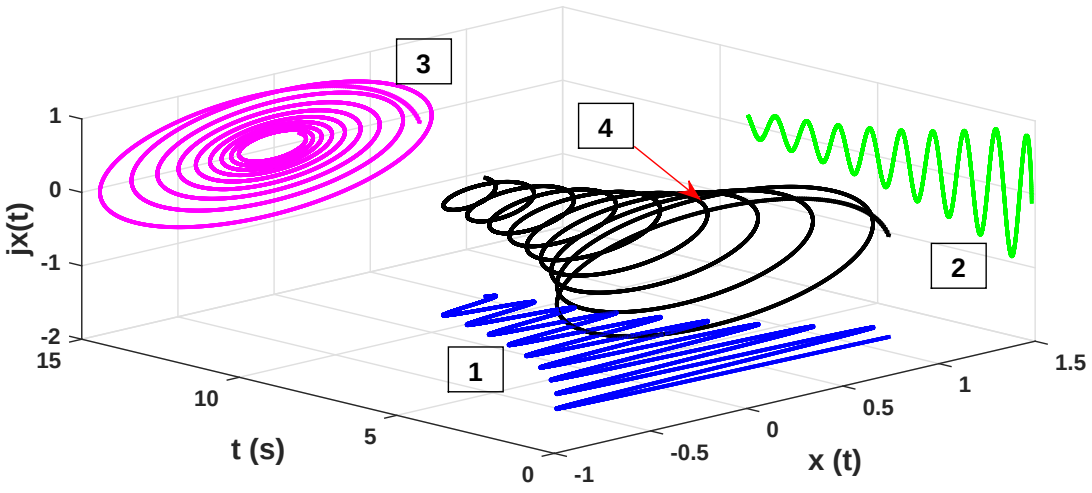

Figure 2.6: Analytic signal and its projection

Using the above formulation, the instantaneous frequency of the signal given in Eq. (2.22) is tracked by HT. Fig. 2.6 shows the details of this transform where every component signals are marked by numerics. In this notation, signal marked 1 in Fig. 2.6 shows the original time function while signal marked 2 represents the HT of 1. Together this two constitute the analytical signal (i.e. 4) and the signal marked 3 shows the instantaneous amplitude (i.e. radial distant from the origin) and instantaneous phase (i.e. radial direction).

2.2.1 Hilbert-Huang Transformation

The previous subsection demonstrates that instantaneous frequency of a monocomponent signal can be obtained by HT. But in practice, most of the signals obtained from the vibrating structure are not monocomponent in nature (i.e they have more than one dominant frequencies). To overcome this issue Huang *et. al.* [50, 59] proposed a method which will decompose the multicomponent signal into monocomponents which are popularly known as intrinsic mode functions (IMFs) and the method is termed as empirical mode decomposition (EMD). Though the methodology is heuristic, it works in different applications [127, 128]. The process of EMD is designed in such a way that each IMF has exactly same number of extrema and zero crossing or at most they differ by one. Therefor, each IMF represents an oscillatory motion corresponding to a particular frequency which is present in the original signal. For brevity, only the key steps to generate IMF filter banks of a signal are outlined here –

- Identify maxima and minima in the original signal and fit cubic splines at these maxima and minima to model the envelopes.

- Evaluate the mean from two cubic splines corresponding to maxima and minima.
- Subtract the mean from the original signal.
- The above iteration will continue until (a) the number of extrema and zeros differ at most by one in the obtained signal or (b) ε goes below tolerance, where ε is given by

$$\varepsilon = \frac{(h^{j-1} - h^j)^2}{(h^j)^2} \tag{2.26}$$

In the above equation, h^j is the signal after subtraction of mean of extrema in the j^{th} iteration.

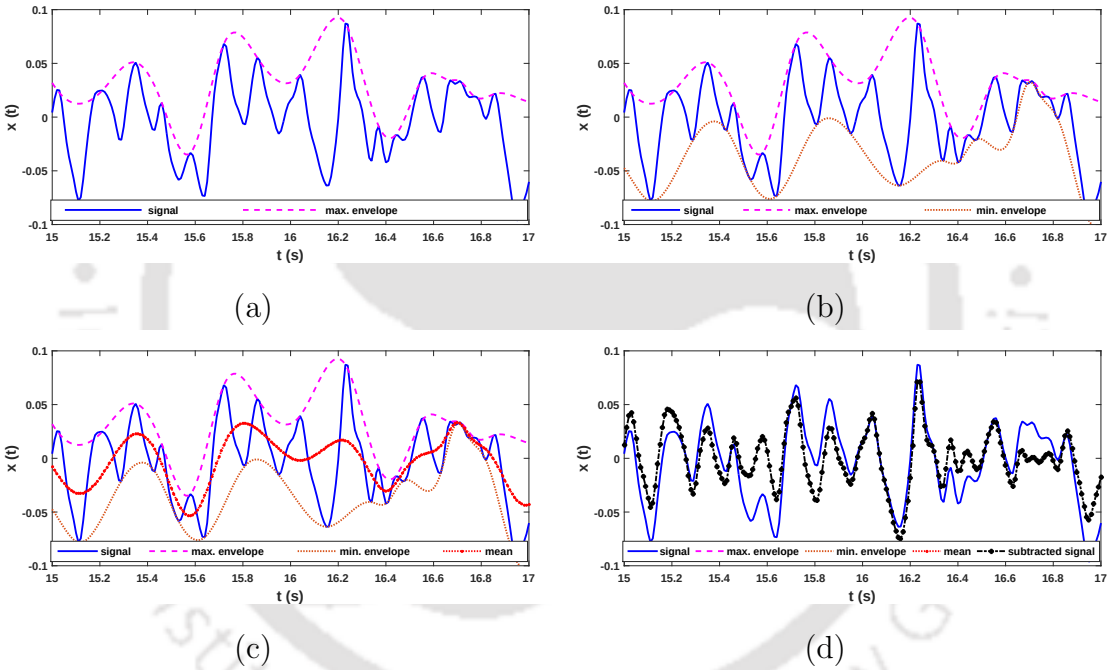

Figure 2.7: Steps of IMF extraction (a) max. envelope, (b) min. envelope, (c) mean estimation and (d) subtracted signal

Fig. 2.7 shows, the steps to estimate the IMF of a typical signal. Using the above mentioned steps, one can decompose the non-stationary signal $x(t)$ in to its filter banks (i.e. IMFs) which is represented by

$$x(t) = \sum_{j=1}^{n} (\text{IMF})_j + R_n(t) \tag{2.27}$$

The above equation shows that a linear summation of all IMFs in the filter bank and the residual $R_n(t)$ gives back a point wise reconstruction the original signal. Once the complete set of IMFs are generated, HT can be employed as outlined in Eq. (2.16) to Eq. (2.25) to estimate the instantaneous frequency content and the phase of the signal $x(t)$.

2.2.2 Ensembled EMD

Above discussion on EMD reveals the adaptation of HT for instantaneous frequency tracking of a non-stationary signal. In this process, IMFs are generated with an assumption that monocomponent signals are derived from the original time function so that it paves the path for Hilbert transformation. In reality, the IMFs often suffers contamination due to contiguous frequencies. This ultimately affects the quality of instantaneous frequency estimation and hence needs further improvements. With this in view, Wu and Huang [84] developed a modified version of EMD which is termed as ensemble EMD. While working with traditional HHT they observed that –

- the reason of mode mixing is due to be presence of noise which can be nullified in time domain by masking with artificial noise with appropriate amplitude.
- this artificial noise augmentation helps to develop the dyadic filter bank as opposed to the original IMFs that are contaminated by the adjacent frequencies.
- as ensemble averaging after augmenting with simulated white noise improves the quality of the IMFs.

The fundamental steps for Ensemble Empirical Mode Decomposition are given bellow

- recorded data is modified by adding a zero mean Gaussian white noise
- IMFs are extracted from the noisy data
- step 1 and 2 are repeated for ensemble average
- ensembled average IMFs are obtained as final results

To evaluate the number (N) of white noise in the ensemble and its amplitude υ, Wu and Huang [84] proposed following relation using standard deviation υ_n

$$\upsilon_n = \frac{\upsilon}{\sqrt{\mathrm{N}}} \tag{2.28}$$

From the above expression, it is clear that the magnitude of the additional white noise does not depends on the magnitude of actual the signal.

2.2.3 Analytical Mode Decomposition

In another proposal to improve the performance of EMD, Chen and Wang [103, 104] used the property of Bedrosian Identity and developed EMD like technique which they termed as analytical

mode decomposition (AMD). As per this proposal, a signal $x(t)$ can be separated out as

$$x(t) = x_1(t) + x_2(t) \tag{2.29}$$

where, $x_1(t)$ has frequency component less than ω_b while $x_2(t)$ has frequency component greater than ω_b. They assumed a set of *sine* and *cosine* functions with frequency ω_b (i.e $s_s(t) = \sin(\omega_b t)$ and $s_c = \cos(\omega_b t)$) to mask the original signal. After this signal masking, Hilbert transform was performed i.e.

$$\mathscr{H}[s_s(t)x(t)] = \mathscr{H}[s_s(t)x_1(t)] + \mathscr{H}[s_s(t)x_2(t)] \tag{2.30a}$$
$$\mathscr{H}[s_c(t)x(t)] = \mathscr{H}[s_c(t)x_1(t)] + \mathscr{H}[s_c(t)x_2(t)] \tag{2.30b}$$

According to Bedrosian Identity as explained in Eq. (2.17), the above set of equation can be modified as

$$\mathscr{H}[s_s(t)x(t)] = x_1(t)\mathscr{H}[s_s(t)] + s_s(t)\mathscr{H}[x_2(t)] \tag{2.31a}$$
$$\mathscr{H}[s_c(t)x(t)] = x_1(t)\mathscr{H}[s_c(t)] + s_c(t)\mathscr{H}[x_2(t)] \tag{2.31b}$$

From above equations, $x_1(t)$ and $\mathscr{H}[x_2(t)]$ can be derived as

$$x_1(t) = [s_c(t)\mathscr{H}[s_c(t)x(t)] - s_c(t)\mathscr{H}[s_s(t)x(t)]][s_s(t)\mathscr{H}[s_c(t)] - s_c(t)\mathscr{H}[s_s(t)]]^{-1} \tag{2.32a}$$
$$\mathscr{H}[x_2(t)] = [\mathscr{H}[s_c(t)]\mathscr{H}[s_s(t)x(t)] - \mathscr{H}[s_s(t)]\mathscr{H}[s_c(t)x(t)]][s_s(t)\mathscr{H}[s_c(t)] - s_c(t)\mathscr{H}[s_s(t)]]^{-1} \tag{2.32b}$$

Using the above set of equations, the components of the original time function can be separated out. This property of AMD can be utilized to identify the modal frequency of linear dynamic systems.

2.2.4 Multivariate EMD

Traditionally, EMD is based on the computation of local mean by averaging the envelopes. However, for multivariate signals, the local extrema may not be well defined. Moreover, the concept of modes in IMFs is not obvious for multivariate signals. To address these issues, multiple envelopes constructed by projecting the signal along different directions in a $n-$dimensional space as proposed by Rehman and Mandic [96, 97]. The envelop obtained from different projections are then averaged to obtain the local mean. Mapping a multivariate signal into many real-valued projected signals to generate the multi-dimensional envelopes, is a generalization of the bivariate and trivariate [98] extensions of the singular EMD algorithm.

The estimation of local mean entails finding a suitable set of direction vectors to perform integration of all the envelopes along those directions in the $n-$dimensional space. The procedure involves uniform angular sampling along a $n-$hypersphere which is a generalization of the surface of an ordinary sphere to arbitrary dimension. For any natural number n, an $n-$hypersphere of radius r is defined as the set of points in $(n+1)-$dimensional Euclidean space which are at distance r from the center. Let $\{\theta_i : \ i = 1-(n-1)\}$ be $(n-1)$ angular coordinates, then an $n-$dimensional coordinate system having $\{x_i\}_{i=1}^{n}$ as the n coordinates on a unit $(n-1)$ sphere are given by

$$x_{n-1} = \left(\prod_{i=1}^{n-2} \sin(\theta_i)\right) \cos(n-1) \tag{2.33}$$

As for example, a $2-$dimensional case in the 3 coordinates can be written as

$$\begin{aligned} x_1 &= \cos(\theta_1) \\ x_2 &= \sin(\theta_1) \times \cos(\theta_2) \\ x_3 &= \sin(\theta_1) \times \sin(\theta_2) \times \cos(\theta_3) \end{aligned} \tag{2.34}$$

Uniform angular sampling method is adequate for bivariate signals, as it produces non-uniformly distributed samples. For trivariate signals, it generates the points having greater concentration at poles of the sphere [98]. To address this problem, a low-discrepancy Hammersley [96, 95] sampling scheme is used to generate the direction vectors in $4-$dimension space. The discrepancy estimates for Hammersely sampling is better compared to other sampling methods (like importance sampling, uniform angular sampling), and thus, it provides more uniformly distributed sampling on a sphere [96]. This, in turn, gives a suitable set of direction vectors for generating signal projections and the corresponding signal envelopes, ensuring enhanced local mean estimates. For the details on Hammersely sampling, the readers may refer to Rehman and Mandic [96].

Consider a sequence of n-dimensional vectors $\mathbf{y}(\mathbf{t}) = \{y_1(t), y_2(t), ..., y_n(t)\}$ that represents a multivariate signal with n components, and $D^k = \{d_1^k, d_2^k, ..., d_n^k\}$ denotes a set of direction vectors along the k^{th} directions on a $(n-1)$ sphere. Then MEMD is performed using the following steps [97]

- Choose a suitable set of direction vectors, D, using Hammersley sequence
- Calculate the k^{th} projection, $p^k(t)$ of the input signal $\mathbf{y}(\mathbf{t})$ along the k^{th} direction vector, X^k, for all k (i.e. $k = 1, 2, ..., L$ where L is the total number of direction vectors in D)
- Find the time instants, t_i^k corresponding to the maxima of the projected signal, $p^k(t)$ for all k
- Interpolate $[t_i^k, \mathbf{y}(\mathbf{t_i^k})]$ to obtain multivariate envelopes, $e^k(t)$, for all k

- For a set of L direction vectors, the mean $E(t)$ of the envelope curves is obtained as

$$E(t) = \frac{1}{l}\sum_{k=1}^{L} e^k(t) \tag{2.35}$$

- Extract the residual $r(t)$ using $r(t) = y(t) - E(t)$. If $r(t)$ satisfies the stoppage criterion for a multivariate IMF, apply the above steps to $(y(t) - r(t))$ to extract the IMF $(\tilde{i}(t))$, otherwise apply it to $r(t)$

2.3 Wavelet Transformation

Beside STFT and HHT, wavelet transform is also a powerful time-frequency analysis tool often referred by the scientist and engineers. The source of the word *wavelet* is traced back to French word *ondelette* which stands for 'small wave' and it is endorsed by Morlet and Grossmann [129, 130] in 80's of the previous century. Wavelet is able to transform a signal into time-frequency spectrum like windowed fourier transform or STFT. Compare to STFT, the window function is replaced by a riding function in wavelet transformation (WT) which provides better spectral resolution.

2.3.1 Continuous Wavelet transformation

An overview of continuous wavelet transform and different basis functions used in this thesis are discussed here. Continuous wavelet transform of signal with finite energy in $L^2(\mathbb{R})$ (i.e. Hilbert space) provides a two dimensional array that shows the time localized frequency content of the signal. The wavelet transform of a time function $x(t)$ is expressed by following integral [118]

$$W_\psi x(a,b) = \frac{1}{\sqrt{|a|}}\int_{-\infty}^{+\infty} x(t)\psi^*\left(\frac{t-b}{a}\right)dt \qquad a \in \Re^+;\ b \in \Re \tag{2.36}$$

In the above equation, a corresponds to scale while b represents time localization. $W_\psi x(a,b)$ are the wavelet coefficients corresponding to a given a and b. Here, $\psi(\cdot)$ is the mother wavelet and the $()^*$ represents complex conjugate. On inverse transforming Eq. (2.36), the original signal $x(t)$ is obtained as follows

$$x(t) = \frac{1}{2\pi C_\psi}\int_{-\infty}^{+\infty}\int_{-\infty}^{+\infty}\frac{1}{a^2}W_\psi x(a,b)\psi_{a,b}(t)\,dadb \tag{2.37}$$

Parameter C_ψ in the above equation is the admissibility criteria that dictates the necessary condition for $\psi(\cdot)$ to be a basis function which is given by

$$C_\psi = \int_{-\infty}^{+\infty} \frac{|\psi(\omega)|^2}{|\omega|} d\omega \qquad 0 < C_\psi < \infty \tag{2.38}$$

The function $\psi_{a,b}(t)$ in Eq. (2.37) represents the dilated time localized version of the mother wavelet which is given by

$$\psi_{a,b}(t) = \frac{1}{\mid a \mid} \psi \left(\frac{t-b}{a} \right) \tag{2.39}$$

In this context, different wavelet bases of are designed in the literature for various applications [131, 132] which are briefly discussed below for completeness.

2.3.1.1 Modified Littlewood-Paley

In the present study, modified Littlewood-Paley (MLP) wavelet basis is used which is described as follows

$$\psi(t) = \frac{1}{\pi\sqrt{2F(\sigma-1)}} \frac{\sin(2\pi F\sigma t) - \sin(2\pi F t)}{t} \tag{2.40}$$

Parameters F and σ in this basis represent the cut-off frequency and the band width respectively. On Fourier transforming Eq. (2.40), the frequency domain description of the MLP basis can be obtained as

$$\begin{aligned} |\psi(\omega)| &= \frac{1}{\sqrt{4\pi F(\sigma-1)}} && 2\pi F \le |\omega_b| \le 2\pi\sigma F \\ &= 0 && \text{otherwise} \end{aligned} \tag{2.41}$$

Eq. (2.41) shows that MLP basis has compact support in frequency domain. This forms the backbone of the present wavelet based frequency filtering of the signal.

2.3.1.2 Complex Morlet

The complex Morlet wavelet basis function is expressed in analogy with the Gaussian window and is expressed as [111]

$$\psi(f) = \frac{C_{f_0}}{\sqrt{2\pi}} \left(e^{i2\pi f_0 f} - e^{-(2\pi f_0)^2/2} \right) e^{-f^2/2} \tag{2.42}$$

Here, f_0 is the resolution parameter and C_{f_0} is a normalizing constant. In this study, C_{f_0} is considered to be unity. Fig. 2.8(a) shows the frequency signature of a complex morlet wavelet with f_0 (i.e. central frequency) as 0.1Hz.

2.3.1.3 Log-Normal

The frequency resolution obtained from Morlet wavelet is uniform while, in practice, resolution varies with the scale where lower frequencies stay dense within a band while higher frequencies are dispersed over a wider range. This, in turn, demands large number of scales to cover the complete range of frequencies present in the response. Under this condition, a basis function whose frequency resolution follows logarithmic variation is expected to perform better. Hence, Log-Normal wavelet basis is developed which is given by [111, 133]

$$\psi(f) = e^{-(2\pi f_0 \log f)^2/2}, \quad f > 0 \tag{2.43}$$

where, f_0 is the resolution parameter.

2.3.1.4 Generalized Morse

Although different wavelet bases are proposed in the literature for specific end use, recent research works show a trend to develop an unified basis that can be tuned for different applications. One such wavelet basis is the Generalized Morse wavelet [134–136] which is given by

$$\psi_{\beta,\gamma}(\omega) = U(\omega)\alpha_{\beta,\gamma}\omega^{\beta}e^{-\omega^{\gamma}} \tag{2.44}$$

Here, $\alpha_{\beta,\gamma}$ is a normalizing constant and its value can be estimated as

$$\alpha_{\beta,\gamma} = 2\frac{\mathbf{e}\gamma}{\beta}^{\frac{\beta}{\gamma}} \tag{2.45}$$

In the above equation, $\mathbf{e}$ is the Euler's number whose value is 2.7182 [136], $U(\omega)$ is a unit Heaviside function. The resolution is controlled by β and γ which are considered to be positive for all practical purpose. By tuning these two parameters, same resolution can be obtained that is achieved by other wavelet bases [136]. Fig. 2.8 shows these three basis functions discussed above.

2.3.2 Discrete Wavelet Transform

Although present study aims to use continuous wavelet transform, a brief discussion on Discrete wavelet transform is presented here for completeness and to show its difference with its continuous version. As in Eq. (2.39), values of the parameters a and b in the basis function of continuous wavelet change continuously. In discrete wavelet transformation, these parameters (i.e. a and b) are discretized with different approaches for different basis functions. Here, the basis function is

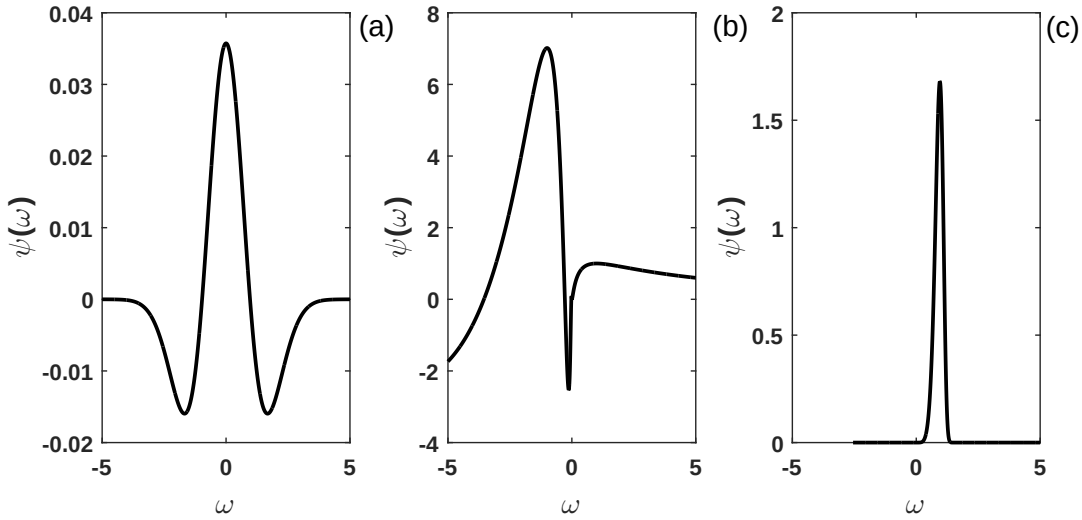

Figure 2.8: (a) Morlet with $f_0 = 0.1$Hz; (b) Log Normal with $f_0 = 0.1$Hz; (c) Generalized Morse with $\beta = 5$ and $\gamma = 7$

expressed [137] in the following form

$$\psi_{m,n}(t) = \frac{1}{|a_0^m|}\psi\left(\frac{t - nb_0a_0^m}{a_0^m}\right) \tag{2.46}$$

where, dilation and translation are controlled by two integer parameter m and n respectively. Here, a_0 and b_0 represents the fixed dilation step parameter and location parameter. In common practice, parameters a_0 and b_0 are considered to be 1/2 and 1 respectively. Substituting these value in Eq. (2.46), the following form is obtained

$$\psi_{m,n}(t) = 2^m\psi\left(2^m t - n\right) \tag{2.47}$$

The above basis function is called dyadic grid as power of two logarithmic scale form the dyadic grid arrangement. Using this discretization, the wavelet coefficient of a time signal $x(t)$ can be expressed in the following form

$$W_{m,n}x(t) = \int_{-\infty}^{\infty} x(t)\psi_{m,n}(t)dt = \int_{-\infty}^{\infty} x(t)2^m\psi\left(2^m t - n\right)dt \tag{2.48}$$

2.3.2.1 Signal Reconstruction

Using inverse discrete wavelet transformation, the signal $x(t)$ can be reconstructed as follows

$$x(t) = \sum_{m=-\infty}^{\infty}\sum_{n=-\infty}^{\infty} W_{m,n}x(t)\psi_{m,n}(t) \tag{2.49}$$

Here, it may be mentioned that signal reconstruction in above form is possible if the discretized wavelets $\psi_{m,n}(t)$ are orthonormal and complete. For the completeness of $\psi_{m,n}(t)$, any function $x(t) \in L^2(\mathbb{R})$ can be expanded as

$$x(t) = \sum_{m=-\infty}^{\infty} \sum_{n=-\infty}^{\infty} c_{m,n} \psi_{m,n}(t) \tag{2.50}$$

where, $c_{m,n}$ represents the appropriate coefficients. Thus, prior to the inverse transformation for reconstruction in discrete wavelet, user needs to ensure that the wavelet basis must (i.e. $\psi_{m,n}(t)$) satisfy orthonormality and completeness.

2.3.2.2 Multiresolution Analysis

As discussed in the previous section, reconstruction of the signal using discrete wavelet transform needs a basis function that follows property of orthonormality and completeness. Multiresolution analysis deals with the framework to construct such discrete wavelet [138]. It provides a set of function spaces $\mathcal{V}_j : j \in \mathbb{Z}$ in the close subspace in $L^2(\mathbb{R})$. The subspace $\mathcal{V}_j$ needs to satisfy the following conditions

1. $\ldots \subset \mathcal{V}_1 \subset \mathcal{V}_0 \subset \mathcal{V}_1 \ldots \subset L^2(\mathbb{R})$
2. $\bigcap_{j=-\infty}^{\infty} \mathcal{V}_j = 0$
3. $y(t) \in \mathcal{V}_j$ if and only if $y(2t) \in \mathcal{V}_{j+1}$ for all integers value j
4. The function $\varphi(t) \in \mathcal{V}_0$ would exist such that the set $\{\varphi(t-\tau), \tau \in \mathbb{Z}\}$ is an orthonormal basis for $\mathcal{V}_0$

These are not discussed further as the reconstruction of signal is not necessary in operational modal analysis. However, reader may refer Shima and Nakayama [137] for further details on this topic.

2.4 Other Time-Frequency Analysis

There are other methods available in the literature for signal processing based on the suitability of their applications. Few of these methods are summaraise here -

2.4.1 Wigner-Ville Distribution

For signal $x(t)$, the Wigner-Ville Distribution (WVD) can be defined as [116, 139]

$$W_z(t,\omega) = \int_{-\infty}^{\infty} \left\{ z(t+\frac{\tau}{2}) z^*(t-\frac{\tau}{2}) \right\} e^{-2\pi \mathrm{j}\tau} d\tau \tag{2.51}$$

where, $z(t)$ is analytic signal to $x(t)$ and * denotes the complex conjugate of $z(t)$. Unlike Wigner distribution, WVD is based on analytic signal which incorporated the contributions made by Ville [140]. The above relation can be express in the following spectral form

$$W_z(\omega,t) = \int_{-\infty}^{\infty} \left\{ \bar{z}_A(\omega+\frac{\theta}{2}) \bar{z}_A^*(\omega-\frac{\theta}{2}) \right\} e^{-2\pi \mathrm{j}\theta t} d\theta \tag{2.52}$$

Here, $\bar{z}_A(\omega)$ denotes the equivalent analytic signal in frequency domain. The spectrum mentioned above will not have any negative frequency which can be obtained as

$$\bar{z}_A(\omega) = \bar{z}(\omega) + \mathrm{j}\tilde{\bar{z}}(\omega) = \bar{z}(\omega) + \mathrm{sgn}[\bar{z}(\omega)] = \begin{cases} 0 & \text{if } \omega < 0 \\ \bar{z}(\omega) & \text{if } \omega = 0 \\ 2\bar{z}(\omega) & \text{if } \omega > 0 \end{cases} \tag{2.53}$$

2.4.2 Gabor Transformation

Gabor transformation is another time-frequency tools applied for signal processing. As per this transformation, signal $x(t)$ will be represented by $\mathscr{G}(\tau,\omega)$ in time frequency domain. $\mathscr{G}(\tau,\omega)$ can be expressed as

$$\mathscr{G}_x(\tau,\omega) = \int_{-\infty}^{\infty} x(t) g(t-b) e^{-\mathrm{j}\omega t} dt \tag{2.54}$$

This transformation has similar features like STFT but the window function $g(\cdot)$ is expressed as

$$g(\tau) = \pi^{-1/4} e^{-\tau^2/2} \tag{2.55}$$

By the above operation, $\mathscr{G}_x(\tau,\omega)$ localize the Fourier transform of the signal $x(t)$ around $t = b$ and it can be interpreted as

$$g_{\omega_0}(t) = g(t-b) e^{\mathrm{j}\omega t} \tag{2.56}$$

2.5 Time-Frequency Analysis of Structural Response

In this section, HHT and WT are used to study the features of the dynamic responses of structure. Fig. 2.9(a) shows a shear building model along with its parameters. The natural frequencies of this model are 4.97, 13.92 and 20.12Hz. First, the free vibration response is generated by Newmark-β [141] time integration technique as shown in Fig. 2.9(b). This is followed by seismic response analysis where ElCentro, 1940 [142] ground motion is used. The response is simulated which is shown in Fig. 2.10(b). Using these two simulated responses, different time-frequency analysis are applied and the results are discussed in the following subsections.

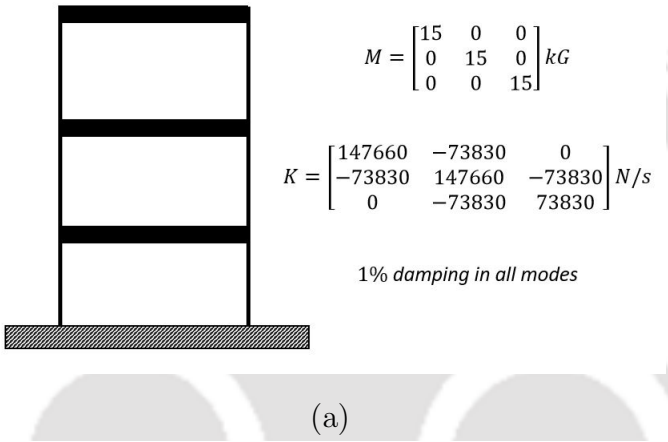

(a)

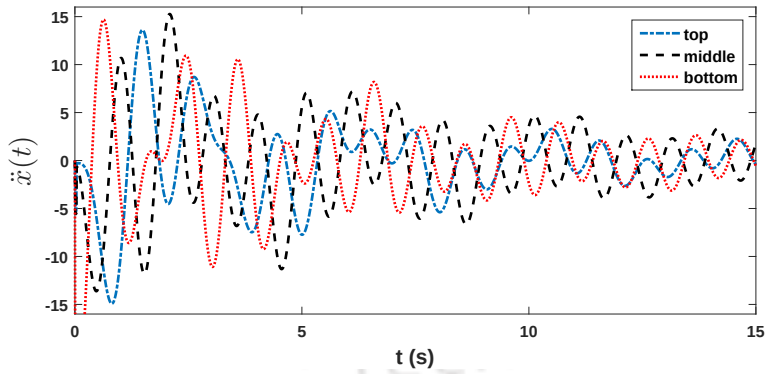

(b)

Figure 2.9: 3dof system with simulated response (a) shear building model and (b) Free response

2.5.1 Hilbert-Huang Transformation

First, HHT is used to study the time-frequency localization in the responses. It is applied on the free vibration responses to evaluate the instantaneous frequency as explained in Eq. (2.25). The

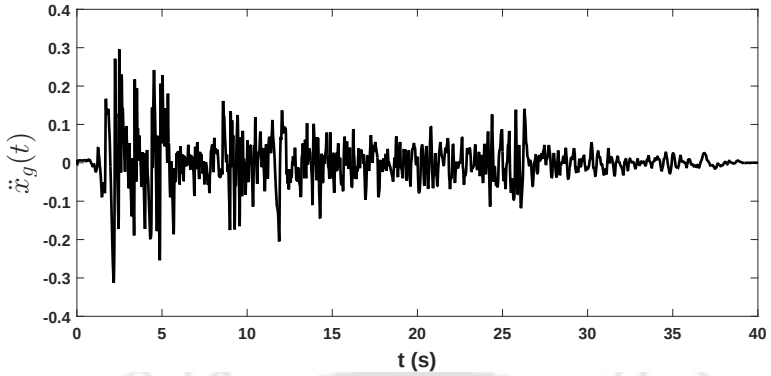

(a)

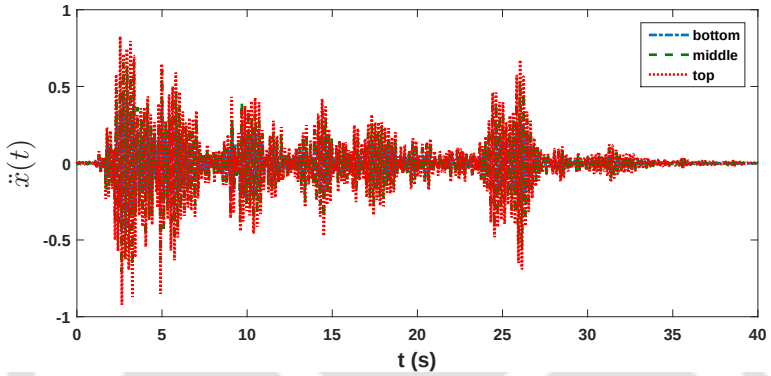

(b)

Figure 2.10: Simulated seismic response (a) ElCentro (1940) ground motion and (b) acceleration response

top floor response is considered here as shown in Fig. 2.9(b). The first two IMFs are obtained after applying EMD on this response that contain the structural frequencies. The third frequency (i.e. 20.12Hz) is not captured by these IMFs. Apart from these two IMFs, there are several other IMFs extracted from the response but none of them contains the natural frequencies. Fig. 2.11(a) and 2.11(c) show the first two IMFs. The instantaneous phases obtained from them as explained in Eq. (2.16) to Eq. (2.25) are shown in Fig. 2.11(b) and 2.11(d). From the slopes of these two plots, the instantaneous frequencies are evaluated as 4.87 and 14.32Hz as opposed to their original values 4.97 and 13.92Hz respectively. Here, it may noted that there is very little variation in estimated values of the instantaneous frequencies from the free vibration analysis (i.e. estimation error) in this case. As for real life structure there are many source of noise which are bound to affect the quality of estimation. To investigate this further, HHT is applied on the earthquake response of the shear building model. As in the previous case, EMD is applied on top floor response shown in Fig. 2.10(b). The IMFs obtained from this analysis are shown in Fig. 2.12. Only two IMFs are shown here for brevity which contains the natural frequencies of the structure. Besides these two, there

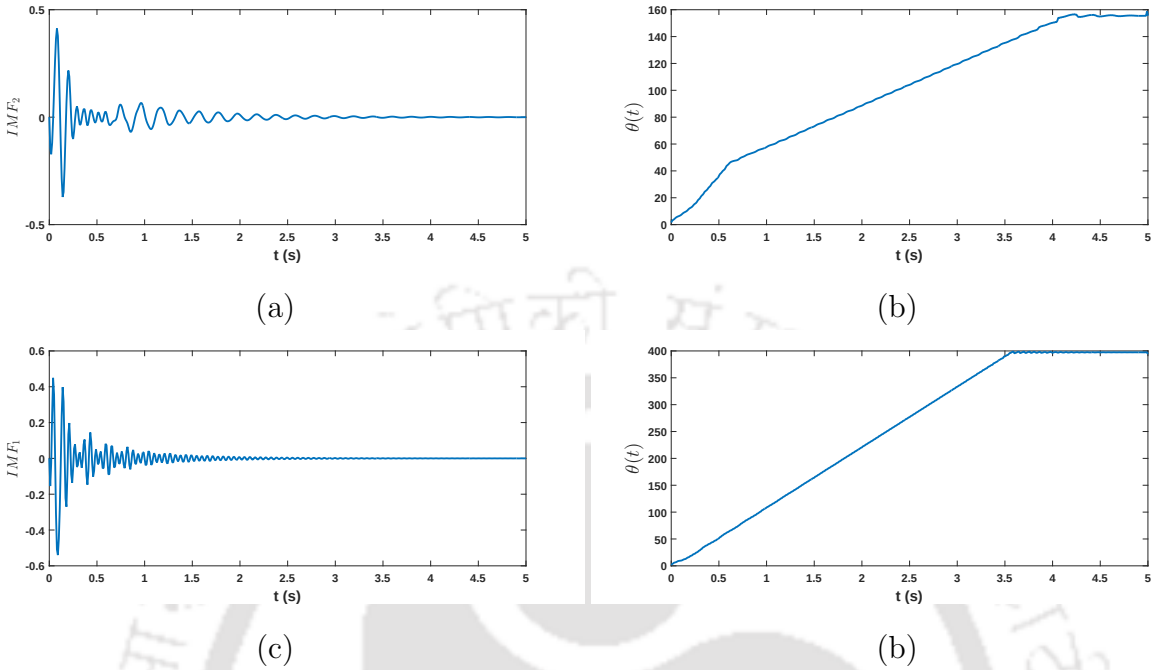

Figure 2.11: HHT of simulated response (a) and (c) IMFs extracted from free response; (b) and (d) Instantaneous phase of 1^{st} and 2^{nd} IMF

are 9 other IMFs generated but none of them contains the natural frequencies and hence, they are spurious modes. Using Eq. (2.18), the analytic signals are formed from the two IMFs and the instantaneous phases are evaluated as given in Fig. 2.12(b) and 2.12(d). The frequency associated to these IMFs are obtained from the slope of these graphs. Here, the mean slopes are evaluated as 4.90 and 12.44Hz as opposed to their theoretical values of 4.97 and 13.92Hz respectively. Maximum error in this case is 11.5% which, again, is attributed to estimation only as the simulated signals are noise free.

2.5.2 Continuous Wavelet Transformation

In this section, performance of continuous wavelet transformation for modal estimation from free and forced vibration responses are demonstrated. Here, the complex morlet basis is chosen for demonstration. First, the wavelet transform is applied on the signal shown in Fig. 2.9(b) and 2.10(b) of top floor response. The spectrogram of the wavelet coefficients are presented in Fig. 2.13. From the first figure (i.e. Fig. 2.13), the frequency localization can be identified, however they are spread over a region. To identify the exact frequencies, ridge of these two spectrograms are evaluated as shown in Fig. 2.14. From these figures, the frequency localizations are more clear. Compare to free vibration scalogram (i.e. Fig. 2.13a) the forced response shows other frequencies in the scalogram. The reason is that the structure is shaken by the ElCentro ground motion that has

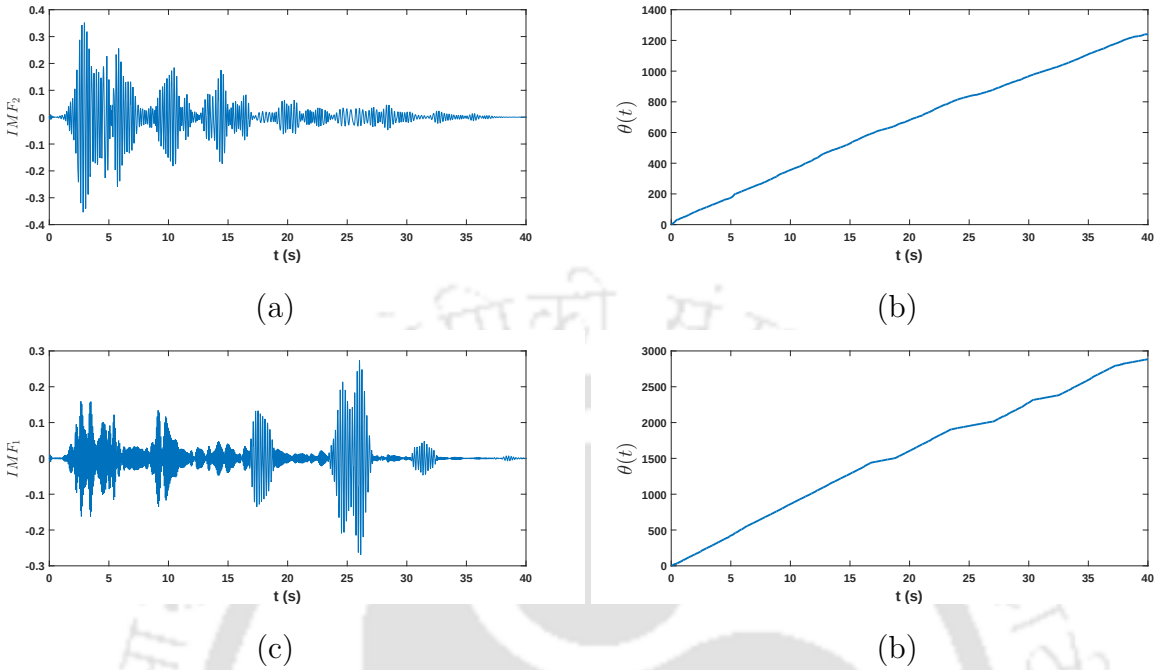

Figure 2.12: HHT of simulated response (a) and (c) IMF extracted from earthquake response; (b) and (d) Instantaneous phase of 1^{st} and 2^{nd} IMF

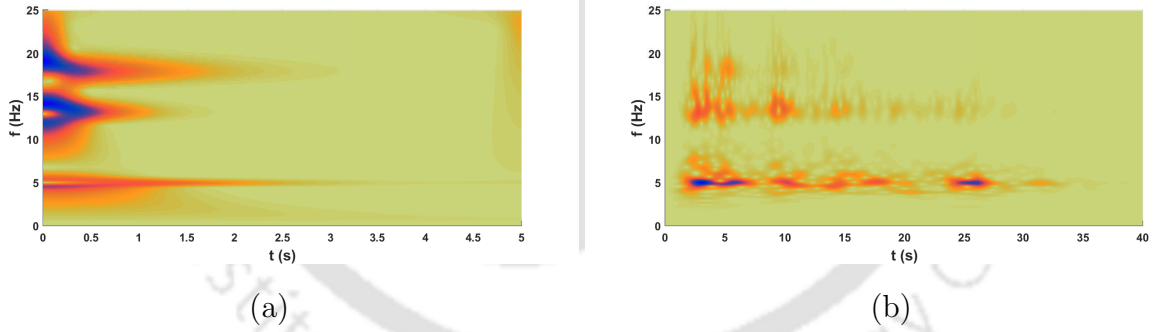

Figure 2.13: Morlet wavelet scalogram for (a) free response and (b) earthquake response

energy content close to the structural frequencies besides the dominant frequencies of the excitation itself. The identified frequencies in this case are 4.99, 13.19 and 18.07Hz with maximum error of 10.2%.

2.6 Summary

In this chapter, different time-frequency analysis popular for the modal identifications are discussed and their performance on different cases are studied. Numerical results demonstrate that frequency obtained from free vibration are more accurate compared to forced vibration. However, free vibra-

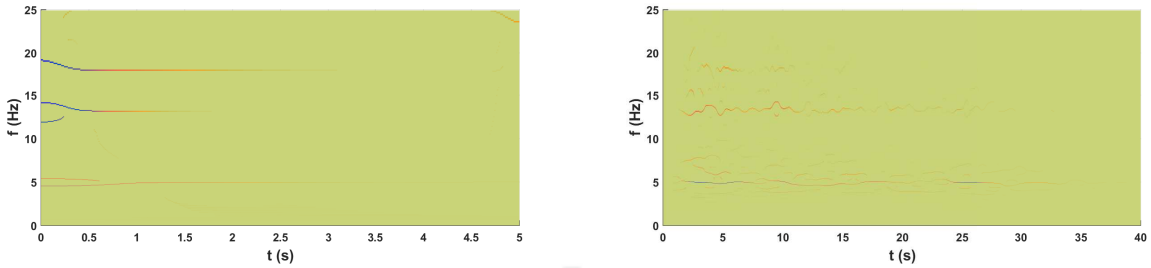

(a) (b)

Figure 2.14: Ridge of the wavelet scalogram from (a) free response and (b) earthquake response

tion responses are not normally available leaving the designer no other option than to use forced vibration response. This is especially important for structural health monitoring immediate after earthquake. The reason behind this is that structural testing after seismic event prior to assess their status is not recommended. Moreover frequency identification during earthquake is equally important to tune the controller. Hence, this study advocates for further improvement of time-frequency analysis for modal identification from forced vibration response of the structural systems.

Chapter 3

Adaptive Time-Frequency Analysis

Time-frequency analysis for signal processing (in particular HHT and WT) and its application in frequency tracking of dynamical system is discussed in the previous chapter. The non-adaptive development of filter banks in these two transformations impose serious restriction on its application for modal identification. They are best suited for free vibration or ambient response. In this section, these time-frequency analysis are aimed to be used in adaptive frame work so that they can be utilized for modal parametric identification from non-stationary response of dynamical systems.

3.1 Improved HHT for Modal Identification

In this section, use of HHT and its advanced version for the modal identification of linear multi degree of freedom (MDOF) dynamic system subjected to multi-component earthquake excitation is discussed, whose governing equation of motion is expressed as

$$\mathbf{M}\ddot{\mathbf{U}}(t) + \mathbf{C}\dot{\mathbf{U}}(t) + \mathbf{K}\mathbf{U}(t) = \mathbf{M}\boldsymbol{\iota}\ddot{\mathbf{U}}_g \tag{3.1}$$

Fig. 2.9(a) shows the schematic diagram of the frame represented by the above equation where, $\mathbf{M}$, $\mathbf{C}$ and $\mathbf{K}$ are $n \times n$ mass, damping and stiffness matrices respectively. In Eq. (3.1), $\mathbf{U} = [U_1, U_2, U_3, ..., U_n]^T$ represents the relative displacement with respect to support and over-dot is differentiation with respect to time. The system is excited by the multi-component support motion $\ddot{\mathbf{U}}_g$ while $\boldsymbol{\iota}$ represents the influence vector that correlates forces in each degrees of freedom (dof) with multi-component support motions. The governing equation of motion in Eq. (3.1) can be decoupled using an orthogonal transformation into its modal coordinates which is given by

$$\mathbf{U}(t) = \sum_{j=1}^{n} \Phi_j \mathbf{Z}_j(t) \tag{3.2}$$

Using the above orthogonal transformation in Eq. (3.1), the response in modal coordinate is expressed as

$$\ddot{\mathbf{Z}}(t) + 2\eta_n\omega_n\dot{\mathbf{Z}}(t) + \omega_n^2\mathbf{Z}(t) = \Phi^T\mathbf{M}\boldsymbol{\iota}\ddot{\mathbf{U}}_g = \mathbf{F}(t) \tag{3.3}$$

where, η_n and ω_n are the modal damping ratio and the natural frequencies respectively. The matrix Φ represents the mode shapes and the force vector $\mathbf{F}$ on right hand side of Eq. (3.3) represents the excitation in each dof in its modal coordinate. The response in the modal coordinate can be obtained using Duhamel's integral which is given by [141]

$$\mathbf{Z}_j(t) = \int_0^t \mathbf{F}_j(\tau)h_j(t-\tau)d\tau \tag{3.4}$$

In the above equation, $h_j(\cdot)$ represents the impulse response function in j^{th} mode i.e.

$$h_j(t) = e^{-\eta_j\omega_{nj}t}\sin\omega_{dj}t \tag{3.5}$$

Using Eq. (3.5) in Eq. (3.4) and differentiating with respect to time, one can evaluate the modal acceleration in each dof. However, numerical evaluation of Eq. (3.4) demands the continuous time parameter 't' to be divided into a set of discrete time points t_i; $i = 1, 2, ..., N$. In this context, it may be noted that n represents the number of dof while N represents the number of time points. Using these discretized time steps, the arbitrary forcing function $\mathbf{F}$ is obtained from the non-stationary multi-component excitation as a train of impulse defined over the entire time span as

$$\mathbf{F}_j(\tau) = \sum_i f_j^i\delta(\tau - t_i) \tag{3.6}$$

Here, f_j^i is the the magnitude of modal force at time t_i and $\delta(\cdot)$ represents the Dirac Delta function. Using the above expression of discretized force at every t_i modal acceleration response can be evaluated by applying the theory of superposition as follows

$$\ddot{\mathbf{Z}}_j(t) = \frac{A_j}{m_j\omega_{dj}}\int_0^t \mathbf{F}_j(\tau)e^{-\eta_j\omega_{nj}(t-\tau)}\sin\{\omega_{dj}(t-\tau) - \psi_j\}d\tau \tag{3.7}$$

In the above equation, amplitude $A_j = \sqrt{(\eta_j^2{\omega_{nj}}^2)^2 + (2\eta_j\omega_{nj}\omega_{dj})^2}$ while $\psi_j = \tan^{-1}\left(\frac{2\eta_j\omega_{nj}\omega_{dj}}{\eta_j^2{\omega_{nj}}^2 - \omega_{dj}^2}\right)$ is the modal phase lag. Further simplification of Eq. (3.7) leads to the following form

$$\ddot{\mathbf{Z}}_j(t) = \sum_i \frac{A_j f_j^i}{m_j\omega_{dj}}e^{-\eta_j\omega_{nj}(t-t_i)}\sin\{\omega_{dj}(t-t_i) - \psi_j\} \tag{3.8}$$

Using Eq. (3.8) and Eq. (3.2), the acceleration response in each dof in its original coordinate can be expressed as

$$\ddot{\mathbf{U}}(t) = \sum_{j=1}^{n} \Phi_j \ddot{\mathbf{Z}}_j(t) = \sum_{j=1}^{n} \sum_{i} R_j f_j^i e^{-\eta_j \omega_{nj}(t-t_i)} \cos\{\omega_{dj}(t-t_i) + \psi^j\} \tag{3.9}$$

where, the response amplitude in the generalized coordinate is given by $R_j = \frac{A_j|\Phi_j|}{m_j \omega_{dj}}$ and the phase lag with the forcing function is $\psi^j = \frac{\pi}{2} - \psi_j$. In inverse problem of parameter estimation, the response is measured at a few selected dof and the parameters (*i.e.* ω_{nj}, η_j, Φ) are estimated using different identification algorithms. In this work, advanced Hilbert transformation based time-frequency analysis of the recorded signal (*i.e.* $\ddot{\mathbf{U}}_j$) is proposed for parameter estimation. The motivation behind this research is the limitation of HHT based modal identification. HHT, in principle, produces an ensemble of IMFs in a non-adaptive framework and is ideally suited for free or ambient vibration response. This non-adaptive nature of the traditional HHT imposes severe restriction on the user to tune it according to the problem. The following sections propose major modification where HHT is adaptively used for efficient parameter estimation and the non-adaptive framework of HHT is relaxed with adaptive versions.

3.1.1 Proposed Adaptive HHT

In this subsection, an adaptive algorithm of HHT is proposed which is discussed below. The analytic signal obtained using HT (i.e. Eq. 2.18), as explained in chapter 2 is suitable for mono-component signals, its efficiency to estimate the instantaneous frequency and the phase of a non-stationary signal is poor. The reason behind this inefficiency is the variation of frequency content in a non-stationary signal with time as observed in earthquake ground motion. For this purpose, a modified form of HT, commonly called Hilbert-Huang transform (HHT) [50] is often used. However, in case of seismic events, the structural response in the original coordinate is essentially the linear combination of the non-stationary responses in its modal coordinates (i.e. as modeled in Eq. (3.2)). Due to this reason, the EMD performed on the measured response often suffers mode mixing, ultimately leading to a poor estimation of modal parameters [143].

To avoid this, a pre-filtering of the recorded motion is recommended in this study before using HHT. The band pass filtering helps to isolate the response so that mode mixing does not affect the evaluation of the instantaneous frequency and the phase while using HHT. However, the major hurdle to implement this pre-filtering is that it requires a prior knowledge of the natural frequencies of the structure which may not be available. To alleviate this problem, an adaptive band pass filtering coupled with HHT in an iterative manner is proposed here. At the beginning, the measured response in different dof are filtered using predefined frequency bands that is sufficient to cover the effective range of modal frequencies. The signal corresponding to each frequency band are then

analyzed by EMD as proposed earlier. The instantaneous frequency and phase of the IMFs in each frequency band are identified. In this context, it may be noted that a coarser frequency band may contain more than one natural frequencies. To identify them, each frequency bands are further sub-divided into smaller segments in the next iteration. If the frequency identified in the finer bands converge (*i.e.* insignificant changes in identified frequencies in the two successive iterations), the iteration for that particular frequency band is terminated. However, it may be noted that a linear time invariant (LTI) system driven by harmonic input also produces harmonic output with a finite phase lag. Therefore, frequency localization in output corresponding to input excitation needs to be identified. With this in view, phase spectrums are compared to identify instantaneous phase difference between the measurements. As the different dofs attain same phase during modal vibration (*i.e.* no phase difference), same will be reflected in their respective IMF. In case of identified frequency corresponding to input excitation, instantaneous frequencies obtained at different dofs from the respective IMF will not be in phase and hence can separate the frequencies corresponding to excitation at source from the modal frequencies.

Therefore, using band pass filtering, one can separate out the response in the j^{th} mode as

$$\ddot{\mathbf{U}}_j(t) = R_j \sum_i f_j^i e^{-\eta_j \omega_{nj}(t-t_i)} \cos\{\omega_{dj}(t-t_i) + \psi^j\} \tag{3.10}$$

This filtering can be carried typically by Butterworth [115, 144] or similar filters readily available in the literature. Now, using Hilbert transformation of Eq. (3.10), one gets

$$\tilde{\ddot{\mathbf{U}}}_j(t) = R_j \sum_i e^{-\eta_j \omega_{nj}(t-t_i)} f_j^i \sin\{\omega_{dj}(t-t_i) + \psi^j\} \tag{3.11}$$

Using Eq. (3.10) and Eq. (3.11), the analytic signal of the acceleration response in the j^{th} frequency band can be calculated as follows

$$\mathbf{Y}_j(t) = \ddot{\mathbf{U}}_j(t) + \mathrm{j}\tilde{\ddot{\mathbf{U}}}_j(t) = \mathbf{S}_j(t) e^{\mathrm{j}\boldsymbol{\theta}_j(t)} \tag{3.12}$$

From the above equation, the instantaneous amplitude and phase of the j^{th} modal response can be evaluated which are given by

$$\mathbf{S}_j(t) = R_j \sum_i f_j^i e^{-\eta_j \omega_{nj}(t-t_i)} \tag{3.13}$$

and

$$\boldsymbol{\theta}_j(t) = \omega_{dj}(t-t_i) + \psi^j \tag{3.14}$$

Taking logarithm of both sides of Eq. (3.13) leads to the following form

$$\ln(\mathbf{S}_j(t)) = -\eta_j \omega_{nj} t + \ln\left(R_j \sum_i f_j^i e^{\eta_j \omega_{nj} t_i}\right) \tag{3.15}$$

It can be concluded from Eq. (3.15), that the first term on the right hand side represents the monotonic (i.e. linear) variation while the second term on the right hand side represents the fluctuation due to arbitrary forcing function modeled as a pulse train in Eq. (3.6). In this context, it may be noted that the mean of the second term on right hand side of Eq. (3.15) is zero as the forcing function $\mathbf{F}(t)$ due to multi-component earthquake ground motions has zero mean. Therefore, it can be concluded that the mean slope of the term $\ln(\mathbf{S}_j(t))$ in Eq. (3.15) obtained by fitting a straight line represents the first term $\eta_j\omega_{nj}$. Furthermore, it can be noticed that the instantaneous frequency can be evaluated form Eq. (3.14) by differentiating the phase $\boldsymbol{\theta}_j(t)$ i.e.

$$\omega_{dj} = \frac{d\boldsymbol{\theta}_j(t)}{dt} \tag{3.16}$$

Finally, the natural frequency corresponding to j^{th} mode may be obtained from

$$\omega_{nj} = \sqrt{(\omega_{dj})^2 + (\eta_j\omega_{nj})^2} \tag{3.17}$$

Once the modal frequency and damping are estimated, the remaining task is to evaluate the mode shape of the structure. Using adaptive HHT (i.e. AHHT) on both side of Eq. (3.2) after differentiating twice with respect to t, one gets

$$AHHT[\ddot{\mathbf{U}}(t)] = \sum_{j=1}^{n} \Phi_j AHHT[\ddot{\mathbf{Z}}_j(t)] \tag{3.18}$$

Now, considering response from two different dofs, the mode shape can be estimated as the ratio which is given by

$$\Pi_j^r = \frac{\Phi_j^r}{\Phi_j^1} = \frac{\text{IMF}_j^r}{\text{IMF}_j^1} \tag{3.19}$$

where, superscript r represents the dof number. Without loss of generality, one can assume $\Phi_j^1 = 1$ and represent the values of the mode shape in other dof as the ratios in the above equation. The complete mode shape is then given by

$$\left\{\Phi_j^r\right\} = \left\{\Pi_j^r\right\}; \quad r = 1, 2, ..., n \tag{3.20}$$

The algorithm of the proposed adaptive HHT or AHHT is is given below (Algo. 1)

3.1.2 Multivariate EMD (MEMD)

In the above subsection, conventional HHT is used in an adaptive framework of pre-filtering where, pre-filtering helps to avoid contamination in IMF (i.e. mode mixing) due to contiguous frequencies. However, recently published research [145, 146] have shown a trend to modify the conventional

Algorithm 1 : Adaptive Hilbert-Huang Transform Based Modal Identification

record acceleration $\ddot{\mathbf{U}}(t)$
initialize $\omega_{nint} = 0$
for $N = 2$ (number of bands) **do**
    design filters
    apply bandpass filter to response as given in Eq. (3.9)
    obtained signal as per Eq. (3.10)
    use Eq. (3.11) to Eq. (3.17) to get ω_{nj} and η_j
    if $|\omega_{nj} - \omega_{nint}| < tolerance$ **then**
        save ω_{nj} and η_j for the specific band
    else
        $\omega_{nint} = \omega_{nj}$
        $N = 2N$
    end if
end for

HHT for better performance. One such proposal is multivariate empirical mode decomposition or MEMD as described in [96, 97]. MEMD based signal processing has shown promising results in time-frequency analysis [97]. Using this signal processing tool, an adaptive MEMD based modal identification of vibrating system is proposed next. For this purpose, MDOF system and its modal responses as described in Eq. (3.1)-(3.3), are considered here. To extract the modal response from the recorded acceleration data, adaptive MEMD method is developed in the similar fashion as in AHHT. On application of MEMD to multichannel recorded acceleration histories, a set of IMFs with a residual error are obtained as follows

$$AMEMD[\ddot{\mathbf{U}}(t)] = MEMD\left[\sum_{j=1}^{n} \Phi_j \ddot{\mathbf{Z}}_j(t)\right] = \sum_{j=1}^{n} \mathbf{c}_j(t) + \mathbf{r}(t) \tag{3.21}$$

Ideally, if MEMD is able to extract the modal response, above equation indicates that j^{th} IMF would correspond to j^{th} mode i.e. $\ddot{\mathbf{Z}}_j(t)$. However, due to mode-mixing j^{th} IMF may contain effects from the surrounding modes. The contributing modes resulting in mode-mixing can be observed from amplitude spectra of the respective IMFs. To separate these modes, adaptive bandpass filtering as in the previous case of AHHT based on a user defined bandwidth level is proposed in this study. In this proposal, Butterworth filter [144, 115] is used as stated in the previous problem. The band width and order is selected by the designer depending upon the problem in hand. Using this user-defined bandwidth parameters, the responses in different dofs are filtered and MEMD is invoked to identify the modal frequencies present in the respective band. The process of filtering and successive multivariate decomposition are repeated to identify the dominant modes present in the structural response. The IMF filter bank obtained from the above scheme will have two distinct constituents – (a) IMF corresponding to synchronous motions in modal co-ordinates and

(b) the IMFs representing excitation frequencies, if any. These two constituents can be delineated using the instantaneous phase of the filtered IMFs corresponding to each channel as described in the previous section. Using the identified modal frequencies from filtered IMF, the mode shapes can be estimated from respective IMFs using finite element model updating as described in [147].

Once the natural frequencies and mode shapes are identified, the remaining task is to evaluate the modal damping ratios. Considering stationary Gaussian white noise forcing function with zero mean, the filtered IMFs obtained from the previous step contains both free and forced modal responses. Estimating modal damping ratios directly from the filtered IMFs will be erroneous due to the non-decaying nature of the forced modal response. This can be addressed by the use of random decrement technique (RDT) as proposed in the literature [148]. Using this technique, the free modal response $\ddot{\mathbf{Z}}^{fr}(\tau)$ can be obtained by

$$\ddot{\mathbf{Z}}^{fr}(\tau) = \frac{1}{R}\sum_{i=1}^{R}\ddot{\mathbf{Z}}(t_i+\tau) \tag{3.22}$$

Here, R represents the triggering value corresponding to the time-point t_i and τ represents the lag parameter. Using Eq. (3.22), the free response corresponding to j^{th} mode is given by

$$\ddot{\mathbf{Z}}^{fr}(t) = e^{-\eta_j\omega_{nj}t}A_j cos(\omega_{dj}t - \phi_j) \tag{3.23}$$

Where, the constant terms are as follows

$$rlA_j = \left[C_{1j}^2 + C_{2j}^2\right]^{0.5} \tag{3.24a}$$

$$\phi_j = \tan^{-1}\left(C_{2j}{C_{1j}}^{-1}\right) \tag{3.24b}$$

$$C_{1j} = \eta_j^2\omega_{nj}^2 a_j + 2\eta_j\omega_{nj}b_j + \omega_{dj}a_j \tag{3.24c}$$

$$C_{2j} = \left[\omega_{dj}^2 b_j - \eta_j^2\omega_{nj}^2 b_j - \eta_j^3\omega_{nj}^3 a_j - \eta_j\omega_{nj}\omega_{dj}^2 a_j\right]\left[\omega_{dj}\right]^{-1} \tag{3.24d}$$

In the above equation, a_j and b_j are the two constants that depend on the initial conditions and ω_{dj} is the damped natural frequency. Applying HT on the free response given in Eq. (3.23), instantaneous amplitude and phase can be obtained as

$$S(t) = A_j e^{-\eta_j\omega_{nj}t} \tag{3.25}$$

and

$$\theta(t) = \omega_{dj}t - \phi_j \tag{3.26}$$

From the above equation, the damped natural frequency ω_{dj} can be estimated using the average slope of the instantaneous phase. The j^{th} modal damping ratio can be obtained in a similar manner as in AHHT i.e. by taking the logarithmic of Eq. (3.25). The key steps of the proposed algorithm

are expressed in Algo. 2.

Algorithm 2 : Proposed MEMD Based Modal Identification Method

```
record acceleration Ü(t)
initialize ω_nint = 0
for N = 2 (number of bands) do
    design filters
    apply bandpass filter following MEMD obtained signal as per Eq. 3.21
    use Eq. 3.11 to Eq. 3.17 to get ω_nj and η_j
    if |ω_nj − ω_nint| < tolerance then
        save ω_nj and η_j for the specific band
    else
        ω_nint = ω_nj
        N = 2N
    end if
end for
```

Once the modal frequencies are identified, r^{th} mode shape corresponding to s^{th} dof can be obtained from the ratio of the modal responses which can be expressed as [149]

$$\Pi_r^s = \frac{\Phi_r^s}{\Phi_r^1} = \frac{h_r^s}{h_r^1} = \frac{\ddot{\mathbf{z}}_r^s}{\ddot{\mathbf{z}}_r^1} \tag{3.27}$$

However, mode shapes obtained as ratios of IMFs has two major disadvantages –

1. It requires responses in each dof to estimate the complete mode shape of the structure which needs large number of sensors. This may not be practically physible for real structures due to cost and in-accessibility.

2. Even if large number of sensors are available for displacement or acceleration measurements, measuring response in rotational dof is practically impossible.

To avoid these difficulties, finite element (FE) model updating is often recommended for mode shape estimation which is discussed in the appendix A.

3.2 Wavelet Based Pre-filtering

In the previous two sections, Butterworth filters are used adaptively to generate mono-component signals in different frequency bands. The success of previous two algorithm depends largely on the efficient filtering. In this context, Butterworth filters may suffer overlapping in frequency domain. To alleviate this issue a wavelet based pre-filtering is discussed in this section. Here, modified

Littlewood-Paley (MLP) based continuous wavelet transformation is proposed for pre-filtering. This basis functions are orthogonal in frequency domain and hence, can be used as an effective filter that does not suffer overlapping. Once the signals are passed through the non-overlapping frequency bands, Hilbert transformation is invoked to obtain the frequency content of the signal in those bands. In this context, continuous wavelet transform of a signal with finite energy in $L^2(\mathbb{R})$ (i.e. Hilbert space) provides a two dimensional array that shows the time localized frequency content of the signal, as described in Eq. 2.36, where the MLP basis function [i.e. Eq. (2.40)] is used. On Fourier transforming both sides of the Eq. (2.36) and using Eq. (2.37), it can be shown that the wavelet coefficient $W_\psi x(a,b)$ is obtained from the Fourier representation of the signal $x(t)$ as follows

$$W_\psi x(a,b) = \frac{\sqrt{|a|}}{2\pi} \int_{-\infty}^{+\infty} x(\omega)\psi^*(a\omega)e^{i\omega b}d\omega \tag{3.28}$$

From this expression, it can be noticed that the integral outside the frequency band corresponding to $\psi^*(a\omega)$ is zero. This, in tern, indicates that $W_\psi x(a,b)$ for a given scale corresponds to the frequency band $[2\pi F\ \sigma 2\pi F]$. On inverse transforming Eq. (3.28) for a particular scale $a = a_j$ as described in Eq. (2.37), the time signal corresponding to j^{th} frequency scale can be expressed as

$$x_j(t) = \frac{1}{2\pi C_\psi} \int_{-\infty}^{+\infty} \frac{1}{a_j^2} W_\psi x(a_j,b)\psi_{a_j,b}(t)\, db \tag{3.29}$$

Using this expression, the time signal in different frequency bands can be obtained, covering the effective frequency range of the original signal or as defined by the user. Furthermore, a linear summation of these signals in different frequency bands returns the original time signal $x(t)$ which may be expressed as

$$x(t) = \sum_{j=1}^{N} x_j(t) + R_w(t) \tag{3.30}$$

where, $R_w(t)$ represents the residue of the signal, if any, outside the frequency bands covered by $j = 1,\ldots,N$. Eq. (3.30) obtained from wavelet analysis has similarity with Eq. (2.27). This property of the MLP based continuous wavelet transform is proposed to be utilized to obtained the IMF (i.e. modal response) in this study to bypass the time consuming EMD which often leads to mode-mixing. Further, it can be shown that the energy in the j^{th} frequency band of the time signal $x(t)$ can be expressed as [149]

$$E_{xj} = \frac{1}{2\pi C_\psi} \int_{-\infty}^{+\infty} \frac{[W_\psi x(a_j,b)^2]}{a_j^2} db \quad \text{where} \quad j = 1,2,\ldots,N \tag{3.31}$$

From this expression, it is clear that the total energy of the signal $x(t)$ can be expressed as linear summation of the energies in different frequency bands. Here, the compact support of the basis

function helps to avoid the possibility of leakage from the adjacent frequency bands. Using this property of the MLP based continuous wavelet transform, Eq. (3.2) can be expressed in the following form

$$W_\psi \mathbf{U}(a,b) = \sum_{r=1}^{N} \Phi_r W_\psi \mathbf{z}_r(a,b) = \sum_{r=1}^{N} \Phi_r \frac{\sqrt{|a|}}{2\pi} \int_{-\infty}^{+\infty} \mathbf{Z}_r(\omega)\psi^*(a\omega)e^{i\omega b}d\omega \tag{3.32}$$

Further, using the above equation in Eq. (3.31), the energy in the j^{th} frequency scale can be obtained as

$$E_{xj} = \sum_{r=1}^{N} \frac{1}{2\pi C_\psi} \Phi_r \int_{-\infty}^{+\infty} \frac{[W_\psi x(a_j,b)^2]}{a_j^2} db \tag{3.33}$$

From the above equation, it can be shown that $\mathbf{X}(t)$ has significant energy, if the r^{th} modal response falls in the j^{th} frequency band i.e.

$$\begin{array}{lll} E_{xj} & \neq 0 & r = j \\ & \approx 0 & \text{otherwise} \end{array} \tag{3.34}$$

Therefore, evaluating the energy content of the signal $\mathbf{X}(t)$ from its wavelet coefficients and IMF (i.e. Eq. (2.27)) it can be shown that

$$E_x = \sum_{j=1}^{n} E_{x_j} = \sum_{g=1}^{m} E_{h_g} \tag{3.35}$$

Here, it may be noticed that j^{th} frequency band may have more than one modal frequency. To identify them, the respective frequency band is further subdivided into smaller bands by modifying the MLP basis as follows

$$\begin{array}{lll} \hat{\psi}^s(\omega) & = \frac{1}{\sqrt{2\pi F(\delta-1)}} & \text{for } 2\pi F \leq |\omega| \leq 2\pi\delta F \\ & = 0 & \text{otherwise} \end{array} \tag{3.36}$$

Once the signal is divided into sufficiently small frequency bands, the energy localization corresponding to each modal frequency can be identified i.e. only one dominant frequency in each band. Finally, using Eq. (3.35) it can be concluded that as the energy in the j^{th} frequency scale matches with the energy of the g^{th} empirical mode (since both of them represent the same mode), the time signal $x_j(t)$ must be equal to the g^{th} IMF. This property of the MLP based continuous wavelet transform helps to reduce the computational burden of EMD which is heuristic and often leads to erroneous results. The advantage of the proposed continuous wavelet transform based filtering will be demonstrated in the numerical analysis. The algorithm of the proposed wavelet-Hilbert based frequency identification is provided below. Once the modes are identified from the signals by comparing phase spectrum, the mode shape and modal damping ratio can be obtained as described

in section 3.1.1.

Algorithm 3 : Wavelet-Hilbert Transform Based Modal Identification

record acceleration $\ddot{\mathbf{U}}(t)$
set number of band and number of frequency n
initilize F & σ
apply MLP on $\ddot{\mathbf{X}}(t)$ *to obtained* $\ddot{x}_j(t)$
find energy localization in j^{th} *band and count the location* P
if $n \neq P$ **then**
    adjust the values F&σ *to increase subband and repeat from step 4*
else
    compare the phases of $\ddot{x}_j(t)$ *for different sensors*
    while *phase lag is zero* **do**
        apply HT to identify ω_{nj} & η_j
    end while
end if
return

3.3 Synchrosqueezed Wavelet Transformation

In the previous section, HHT is combined with adaptive pre-filtering for modal identification from the response due to non-stationary seismic input. It is observed that pre-filtering using wavelet transformation is mathematically more sound due to the compact support of MLP basis function. It not only helps to evaluate the mono-component signals, but also helps to bypass EMD operation as it becomes redundant after segregation of the modal responses. This indicates that wavelet transformation is inherently more powerful compared to HHT. However, traditional wavelet transformation as described in Chapter 2 is non-adaptive and offers no flexibility to the designer. However, recently developed synchrosqueezed transformation operates an EMD like transformation in wavelet domain. It improve the resolution of the original wavelet transformation as it operates over the wavelet coefficients. This property of the synchrosqueezed wavelet transformation is proposed to be utilized in the present study for modal identification.

Here, a overview of the wavelet transform and its synchrosqueezed variant used for signal processing are presented. Reader may refer [106, 150, 134] for further details of these time-frequency based signal processing tool. The continuous wavelet transform of a finite energy signal $x(t)$ in $\mathbf{L}^2\mathbb{R}$ i.e $W_\psi x(a,b)$ can be obtained as described in Eq. (2.36). Unlike Fourier transform where the exponential function is used as a basis function, different bases are proposed in the literature for wavelet transformation as mentioned in Chapter 2. In this study, three different bases (i.e. Complex Morlet, Log-Normal and Generalized Morse) are considered to demonstrate their performance in

parameter estimation. The signal is decomposed in logarithmic frequency levels as follows [111]

$$\omega_j = 2\pi 2^{(j-j_0)/n_s} \tag{3.37}$$

Here, j represents the index of the discretized frequency and n_s is the number of scales in which the frequencies are segregated. It depends upon the frequency range $[f_1, f_2]$ over which the signal is decomposed i.e. [111]

$$n_s = \frac{N \log 2}{\log f_2 - \log f_1} \tag{3.38}$$

Parameter N is an integer whose value is greater than 1. The lower and upper bound of the frequency interval [i.e. f_1 and f_2 respectively] depends on the search domain of the specific problem. For example, the dominant natural frequencies of civil infrastructure normally remain within 0 to 10 Hz. Therefore, these values of f_1 and f_2 can be adopted for modal identification of building and bridges. This discretized frequency is equivalent to pseudo frequency described in Eq. (1.1) which may be combined in the following form

$$\omega_j = 2\pi f_{ps_j} = 2\pi \frac{f_c}{\Delta_f} \frac{1}{a_j} \tag{3.39}$$

This study is aimed at the use of adaptive HHT like application of the advanced version of wavelet transformation i.e. synchrosqueezed transformation. This is discussed in the following subsections.

3.3.1 Synchrosqueezing and Instantaneous Frequency

Using continuous wavelet transformation along with a given basis function, the instantaneous frequency of a time signal can be tracked which is explained here. For this purpose, let us consider an amplitude modulated harmonic signal of the form $x(t) = F_0 e^{-\eta t} \cos(\omega t)$ as this trend is commonly observed in the response of linear dynamic systems. Applying wavelet transform on this signal using Eq. 2.36, the coefficient can be expressed as

$$W_\psi x(a,b) = \frac{F_0 \sqrt{a}}{4\pi} e^{-\eta t} \psi^*(a\omega) e^{\mathrm{i}b\omega} \tag{3.40}$$

From this expression, the instantaneous frequency of the signal $x(t)$ can be evaluated as

$$\omega_x(a,b) = -\mathrm{j} \left(W_\psi x(a,b)\right)^{-1} \frac{\partial}{\partial b} W_\psi x(a,b) \tag{3.41}$$

Above mathematical operation is known as synchrosqueezing. This operation enhances the gradient of the wavelet coefficients near the instantaneous frequencies as it uses differential of the coefficients with respect to 'b'. Thus it increases the resolution near the dominant frequencies present in the signal. Further, the energy of the time signal $x(t)$ in the j^{th} scale after synchrosqueezing can be

obtained as [12]

$$E_{xj} = \frac{1}{2\pi C_\psi} \int_{-\infty}^{+\infty} \frac{[\omega_x(a,b)^2]}{a_j^2} db \text{ where } j = 1, 2, \ldots, J \tag{3.42}$$

Thus, the energy of the signal described above is localized in and around the harmonic frequencies ω. Therefore, the scale a_j corresponding to ω shows sharp energy concentration in the scalogram obtained from Eq. (3.42). Once the instantaneous frequency ω_{int} is identified, the response in the wavelet domain can be reconstructed in the following way [107]

$$T(\omega_{int}, b) = (\Delta\omega)^{-1} \sum W_\psi x(a_n, b) a_n^{-3/2} (\Delta a)_n \tag{3.43}$$

Here, the scale a_n should be selected such that

$$a_n : |\omega(a_n, b) - \omega_{int}| \leq \Delta\omega/2 \tag{3.44}$$

An inverse wavelet transform in and around a particular scale (say a_n) using Eq. (3.43) will produce a single tone time signal (i.e. mono-component). Theoretically, synchrosqueezing can separate out dominant frequencies present in the signal, if the separation of these frequencies are larger than $\Delta\omega$ [107]. In practice, $\Delta\omega$ is constant once the data is collected from the experiment. Therefore, if the sampling rate is more than the separation between the two closely spaced mode, SST fails to segregate even when the scales are increased [107].

The above mentioned [i.e. in Eq. (3.41)] property of SST helps to improve the resolution of the signal significantly compared to scalogram obtained from wavelet transformation alone. Thus, identification of instantaneous frequency becomes more easier in SST than wavelet scalogram where ridges and skeletons are used. The conventional use of ridge and skeleton demands significant intermittency (where the user needs to identify each of them) and also produces spurious modes. As outlined in the objective of this thesis, this obvious advantage of SST is planned to be utilized for modal identification which is described in the following section.

3.4 Proposed Synchrosqueezed-Clustering for Modal Identification for Modal Identification

In this section, first the dynamics of a structural system is expressed in the wavelet domain. The equilibrium equation of a linear multi-degree of freedom system takes the following form

$$[\mathbf{M}]\{\ddot{\mathbf{u}}(t)\} + [\mathbf{C}]\{\dot{\mathbf{u}}(t)\} + [\mathbf{K}]\{\mathbf{u}(t)\} = \{\mathbf{P}(t)\} \tag{3.45}$$

Here, [**M**], [**C**] and [**K**] are the system matrices i.e. mass, damping and stiffness respectively. The displacement vector is denoted by **u** and the upper dot represents derivative with respect to time. In the above equation, **P** is the generalized force vector. Applying WT on both sides of Eq. (3.45), it can be expressed in the wavelet domain as follows [151]

$$\begin{aligned}&[\mathbf{M}]\left\{\frac{\partial^2}{\partial b^2}W_\psi \mathbf{u}(a,b)\right\}+[\mathbf{C}]\left\{\frac{\partial}{\partial b}W_\psi \mathbf{u}(a,b)\right\}+\\&[\mathbf{K}]\left\{W_\psi \mathbf{u}(a,b)\right\}=\left\{W_\psi \mathbf{P}(a,b)\right\}\end{aligned} \tag{3.46}$$

Above expression shows that the dynamic equilibrium expressed in Eq. (3.45) is valid in 'b' domain for a given scale 'a' that corresponds to a particular frequency. Moreover, it can be observed that coupling in the generalized coordinate (as in Eq. (3.45)) is also present in the wavelet domain. Therefore, decoupling using modal coordinates are also applicable in the wavelet domain which is given by

$$W_\psi \mathbf{u}(a,b)=\sum_q \mathbf{\Phi}^q W_\psi u^q(a,b) \tag{3.47}$$

Where, $\mathbf{\Phi}$ is the mode shape vector obtained from the eigen analysis of mass and stiffness matrices. Using this orthogonal decomposition, Eq. (3.46) in the wavelet domain can be expressed in the modal coordinates as

$$\begin{aligned}&[\mathbf{M}_l]\left\{\frac{\partial^2}{\partial b^2}W_\psi u^q(a,b)\right\}+[\mathbf{C}_l]\left\{\frac{\partial}{\partial b}W_\psi u^q(a,b)\right\}+\\&[\mathbf{K}_l]\left\{W_\psi u^q(a,b)\right\}=\left\{W_\psi P^q(a,b)\right\}\end{aligned} \tag{3.48}$$

In the above equation, [$\mathbf{M}_l$], [$\mathbf{C}_l$] and [$\mathbf{K}_l$] are the modal mass, damping and stiffness matrices while $\{W_\psi P^q(a,b)\}$ is the modal load vector in the wavelet domain corresponding to scale 'a'. Here, it may be observed that modal dynamics in the wavelet domain follow the same mathematical framework as in the original time domain. Hence, convolution integral can be adopted to evaluate the response in the wavelet domain corresponding to the scale factor 'a'. Following this analogy, the response due to the modal force vector $\{W_\psi P^q(a,b)\}$ can be expressed as

$$W_\psi u_k^q(a,b)=\int_0^b h_k(b-\tau)W_\psi P_k^q(a,\tau)d\tau \tag{3.49}$$

Here, $h_k(b-\tau)$ is the Impulse Response Function of the decoupled system in the q^{th} mode. In the above equation, $\{W_\psi P_k^q(a,b)\}$ can be considered as a pulse train where the total response is obtained by linear summation of the response due to the individual pulse acting at a time instant τ. Therefore, the modal load vector can be expressed as follows

$$W_\psi P_k^q(a,\tau)=\sum_i {P_k}_i^q \delta(\tau-b_i) \tag{3.50}$$

Using Eq. (3.50) in Eq. (3.49), the acceleration response in the wavelet domain corresponding to a scale 'a' can be derived as follows

$$\begin{aligned} W_\psi \ddot{u}_k^q(a,b) &= \int_0^b \frac{A_k}{m_k\omega_{dk}} e^{-\eta_k\omega_{nk}(b-\tau)} \sin\left\{\omega_{dk}(b-\tau)-\vartheta_k\right\} \\ &\quad \sum_i P_{ki}^q \delta(\tau-b_i)d\tau \\ &= \sum_i \frac{A_k P_{ki}^q}{m_k\omega_{dk}} e^{-\eta_k\omega_{nk}(b-b_i)} \sin\left\{\omega_{dk}(b-b_i)-\vartheta_k\right\} \end{aligned} \tag{3.51}$$

where, $A_k = \eta_k\omega_{nk}^2\sqrt{4-3\eta_k^2}$ and $\vartheta_k = \tan^{-1}\frac{2\eta_k\sqrt{1-\eta_k^2}}{2\eta_k^2-1}$. In the above equation, m_k, ω_{dk} and η_k are the modal mass, natural frequency and modal damping ratio respectively. Using Eq. (3.47) and Eq. (3.51), the global acceleration response in the wavelet domain corresponding to scale 'a' is evaluated as

$$\begin{aligned} W_\psi \ddot{\mathbf{u}}(a,b) &= \sum_q \sum_i \frac{A_k P_{ki}^q}{m_k\omega_{dk}} e^{-\eta_k\omega_{nk}(b-b_i)} \\ &\quad \cos\left\{\omega_{dk}(b-b_i)+\vartheta^k\right\} \end{aligned} \tag{3.52}$$

where, $\vartheta^k = \frac{\pi}{2} - \vartheta_k$ is the phase lag between the modal load and the response in the wavelet domain corresponding to scale 'a'. Once the total response is obtained in the wavelet domain, the analytical signal can be reconstructed as

$$\begin{aligned} W_\psi \ddot{\mathbf{u}}^{an}(a,b) &= W_\psi \ddot{\mathbf{u}}(a,b) + \mathcal{H}(W_\psi \ddot{\mathbf{u}}(a,b)) \quad \forall a \in +\mathbb{R} \\ &= \sum_q \sum_i \frac{A_k P_{ki}^q}{m_k\omega_{dk}} e^{-\eta_k\omega_{nk}(b-b_i)} e^{\mathrm{i}\theta} \end{aligned} \tag{3.53}$$

In the above mathematical expression, $\mathcal{H}(\cdot)$ represents Hilbert transform [122]. Here, superscript ^{an} represents the analytic signal, where $\theta = \omega_{dk}(b-b_i)+\vartheta^k$ and $\mathrm{i} = \sqrt{-1}$. The energy content of the signal in different scales are evaluated which is expressed in the following equation

$$E_{\ddot{\mathbf{u}}^{an}j} = \frac{1}{2\pi C_\psi} \int_{-\infty}^{+\infty} \frac{\left[W_\psi \ddot{\mathbf{u}}^{an}(a_j,b)^2\right]}{a_j^2} db \tag{3.54}$$

Since the total response is expressed by linear summation of the modal responses (i.e. Eq. (3.47)), the energy content of the measured response is also localized in and around different frequencies (i.e. scales in wavelet domain) corresponding to structural modes and input forces. In traditional wavelet transform based identification, the wavelet scalograms of the measured responses are used to develop the ridges and skeletons. This algorithm is not discuss here to avoid repetition. Reader may refer [152, 153] for the details of this technique. However, the ridge-skeleton based identification demand user intermittency to locate the scales. Moreover, traditional modal identification uses either broad banded excitation or ambient vibration which has inherent advantage as the output is featured with modal frequencies only. The use of these technique for non-stationary forced excitation is often heuristic. Due to this reason, present study aims to use advanced time-frequency analysis

(i.e. synchrosqueezed transformation) for efficient modal identification as stated in the objectives. This is achieved in two steps - synchrosqueezing for better resolution followed by machine learning for unbiased frequency localization.

Thus, the above analytic signal in Eq. (3.53) is used for SST to enhance the resolution of instantaneous amplitude and phase as explained in Eq. (3.41) i.e.

$$\omega_s(a,b) = -\mathrm{i}[W_\psi \ddot{\mathbf{u}}^{an}(a,b)]^{-1}\frac{\partial}{\partial b}W_\psi \ddot{\mathbf{u}}^{an}(a,b) = \omega_{dk} + \mathrm{i}\eta_k\omega_{nk} \tag{3.55}$$

Here, it may be noted that above instantaneous frequency obtained from the analytic signal contains both real and imaginary parts. Thus, the modal frequency and damping ratio can be evaluated from the above expression which are given by

$$\omega_{nk} = \mathrm{abs}(\omega_s) = \sqrt{{\omega_{dk}}^2 + \eta_k^2 {\omega_n}_k^2} \tag{3.56a}$$

$$\eta_k = \tan\left(\arg(\omega_s)\right) \tag{3.56b}$$

However, Eq. (3.55) provides instantaneous frequency corresponding to every scale which may be either modal frequencies or frequencies corresponding to the input force.

These frequencies are separated by exploiting the inherent properties of modes (i.e modal responses are in phase). Using Eq. (3.43) near ω_n, corresponding wavelet coefficients can be used to reconstruct the signal as follows

$$T(\omega_n, b) = (\Delta\omega)^{-1}\sum W_\psi \ddot{\mathbf{u}}(a_n, b) a_n^{-3/2}(\Delta a)_n \tag{3.57}$$

Thus, by inverse wavelet transformation of $T(\omega_n, b)$ for each ω_n, response $\ddot{\mathbf{u}}^q(t)$ can be generated in the time domain. To check whether the extracted mono-component (as per theory) response represents the modal frequency or not, phase portrait of the same signal obtained from different sensors are used. Here, it may be noted that instantaneous phase can also be found out by constructing the analytic signal as follows

$$\theta_k^q = phase[\ddot{\mathbf{u}}^q(t) + \mathcal{H}(\ddot{\mathbf{u}}^q(t))] \tag{3.58}$$

Nevertheless, once the phase portrait of the signals from different sensors are obtained corresponding to the scales where energies are localized, they are compared to check the unison (i.e. crossing zero or obtaining peaks at the same time) which is the typical behavior of modal vibration. In this context, synchrosqueezed wavelet scalogram with improved resolution helps to segregate energies in different scales as opposed to traditional ridge and skeleton of the wavelet coefficients obtained from free or ambient vibration analysis. In reality, measured responses are often transient due to arbitrary forcing functions contaminated with noise and other interference. Due to this reason, wavelet scalogram often shows energy localization over different regions instead of specific scales and also suffers discontinuity in 'b' domain. Hence, it is difficult to identify dominant frequencies

from the wavelet scalogram. The problem is more prominent where large number of modes are available with closely spaced frequencies. To avoid these problems (i.e. user interface to decide the dominant frequencies that involves subjectivity leading to erroneous estimation), further analysis of the synchrosqueezed wavelet coefficients are proposed in this paper. Here, two major improvisations are adopted - a) apply machine learning over synchrosqueezed wavelet transform data to segregate them into different frequency bins and b) then extract phase portrait to locate modal frequencies as they are in unison which are explained below. The second step, in particular, is very helpful where only limited clusters are searched as opposed to large as of ridge and skeleton in original wavelet based identification.

3.4.1 k-means Clustering for Energy Localization

As discussed above, energy concentration of the response varies with time as the system vibrates under arbitrary excitation and suspectable to measurement noise. This change is difficult to arrest by visual inspection of ridge and skeleton obtained from the spectrogram of the WT or SST. Thus, clustering is adopted to identify the energy concentration in a signal in different scales. Here, popular partition based stable *k-means* clustering algorithm is used to extract the underlying pattern of the energy localization from the spectrogram of SST analysis. The details of this algorithm may be found in Abonyi and Feil [154]. Here, only the relevant equations in the light of the present problem are explained. The *k-means* clustering of a data is defined as

$$\mathcal{J}(x,v) = \sum_{i=1}^{c} \sum_{\substack{k=1 \\ x_k \in c_i}}^{n} \| x_k - v_i \|^2 \tag{3.59}$$

In the above equation, $x_k = |W_\psi \ddot{\mathbf{u}}(a,b)|^2$. Here, n and c are the number of data and clusters respectively, where the center of the cluster is defined by v_i. The individual weight index of each cluster is given by

$$\lambda = \frac{\sum_{i=1}^{n} |W_\psi \ddot{\mathbf{u}}(a,b_i)|^2}{\sum_{k=1}^{c} \sum_{\substack{i=1 \\ x_k \in c_k}}^{n} |W_\psi \ddot{\mathbf{u}}(a,b_i)|^2} \tag{3.60}$$

Based on this weight index, it is possible to locate the energy concentration at some scales in the SST spectrogram and subsequently, the underlying dominant frequencies. To identify the optimum number of cluster c, gap value (GV) is estimated which is given by

$$GV_n(c) = E_n \{\log W_c\} - \log (W_c) \tag{3.61}$$

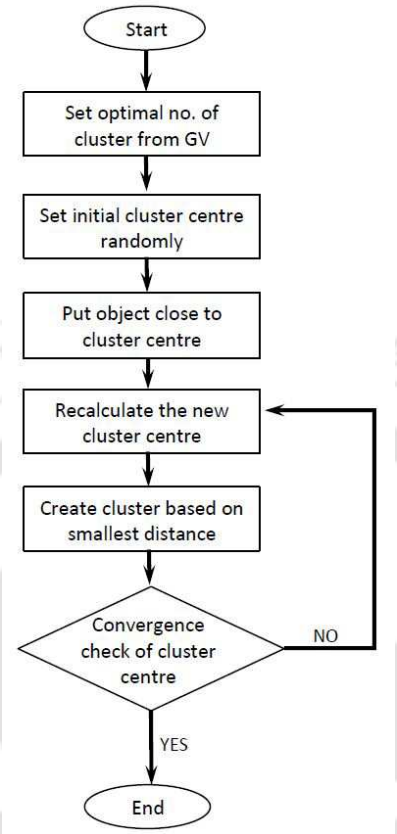

Figure 3.1: *k-means* clustering

In the above equation, W_c represents the pool within the cluster dispersion which is evaluated as

$$W_c = \sum_{i=1}^{c} \frac{1}{2n_i} d_i \tag{3.62}$$

Here, the number of data point in the i^{th} cluster is represented by n_i whereas, d_i is the sum of the pairwise distances for all points within that cluster. The optimal number of cluster c is obtained in iterative manner. Thus, the clustering is started with initial number c (typically 1) and increase by 1 in every successive iteration and the gap values are studied over a wider range of c. From this analysis, optimal c is identified as GV saturate after some iterations. The detailed procedure is shown in Fig. 3.1. Here, the optimal number of cluster is evaluated from GV as describe earlier and then, the clustering algorithm is followed by generating random cluster centers as many clusters are defined. Then, the objects are put in these clusters. After that, the center or median of the clusters are recalculated and again the objects are put in the cluster based on distance. This iteration continues until the cluster center becomes stable. In this context, it is relevant to explain the use of unsupervised learning in the proposed modal identification strategy over supervised learning. The reason behind the selection of *k-means* algorithm (i.e. unsupervised learning) are -

- to avoid bias associated with the training data used in supervised learning which will correspond to a specific class of modal frequencies and nonstationary excitation used for training. In reality, there is no guarantee that the actual frequencies will be in the same pool used for training and similar nonstationary excitation will occur in testing.
- as the machine learning is used in this study to segregate the data in groups of dominant frequencies to avoid user intermittency, unsupervised learning is enough to carry out this task.

Using this technique, energy localization in different clusters are identified and the signal corresponding to those clusters are obtained by inverse synchrosqueezed transformation as explained in the previous section. These signals are further used to identify the modal damping as explained in section 3.1.1.

3.4.2 Algorithm of the Proposed Identification Strategy

In this subsection, the algorithm of the sequential clustering of the synchrosqueezed wavelet transform coefficients as explained in the previous sections is presented (Algo. 4). The methodology given in section 3.4 is given in from step 1 to step 27. The later part i.e. from step 28 to 38 are utilized to separate out any spurious modes or any frequencies which are not associated to the structure by comparing the phase difference. To do so, the extracted modes are transformed from wavelet domain to time domain and then the phases of the signals are evaluated.

3.5 Numerical Implementation

In this section, adaptive versions of HHT and WT provided earlier are used for their numerical validation. For this purpose, simulated response of different structures are used which are descried in the following sections.

3.5.1 Adaptive HHT

Numerical implementations of the adaptive HHT based identification strategy suggested in the previous section are presented here. To study the efficiency of the adaptive filtered HHT based identification strategy, a RC framed building is considered. Fig. 3.2 shows details of the building constructed in IIT Guwahati for research purpose. Two buildings on the either side of the staircase are identical and separate. However, one of them is firmly held at ground using conventional design and is used as a test bed for the present study. The project is sponsored by Board of Research in

Algorithm 4 : Sequential Clustering of SST Based Identification

record acceleration response $\ddot{\mathbf{u}}(t)$
set frequency range f_1 and f_2
select a basis function and associated parameters
initialize $f_{inz} = 0$
for $n_s = 2^8$ **do**
    evaluate $W_\psi \ddot{\mathbf{u}}^{an}(a, b)$ per Eq. (3.53)
    apply SST over WT scalogram
    find out $E_{\ddot{\mathbf{u}}^{an}}$ using SST coefficients for all scales following Eq. (3.54)
    initialize $GV_n = 0$
    for $c = 1$ **do**
        evaluate $GV_n(c)$ using Eq. (3.61) and (3.62)
        if $\{GV_n(c) - GV_n(c-1)\}/GV_n(c) < 0.1$ **then**
            $c^* = c$ [optimum cluster number]
        else
            $c = c + 1$
        end if
    end for
    apply k-means clustering over $E_{\ddot{\mathbf{u}}^{an}} \approx |W_\psi \ddot{\mathbf{u}}(a, b)|^2$
    f_{idf} = median of the cluster
    $\kappa = |f_{idf} - f_{inz}|$
    if $\kappa > tolerance$ **then**
        $n_s = int\{n_s + \gamma * n_s\}$
        $f_{inz} = f_{idf}$
    else
        `break`
    end if
end for
for $i = 1$ to c^* **do**
    evaluate $T(\omega_n, b)$ for each median from Eq. (3.57)
    calculate $\ddot{\mathbf{u}}^q(t)$ by inverse transform of $T(\omega_n, b)$
    evaluate θ_k^q using Eq. (3.58)
    calculate phase difference $\Delta\theta_i = \theta_k^q - \theta_k^{q-1}$
    if $\Delta\theta_i \approx 0$ or π **then**
        $f_{idf\,i}$ is mode
    else
        $f_{idf\,i}$ is not a mode
    end if
end for

Nuclear Sciences (BRNS) and hence the building is referred as BRNS Building in this study. The other building on the right of the staircase has base isolators. Both the buildings are separated from staircase and free to move during any seismic event. The fixed base building has sensors at 1^{st} and 4^{th} (roof) floor to measure the bi-axial accelerations. While the ground acceleration is measured at the base as mentioned in Fig. 3.2. The geometric details (*i.e.* dimensions, section property etc) and material details (*i.e.* concrete and rebar strengths) are also provided in Fig. 3.2. A lumped mass model is considered here which has two dof (*i.e.* X and Y as shown in Fig. 3.2) at each floor level. The structure is made of M25 grade concrete and Fe415 grade steel. Using these parameters, the FE model is developed in MATLAB and eigen analysis is carried out to study the natural frequencies and Table 3.1 shows the values of expected natural frequencies of the structure as per design. It may be noticed that fundamental frequency is 4.75 Hz. Two different cases are studied (*i.e.* synthetic measurement and filed experiment during actual earthquake) here to establish the efficiency of the proposed identification strategy. The reason behind using synthetic measurement is that the identified modal damping ratio from the response due to earthquake can not be compared.

Using lumped mass model of the BRNS building (details in Appendix B), forward problem is solved by direct time integration scheme using Newmark-β method. For this purpose, the E-W and N-S components of measured acceleration during El-Centro (1940) earthquake are applied along X and Y directions. Fig. 3.3 shows these ground motion records. The modal damping ratio considered for this analysis are 2% in the first two modes and 1% in rest of the modes [155]. As the proposed identification scheme is based on limited measurements, only 3^{rd} and 4^{th} floor response in X and Y directions are used for this numerical study. Fig. 3.4 shows these synthetic records which are used for further numerical analysis. First, the frequency ranging from 0 to 40 Hz is sub-divided into five equally spaced frequency bands and a fft based algorithm in MATLAB is used to filter the measured signals. Using these band pass signals from four locations, HHT based identification strategy is applied to evaluate the modal frequencies and the phase angles are compared to separate the modal frequencies from the excitation frequencies. Once the frequencies are identified, each band is further sub-divided into two divisions and HHT based scheme is adopted again on the band passed signals until to convergence in frequency estimation is achieved. Fig. 3.5 shows the IMFs in first and second mode and respective instantaneous phase and instantaneous amplitude in logarithmic scale obtained from $\ddot{Y}_4$. To avoid repetition of similar plots, only first two modes from $\ddot{Y}_4$ are shown here. Using these plots, the modal frequency and damping ratio are identified by fitting the linear polynomial as described in Eq. 3.15 to Eq. 3.17. The natural frequencies identified from all four measurements are shown in Table 3.1. The identified natural frequencies match with the theoretical values closely. The maximum error is found to be well within 10%. Furthermore, it may be noticed that all eight frequencies are identified from each measurements which is clearly an advantage of the proposed method. From Table 3.1, it can be noticed that the modal damping estimated from the forced vibration has poor accuracy compared to its original

values. This behavior is expected as the forced vibration does not contain any free decay due to damping characteristic of the structure and hence their estimation is inaccurate. To study the accuracy of damping estimation, proposed adaptive HHT scheme is applied on impulse responses of the structure. Only the identified damping values are tabulated here for brevity. The initial band pass filtering scheme is kept same. Table 3.1 shows the identified modal damping from acceleration responses at (X_1,Y_1) and (X_4,Y_4) due to impulse. It may be noticed that the estimated damping values closely match with their theoretical values. Moreover, all the eight modal damping ratio are obtained from each measurement as it is done in case of the natural frequencies. Therefore, it may be concluded that the proposed adaptive HHT based identification strategy can be used for modal identification of structures subjected to multi-component earthquake excitations. However, the damping of the structure may be identified from impulse response separately as the estimation of damping is not accurate from the forced response.

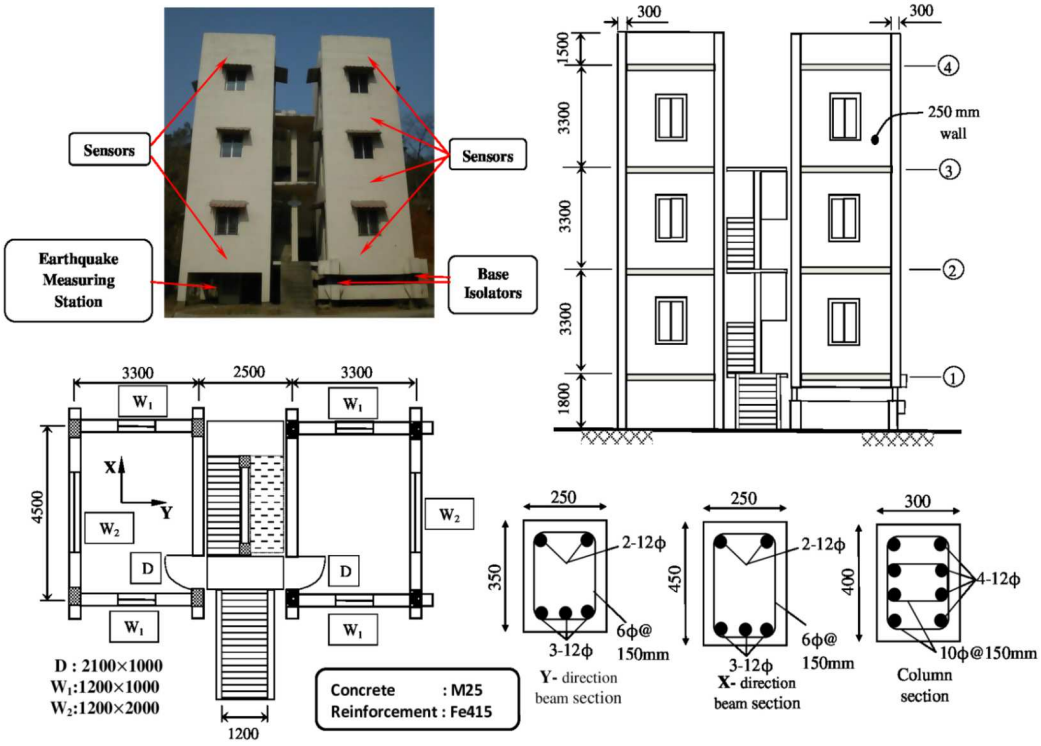

Figure 3.2: Details of BRNS Building in IIT Guwahati (all dimensions are in mm); Building on left side of the staircase is used in this study

3.5.2 Modified MEMD

The adaptive MEMD method proposed in section 3.1.2 is used here for numerical analysis to demonstrate its efficiency of this method for structural system identification. This example is a simulated response of a 5DOF system which is excited by zero mean Gaussian white noise. In this

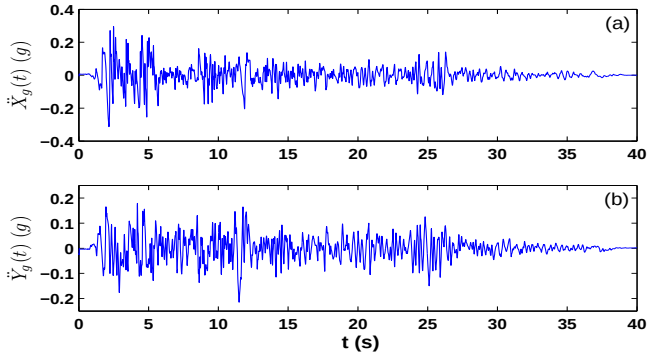

Figure 3.3: Recorded ElCentro ground motions (a) E-W component (b) N-S component

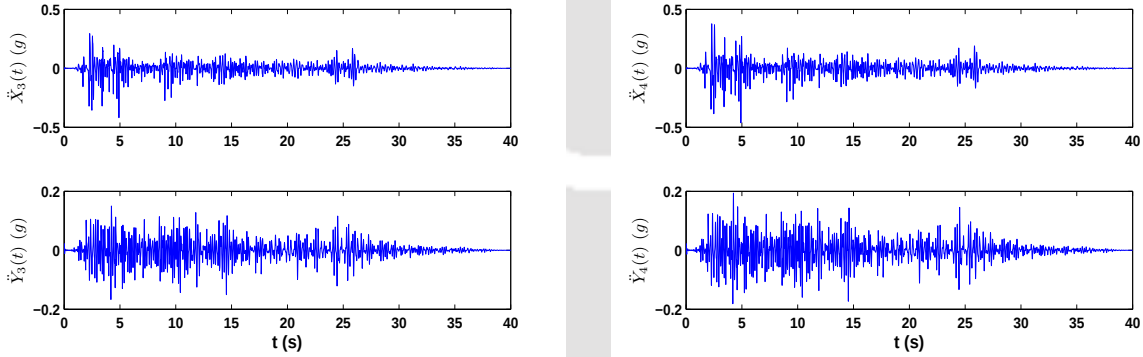

(a) (b)

Figure 3.4: Simulate acceleration response of BRNS Building (a) 3^{rd} floor and (b) 4^{th} floor

example, a 5DOF system having equal mass of 19.5Kg at each DOF is considered whose stiffness matrix is given by [156]

$$K = \begin{bmatrix} 77108 & -36564 & 4549 & 1612 & -211 \\ -36564 & 58596 & -35825 & 5481 & 1169 \\ 4549 & -35825 & 58344 & -36587 & 7463 \\ 1612 & 5481 & -36587 & 52688 & -22962 \\ -211 & 1169 & 7463 & -22962 & 14621 \end{bmatrix} N/m \tag{3.63}$$

The first five natural frequencies of this system are 0.91, 3.37, 7.11, 10.66 and 12.73 Hz while the critical damping ratio is assumed to be 2% in all modes. The model is excited by the zero mean Gaussian white noise with unit variance at all floor level. The top floor response (channel-1; here floor response referred as channels) for this input is shown in Fig. 3.6 with the spectrogram of this acceleration record which clearly shows the energy localization in time-frequency scale.

First, the five responses are analyzed using EMD. Fig. 3.7 shows the first 4 IMFs obtained from

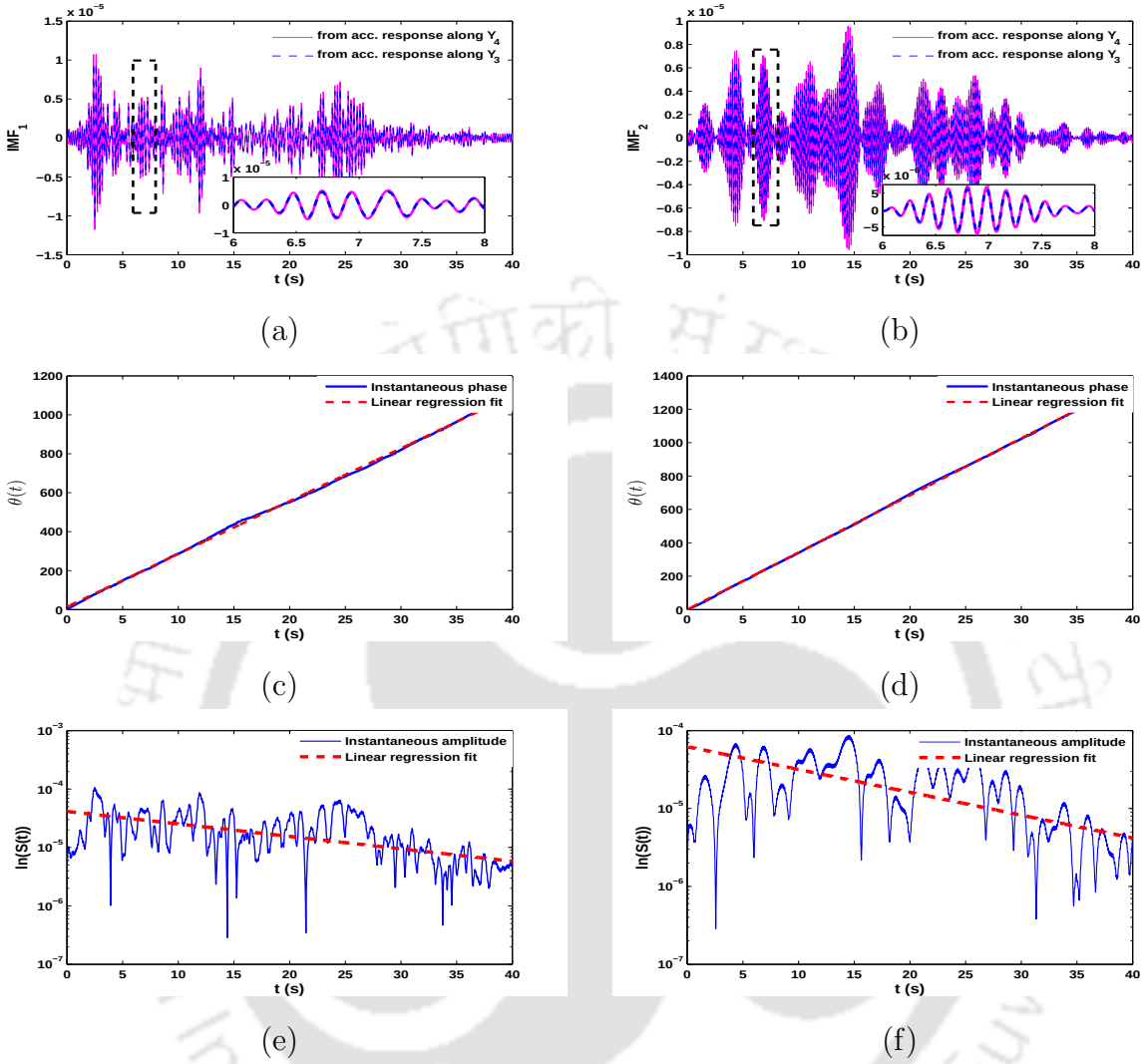

Figure 3.5: IMFs extracted from synthetic responses (a) 1^{st} mode and (b) 2^{nd} mode; instantaneous phase angles of response $\ddot{Y}_4$ (c) 1^{st} mode and (d) 2^{nd} mode; instantaneous amplitudes of response $\ddot{Y}_4$ (e) 1^{st} mode and (f) 2^{nd} mode

this analysis. It is clear that for channel-1 (i.e. the top floor response) EMD can identify first mode only with proper signal to noise ratio (SNR). The second and third IMFs are significantly corrupted by noise while the fourth IMF is severely affected by mode-mixing. The spectral contents of these IMFs are inconsistent across all the channels and no definitive conclusion can be derived regarding the peak frequency and the bandwidth to facilitate their interpretation as modes.

Proceeding to MEMD, the difference in the spectral quality and the consistency of the decomposed IMFs is very clear and obvious from Fig. 3.8 which shows the amplitude spectra of the IMFs obtained from the MEMD of the complete data set. The first mode is consistent across all the channels and the presence of the first three modes in the neighborhood of 0.9Hz, 3.35Hz and 7.161Hz can be inferred by observing the first three IMFs. However, the fourth mode obtained

from the MEMD fails to identify the 4^{th} and 5^{th} mode owing to the presence of mode-mixing. Although, the 4^{th} mode can be inferred from the 4^{th} IMFs of the channels 4 and 5, the noise content and the consistency across all the channels forbids a safe interpretation. From this study two conclusion are apparent – (1) MEMD is more robust compared to EMD from the view-point of mode-mixing and (2) MEMD performs as a better filter-bank which is clear from the superior SNR of the IMFs obtained using MEMD compared to MED. On the downside however, MEMD IMFs are not free from mode-mixing in the higher mode with low energy content. This demerit forms the main motivation for proposing the adaptive MEMD algorithm.

From this Fig. 3.8, the 4^{th} IMF clearly shows mode-mixing between the 4^{th} and 5^{th} modes. To identify these two modes, filtering of the signal is proposed around the frequencies corresponding to 4^{th} and 5^{th} modes. For this purpose, the peak frequencies are identified and the bandwidth are selected in an iterative manner from wider to narrower in successive iteration as described in proposed methodology section. Fig. 3.9 shows the final IMFs corresponding to first five modes after filtering the signals followed by MEMD. Tablee 3.2 shows the identified frequency from five channels of the the system using the proposed adaptive MEMD. It may be noted that the error in frequency estimation is within 5% of their respective original value. Using these identified frequencies, the model of the 5DOF system is updated to obtained the mode shapes of the system. Readers may refer to [147] for details of this updating scheme. Fig. 3.11 shows the actual and identified mode shapes for the 5DOF system. It is clear that the five identified mode shapes closely resemble with their respective original values.

Finally, the modal damping ratios are identified from the IMFs as discussed in the proposed methodology. For this purpose, RDT is applied on the IMFs obtained using proposed adaptive MEMD to obtain the free response, as shown in Fig. 3.10. Table 3.2 shows the identified damping values in first four modes which are well within 10% of the respective original values and hence can be considered satisfactory. As the energy content in 5^{th} mode is very low, the modal damping ratio evaluated in this method is close to zero and hence, not reported here. Finally, sensitivity analysis is performed to study the robustness of the proposed adaptive MEMD algorithm. For this purpose, two different levels of zero mean Gaussian white noise with SNR 5% and 10% are added. The results from the noise contaminated data are shown in Table 3.3. From this table it is clear that expect the first mode, the other modal frequencies are not effected by the measurement noise. The bandpass pre-filtering proposed in this thesis is inherently capable to remove the ill effects of additive measurement noise modeled as zero mean Gaussian white noise. However, the percentage error in first mode increases with the magnitude of the measurement noise. This may be attributed to the magnitude of the first mode which leads to higher value of error in frequency estimation while evaluating the percentage change. In this context, it may be noted that absolute change in the magnitude of first mode is very small even for higher values of measurement noise. This indicates that proposed pre-filtering based modal identification algorithm is unaffected by the presence of

additive Gaussian measurement noise. From this analysis, it may be concluded that that proposed adaptive MEMD performs satisfactorily for modal parameter estimation even in presence of noise contamination.

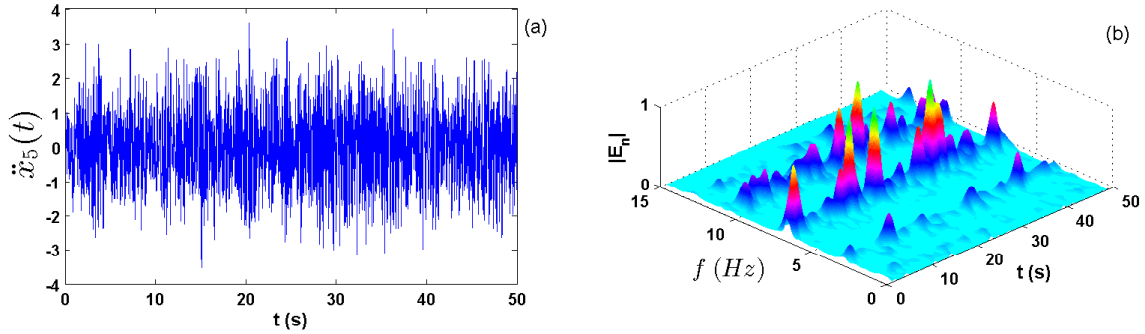

Figure 3.6: 5^{th} dof response of the numerical model – (a) acceleration and (b) spectrogram

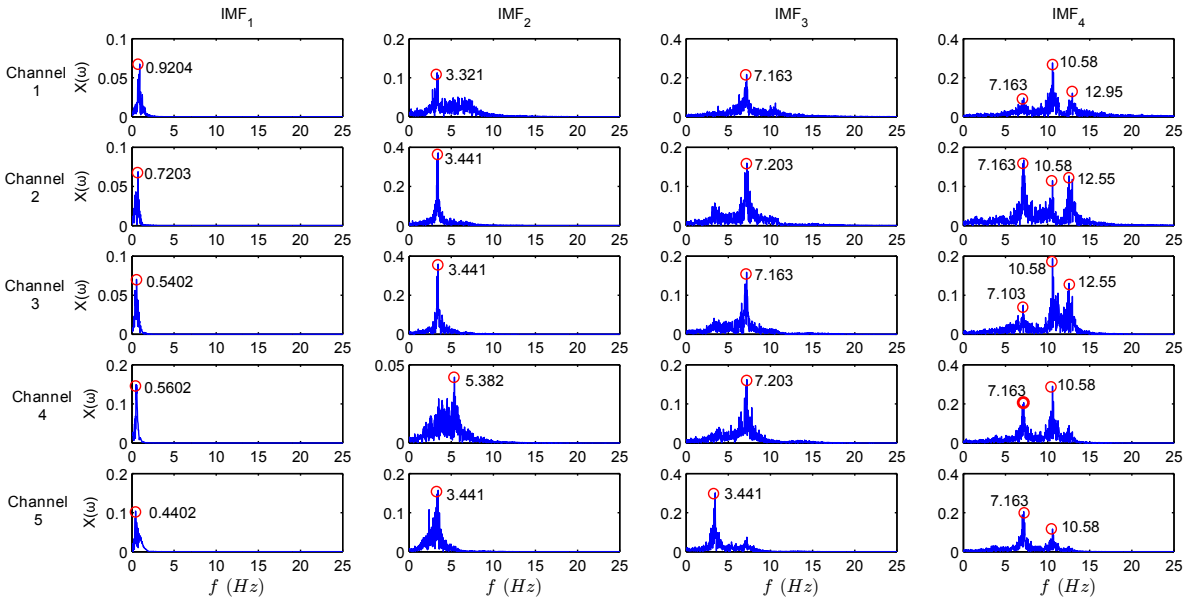

Figure 3.7: EMD-IMFs for the numerical model

3.5.3 Combined Wavelet-Hilbert Transform

In this section, the proposed Wavelet-Hilbert transformation based modal identification strategy is used for numerical analysis to verify its performance. The algorithm for this identification strategy is provided below (Algo. 3). This example is a simulated case of a 3-dof system as shown in Table 3.4. Here, two cases are considered which have closely spaced strong modes and closely spaced weak modes as describe by Case II and Case III Table 3.4. These two examples are chosen purposefully

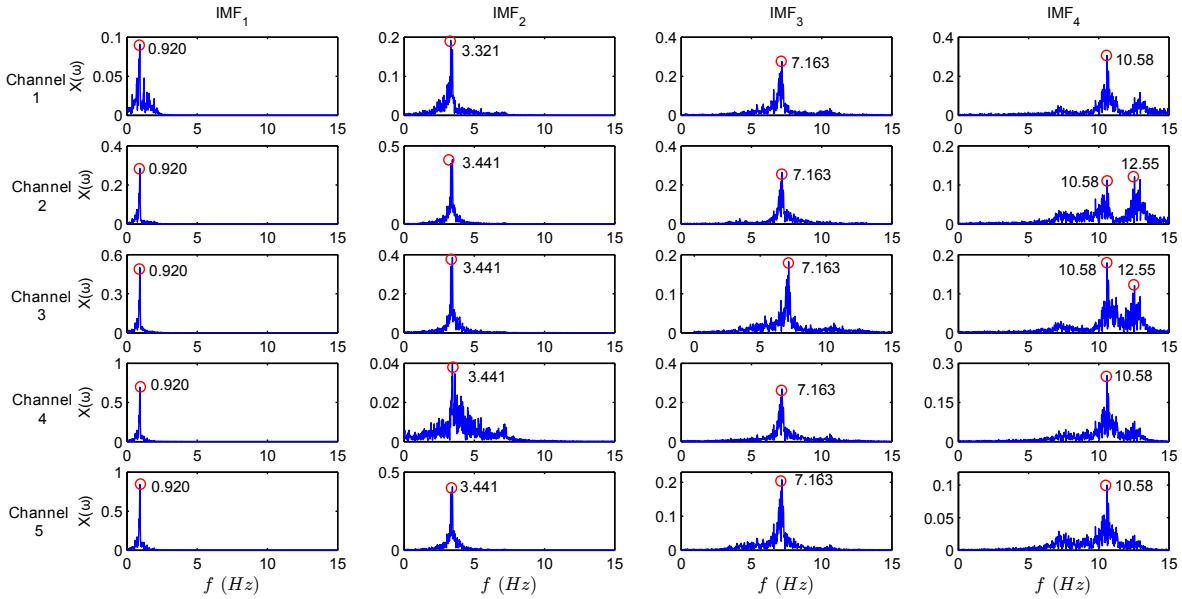

Figure 3.8: MEMD-IMFs for the numerical model

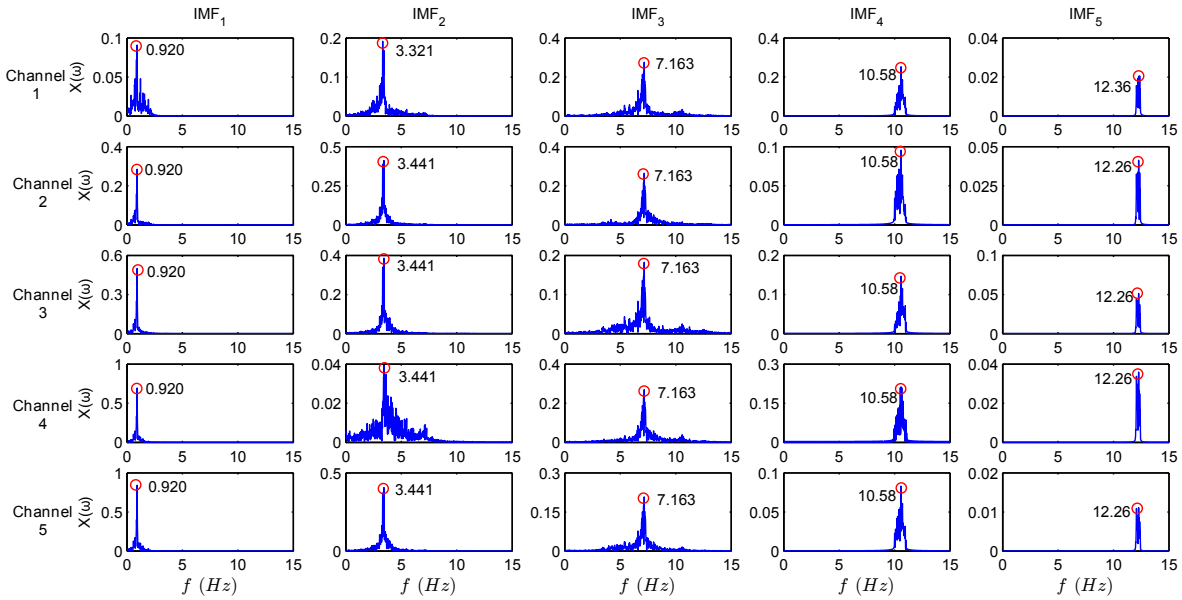

Figure 3.9: IMFs obtained using the proposed algorithm

(from [152]) to test the efficiency of the proposed method as the energies are localized within a short frequency range. Case II has closely spaced 2^{nd} and 3^{rd} modes with almost equal energy content while Case III has closely spaced last two modes with uneven energy contribution. The 1^{st} mode is weak in both the cases.

Modal damping ratio are assumed to be 5%, 3% and 2% in three modes respectively. In this

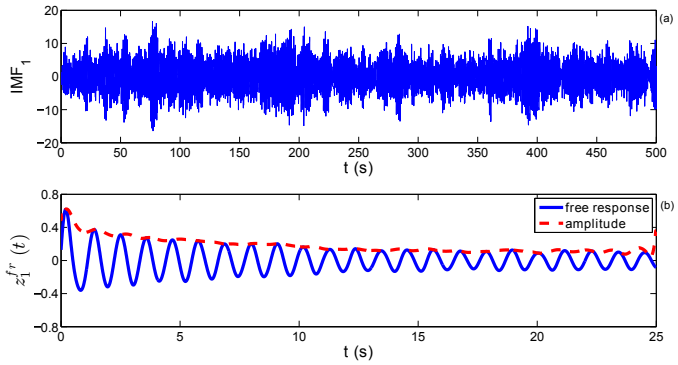

Figure 3.10: Free response estimate by RDT for 1^{st} mode

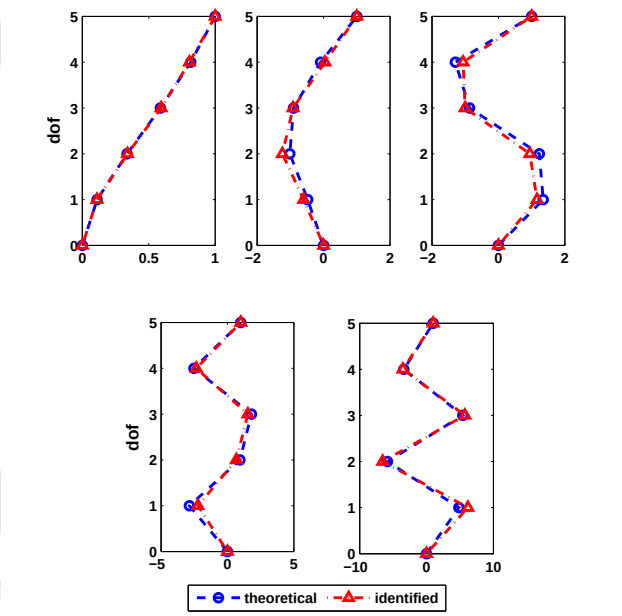

Figure 3.11: Identified mode-shapes of the numerical model

example, base excitation is assumed to be zero mean Gaussian white noise process for both the cases. Using this excitation, responses are simulated and acceleration records are used for identification. Fig. 3.12(a) and 3.12(b), show the response for Case II in both time and frequency domain. The Fourier amplitude spectrum shows three modal frequencies and their relative energy contents. It is clear from this figure that 2^{nd} and 3^{rd} modes are dominant while the 1^{st} mode contributes less in the total response. For the second system, time and frequency domain responses are shown in Fig. 3.12(c) and 3.12(d). In this case, the energy content in 1^{st} mode increases compare to Case II while the modal energy decreases from 2^{nd} to 3^{rd} mode. First the conventional HHT is applied over these vibration response. Fig. 3.13 shows the IMF obtained in Case II. Both time and frequency signature of the first four IMFs with significant energy content compared to many others are shown

in this plot. It can be observed that the first IMF having maximum energy content represents a spurious mode. Second IMF corresponds to 3^{rd} mode of the system in Case II while the last two IMFs shown in Fig. 3.13 shows peaks which do not corresponds to 1^{st} and 2^{nd} frequency. These are due to mode-mixing where peaks corresponds to other frequency due to ill effects of contiguous modes.

Using these simulated responses, the proposed wavelet based filtering technique coupled with Hilbert transform is applied for parameter estimation. For these purpose, the number of band is set to 12 and the F & σ values are considered as 1.75 & 1.1667 respectively covering a frequency range of 0.5 to 4Hz. The details of this discretization scheme for MLP based CWT may be found in Basu and Gupta [157]. In this context, Eq. 2.36 and Eq. 2.37 have limits to infinity. As the signal is only valid over a particular time interval (say 0 to t) the limits of time localization parameter b in Eq. 2.37 are set to $0 - 2.5$s to $t + 2.5$s. Using these parameters, the simulated time histories are filtered and the energy corresponding to each frequency scale is evaluated. Then the process is repeated with smaller frequency bands as described in Eq. 3.36. If the convergence is achieved (i.e. each band having one energy peak), the time signal corresponding to these bands are obtained using inverse wavelet transformation. As proved in the previous section, these time signal must be equal to the IMF generated using modified versions of HHT [158]. Fig. 3.14 shows the wavelet based filtered signal and IMF as described by Peng et. al. [158]. A close match is observed between these two signals which proves the validity of the claim made in Eq. 3.35. This, in term, shows that the proposed CWT based filtering helps to extract mono-component IMF which otherwise difficult from the conventional HHT as it often leads to spurious modes or having ill-effects of contiguous frequencies. Using these filtered signals, Hilbert transform is applied for modal frequency identification as described in section 2.2. Further, to identify the modal damping, RDT is used to obtained the free responses. From the free responses, damping ratio are estimated as describe in the previous section. A similar observation regarding filtered signals using CWT and modified HHT were observed in Case III (Fig. 3.15) which are not included here to avoid repetition. Table 3.5 shows the identified parameters (i.e. ω_n and η) in three modes for different simulated measurement noise levels. From these results, it may be noticed that the error in natural frequency estimation is well within 5% in all the cases. The error in damping ratios are also within in 10% except in one case where the damping ratio in 3^{rd} mode (which is a weak mode) is 10.27%. Therefore, the proposed algorithm can be considered satisfactory and can be used for modal parameter estimation which has distinct advantage over traditional HHT or filtered HHT [158, 147].

3.5.4 Synchrosqueezed Transformation

In this simulated case, the 3-dof system [152] with white noise as support excitation as described in Table 3.4 is used. Here, all three cases are studied - a) strong and separated modes, b) two

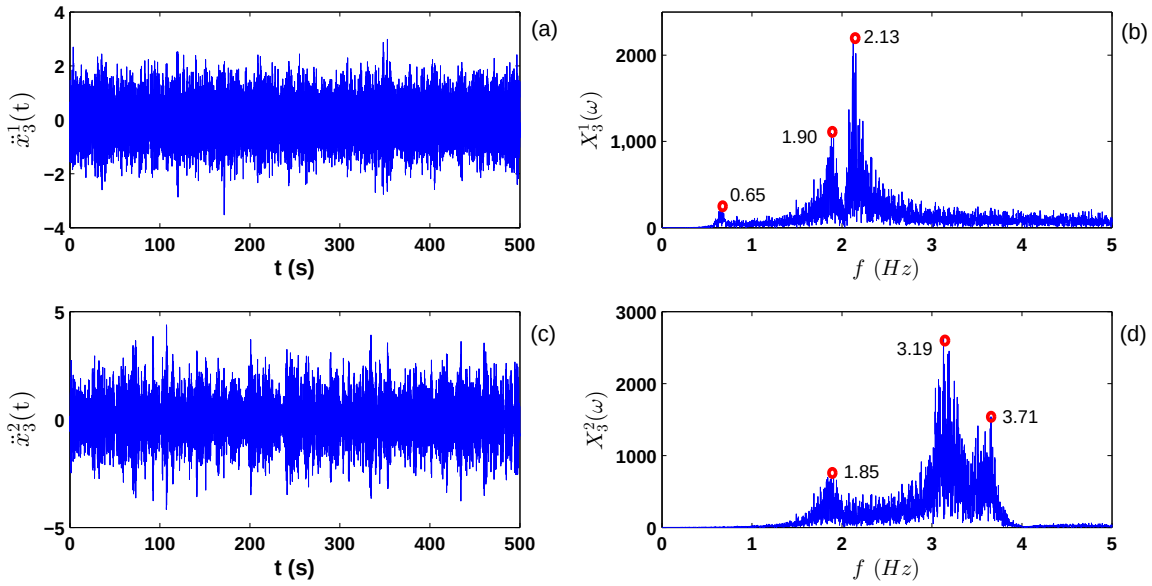

Figure 3.12: Acceleration response at 3^{rd} dof – (a) & (c) are time histories, (b) & (d) are Fourier amplitude spectrum (n.b. subscript represents dof while superscript represents cases)

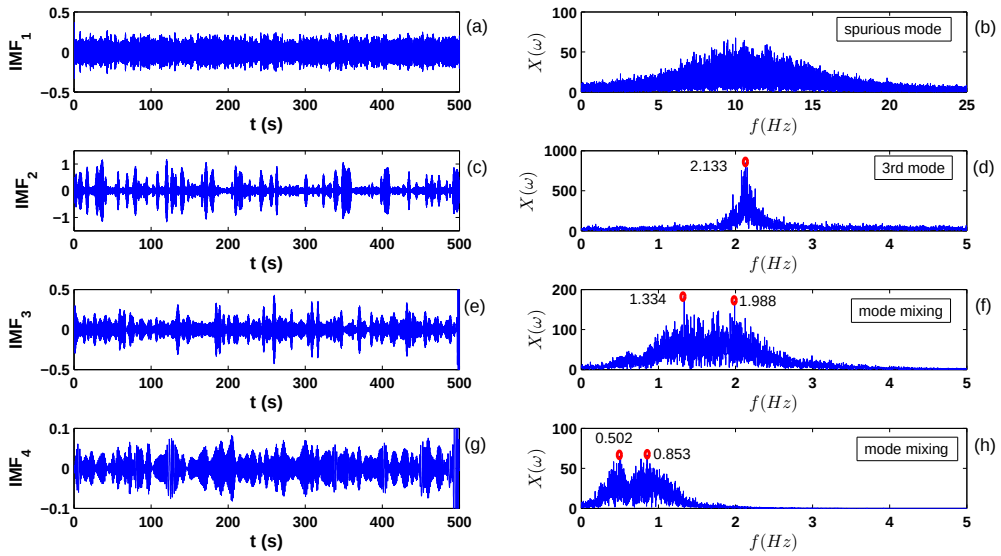

Figure 3.13: Candidate modes by EMD method for Case II

closely spaced strong modes and c) two closely spaced weak modes whose properties are shown in table (3.4). It may be noted that all three systems are independent i.e. Case II and Case III are not derived from Case I. They, in principle, represent three different eigen systems to validate the performance of the proposed algorithm. Fig. 3.16 shows the frequency response function

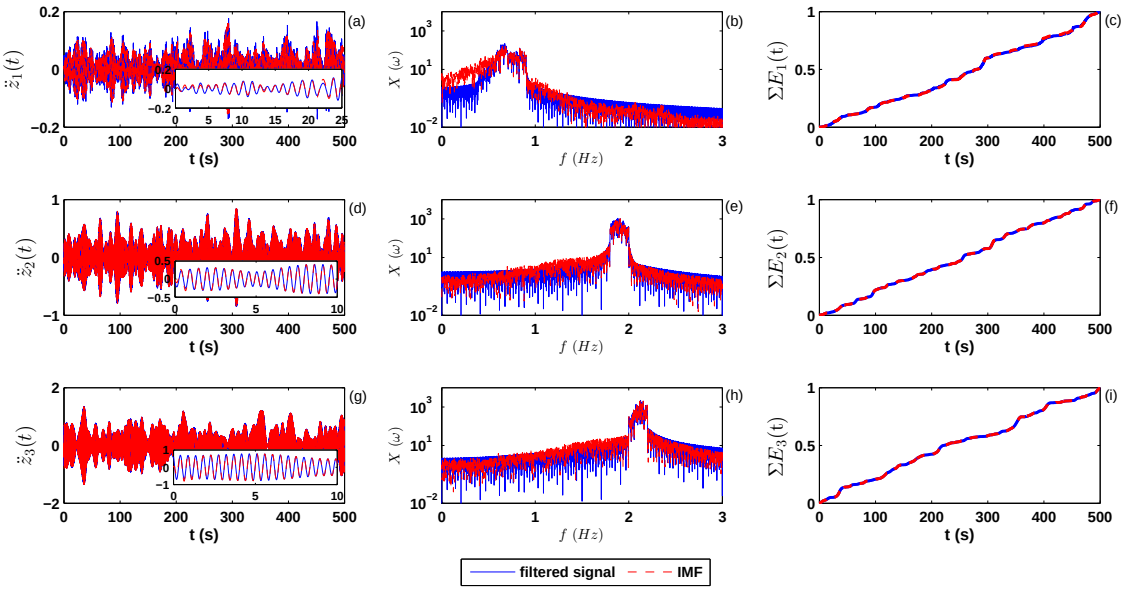

Figure 3.14: Case II - CWT based filtered response in three modes (Column1: Time history; Column2: Fourier amplitude spectrum & Column3: cumulative energy growth)

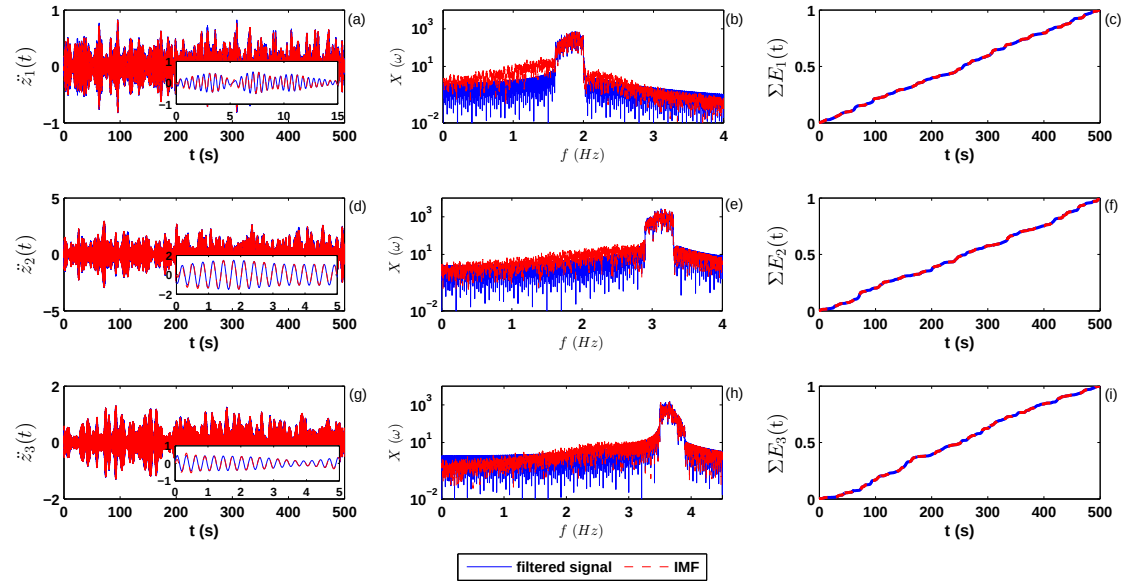

Figure 3.15: Case III - CWT based filtered response in three modes (Column1: Time history; Column2: Fourier amplitude spectrum & Column3: cumulative energy growth)

(FRF) of the 3^{rd} dof for all 3 cases. From this figure, it may be noted that Case II is the most challenging as the two frequencies (i.e. 2^{nd} and 3^{rd}) are very close to each other with almost similar energy content. Fig. 3.17(a) shows the response of the 3^{rd} dof due to simulated white noise excitation. Here, it should be noted that the same excitation is used for all three cases. This

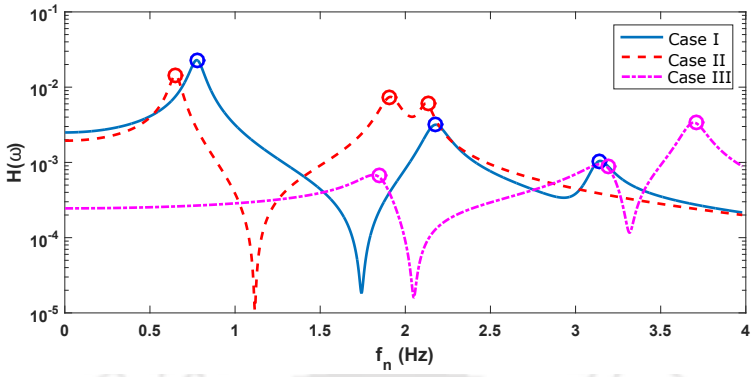

Figure 3.16: Frequency response function (FRF) of 3dof system

simulated response is used for wavelet transformation with complex morlet basis with 2^8 scales initially covering a frequency range of 0.001 to 10Hz. The algorithm finally converges with 2980 scales. Here, the frequencies identified in two successive iteration are used to check the convergence where the iteration is stopped if the absolute error is below the tolerance limit (say 10^{-2}, which remains same for the other examples). The scalogram of this WT is shown in Fig. 3.17(b). It is extremely difficult to identify the frequencies using visual inspection of this scalogram, although different regions of scales containing the dominant frequencies can be detected. To improve it further, synchrosqueezing is applied on the WT coefficients and the scalogram is shown in Fig. 3.17(c). From these figures, it is clear that the frequency localization has improved after SST, but it is still difficult to identify the frequencies by visual inspection or ridge and skeleton as proposed in the literature [113]. To alleviate these issue as stated in the objective, k-means clustering is applied on the SST coefficients. Clusters are formed on the basis of energy concentration which is equivalent to the square of the modulus of coefficients obtained from SST analysis as given in Eq. 3.54. For this purpose, optimum cluster number is determined using gap statistics as discussed in Eq. 3.61 and 3.62. This is achieved in an iterative manner over a realistic range (typically upto 15) with $c = 1$ as the initial number that is raised by one in every succesive iteration. The gap values for every iteration is evaluated and are plotted in fig 3.18(a). From this figure, optimal number of cluster can be identified as 4. Based on this analysis, 4 clusters are formed and the median of each cluster is considered as the identified frequency. These cluster are arranged as per cluster weights described in Eq. 3.60 which are shown in Fig. 3.18(b). Here, it can be observed that 4 frequencies are identified from the median values of these clusters as opposed to 3 modal frequencies of the system. Now, to identify the mode, phase spectrum of the response corresponding to the median frequencies of the cluster are evaluated as per Eq. 3.58. Fig. 3.19 shows the responses in the time domain obtained from Eq. 3.57 corresponding to each cluster median with ±2.5% width on the either side of this value. Fig. 3.20 shows the phase difference where 1^{st} dof is considered as reference. It may be noted that response corresponding to first three clusters are mode as the phases are in unison while the response in the 4^{th} cluster shows randomness which is against the

fundamental property of the mode. Based on this analysis, the identified frequencies are 0.801, 2.164 and 3.251 Hz in Case I which are very close to their theoretical values as shown Table 3.6. Once the frequencies are identified, modal responses are considered for the estimation of the damping ratio. However, it may be noted from Fig. 3.19 that time history corresponding to each cluster do not exhibit decay as these are forced responses. Hence, they are not directly used for damping estimation as the modal damping ratio is very sensitive and are best evaluated from the decay of the transient response. For this purpose, NExT [33] is applied over this modal responses prior to the damping estimation which is not discussed here as it is not the theme of this study. Once the free response is obtained from NExT, Eq. 3.56b is adopted to evaluate the critical modal damping ratio. The estimated modal damping ratio are 0.053, 0.03 and 0.02 respectively in Case I which are very close to their respective theoretical values.

Using similar steps as stated above, Case II and Case III are solved and the scalograms using WT and SST are shown in Fig. 3.22 and Fig. 3.23 respectively. The number of scales needed in Case II and Case III are 2980 and 4476 respectively. This shows that a large number of scales are required for closely spaced weak modes as in Case III. However, visual inspection of the scalograms do not reveal the modal frequencies as usual. Hence, the scalograms with improved resolution (i.e. after SST) are used for clustering and the optimal clusters for both of them remain 4. These plots are not shown here to avoid repetition. In this context, it is relevant to explain why clustering is performed over SST coefficients and not directly over WT coefficients. WT coefficients being poor in resolution offers spurious modes and hence spurious clusters as the energies are dispersed over different frequency bands instead of being localized in and around few scales as observed in the SST scalogram. Due to this reason, spurious modes are generated leading to inaccurate estimation of the modal frequencies as shown in Fig. 3.21 which shows additional clusters obtained from wavelet transformation coefficients. Finally, instantaneous phases are compared as described in Case I to identify the modal frequencies. Table 3.6 shows the identified frequencies and modal damping ratio for all these cases. It can be observed that the estimated values are well within 5% of their respective theoretical values, except in one case where the error is found to be 7%. This is in Case II which is the most critical as the 2^{nd} and 3^{rd} frequencies are closely spaced with almost same energy content. Due to this reason, extraction of monocomponent signals through SST is difficult which leads to higher estimation error. As mentioned earlier, SST also fails to pin point scales (and respective frequencies) if the difference between them is close to or below $\Delta\omega$ (i.e. sampling rate). With these validation exercise, it may be concluded that the performance of the proposed algorithm is satisfactory and can be used for field implementation.

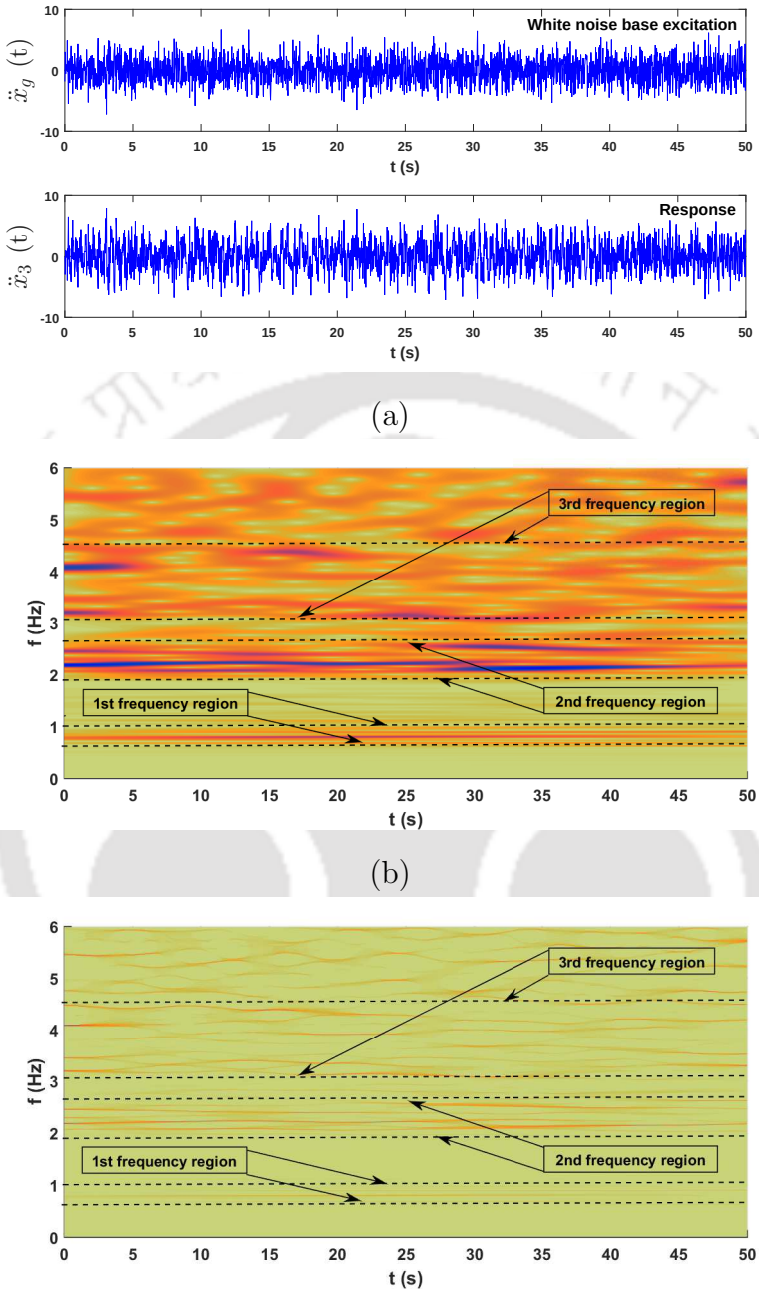

Figure 3.17: Time histories and scalogram - (a) input and output; (b) WT scalogram for Case I; (c) SST scalogram for Case I

3.6 Summary

The numerical results presented in this section clearly demonstrate the performance of the adaptive versions of HHT and WT for modal parametric identification using non-stationary excitation.

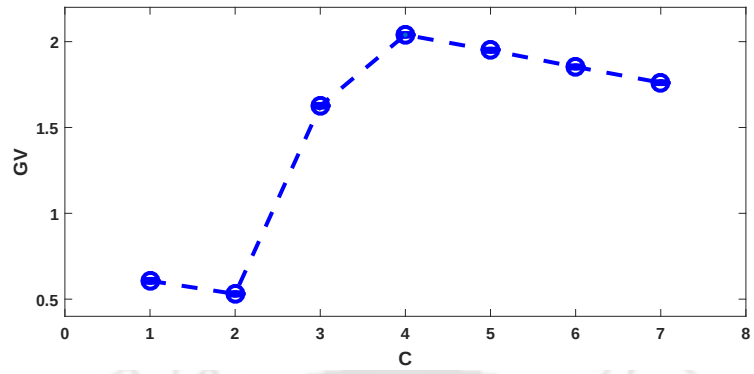

(a)

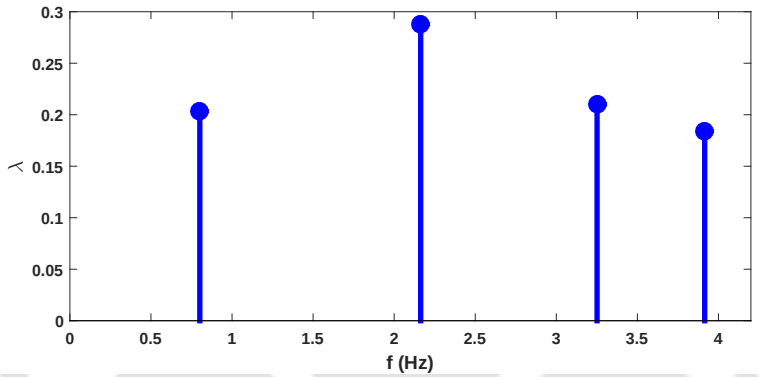

(b)

Figure 3.18: k-means clustering - (a) GV statistics and (b) clusters

For this purpose, HHT is first considered with adaptive pre-filtering. The digital filters used in this algorithm is available in different signal processing toolbox. It is shown that adaptive HHT can efficiently track the frequency from the forced vibration response as opposed to free or ambient vibration response in HHT based approach. The empirical mode decomposition in the HHT algorithm is then modified by its recently developed multi-response version (i.e. MEMD). It is noticed to perform well within the adaptive filtering framework. However, effect of MEMD is noticed to be marginal as it carries all basic features of EMD. The success of adaptive filtering is further explored as the digital filters used in these two proposal is prone to overlapping and leakage which may be detrimental for closely spaced frequencies. With this in view, wavelet based filtering is introduced using MLP basis function. This wavelet basis offers leakage free filtering as the basis function has compact support in frequency domain. It is shown that this wavelet based filtering makes the application of EMD (as the previous two cases) redundant. The reason behind this lies with the mono-component filtering of the response where Hilbert transformation alone is sufficient to identify the modal parameters. Thus, combined wavelet-Hilbert transformation based algorithm is developed. The performance of wavelet based filtering further motivates to explore its

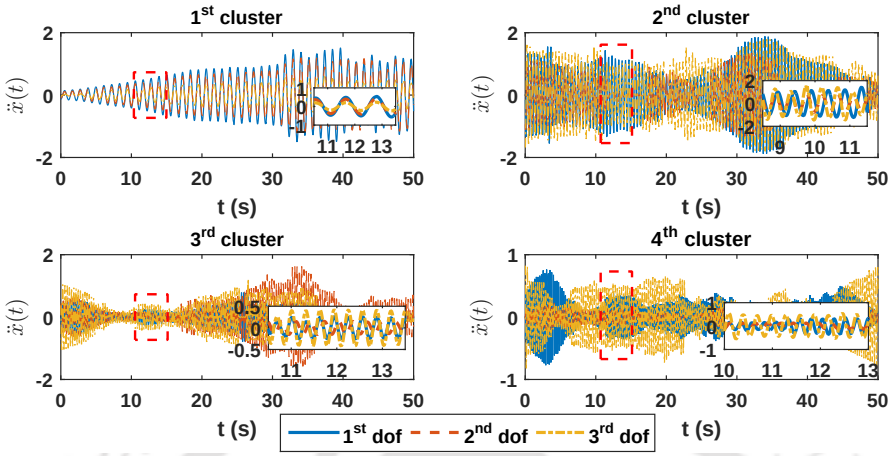

Figure 3.19: Reconstructed signals corresponding to median frequencies

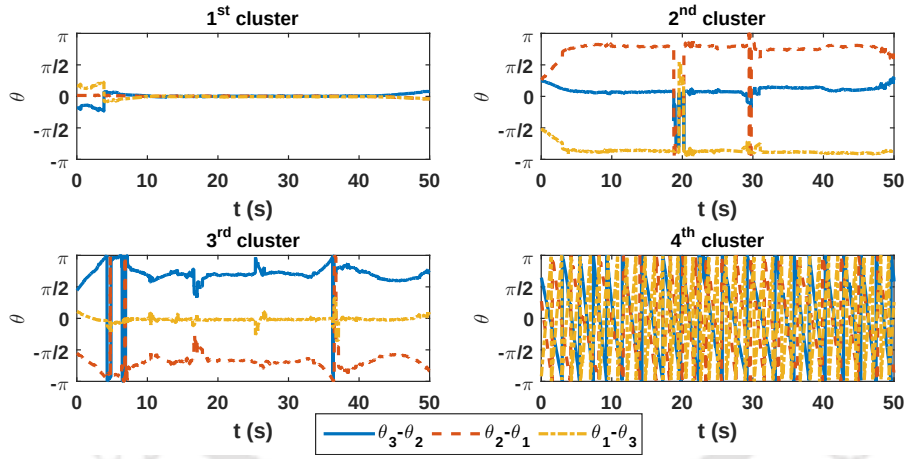

Figure 3.20: Phase portrait of reconstructed signals (subscript in legend represents dof)

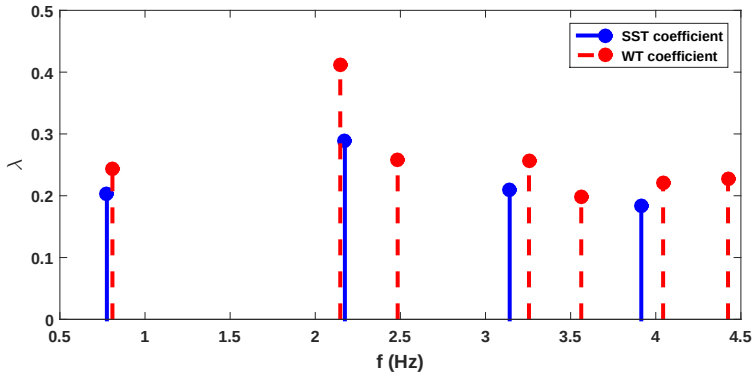

Figure 3.21: Clusters from WT and SST analysis for Case I

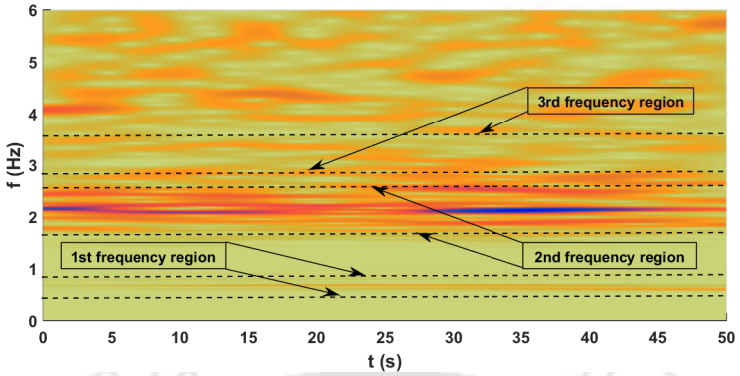

(a)

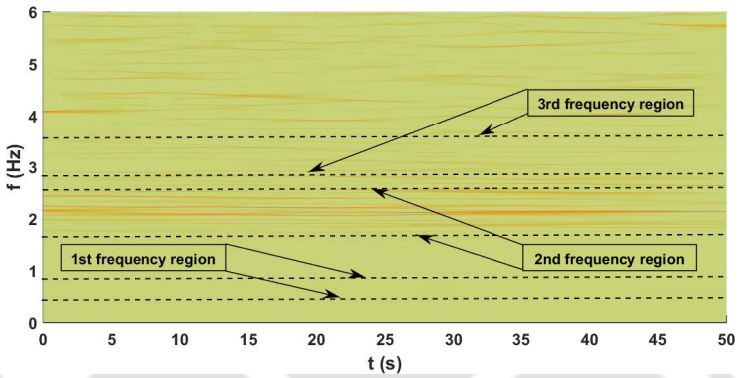

(b)

Figure 3.22: Scalograms - (a) Wavelet coefficients in Case II ; (b) SST coefficients in Case II

performance. With this in view, recently developed synchrosqueezed transformation is explored and an automated identification strategy is developed where synchrosqueezing is combined with *k-means* clustering. This unsupervised clustering on synchrosqueezing coefficients helps to locate modal frequencies without any intermittency or user interfacing. The numerical results presented here clearly demonstrate the performance of the proposed algorithm for modal parametric identification from the forced responses. This will be further demonstrated using field test data of the actual structure in their operational environment in the next chapter.

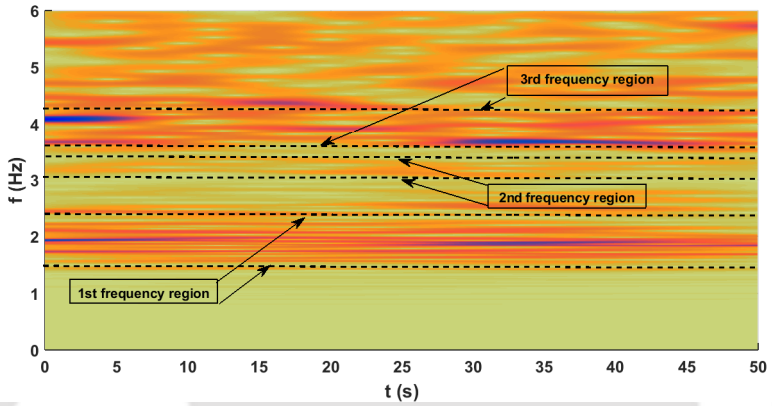

(a)

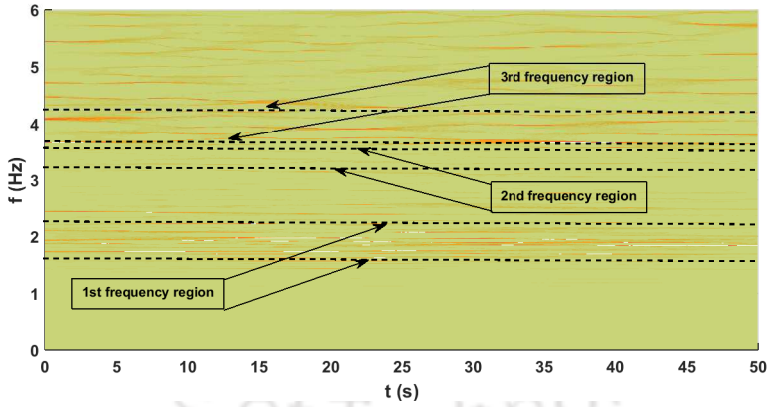

(b)

Figure 3.23: Scalograms - (a) Wavelet coefficients in Case III ; (b) SST coefficients in Case III

Table 3.1: Estimated parameters from synthetic measurements

Mode	Theoretical Value		Estimated Value											
			From Forced Response								From Impulse Response			
			ω (Hz)				η (%)				η (%)			
	ω (Hz)	η (%)	X_3	Y_3	X_4	Y_4	X_3	Y_3	X_4	Y_4	X_3	Y_3	X_4	Y_4
1	4.75	2	4.29	4.32	4.27	4.32	1.52	1.14	1.53	1.14	2.07	2.02	2.07	2.02
2	5.84	2	5.68	5.44	5.68	5.44	1.02	1.24	1.02	1.24	2.07	2.08	2.08	2.08
3	13.20	1	12.55	12.46	12.15	12.50	0.72	0.77	0.82	0.77	1.04	1.03	1.10	0.84
4	16.25	1	15.16	15.29	15.11	14.79	0.65	0.55	0.65	0.53	1.06	1.04	1.11	1.13
5	19.98	1	18.90	18.76	19.10	19.23	0.31	0.50	0.33	0.47	1.01	1.07	1.15	0.87
6	24.57	1	22.98	23.01	22.98	23.06	0.37	0.39	0.36	0.39	0.96	0.96	0.95	0.98
7	27.05	1	26.32	26.31	26.29	26.19	0.40	0.27	0.40	0.28	1.04	1.06	1.03	1.04
8	33.10	1	31.46	31.12	31.41	31.14	0.20	0.17	0.20	0.17	0.96	0.96	0.96	0.94

Table 3.2: Identified parameters of the numerical model using the proposed algorithm

Theoretical Values		Identified Values									
		Chanel 1		Chanel 2		Chanel 3		Chanel 4		Chanel 5		
f_n (Hz)	η (%)	f_n (Hz)	ϵ	f_n (Hz)	ϵ	f_n (Hz)	ϵ	f_n (Hz)	ϵ	f_n (Hz)	ϵ	η (%)	ϵ
0.9146	2	0.9204	-0.63%	0.9204	-0.63%	0.9204	-0.63%	0.9204	-0.63%	0.9204	-0.63%	2.09	-4.50%
3.3710	2	3.3210	1.48%	3.4410	-2.08%	3.4410	-2.08%	3.4410	-2.08%	3.4410	-2.08%	2.16	-8.00%
7.1066	2	7.1630	-0.79%	7.1630	-0.79%	7.1630	-0.79%	7.1630	-0.79%	7.1630	-0.79%	1.99	0.50%
10.6569	2	10.5800	0.72%	10.5800	0.72%	10.5800	0.72%	10.5800	0.72%	10.5800	0.72%	1.81	9.50%
12.7284	2	12.3600	2.89%	12.2600	3.68%	12.2600	3.68%	12.2600	3.68%	12.2600	3.68%	-	-

Table 3.3: Identified natural frequencies for different SNRs

Theoretical Values	Identified f_n			
	5%		10%	
f_n (Hz)	f_n	ϵ	f_n	ϵ
0.9146	0.9204	-0.63%	0.9583	-4.78%
3.3710	3.4233	-1.55%	3.4233	-1.55%
7.1066	7.1373	-0.43%	7.1373	-0.43%
10.6569	10.4409	2.03%	10.4409	2.03%
12.7284	12.1161	4.81%	12.1161	4.81%

Table 3.4: Parameters of 3dof system

	$[M]$	$[K]$	f (Hz)	η
Case I	$\begin{bmatrix} 10 & 0 & 0 \\ 0 & 10 & 0 \\ 0 & 0 & 10 \end{bmatrix}$	$\begin{bmatrix} 1200 & -1200 & 0 \\ -1200 & 2400 & -1200 \\ 0 & -1200 & 1200 \end{bmatrix}$	0.776 2.174 3.142	0.05 0.03 0.02
Case II	$\begin{bmatrix} 10 & 0 & 0 \\ 0 & 40 & 0 \\ 0 & 0 & 30 \end{bmatrix}$	$\begin{bmatrix} 1200 & -1200 & 0 \\ -1200 & 2400 & -1200 \\ 0 & -1200 & 4800 \end{bmatrix}$	0.652 1.905 2.135	0.05 0.03 0.02
Case III	$\begin{bmatrix} 10 & 0 & 0 \\ 0 & 10 & 0 \\ 0 & 0 & 10 \end{bmatrix}$	$\begin{bmatrix} 4800 & -1200 & 0 \\ -1200 & 2400 & -1200 \\ 0 & -1200 & 3600 \end{bmatrix}$	1.846 3.190 3.712	0.05 0.03 0.02

Table 3.5: Identified frequencies from two systems

Case	Theoretical value		Identified Values for different noise level							
			0%		5%		10%			
	f	η (%)	f	η (%)	f	η (%)	f	η (%)		
II	0.6515	5.0	0.6496	[0.29]	4.84	[3.20]	0.6592	[1.18]	4.94	[1.16]	0.6333	[2.79]	5.14	[2.79]
	1.9048	3.0	1.8491	[2.92]	2.92	[2.67]	1.8507	[2.84]	3.01	[0.26]	1.8529	[2.72]	3.14	[4.74]
	2.1353	2.0	2.1218	[0.63]	1.86	[7.00]	2.1161	[0.90]	2.11	[5.38]	2.1179	[0.81]	1.98	[0.90]
III	1.8456	5.0	1.8308	[0.80]	4.62	[7.60]	1.8830	[2.03]	5.08	[1.53]	1.8420	[0.20]	4.56	[8.76]
	3.1898	3.0	3.2065	[0.52]	2.82	[6.00]	3.1495	[1.26]	3.08	[2.69]	3.1385	[1.61]	2.79	[6.99]
	3.7116	2.0	3.6391	[1.95]	2.03	[1.50]	3.5359	[4.73]	1.79	[10.27]	3.6560	[1.50]	1.88	[6.04]

(n.b.: % error in parentheses)

Table 3.6: Identified parameters of 3dof system

Case 1				Case 2				Case 3			
Theoretical		Identified		Theoretical		Identified		Theoretical		Identified	
f_n	η	f_n	η	f_n	η	f_n	η	f_n	η	f_n	η
0.776	0.05	0.801	0.053	0.652	0.05	0.675	0.049	1.846	0.05	1.937	0.049
2.174	0.03	2.164	0.030	1.905	0.03	**2.029**	0.029	3.190	0.03	3.173	0.030
3.142	0.02	3.251	0.020	2.135	0.02	2.133	0.021	3.712	0.02	3.663	0.020

[NB: Bold case has 7% error, all other cases have error between 0-5%]

Chapter 4

Field Implementation

In this chapter, different adaptive versions of time-frequency analysis, developed in earlier chapters are adopted for field implementation. For this purpose, one full scale building and a bridge in the Indian Institute of Technology Guwahati (IITG) are considered for testing. While the building is excited by naturally occurring earthquake ground motions, the bridge is excited by a moving loaded truck. Acceleration response are recorded at different locations and the performance of different proposals are studied to check their suitability for field implementation. Finally, one laboratory test setup is used that have modal frequencies randomly changing from one experiment to another [159]. These test results are used to study the automated OMA developed by combining synchrosqueezed wavelet transformation with machine learning. These results are discussed sequentially in the following subsections.

4.1 Field Implementation of HT based methods

As the previous chapter shows the application of HT based identification technique on synthetic responses, the application on real structure's responses are presented in this section. Here, the responses are considered from different types of structures i.e. building, bridge to prove the efficiency of the methods.

4.1.1 Adaptive HHT on BRNS Building Response

With successful implementation of the adaptive HHT on synthetic data, attempt has been made to identify the system parameters from the response due to actual earthquake ground motions. The BRNS building shown in Fig. 3.2 has two force balance accelerometers at 1^{st} and 4^{th} floor to record the acceleration responses in two orthogonal horizontal direction (i.e. X and Y). Also

there is a ground motion recorder at the base. Using this set-up, the response of the building was recorded on 3^{rd} Sept'09 due to the tectonic movements of the Indo-Tibetan plate. Fig. 4.1 shows the recorded ground motions in X and Y directions and Fig. 4.2 shows the acceleration responses of the structure. To identify the modes, a similar band pass filtering scheme as in case of synthetic experiment is adopted here. Once the recorded signals are filtered, HHT is adopted to extract the IMFs which is further analysed to identify the instantaneous frequencies and the phase. Each band is then further subdivided and the instantaneous frequencies are identified until the error between the two successive iteration falls below the tolerance. Fig. 4.3 shows the IMFs corresponding to all eight modes obtained from $\ddot{Y}_4$ measurement. In this context, similar IMF are obtained from response in other directions. However, only the result obtained from $\ddot{Y}_4$ are plotted here to avoid repetition. Fig. 4.4 shows the instantaneous phase angle obtained from $\ddot{Y}_4$. The firm line indicates the instantaneous phase obtained from raw data while the dotted line shows the straight line regressed through these phase angle as describe in Eq. 3.14. In this context, one may notice that the two lines match closely and passes through origin indicating zero phase initially. Fig. 4.5 shows the plot of the instantaneous amplitude in logarithmic scale in all eight mode as mentioned in Eq. 3.15. Here also the firm line indicates the instantaneous amplitude obtained from the raw data while the chain line represents the linear fit using regression. The fluctuation in firm line indicates the transients due to arbitrary pulse train arriving at each time instant. However, as the ground motion has zero mean, the fitted straight line provides the mean slope as described in Eq. 3.15. Using these mean slopes obtained from linear fit, one can evaluate the term $\eta_j\omega_{n_j}$. Together using linear fit in Fig. 4.4 and 4.5, one can estimate the natural frequency and damping in all eight modes from each measurements. Table 4.1 shows the identified natural frequencies and modal damping ratio obtained from all measurements in X and Y direction at 1^{st} and 4^{th} floor. It may be noticed that the natural frequency obtained from each measurement in all eight modes closely matches with their designed values. In this context, Fig. 4.6 shows the spectrogram obtained by applying HHT on the measured acceleration response $\ddot{Y}_4$ without pre-filtering and with pre-filtering. The effect of pre-filtering is clearly visible as the HHT on the raw data fails to localize energies at the modal frequencies. However, pre-filtering as discussed in the proposed adaptive HHT clearly identifies the eight frequencies as shown in Fig. 4.6(b). Once the natural frequencies are estimated, modal damping ratio (see Table 4.1) can also be estimated as discussed in the previous section. The estimated modal damping ratio may not be reliable as discussed in the synthetic experiment. However, damping values tabulated in all eight modes could not be compared.

After identifying the modal frequencies and damping ratio, the remaining task is to estimate the mode shapes. In this case, Eq. 3.19 fails to provide complete mode shape due to limited measurements only at 1^{st} and 4^{th} floor. For this purpose, the objective function in Eq. A.1 is optimized so that the error between the modeled frequencies and identified frequencies is minimized. Finally, the mode shapes are obtained by updating the FE model of the building as Fig. 4.7 shows the

mode shapes in first four modes. Here, a close match between designed and identified values are observed in these cases.

The numerical results presented above indicate that the proposed output only adaptive HHT based signal processing helps to identify the model parameters from the non-stationary earthquake responses of the structure. The adaptive HHT based method is capable to extract all eight modes from each measurement. It is extremely helpful in case of limited measurements as the mode shapes can be estimated using FE model updating scheme where these identified frequencies form the reference.

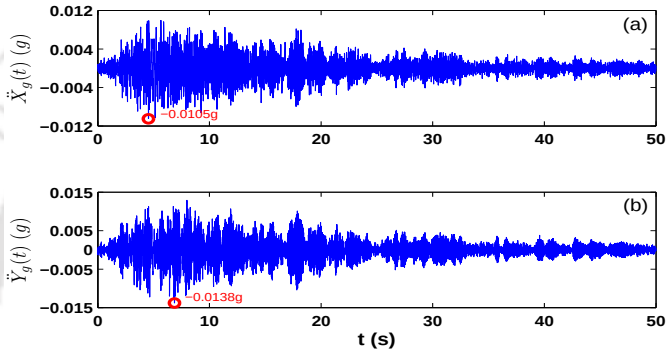

Figure 4.1: Recorded ground motions at the base of BRNS Building on 3^{rd} September'09 (a) E-W component (b) N-S component

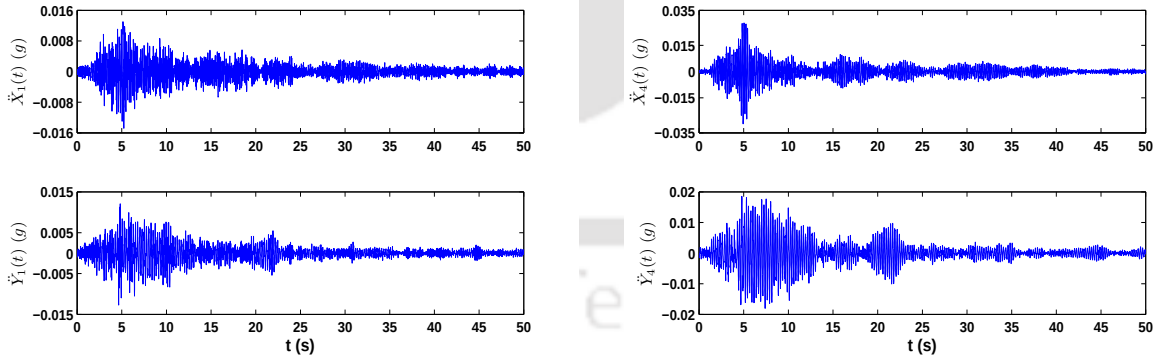

(a) (b)

Figure 4.2: Recorded responses of BRNS building on 3^{rd} September'09 (a) 1^{st} floor and (b) 4^{th} floor

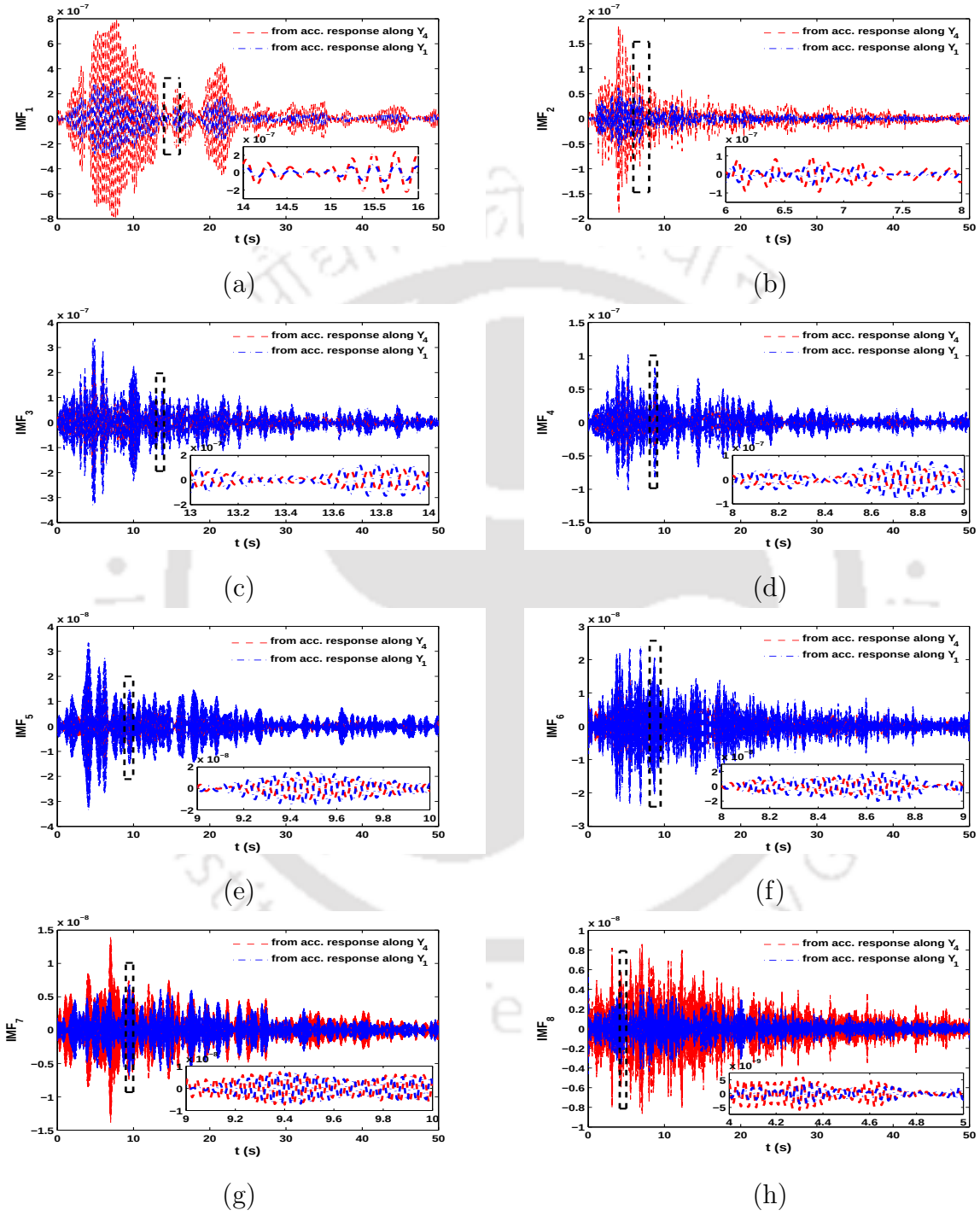

Figure 4.3: IMFs obtained from the responses in Y direction (1^{st} and 4^{th} floor) (a) 1^{st} mode, (b) 2^{nd} mode, (c) 3^{rd} mode, (d) 4^{th} mode, (e) 5^{th} mode, (f) 6^{th} mode, (g) 7^{th} mode and (h) 8^{th} mode

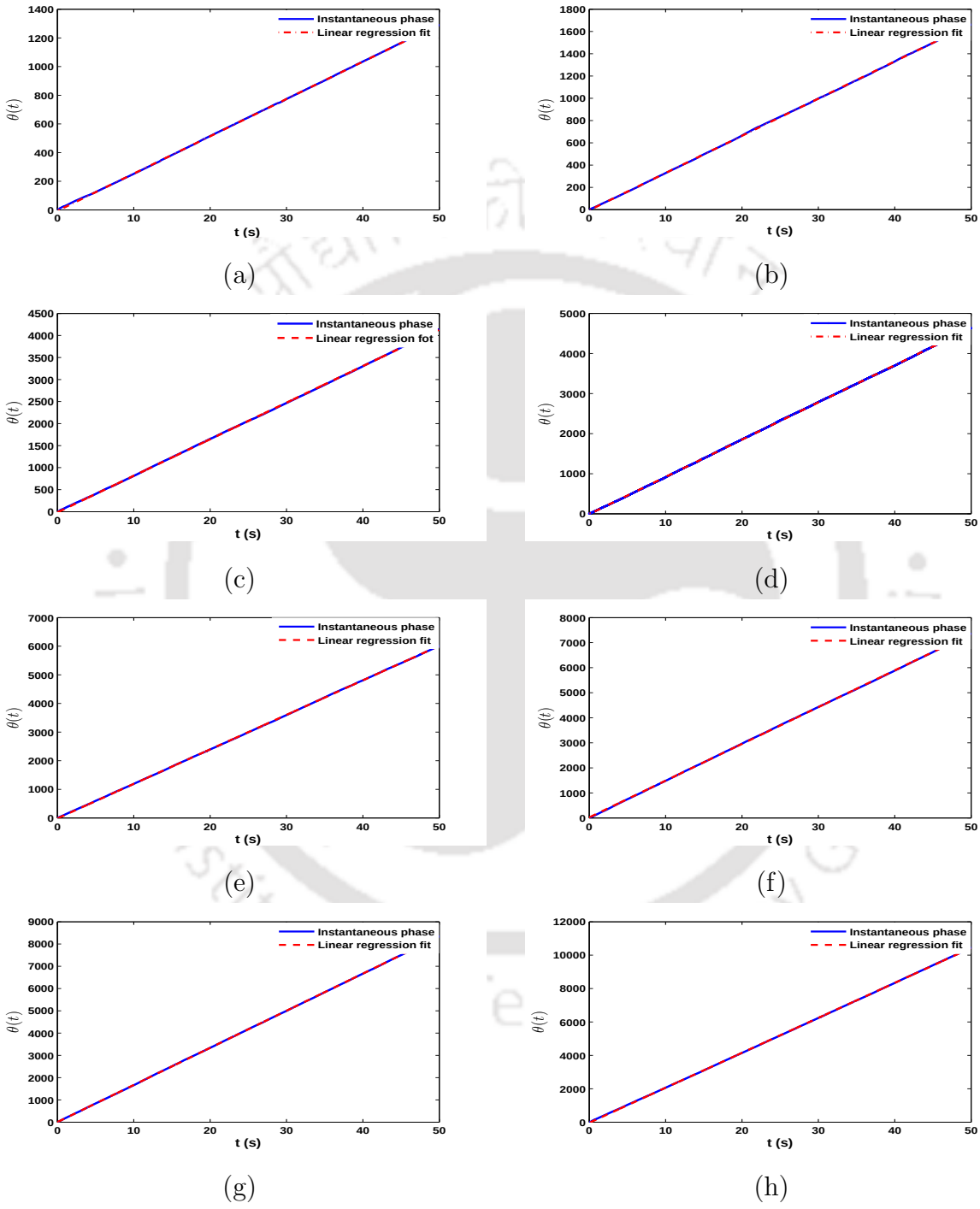

Figure 4.4: Instantaneous phase angle obtained from the response $\ddot{Y}_4$ (a) 1^{st} mode, (b) 2^{nd} mode, (c) 3^{rd} mode, (d) 4^{th} mode, (e) 5^{th} mode, (f) 6^{th} mode, (g) 7^{th} mode and (h) 8^{th} mode

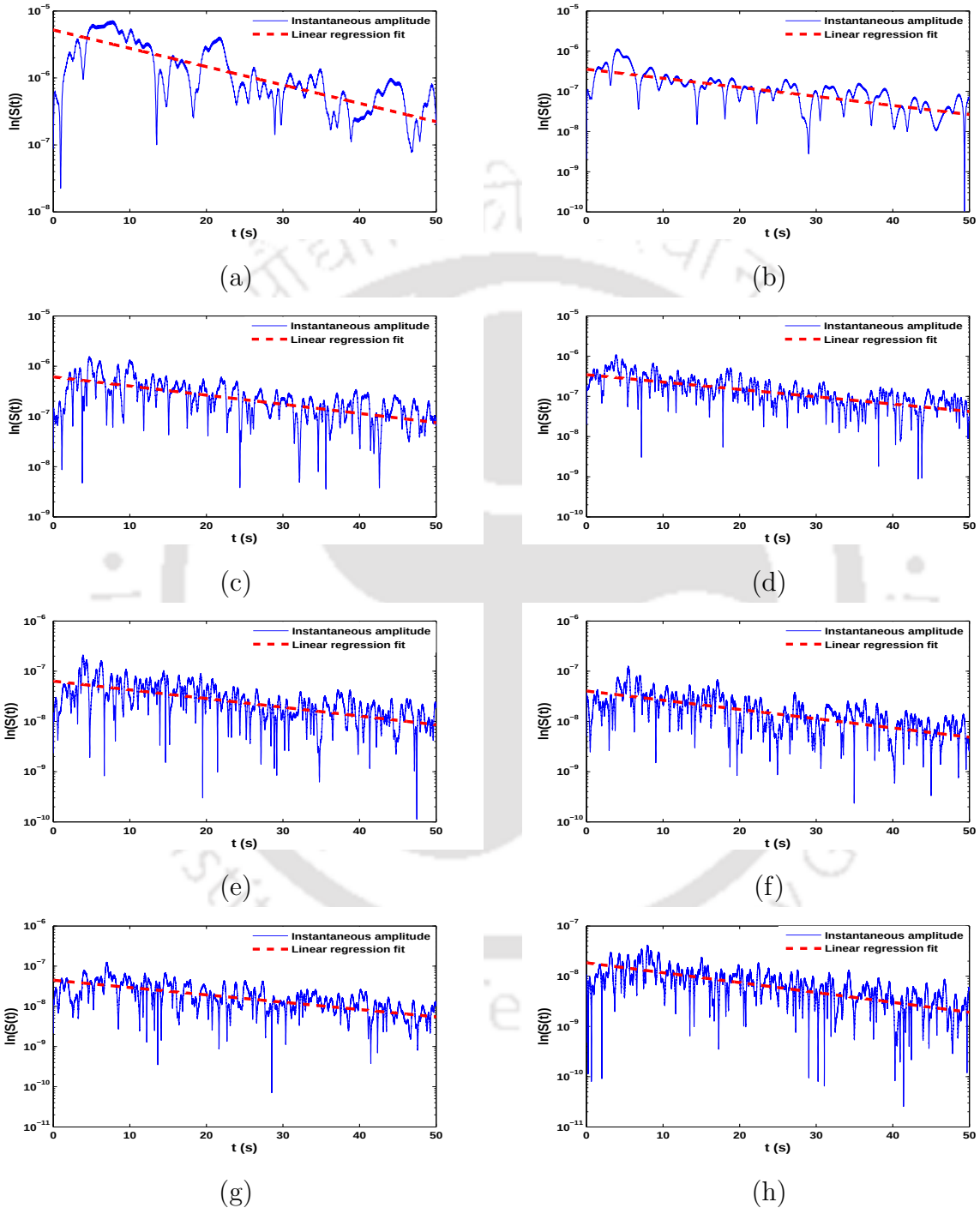

Figure 4.5: Instantaneous amplitude obtained from the response $\ddot{Y}_4$ (a) 1^{st} mode, (b) 2^{nd} mode, (c) 3^{rd} mode, (d) 4^{th} mode, (e) 5^{th} mode, (f) 6^{th} mode, (g) 7^{th} mode and (h) 8^{th} mode

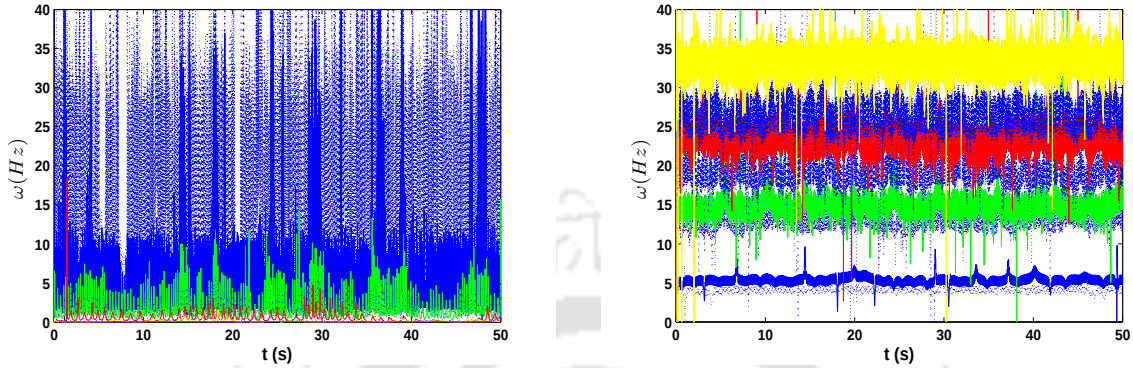

(a) (b)

Figure 4.6: Hilbert spectrum of $\ddot{Y}_4$ (a) conventional HHT and (b) adaptive HHT

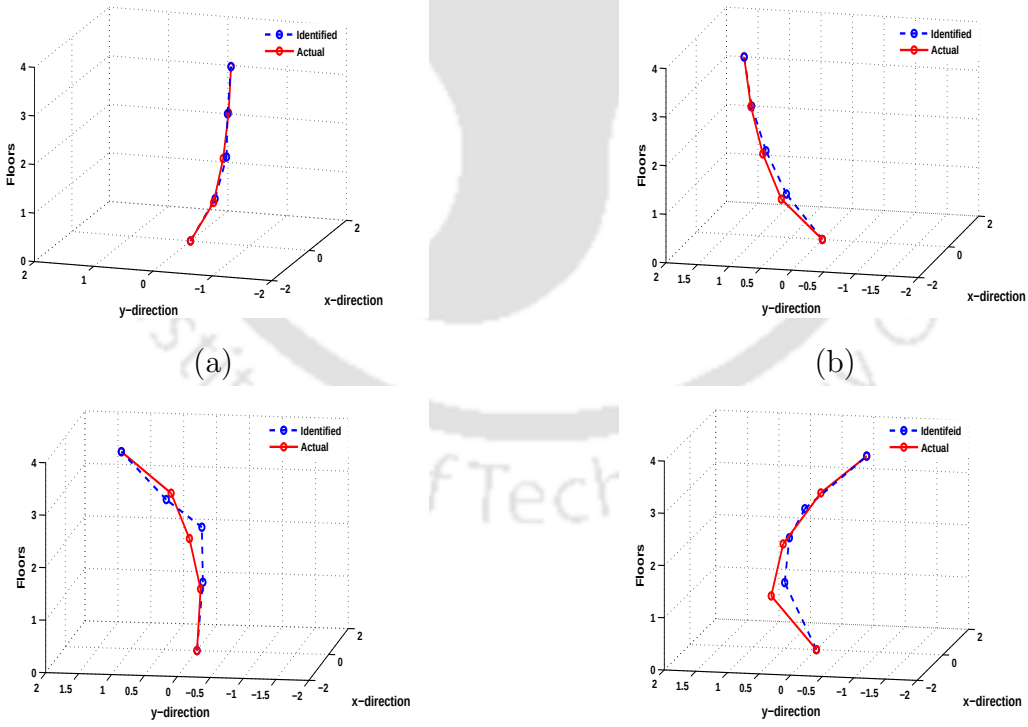

(a) (b)

(c) (d)

Figure 4.7: Mode shapes of BRNS Building (a) 1^{st} mode, (b) 2^{nd} mode, (c) 3^{rd} mode and (d) 4^{th} mode

Table 4.1: Estimated parameters from actual measurements during earthquake on 3^{rd} September'09

Mode	Estimated values							
	ω_n (Hz)				η (%)			
	X_1	Y_1	X_4	Y_4	X_1	Y_1	X_4	Y_4
1	4.62	4.12	4.72	4.14	1.28	1.54	1.23	1.52
2	5.07	5.27	5.07	5.32	1.11	0.80	1.09	0.98
3	13.19	13.27	12.94	13.21	0.27	0.31	0.29	0.32
4	16.27	14.89	16.32	14.79	0.27	0.28	0.27	0.28
5	18.84	19.08	18.87	19.19	0.24	0.21	0.24	0.21
6	23.24	23.39	23.51	23.36	0.19	0.17	0.19	0.18
7	26.26	25.94	26.39	26.53	0.16	0.15	0.16	0.16
8	33.25	33.66	33.33	33.32	0.11	0.12	0.12	0.14

4.1.2 Adaptive MEMD for OMA of Bridge

Here, a reinforced concrete road bridge near IIT Guwahati is considered for field implementation of the proposed adaptive MEMD algorithm for operational modal analysis. Fig. 4.8 shows the reinforced concrete road bridge connecting IIT Guwahati and National Highway–31. It has three spans which are simply supported at both ends and are separated from each other by the expansion joints. The length of the central span is 39m which is instrumented for the experimental verification of the proposed identification strategy. Fig. 4.8 shows the cross section of the bridge along with other details (e.g. girder dimension and spacing etc.). Fig. 4.8(c) shows the cross section of the bridge deck which facilitates two-way traffic and each side of the bridge deck is structurally independent. Each longitudinal girder are placed at a spacing of 2.4m. To provide adequate lateral stiffness, eight 0.25m wide diaphragms are placed in the central span with equal spacing. In this experiment, five uniaxial force-balanced EpiSensor ES-U2 accelerometers are used with sensitivity upto the order of 0.0008 g/mV. Fig. 4.8(d) shows the placement of these sensors on the deck of the central span. The sensors are placed corresponding to the location of peak displacement in 1^{st}, 2^{nd} and 3^{rd} modes. It is envisaged that the first three modes will contribute most in the response. To excite the bridge, a loaded truck of weight 19.46t is allowed to move with constant velocity. Although, both forced and free vibration responses are recorded, only free vibration records are utilized here for parameter estimation.

Fig. 4.9 shows the free vibration response of the bridge and their respective Fourier amplitude spectrum which clearly shows only one peak corresponding to the first natural frequency of the bridge. The recorded acceleration time histories from different channels are analyzed by EMD and the IMFs corresponding to each channels are considered here for modal identification. Fig. 4.10 shows two IMFs obtained from EMD analysis of the measured data. From this figure, one can

clearly identify the first mode of the bridge (i.e 3.113Hz) while the second IMF fails to suggest the presence of any mode owing to poor SNR. In this context, it may be mentioned that the two IMFs shown in Fig. 4.10 has significant energy as compared to other spurious modes.

MEMD is then applied on the five recorded data set and the two dominant IMFs are shown in Fig. 4.11. From this figure, one can distinctly identify the first mode of the structure while the second IMF shows mode-mixing with some distinct peaks and their respective frequency values. Once mode-mixing zone is identified as shown in Fig. 4.11, signals from different channels are filtered around the peaks in an iterative manner similarly as explained in the proposed algorithm for adaptive MEMD based identification. MEMD is then performed using the filtered signals from all five channels and the modified IMFs are shown in Fig. 4.12. All four IMFs in Fig. 4.12 distinctly show the modal frequencies with high SNR. This, in turn, highlights the efficiency of the proposed adaptive identification scheme. Table 4.2 shows the identified frequencies are obtained. From this table, it can be noticed that identified frequencies are well within 5% of the values obtained from the modal analysis of the bridge in ANSYS. Once the dominant modal frequencies are identified, mode shapes corresponding to these natural frequencies are obtained from the updated finite element model as shown in Fig. 4.13. Finally, the modal damping ratios are evaluated from the filtered IMFs. Table 4.2 shows the modal damping ratios which could not be verified as the original damping ratios are not known. However, damping values obtained from different channels are found to be consistent with each other. Together, the results in Fig. 4.11 and Table 4.2 clearly indicates the superiority and efficiency of the proposed identification strategy as compared to conventional EMD for operational modal analysis.

4.1.3 Combined Wavelet-Hilbert Transform: RC Bridge

In this case, same RC road bridge that serves as a major link between IIT Guwahati and NH-31 is used for experimental validation of the proposed identification scheme. The data is recorded with a sampling rate of 1200Hz and the ambient responses are shown in Fig. 4.14(a), 4.14(b) & 4.14(c) for sensor 1, 2 and 3. Responses in locations 4 and 5 are same as in sensor 1 and 2 due to symmetry and hence omitted. The spectrogram of these response using short time Fourier transform are shown in Fig. 4.14(c), 4.14(d) and 4.14(e). It is clear from these plots that energies are localized between 0 to 20Hz indicating existence of modal frequencies. First the OMA is performed using NExT-ERA [36] technique on the recorded responses and the stabilization diagram is shown in Fig. 4.15. From this figure, convergence in frequency and MAC values are noticed upto 35Hz. Therefore, a frequency range of 0 to 35Hz is considered for modal identification using the proposed Wavelet-Hilbert scheme. For this purpose, initially 63 bands are considered with F and σ values are 19Hz and 1.043 respectively, covering a frequency range of 2.6266 to 37.2650Hz. Using these parameters, the responses are filtered as explained in Eq. 3.29 and energy concentration are identified as described

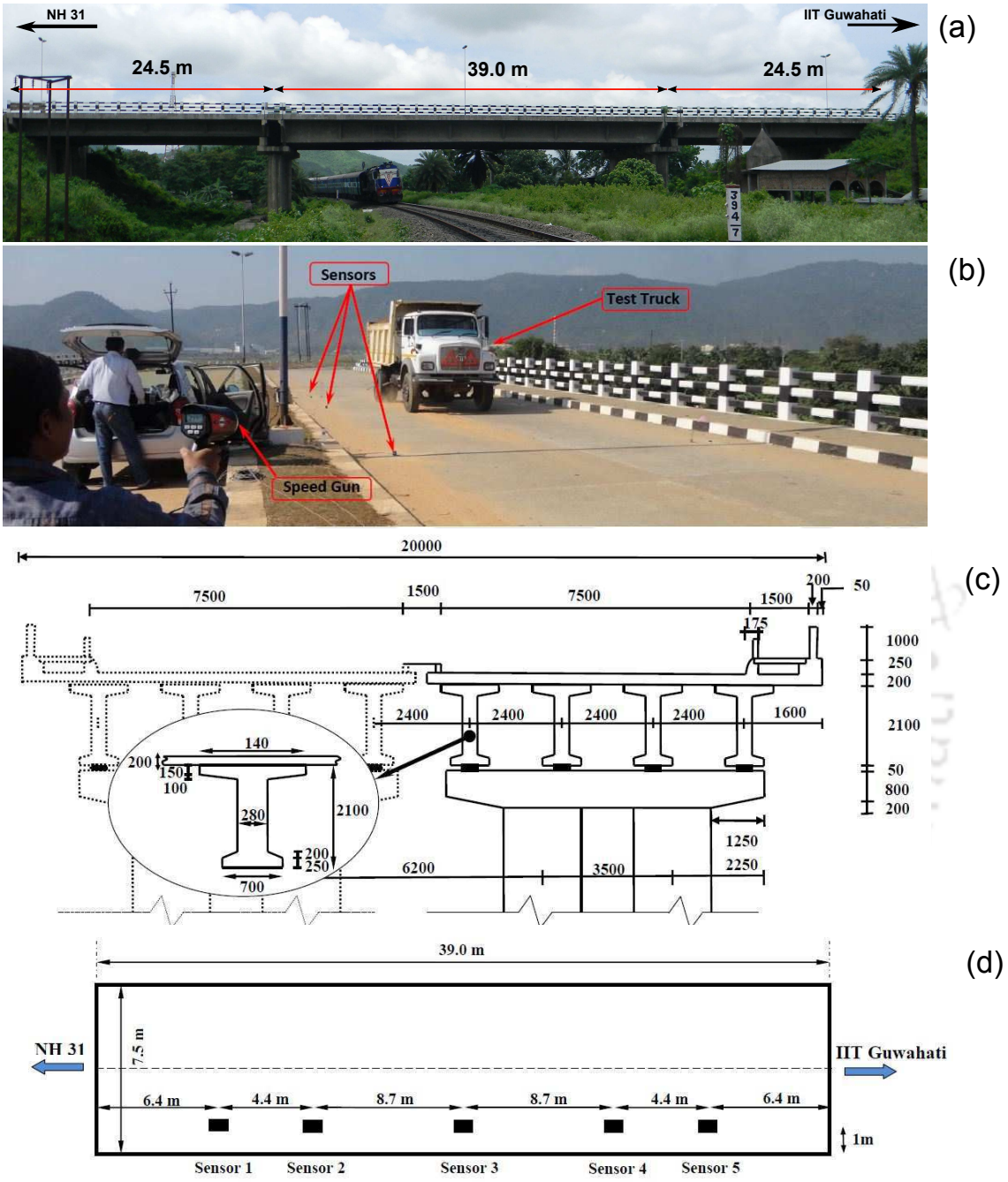

Figure 4.8: Operational modal analysis of RC bridge – (a) longitudinal view, (b) experiment setup, (c) cross section & (d) sensor location (Concrete is M35 grade and reinforcement is Fe415 grade)

in the previous example. Fig. 4.16 shows the filtered response and the IMF obtained using adaptive HHT. For brevity, only one response in 1^{st} mode corresponding to sensor 3 is shown here. A close match is again observed in this case as it was in the previous example. This clearly shows that the band pass filters using MLP basis can directly provide the IMF corresponding to each mode. Also,

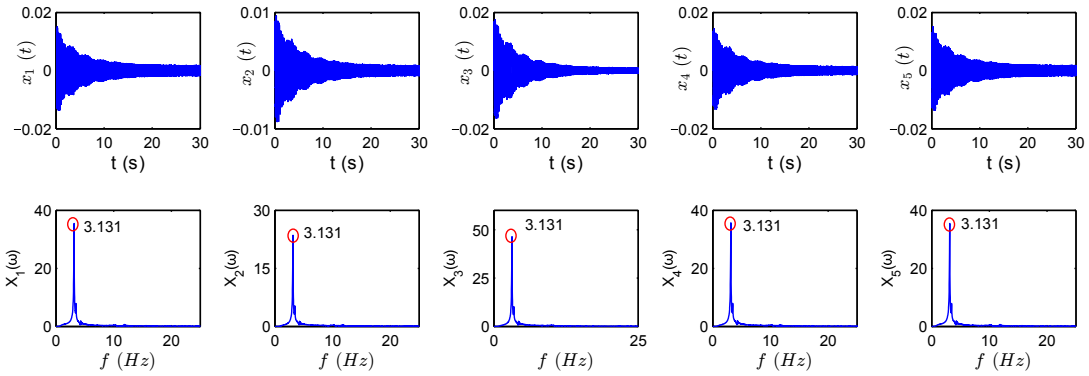

Figure 4.9: Recorded accelerations and their spectra

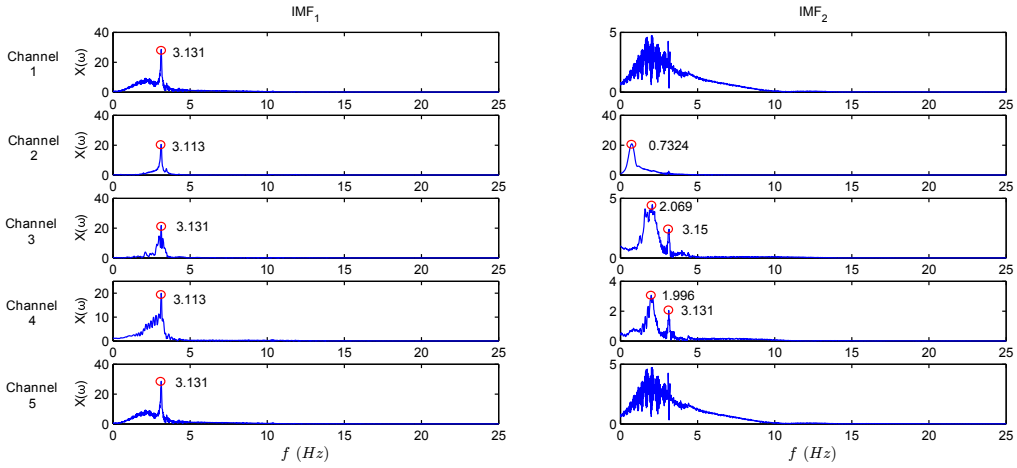

Figure 4.10: Extracted IMFs using EMD

the ill effect of mode-mixing and the generation of spurious modes as in traditional HHT or its adaptive variants are avoided in the present CWT based filtering. Once the energy localization are identified, HT is applied for modal identification. In this context, iterative wavelet based filtering is stopped when each frequency band contains single energy peak corresponding to either modal frequency or frequency of input excitation. Once the iteration for filtering is converged, the filtered signals are segregated into two groups – a) modal response and b) response containing the input frequency. This is achieved by comparing the instantaneous phases obtained from different sensors in a particular band. Fig. 4.17 shows the instantaneous phase difference corresponding to the frequency bands 3.1084 to 3.2420Hz (i.e. band containing 1^{st} mode) and 4.6 to 5.0Hz (i.e. band in between 1^{st} and 2^{nd} mode). It may be observed that responses are in phase when the filtered responses correspond to modal frequency (i.e. Fig. 4.17(a)) while they are out of phase if the filtered signal represents response other than modal frequency. Fig. 4.18 shows the instantaneous phases corresponding to frequency band of 27.7531 to 28.9465Hz (i.e. band containing 6^{th} mode)

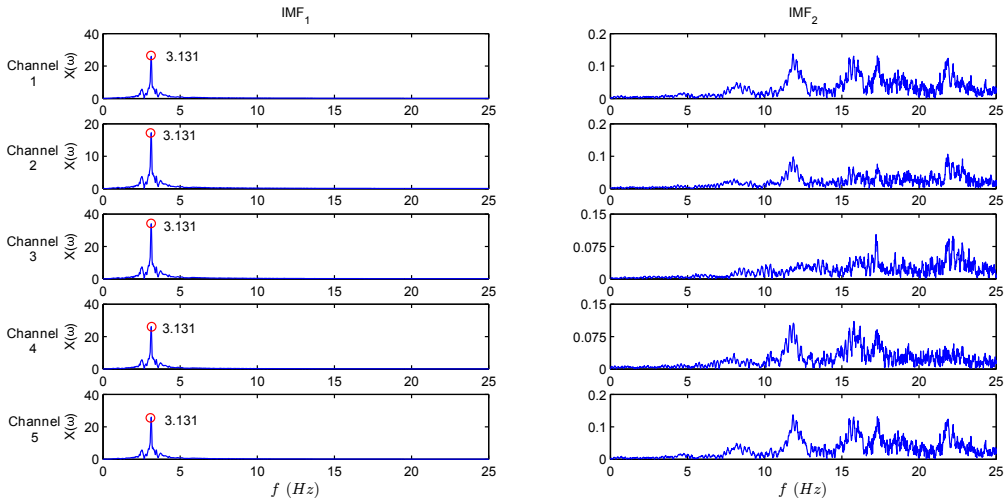

Figure 4.11: Extracted IMFs using MEMD (mode-mixing in 2^{nd} IMF)

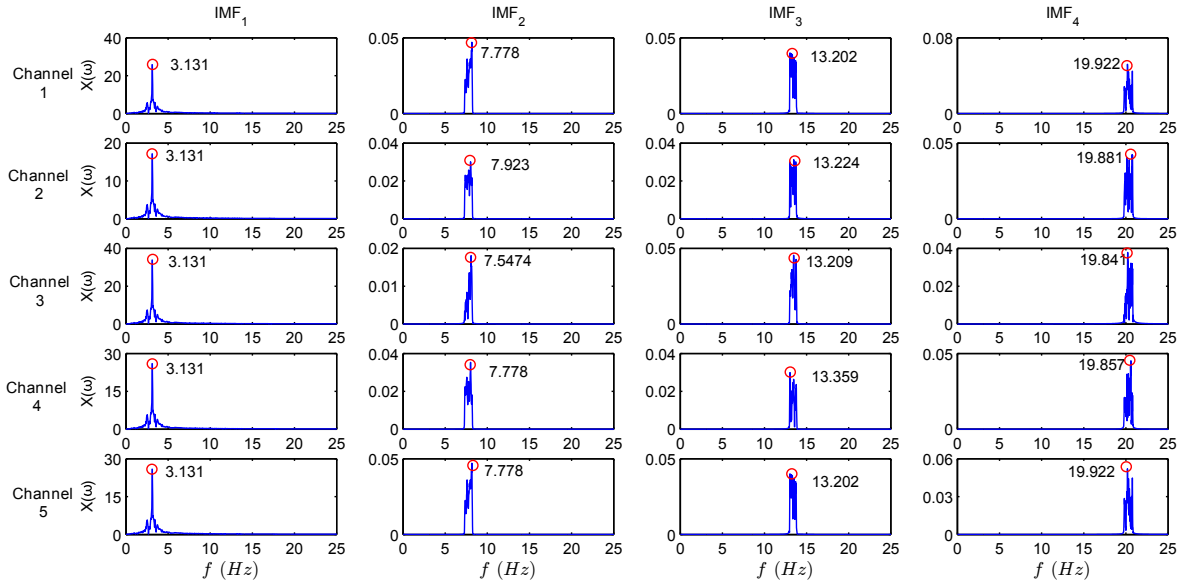

Figure 4.12: IMFs obtained using the proposed algorithm

and 27.2 to 27.6Hz (i.e. band in between 5^{th} and 6^{th} mode). Although, the energy content is low in 6^{th} mode, however, the proposed identification scheme is able to find in-phase characteristic of the modal responses in higher modes (i.e. Fig. 4.18(a)). Fig. 4.18(b) shows that instantaneous phases are having phase lag identifying response other than modal frequency. Table 4.3 shows the modal frequencies identified by the proposed methodology.

To verify the accuracy of the proposed methodology, a finite element model of the bridge is prepared in ANSYS® v13.0. The bridge is modeled as thick shell element (i.e. SHELL181) while the girders are modeled as 3D beam element (i.e. BEAM188) with proper eccentricity. The concrete used in

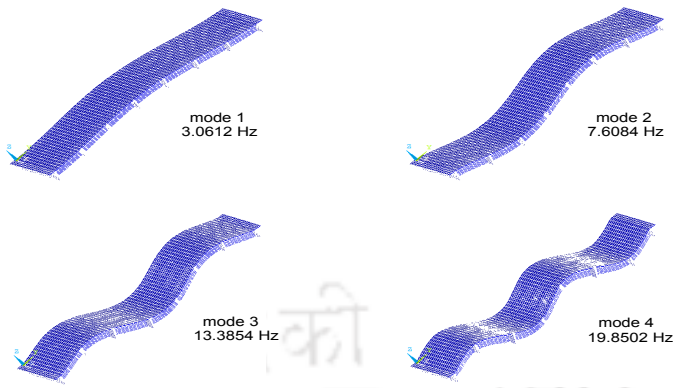

Figure 4.13: Identified mode-shapes

design has a compressive strength of 35MPa while the reinforcement has a strength of 415MPa. The density of the concrete is assumed to be 24 kN/m^3 as per IS 456:2000 for design. The gross property of reinforce concrete is calculated as per Indian Standard and it added to the material section. As per the construction detailing, middle span of the bridge is simply supported which is confirmed by physical examination. While modeling the pinned support, the translations of three direction are restrain and rotation against vertical and longitudinal direction is restrain. On the other end, the translations of transverse and vertical direction are restrain and rotation against vertical and longitudinal direction is restrain for roller support. The finite element model of the bridge has 2136 element with total number of degrees of freedom is 5313. Table 4.3 shows the first ten natural frequencies as per structural design and the identified frequencies using the proposed scheme. From this table, it may be noticed that the errors in modal frequency estimation are well within 5% which can be considered satisfactory for all practical purpose. In this context, modal damping are only estimated in first four modes as the damping ratio beyond fourth mode becomes insignificant as the energy concentration in these modes are extremely low. Moreover, the damping ratio could not be verified as the original values are unknown. However, a consistency in the estimated damping ratio is observed from response at different sensor location indicating their convergence. Finally, the mode shapes are identified by direct FE model updating as described in appendix A. In this context, only first four identified frequency are used for updating as they have significant modal energy while rest is used for verification. Fig. 4.19 shows the sensitivity of the objective function, with respect to the model parameters (i.e. Young's modulus E and density ρ of RC). It may be observed that objective function has no distinct global minima. Instead, different combination of E and ρ provides optimal value as marked by the straight line in Fig. 4.19. Under this scenario, it is assumed that ρ is less affected in field compare to E even the in presence of damage or weathering. Here, as the bridge is new, the density is assumed to be 2400kg/m^3 as recommended in IS code. With this density, optimal FE model is obtained and the mode shapes are plotted as shown in Fig. 4.20. With these mode shapes, modal assurance criteria (MAC) are evaluated as described in Eq. A.3. Fig 4.21 shows the MAC values corresponding to the identified

modes. From this figure, it may be concluded that the modal assurance values are high indicating the accuracy of the proposed identification scheme. It has the ability to identify large number of modes compared to other traditional methods like NExT-ERA (see Fig. 4.15) even when the modal energy is significantly low especially in higher modes. This feature of wavelet based filtering is also beneficial in updating large FE models. With all these in view, it may be concluded that the MLP based filtering coupled with Hilbert transformation serve as an effective tool for operational modal analysis of large infrastructures.

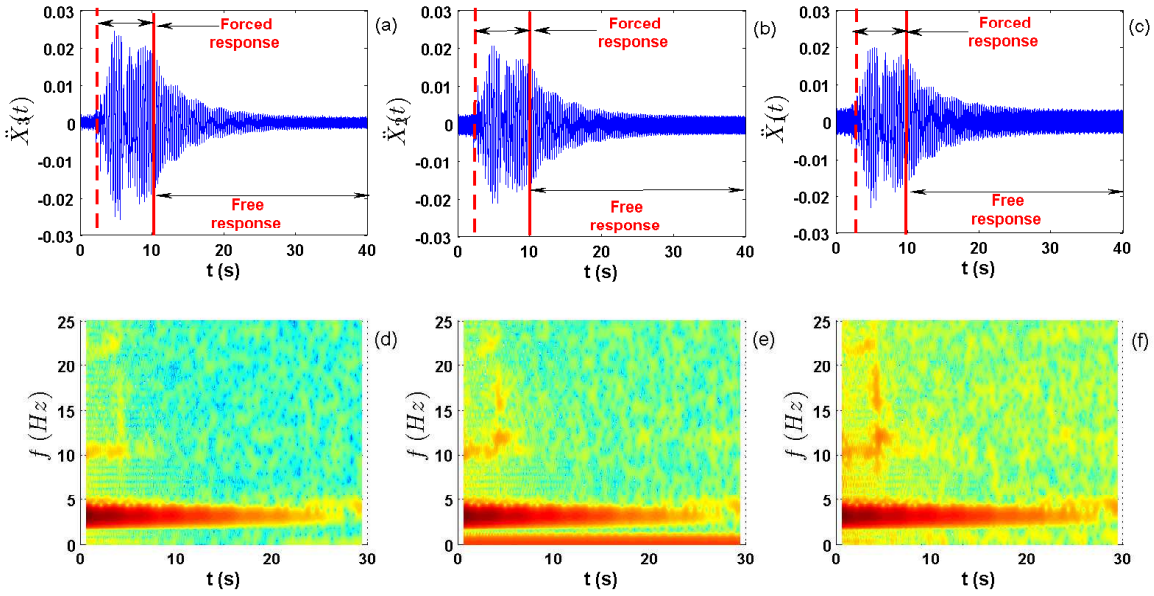

Figure 4.14: Acceleration response of bridge – time histories in 1^{st} row and spectrogram in 2^{nd} row (n.b. subscript represents sensor number)

4.2 Synchrosqueezed Transformation for OMA of RC Building

In this example, a full scale building in IIT Guwahati campus described in section 3.5.1 is used for experimental verification. Fig. 3.2 shows the photograph of this building along with its structural dimensions. It can be noticed that there are two identical buildings on either side of the central staircase. Buildings are separated from the staircase so that they can act freely. The building on the right side has base isolators while building on the left side is supported over isolated footings (i.e. fixed base) which is used in this study for modal identification. The sensor details of this building are provided in in section 3.5.1. Accelerations at the top floor are recorded during actual seismic events which are used here for identification. Fig. 4.22 and Fig. 4.23 shows the top floor

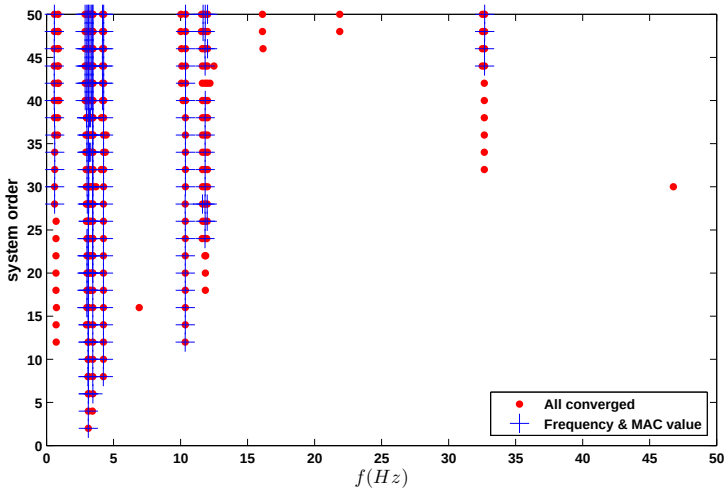

Figure 4.15: Stabilization diagram of RC bridge response

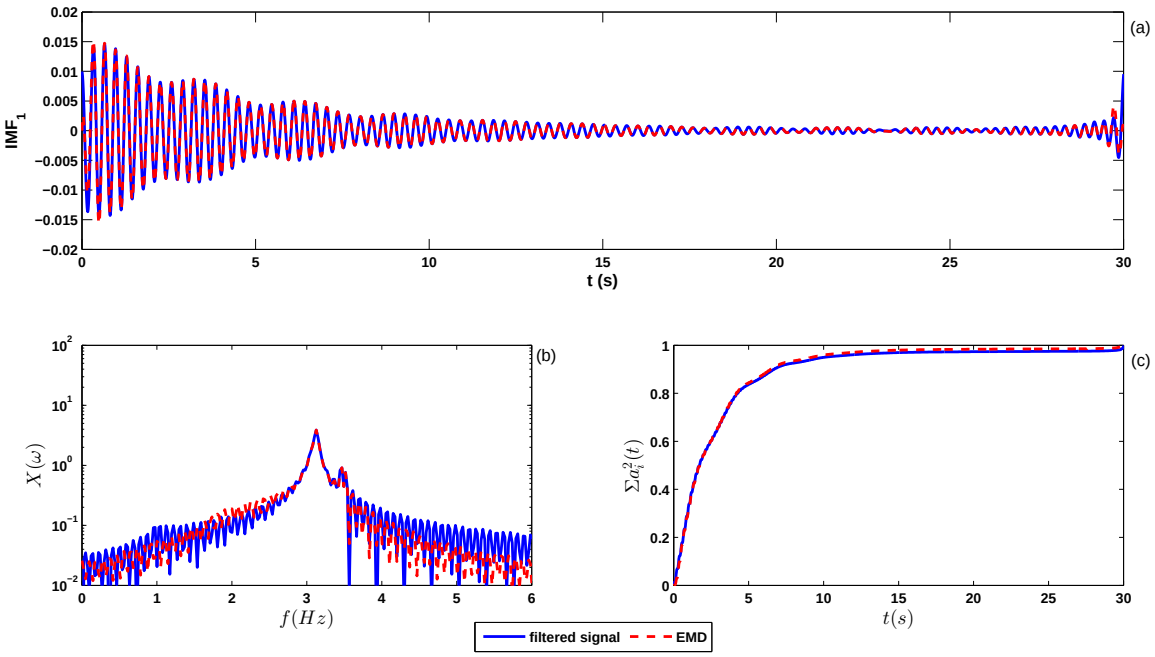

Figure 4.16: Bridge response in first frequency band – (a) Filtered response and IMF in 1^{st} mode, (b) Fourier amplitude spectrum and (c) cumulative energy

responses in X and Y directions which were recorded on 3^{rd} September 2009. The first column of this figure shows the recorded earthquake ground motions in X and Y directions along with the building responses. Wavelet transformation of these responses are carried out as described earlier, with $n_s = 2^8$ as the initial value. The middle column of Fig. 4.22 shows the scalogram of the responses using complex morlet wavelet. The central frequency of this basis function is considered

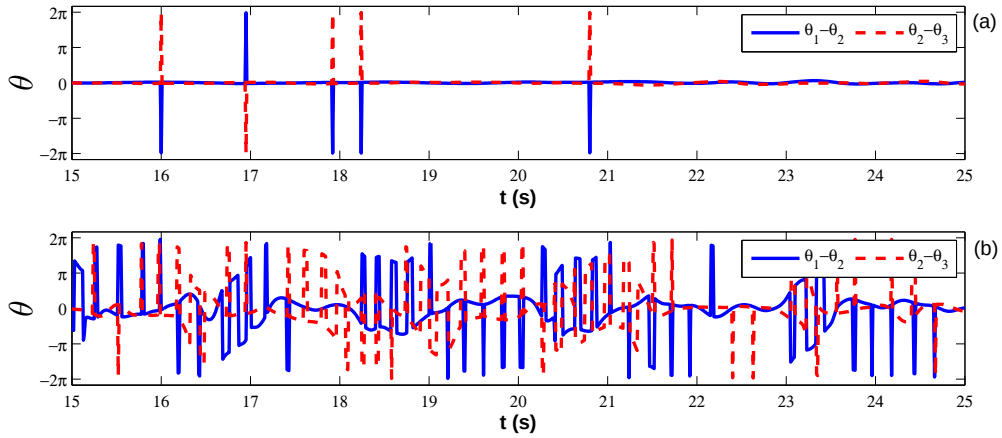

Figure 4.17: phase information of signals corresponding to mode 1 (a) with natural frequency and (b) without natural frequency

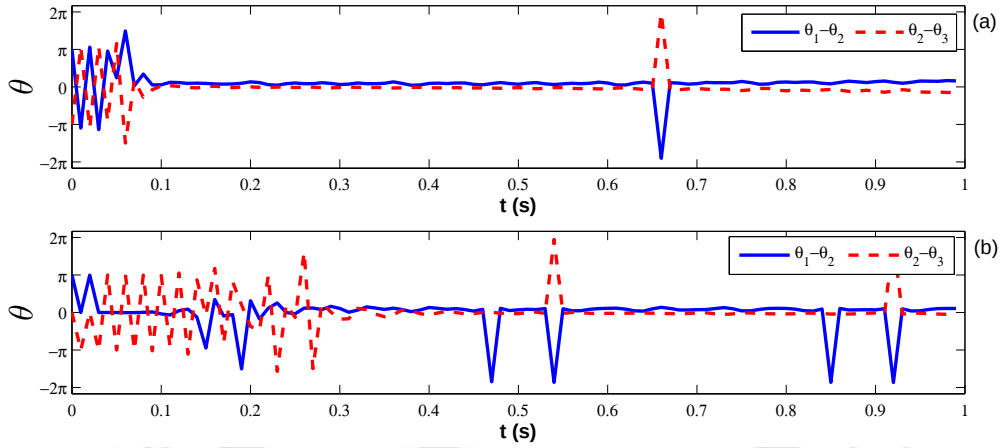

Figure 4.18: phase information of signals corresponding to mode 6 (a) with natural frequency and (b) without natural frequency

to be 3Hz in this study and after convergence the number of scales is 1904 to cover a frequency range of 0.001 to 30Hz. It can be observed from Fig. 4.22 that frequencies are localized in different zones but their resolution is not very high to identify them clearly. Thus to improve the resolution further, synchrosqueezing is adopted which are shown in the third column of Fig. 4.22. Here, the clarity of the scalogram has improved, however, it also fails to locate the modal frequencies directly as the relative magnitude of energy distribution is very low. Thus, k-means clustering is invoked to segregate the frequencies based on their energy content which is shown in Fig. 4.25. In this context, the optimal number of clusters is estimated to be 7. Finally, the modes are identified using instantaneous phase portrait whose difference in two dof for the same mode are shown in Fig. 4.26. For this purpose, 1st and 4th dof are considered and the responses in 1st and 4th cluster are used for demonstration. Here, time domain responses are obtained by inverse transformation

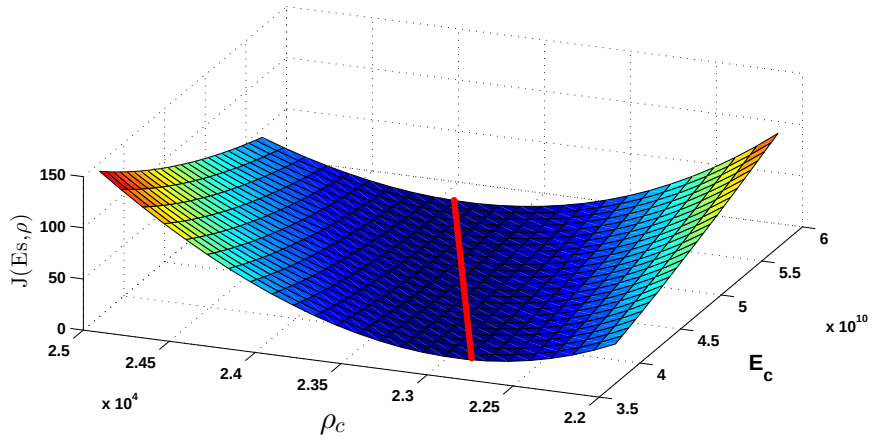

Figure 4.19: Objective function

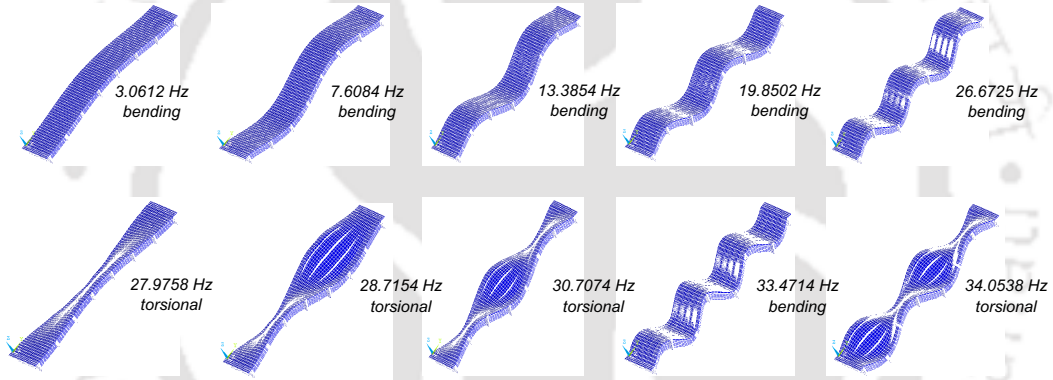

Figure 4.20: Identified mode shape of RC bridge

as described in the previous example and the instantaneous phases are evaluated using Eq. 3.58. The first row in Fig. 4.26 shows the responses in 1st and 4th clusters while the second row shows their phase difference. From this figure, it can be concluded that 1st cluster corresponds to 1st mode as the phase difference is zero in most of the time instant (except near zero crossing of the individual signals which are reflected in large spikes) while the 4th cluster is a spurious mode. Using similar technique, other cluster are also verified to identify the modal frequencies. These identified frequencies are listed in Table 4.4.

In this table, the first column refers to discrete model where infill walls are characterized by diagonal strut as shown in Fig. 4.24a. This model is created as per Indian Standard guidelines for reinforce concrete structures and the strut is model as proposed by Mondal and Jain [160] which is based on the static analysis of 2D frame with infills. Therefore, the discrete model is the best possible representation of the field structure and not the exact one. However, the discrete model is tuned in such a way that it can replicate the fundamental modes obtained from fourier analysis as closely as possible. Therefore, error estimation using these values are not carried out here as the exact

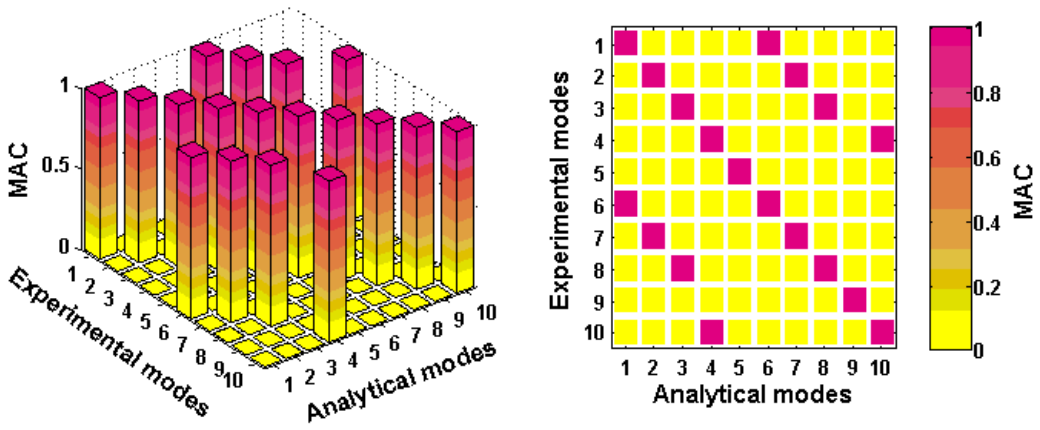

Figure 4.21: Comparison to analytical and experimental mode by MAC values

benchmark is not available in this case. In absence of the actual benchmark values, only the consistency of the estimated modes are checked by the proposed algorithm and found to be in accordance with the value obtained from the discrete model and other identification strategy [161]. To study the behavior of the full scale building, recorded responses in two different occasions are reported here. For this purpose, the seismic events on 3^{rd} Sept 2009 and 21^{st} Sept 2009 are used. The peak ground acceleration of the major components at these two dates are 0.0138g and 0.026g respectively which is far below the level used to design the structure. Hence, there is no chance of damage caused by these two successive events. Moreover, the date of occurrence is so close that the structure does not experience any change in material properties due to weathering or other activities surrounding it. Fig. 4.24b and Fig. 4.24c show the Fourier transform of the X and Y components of acceleration response at the top floor. These amplitude spectrum clearly shows the difference in fundamental frequencies which is due to the uncertainty associated with the field experiments involving non-stationary excitation. Table 4.4 shows the identified modal parameters for these two seismic events. Although, the values differs from each other, but the estimation by the proposed algorithm are found to follow the trend in both these events. However, these deviations should not be attributed to the change in structural properties (i.e. damage) or under performance of the identification strategy. As the non-stationary input has frequencies close to structural frequencies, they are bound to interact. In this context, it may be noted that non-stationary excitation are not recommended for damage detection which is better estimated from the free response or the response due to broad banded excitation (if possible). In this context, author wish to clarify that the proposed algorithm is specifically used for the identification of the actual building from the seismic excitation not to locate possible damage but to pinpoint the dominant frequencies and its variations in different seismic events for the tuning of the the passive controller which is not

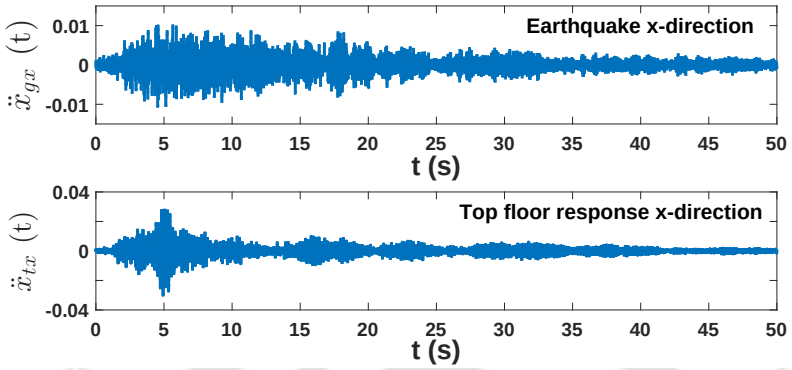

(a)

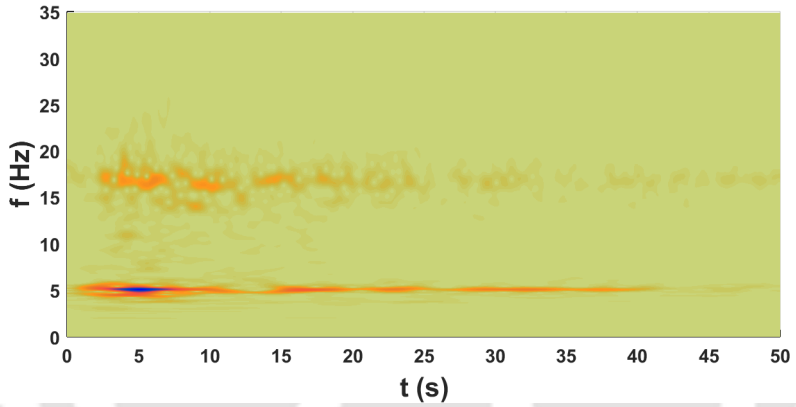

(b)

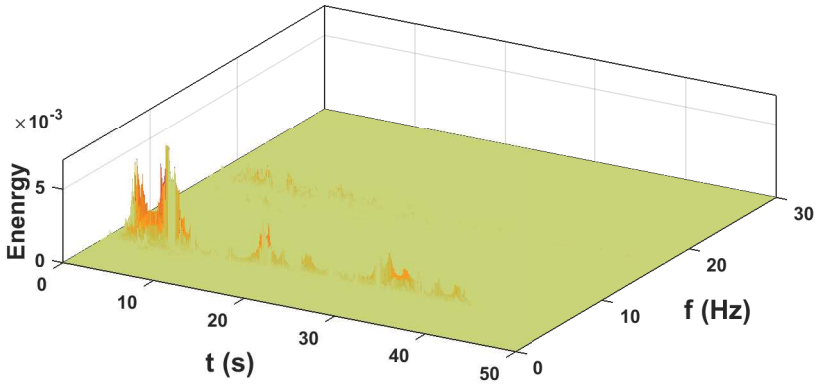

(c)

Figure 4.22: Earthquake responses and scalogram - (a) recorded motion on 03/09/09 and top floor response in x-direction; (b) Wavelet coefficients of top floor response in x-direction; (c) Synchrosqueezed transform coefficients of top floor response in x-direction

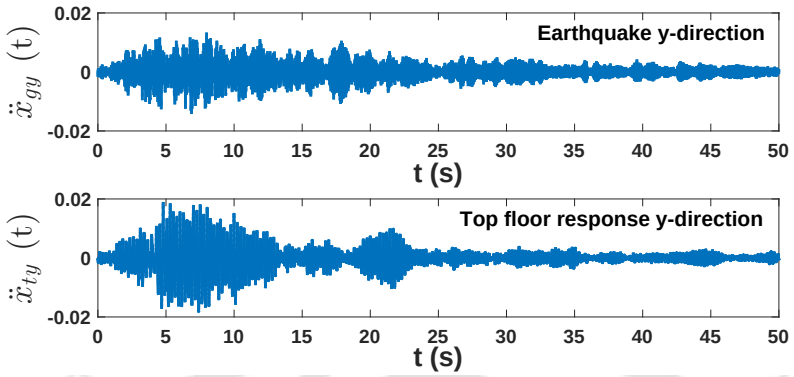

(a)

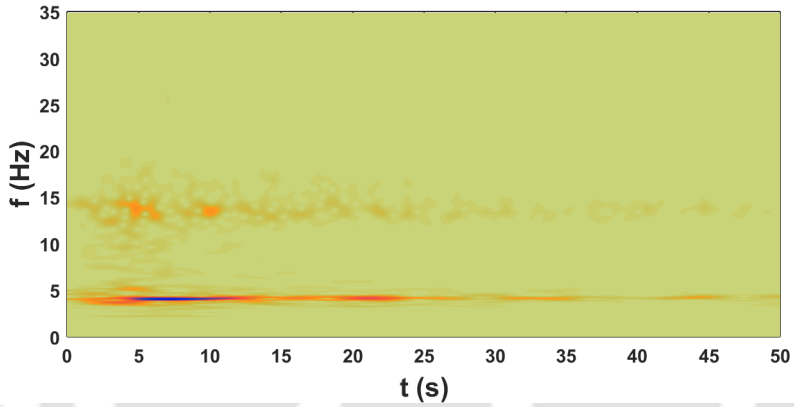

(b)

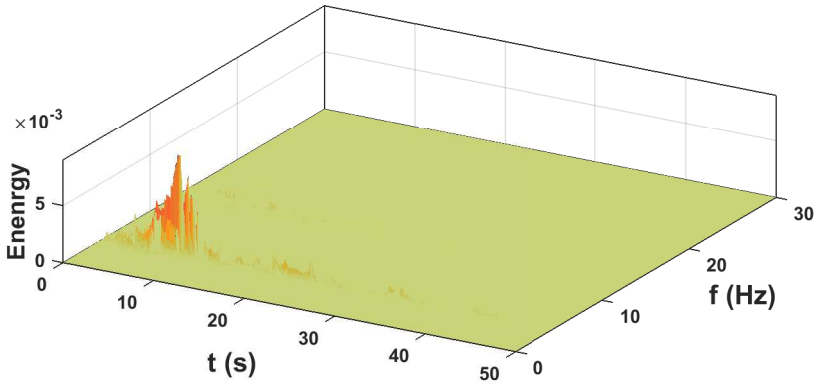

(c)

Figure 4.23: Earthquake responses and scalogram - (a) recorded motion on 03/09/09 and top floor response in y-direction; (b) Wavelet coefficients of top floor response in y-direction and (c) Synchrosqueezed transform coefficients of top floor response in y-direction

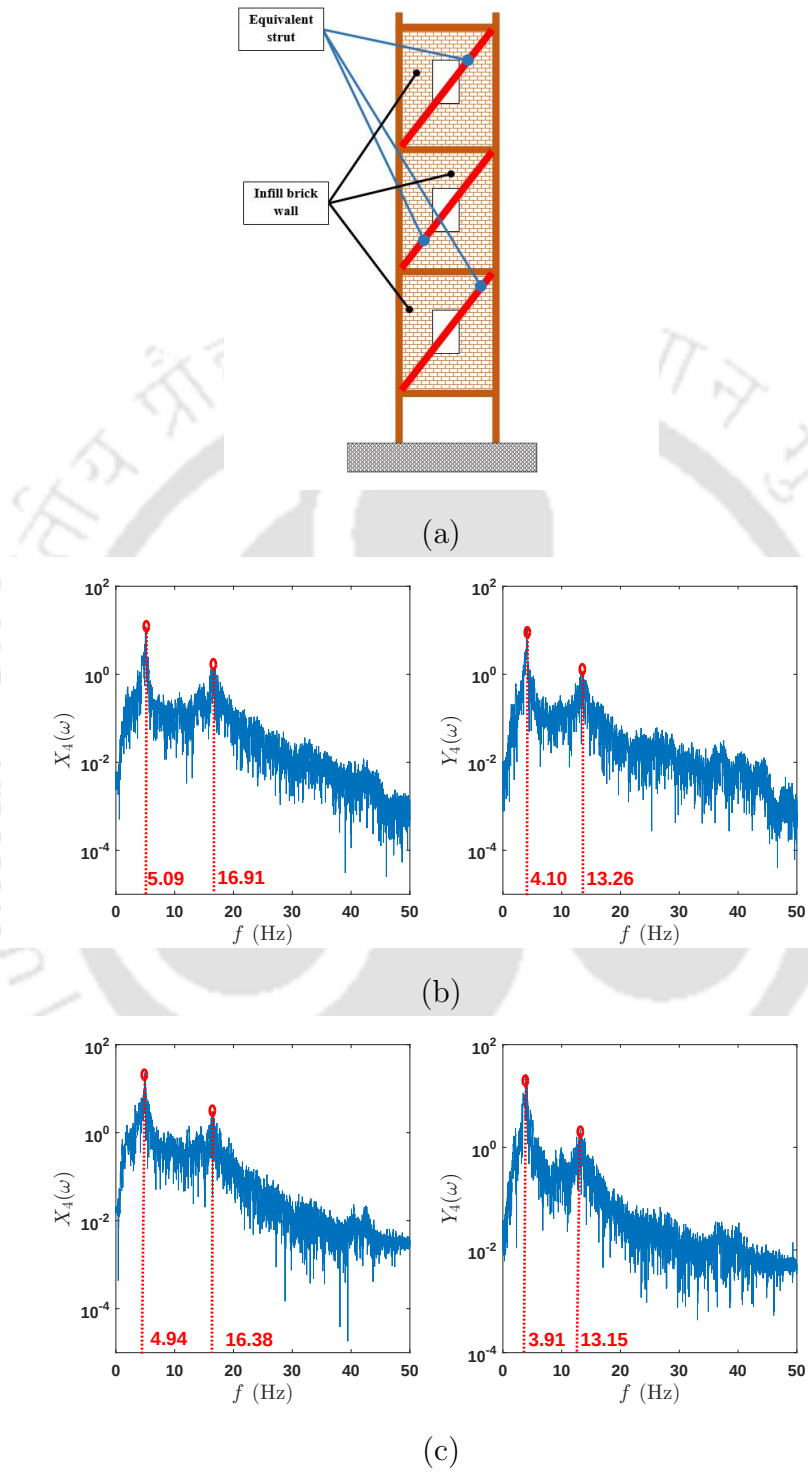

Figure 4.24: (a) Equivalent strut model of the building, (b) Fourier amplitude spectrum of response on 03/09/09 and (b) Fourier amplitude spectrum of response on 21/09/09

discussed here as it is beyond the scope of this work. Once, the frequencies are identified, modal damping is estimated using NExT as described in the previous example. Table 4.4 shows the

identified modal damping of the BRNS building.

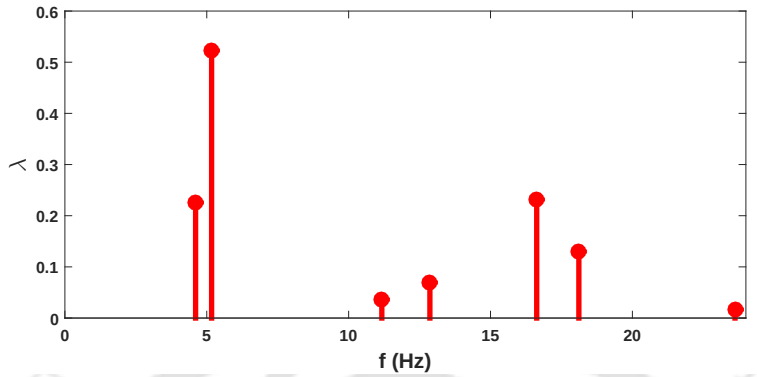

(a)

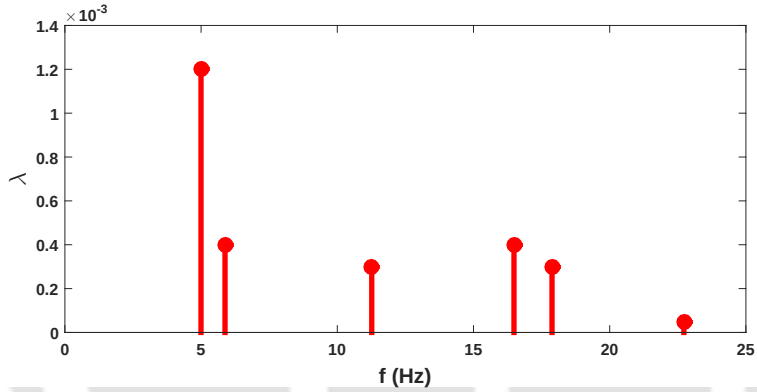

(b)

Figure 4.25: k-means clustering - (a) median of clusters for response due to recorded earthquake on 03/09/09 and (b) median of clusters for response due to recorded earthquake on 21/09/09

4.2.1 Synchrosqueezed Transformation for OMA of Random Eigen Value Problem

The final problem considered in this study is a thin beam with lumped masses at different locations. The test was carried out by Adhikari *et. al.* [162] in the Bristol Laboratory for Advanced Dynamic Engineering and the data is freely available in the internet [159]. Fig. 4.27 shows the schematic diagram of this beam. The beam is 1.2m long and 2.05mm thick whose both ends are fixed. Twelve discrete masses, each weighing 2gm are placed on this beam whose locations can be changed for different tests. Table 4.5 summarizes these locations for different tests in this study. In total, all discrete masses together contribute only 1.6% of the mass of the beam. Three accelerometers are placed at 23cm, 50cm and 102cm from the left end. As the locations of these discrete masses

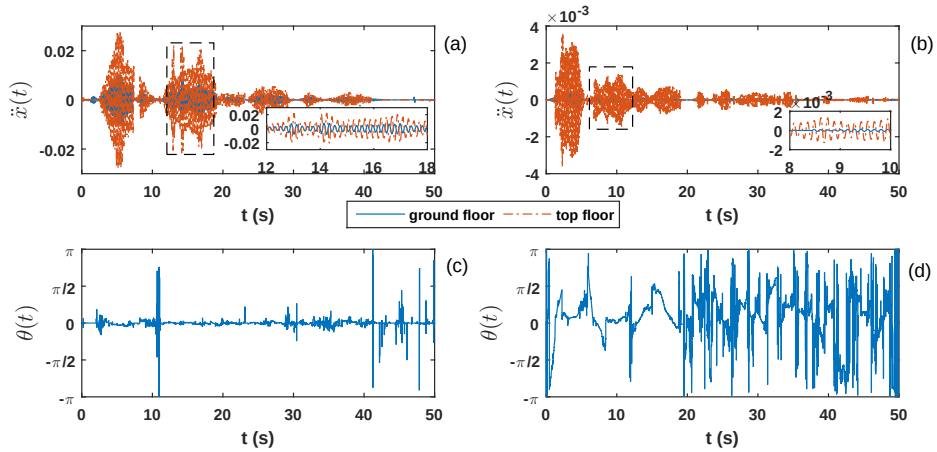

Figure 4.26: Phase portrait for seismic event on 03/09/09 - (a) response in 1st cluster; (b) response in 4th cluster; (c) phase difference in 1st cluster and (d) phase difference in 4th cluster

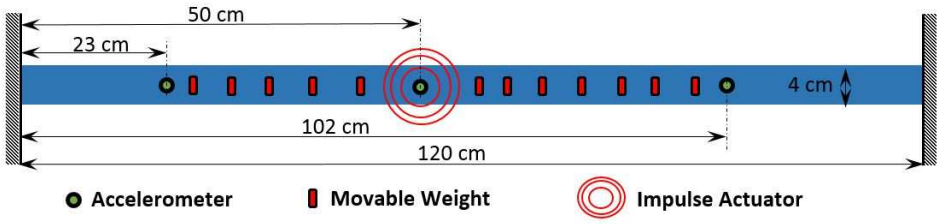

Figure 4.27: Schematic diagram of experimental setup

change, the frequencies of the beam also change. The beam is excited by impulse at the middle and the responses are recorded with a sampling rate of 16384Hz which are shown in Fig. 4.28. The data is recorded in FFT analyzer and the subsequent time domain data is generated by inverse fourier transformation after down sizing the sampling rate to 4096Hz. The peak acceleration response in all sensors are very high. Here, it may be noted that the beam is very thin and the effective length is very high so that large number of frequencies can be excited. This thin beam is excited by impulse hammer which is reflected in large acceleration response so that response energy in the higher modes are significant. In this context, it may be noted that the proposed algorithm is based on the frequency distribution in the scalogram and its phase spectrum. Hence, the proposed algorithm in this paper never uses the absolute amplitude of the response for modal identification. In this example, three different wavelet basis functions are used to study their relative performance on the same problem. First, the complex morlet basis is used with $n_s = 1024$ i.e. 2^{10}. The iteration in the proposed algorithm is continued until the process is converged. It is found that complex morlet basis converges with $n_s = 1255$ which remain same for Morse basis while lognarmal basis converge with $n_s = 5020$. Fig. 5.1 shows the scalogram of the wavelet coefficients obtained from the three different basis functions to demonstrate their relative performances, covering the frequency range

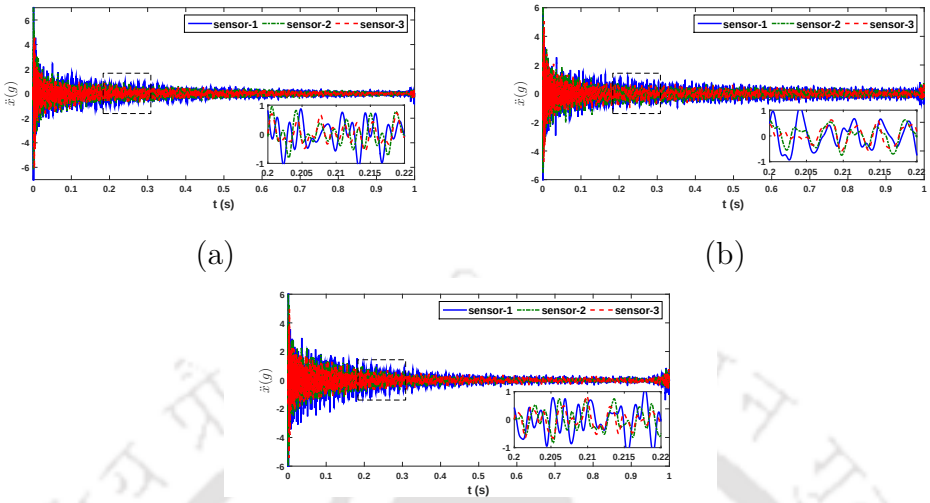

Figure 4.28: Recorded time histories - (a) test-1, (b) test-2 and (c) test-3

of 0.001 to 800Hz. As expected, the frequencies are localized at different regions of these scales (i.e. they are segregated into different bands). It can be easily shown that even the ridges and skeletons at these scales fail to separate out these frequencies. This, in turn, advocates for better frequency resolution of the scalograms. With this in view, synchrosqueezing of the original wavelet coefficients are carried out and the enhanced scalograms are also plotted in the second column of Fig. 5.1 which shows that resolution improves drastically due to synchrosqueezing. Here, only the scalograms of the response from sensor 2 in test 1 are shown to avoid repetition. However, these scalograms are not clear enough to distinctly identify the modal frequencies. Thus, k-means clustering based machine learning is adopted as described in the proposed algorithm. Here, the optimal number of clusters are identified in a similar way as described in the algorithm which is found to be 15 for all three basis. Fig. 4.30 shows the cluster weights corresponding to the median frequencies for three different tests. It may be noted that relative weights in each cluster indicate the energy associated with that frequency. To avoid any false alarm (i.e. spurious modes), phase portraits are then obtained from the signals by inverse synchrosqueezing as described in Eq. 3.58. Fig. 4.31 shows the difference in phase angles obtained from three different sensors. Here, only 2nd and 4th clusters are used for demonstration purpose. The first row of Fig. 4.31 shows the time history corresponding to the median frequency of the 2nd and 4th cluster obtained from inverse synchrosqueezed transformation. The second row of the same figure shows the instantaneous phase difference for all three sensors. As the responses are in mode, the phase difference is found to be in unison (i.e. attaining peaks and zero crossing simultaneously) in the second cluster indicating it to be a modal frequency. Table 4.6 summarizes the modal frequencies obtained using the proposed algorithm. Altogether 14 modal frequencies are identified in each test with error well below 5% except in the 1st mode where the error is 7%. Here, it may be noted that f_{exp} in Table 4.6 for each

test is obtained from FFT analyzer and not from the exact theoretical model. Thus, f_{exp} reported in Table 4.6 also has measurement error. However, these values are preferred over theoretical values as these are observed during the experiment. Hence, the magnitude of error reported for the present algorithm is not absolute. Moreover, the relatively high error in mode 1 is due to weak energy concentration in the 1st mode and should not be attributed to the drawback of the proposed algorithm. The weakness of the 1st modal frequency is also reported by Adhikary and Phani [163]. The frequency response functions (FRF) are obtained from the identified modal parameters and are compared with the experimental observations as shown in Fig. 4.32. A close match in frequencies between them are observed indicating accurate estimation of these parameters. There is a difference in shape of the identified and experimental FRF which is attributed to the approximate damping ratio used in identified FRF. Here, it may be mentioned that an effort was made to identify the modal damping of this thin beam. However, being very flexible with ultra high modal frequencies, the estimation of viscous damping suffers large errors and hence an approximated value of modal damping is used as suggested by Adhikari et. al. [162]. Finally, the performance of different basis functions are investigated and the results are tabulated in Table 4.7. It can be observed from this table that choice of basis function does not affect the quality of estimation in the proposed algorithm as the same frequencies are identified using three different bases. However, the number of scales are different for different basis functions. Here, only first five frequencies upto two decimal places are used for comparison. This is another advantage of the proposed algorithm which automatically adjust the scales to achieve the desire accuracy in estimation. Based on these results, it can be inferred that modal frequencies are identified satisfactory without any prior knowledge of the system/input and any user intervention.

4.3 Summary

Proposed adaptive versions of popular time-frequency analysis are considered here for field implementation. The main aim of this analysis is to establish the performance and efficiency of the proposed methods for real life structure where non-stationary and measurement noises are inherent in the experiment. For this purpose one multi-storied building and a prestressed concrete bridge are considered for testing. Numerical results presented here clearly establishes the superiority of proposed algorithm for OMA of full scale structure where traditional HHT or WT fails to identify the modal frequencies. This study also demonstrates the gradual development from adaptive HHT to unsupervised synchrosqueezed wavelet transformation with machine learning for fully automated OMA. Based on this analysis, it may inferred that the proposed adaptive versions of time-frequency analysis can be effective for field implementation of OMA for structures under forced vibration. These results also advocate that the proposed technique can be further extended for decision making process (e.g. damage detection, rehabilitation/retrofitting and vibration controller training).

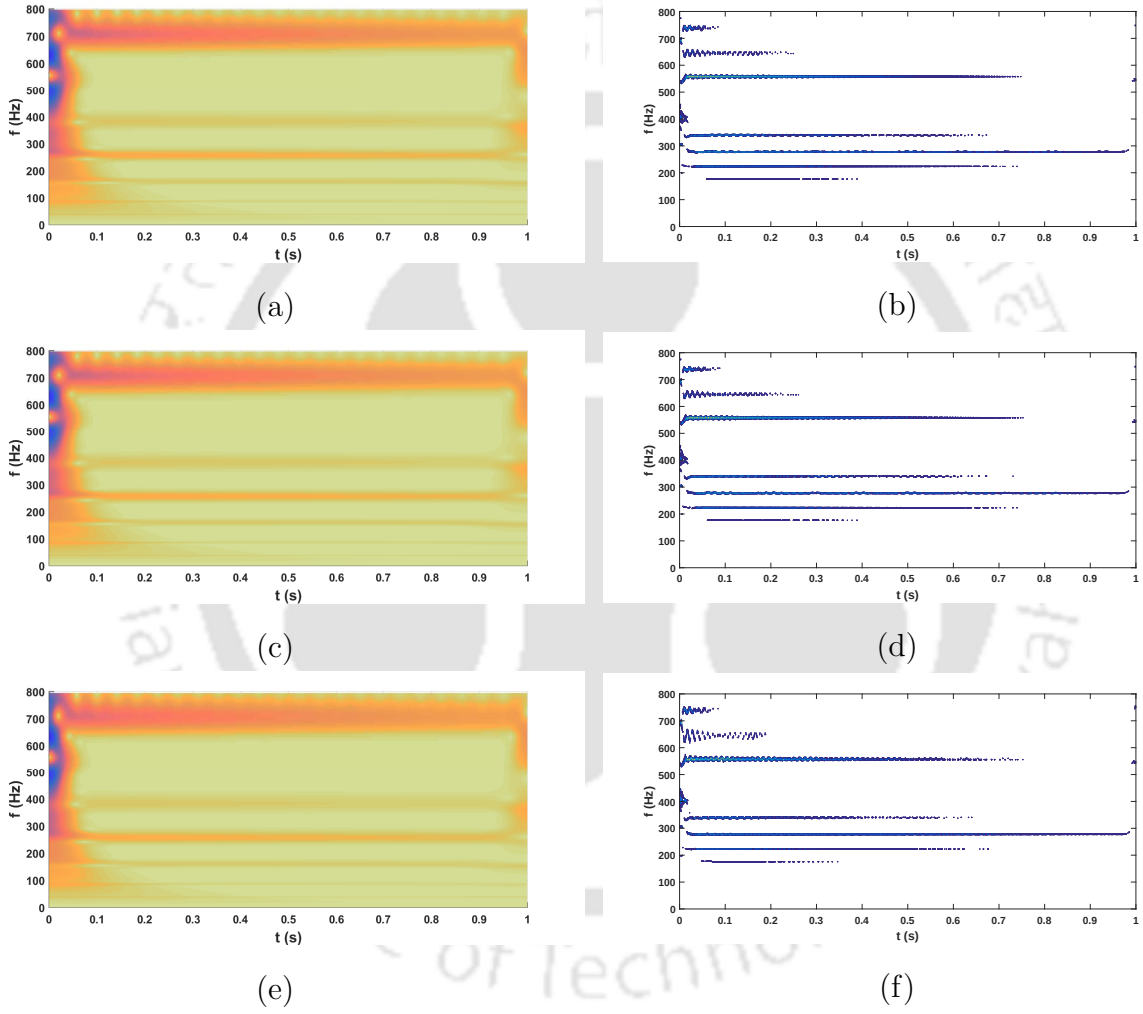

Figure 4.29: Scalograms obtained from WT (1st column) and SST (2nd column) of sensor 2 for test 1; (a) & (b) Complex Morlet ; (c) & (d) Lognormal Wavelet and (e) & (f) Morse Wavelet

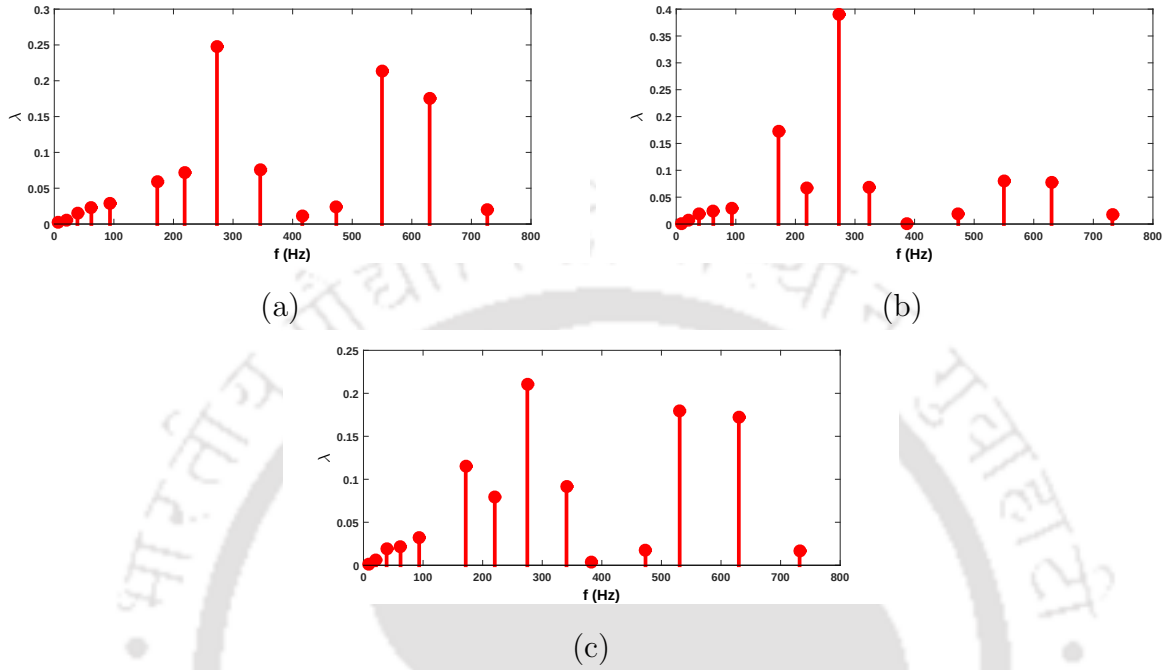

Figure 4.30: Median of the each cluster estimated from sensor 2 data (a) test-1, (b) test-2 and (c) test-3

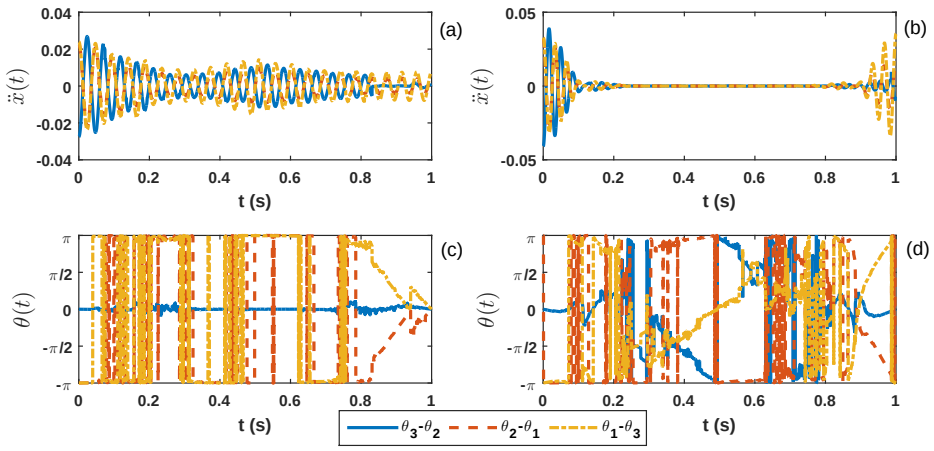

Figure 4.31: Phase portrait - (a) response in 2nd cluster; (b) response in 4th cluster; (c) phase difference in 2nd cluster and (d) phase difference in 4th cluster

Table 4.2: Identified parameters from bridge response

Analytical Values	Identified Values									
	Channel 1		Channel 2		Channel 3		Channel 4		Channel 5	
f_n (Hz)	f_n (Hz)	η (%)	f_n (Hz)	η (%)	f_n (Hz)	η (%)	f_n (Hz)	η (%)	f_n (Hz)	η (%)
3.1187	3.1310 [0.39]	5.48	3.1310 [0.39]	5.21	3.1310 [0.39]	5.84	3.1310 [0.39]	5.35	3.1310 [0.39]	5.48
7.7353	7.7779 [0.55]	0.55	7.9230 [2.43]	0.82	7.5474 [2.43]	0.51	7.7780 [0.55]	0.94	7.7779 [0.55]	0.55
13.587	13.2017 [2.84]	0.20	13.2236 [2.67]	0.40	13.2097 [2.78]	0.27	13.3591 [1.68]	0.22	13.2017 [2.84]	0.20
20.123	19.9224 [1.00]	0.18	19.8808 [1.20]	0.30	19.8415 [1.40]	0.20	19.8569 [1.32]	0.21	19.9224 [1.00]	0.18

[% error given in parenthesis]

Table 4.3: Identified modal parameters by combined wavelet-Hilbert transform

Mode	Type	Analytical f (Hz)	Identified Parameter from adaptive HT						Remarks
			f (Hz)			η (%)			
			S_1	S_2	S_3	S_1	S_2	S_3	
1	bending	3.1187	3.1360 [0.55]	3.1291 [0.33]	3.1287 [0.32]	5.5862	5.5381	5.7552	used for model updating
2	bending	7.7353	7.7301 [0.07]	7.9005 [2.14]	7.7441 [0.11]	0.5462	0.6026	0.6796	
3	bending	13.5870	13.6033 [0.12]	13.8102 [1.64]	13.6173 [0.22]	0.2287	0.2310	0.2303	
4	bending	20.1230	19.7720 [1.74]	19.7131 [2.04]	19.7218 [1.99]	0.0863	0.1554	0.1429	
5	bending	27.0140	26.5805 [1.60]	26.6777 [1.24]	26.7059 [1.14]	-	-	-	used for verification
6	torsional	28.5870	28.1429 [1.55]	28.1746 [1.44]	28.2092 [1.32]	-	-	-	
7	torsional	29.3430	29.5869 [0.83]	29.5394 [0.67]	29.5572 [0.73]	-	-	-	
8	torsional	31.3580	31.0897 [0.86]	30.8744 [1.54]	31.0088 [1.11]	-	-	-	
9	bending	33.8730	32.9059 [2.86]	32.7146 [3.42]	32.5933 [3.78]	-	-	-	
10	torsional	34.7320	34.4947 [0.68]	34.4962 [0.68]	34.4122 [0.92]	-	-	-	

(n.b.: % error in parentheses)

Table 4.4: Identified modal parameters of BRNS building from different seismic events

Natural frequency* f_n	Modal damping† $\eta(\%)$	03/9/2009 f_n X_{dir}	03/9/2009 f_n Y_{dir}	03/9/2009 $\eta(\%)$	21/9/2009 f_n X_{dir}	21/9/2009 f_n Y_{dir}	21/9/2009 $\eta(\%)$
4.75	1.28	4.61	4.98	1.30	4.99	4.73	1.31
5.84	1.11	5.17	6.68	1.16	5.87	6.32	1.16
13.20	0.27	12.86	13.77	0.30	11.27	13.54	0.32
16.25	0.27	16.63	16.28	0.30	16.28	14.88	0.30
19.98	0.24	18.11	-	0.30	17.73	-	0.31
24.57	0.19	23.62	26.51	0.22	22.72	-	0.25

[* obtained from equivalent strut model; † estimated by Mahato et. al. [161]]

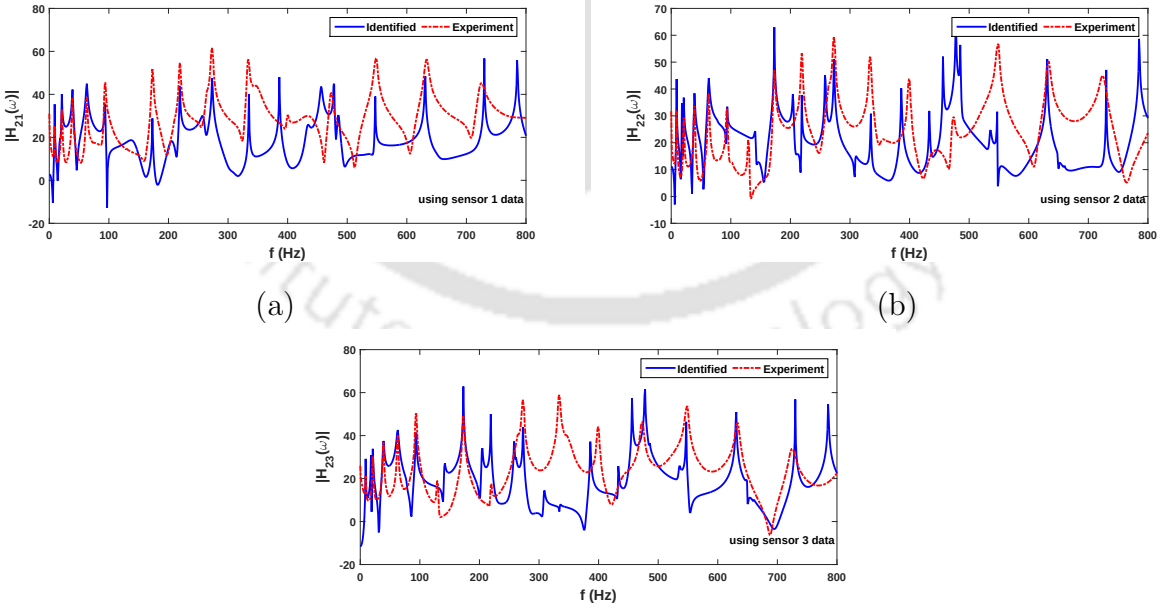

Figure 4.32: FRF at sensor location 2 for test- 1

Table 4.5: Mass locations for different tests (in cm.)

	Distance from left end in m											
	1	2	3	4	5	6	7	8	9	10	11	12
Test 1	0.25	0.30	0.38	0.39	0.47	0.63	0.69	0.73	0.74	0.80	0.94	0.98
Test 2	0.23	0.24	0.24	0.28	0.30	0.30	0.45	0.56	0.61	0.68	0.77	0.99
Test 3	0.29	0.30	0.30	0.41	0.46	0.48	0.56	0.56	0.67	0.77	0.77	0.78

Table 4.6: Identified modal frequencies of thin beam

Test 1				Test 2				Test 3			
f_{exp}	f_{idf}			f_{exp}	f_{idf}			f_{exp}	f_{idf}		
	Sensor 1	Sensor 2	Sensor 3		Sensor 1	Sensor 2	Sensor 3		Sensor 1	Sensor 2	Sensor 3
9.0	9.03	8.97	**8.41**	9.0	9.23	8.72	**8.53**	9.0	8.91	8.97	**8.47**
21.0	20.69	20.69	20.55	21.0	20.69	20.84	20.69	21.0	20.84	20.84	20.84
39.0	38.81	38.81	38.81	38.0	38.26	38.26	38.26	39.0	38.81	38.81	38.81
62.0	62.20	62.20	62.20	62.0	62.20	62.20	62.20	62.0	62.20	62.20	62.20
94.0	93.47	93.47	93.47	94.0	93.47	94.14	93.47	93.0	93.47	93.47	93.47
172.0	172.80	172.80	172.80	172.0	171.57	171.57	171.57	172.0	171.57	171.57	171.57
218.0	218.76	218.76	211.08	219.0	218.76	218.76	217.20	220.0	220.33	218.76	217.20
272.0	273.01	273.01	273.01	273.0	273.01	273.01	273.01	274.0	274.96	274.96	274.96
335.0	345.61	335.87	345.61	332.0	324.08	326.40	331.10	331.0	340.70	338.28	331.10
398.0	416.17	381.97	384.71	400.0	387.47	384.71	384.71	399.0	381.97	384.71	387.47
472.0	473.30	480.11	473.30	474.0	473.30	480.11	473.30	473.0	473.30	476.69	473.30
550.0	549.93	549.93	549.93	547.0	549.93	534.43	553.87	549.0	557.84	565.87	561.84
629.0	629.90	629.90	629.90	632.0	629.90	629.90	629.90	632.0	629.90	629.90	629.90
727.0	726.67	731.88	731.88	723.0	731.88	731.88	726.67	727.0	731.88	731.88	726.67

[bold cases have error between 5-7%. All other cases have error between 0-4%]

Table 4.7: Identified frequencies from sensor 1 in test 1 with different wavelet bases

f_{exp}	f_{idf} complex morlet (n_s)	f_{idf} logmromal (n_s)		f_{idf} morse (n_s)	
	1255	1255	5020	654	1255
9.00	8.23	8.23	8.23	8.23	8.23
21.00	20.99	20.99	20.99	20.99	20.99
39.00	38.92	38.92	38.92	38.92	38.92
63.00	62.79	-	62.79	-	62.79
94.00	93.74	93.74	93.74	93.74	93.74

Chapter 5

Uncertainty Quantification

Randomness and uncertainty are considered as a natural phenomena in engineering and science. Though in many cases it is simplified upto certain levels to reduce the complexity, but in many cases this simplification dilute the objective to many folds. In such scenario, researchers have to deal with this issue with advanced methodology and instruments. Here, this study does not focus on the modeling of random eigen value formulation, rather concentrate on the identification of the frequencies using proposed time-frequency analysis that can be adopted for actual applications. Thus, OMA is used here to model the statistical properties of the modal frequencies observed in the random experiment. The advantage of the proposed methodology for modal identification is that it does not require prior system information. So, the whole study is independent of the forward modeling. Though, for completeness of this study, the modeling of random eigen value problem is discussed here.

5.1 Description of Random Eigen Value Problems

Here, mathematical models of random eigen value problems are discussed in brief. This formulation is aimed to provide probability distribution of eigen values form a random structural system. The methods presented here are mostly followed as proposed by Adhikari and Frishwell [164]. The logic behind this formulation is to expand the random eigen value problem in Taylor's series expansion. Then the randomness of the parameters are introduced considering the mean value of the parameters as the reference point. For further details about this method, readers may refer to Pradlwarter *et. al.* [165], Desceliers *et. al.* [166], Rahman [167] and Cotoni *et. al.* [168].

5.1.1 Perturbation Based Formulation

The source of uncertainty in any structural dynamical system associated with the system matrices i.e. [**M**], [**K**] and [**C**]. The damping matrix [**C**] can be modeled as a combination of mass [**M**(**x**)] and stiffness [**K**(**x**)] matrices where **x** represents the set of random parameters that defines the dynamical system. In practice, these uncertainties (i.e. material, geometry and other modelling parameters) directly influence the system matrices. To observe the uncertainty propagated through the physical system, the common way is to adopt its underlying eigen analysis. As the system matrices carry the uncertainties associated with it, the eigen values are bound to be random in nature. Researchers [169–171] have tried to formulate these random eigen value functions analytically, by a mean-centered perturbation technique. According to this technique, the eigen function $\lambda(\mathbf{x})$ needs to be expanded in Taylor's series as given below

$$\lambda_j(\mathbf{x}) \approx \lambda_j(\boldsymbol{\alpha}) + \mathbf{d}^T_{\lambda_j}(\boldsymbol{\alpha})(\mathbf{x}-\boldsymbol{\alpha}) + \frac{1}{2}(\mathbf{x}-\boldsymbol{\alpha})^T\mathbf{D}_{\lambda_j}(\boldsymbol{\alpha})(\mathbf{x}-\boldsymbol{\alpha}) \tag{5.1}$$

Here, the linear system is discretized and $\mathbf{M}(\mathbf{x})$ and $\mathbf{K}(\mathbf{x})$ are random mass and stiffness matrices respectively with a random vector $\mathbf{x}$. The randomness $\mathbf{x}$ may have source from Yong's modulus, Poison's ratio, material properties, membrane orientation and geometric variable (i.e. length, width and thickness etc). In above equation $\mathbf{d}(\cdot)$ and $\mathbf{D}(\cdot)$ represent Jacobian and Hermitian matrices. To describe the statistical properties of these random vectors, probability distribution function is given below

$$p_{\mathbf{x}}(\mathbf{x}) = e^{-L(\mathbf{x})} \tag{5.2}$$

where, $L(\mathbf{x})$ is often known as the Log-likelihood function. Here, if $\mathbf{x}$ is considered as m-dimensional multivariate Gaussian random vector with mean $\boldsymbol{\mu} \in \mathbb{R}$ and covariance matrix $\boldsymbol{\Sigma} \in \mathbb{R}$ then $L(\mathbf{x})$ is given by

$$L(\mathbf{x}) = \frac{m}{2}\ln(2\pi) + \frac{1}{2}\ln\|\boldsymbol{\Sigma}\| + \frac{1}{2}(\mathbf{x}-\boldsymbol{\mu})^T\boldsymbol{\Sigma}^{-1}(\mathbf{x}-\boldsymbol{\mu}) \tag{5.3}$$

In Eq. (5.1), $\boldsymbol{\alpha}$ represents the optimal point related to saddle point approximation. Analytically $\boldsymbol{\alpha}$ can be found out in various ways. In this context, the mean of the eigen values are often most important reference point in all practical applications. For this reason, the optimal point $\boldsymbol{\alpha}$ is selected such that the mean or the first moment of each eigen value is calculated most accurately. Using Eq. (5.2), the mean of $\lambda(\mathbf{x})$ can be obtained as

$$\hat{\lambda}_j = E[\lambda_j(\mathbf{x})] = \int_{\mathbb{R}^m} \lambda_j(\mathbf{x}) p_{\mathbf{x}}(\mathbf{x}) d\mathbf{x} = \int_{\mathbb{R}^m} \lambda_j(\mathbf{x}) e^{-L(\mathbf{x})} d\mathbf{x} \tag{5.4}$$

It may be noted that, $\lambda(\mathbf{x})$ and $L(\mathbf{x})$ are nonlinear functions of $\mathbf{x}$. Eq. (5.4) is difficult to evaluate as the explicit form of $\lambda(\mathbf{x})$ is not readily available and hence, requires numerical approximation. From Eq. (5.4), it can be proved that the maximum contribution to this integral comes from the neighborhood where $[L(\mathbf{x}) - ln\lambda(\mathbf{x})]$ is minimum. Therefore, the function $[L(\mathbf{x}) - ln\lambda(\mathbf{x})]$ is

expanded in a Taylor series about the reference point where $[L(x) - ln\lambda(\mathbf{x})]$ has its global minimum. By doing so, the error in the integral of Eq. (5.4) becomes minimum. These optimal points can be obtained from

$$\frac{\partial\{L(\mathbf{x}) - \ln\lambda_j(\mathbf{x})\}}{dx_k} = 0 \qquad \text{or} \qquad \frac{\partial L(\mathbf{x})}{dx_k} = \frac{1}{\lambda_j(\mathbf{x})}\frac{\partial\lambda_j(\mathbf{x})}{dx_k} \qquad \forall k \tag{5.5}$$

From the above equation for all k (where k represents indices of random parameters) at $\mathbf{x} = \alpha$ the Jacobian matrix can evaluated as follows

$$\mathbf{d}_{\lambda_j}(\boldsymbol{\alpha}) = \lambda_j(\boldsymbol{\alpha})\mathbf{d}_L(\boldsymbol{\alpha}) \tag{5.6}$$

Above equation shows that at optimal point, gradient vectors of the Log-likelihood function and the eigen vectors are parallel. Eq. (5.6) is the set of nonlinear equations whose roots represent the optimal points. However, Eq. (5.6) reveals that $\mathbf{d}_{\lambda_j}(\boldsymbol{\alpha})$ on the left hand side demands evaluation of $\mathbf{d}_L(\boldsymbol{\alpha})$ using the system matrices [i.e. $\mathbf{M}(\mathbf{x})$ and $\mathbf{K}(\mathbf{x})$] at each optimal point. This is numerically challenging and hence, an approximation is prescribed in the literature [164] which takes the following form

$$\mathbf{d}_L(\mathbf{x}) = \boldsymbol{\Sigma}^{-1}(\mathbf{x} - \boldsymbol{\mu}) \tag{5.7}$$

Using above approximation in Eq. (5.6), the optimal point can be evaluated as given below

$$\boldsymbol{\alpha} = \boldsymbol{\mu} + \frac{1}{\lambda_j(\boldsymbol{\alpha})}\boldsymbol{\Sigma}\mathbf{d}_{\lambda_j}(\boldsymbol{\alpha}) \tag{5.8}$$

However, above equation revels that the optimal point $\boldsymbol{\alpha}$ can be evaluated in an iterative manner. The iteration to starts with an initial value of $\boldsymbol{\alpha}$ and evaluate the value of $d_L(\boldsymbol{\alpha})$, $\lambda_j(\boldsymbol{\alpha})$ and $d_{\lambda_j}(\boldsymbol{\alpha})$ in every step and convergence is checked after every successive iteration.

5.1.2 pdf Estimation by Asymptotic Integral

The optimal value of $\boldsymbol{\alpha}$ estimated above can be used in Eq. (5.1) to numerically get the probability distribution of the respective random eigen value. Present study aims to trace this distribution numerically from ensemble of the test results using modified synchrosqueezed OMA described in section 3.4. However, the theoretical probability distribution of the random eigen values can also be evaluated using first few moments asymptotically. This asymptotic evaluation using moment generating function is briefly described here for completeness.

In this technique, the moments of the eigenvalues are obtained based on an asymptotic approximation of the multi-dimensional integral. Consider a function $f(\mathbf{x}) : \mathbb{R}$ which is smooth and at least

twice differentiable and the integral form will be

$$\mathfrak{f} = \int_{\mathbb{R}^m} e^{-f(\mathbf{x})} d\mathbf{x} \tag{5.9}$$

The maximum contribution to this integral comes from the neighborhood where $f(\mathbf{x})$ reaches its global minimum and if these points are $\boldsymbol{\theta}$, then

$$\frac{\partial f(\mathbf{x})}{\partial x_k} = 0 \quad \forall k \qquad \text{or} \qquad \mathbf{d}_f(\boldsymbol{\theta}) = 0 \tag{5.10}$$

Using this, $f(\mathbf{x})$ is expanded in a Taylor series about $\boldsymbol{\theta}$ and Eq. (5.9) is rewritten as follows

$$\mathfrak{f} = \int_{\mathbb{R}^m} e^{-\left\{f(\boldsymbol{\theta}) + \frac{1}{2}(\mathbf{x}-\boldsymbol{\theta})^T \mathbf{D}_f (\mathbf{x}-\boldsymbol{\theta}) + \varepsilon(\mathbf{x},\boldsymbol{\theta})\right\}} d\mathbf{x} \tag{5.11a}$$

$$= e^{-f(\boldsymbol{\theta})} \int_{\mathbb{R}^m} e^{-\frac{1}{2}(\mathbf{x}-\boldsymbol{\theta})^T \mathbf{D}_f (\mathbf{x}-\boldsymbol{\theta}) - \varepsilon(\mathbf{x},\boldsymbol{\theta})} d\mathbf{x} \tag{5.11b}$$

Here, $\varepsilon(\mathbf{x}, \boldsymbol{\theta})$ is the error modeling due to the truncation of the Taylor series expansion after 2^{nd} order terms. With suitable scaling of $\mathbf{x}$, the integral in Eq. (5.9) can be transformed to the so-called 'Laplace Integral'. The error $\varepsilon(\mathbf{x}, \boldsymbol{\theta})$ depends on higher order derivatives of $f(\mathbf{x})$ at $\mathbf{x} = \boldsymbol{\theta}$. If they are small compared to $f(\boldsymbol{\theta})$ and the elements of $D_f(\boldsymbol{\theta})$, their contribution will be negligible to the value of this integral. Therefore, it assumes $f(\boldsymbol{\theta})$ and the elements of $D_f(\boldsymbol{\theta})$ are large so that

$$\left| \frac{1}{f(\boldsymbol{\theta})} \mathcal{D}^{(j)}(f(\boldsymbol{\theta})) \right| \to 0 \quad \text{and} \quad \forall k,l \quad \left| \frac{1}{[\mathbf{D}_f(\boldsymbol{\theta})]_{kl}} \mathcal{D}^{(j)}(f(\boldsymbol{\theta})) \right| \to 0 \quad \text{for} \quad j > 2 \tag{5.12}$$

where, $\mathcal{D}^{(j)}(f(\boldsymbol{\theta}))$ is j^{th} order derivative of $f(\mathbf{x})$ evaluated at $\mathbf{x} = \boldsymbol{\theta}$, which leads to $\varepsilon(\mathbf{x}, \boldsymbol{\theta}) \to 0$. Therefore, the integral in Eq. (5.11b) can be approximated as

$$\mathfrak{f} = e^{-f(\boldsymbol{\theta})} \int_{\mathbb{R}^m} e^{-\frac{1}{2}(\mathbf{x}-\boldsymbol{\theta})^T \mathbf{D}_f(\boldsymbol{\theta})(\mathbf{x}-\boldsymbol{\theta})} d\mathbf{x} \tag{5.13}$$

If $\boldsymbol{\theta}$ is the global minimum of $f(\mathbf{x})$ in $\mathbb{R}$, the symmetric Hessian matrix $\mathbf{D}_f(\boldsymbol{\theta}) \in \mathbb{R}$ is also positive definite. Now, coordinate transformation leads to the following form

$$\boldsymbol{\xi} = (\mathbf{x} - \boldsymbol{\theta}) \mathbf{D}_f^{-1/2}(\boldsymbol{\theta}) \tag{5.14}$$

The Jacobian of this transformation is given by

$$\|\mathbf{J}\| = \|\mathbf{D}_f(\boldsymbol{\theta})\|^{-1/2} \tag{5.15}$$

Using Eq. (5.14), the integral in Eq. (5.13) can be evaluated as

$$\mathfrak{f} \approx e^{-f(\boldsymbol{\theta})} \int_{\mathbb{R}^m} \|\mathbf{D}_f(\boldsymbol{\theta})\|^{-1/2} e^{-\frac{1}{2}(\boldsymbol{\xi}^T\boldsymbol{\xi})} d\xi \tag{5.16a}$$

$$\approx (2\pi)^{m/2} e^{-f\boldsymbol{\theta}} \|\mathbf{D}_f(\boldsymbol{\theta})\|^{-1/2} \tag{5.16b}$$

This approximation is expected to yield good results if the minima of $f(\mathbf{x})$ around $\mathbf{x} = \boldsymbol{\theta}$ is sharp. If $\boldsymbol{\theta}$ is not unique then it is required to sum the contributions arising from all such optimal points separately.

5.1.3 Challenges and Possible Remedies

To determine the uncertainty in inverse modal analysis using the above formulation, all parameters of the forward problem associated to the system matrices are required. In practice, it is difficult to get element wise description of random matrices $[\mathbf{M}(\mathbf{x})]$ and $[\mathbf{K}(\mathbf{x})]$. To alleviate this problem, the proposed output only time-frequency analysis using combined synchrosqueezed transformation and unsupervised machine learning is adopted here. The aim is to get the automated estimation of eigen frequencies from the individual tests without any intermittency with the user/designer. This process is repeated for the entire ensemble of the test performed over the test structure. These numerical evaluation of the outcomes (i.e. eigen frequencies) in every test finally provides the probability distribution of the underlying random eigen values. It is described below along with the error estimation to evaluate the reliability of the proposed identification strategy.

To identify the natural frequencies from the response of the test structure, Algo. 5 is adopted. This method is based on the synchrosqueezed transformation discussed in Chapter 3. The error function for each modal frequencies are calculated using the values reported by Adhikari *et. al.* [162]. Here, the identified frequencies are $\omega_{ind}^{s,n}$. The superscript s and n represents the sensor and test number respectively. Thus for all the modal frequencies, error function can be expressed as

$$\epsilon^{s,n} = \frac{\omega_{exp}^{s,n} - \omega_{ind}^{s,n}}{\omega_{exp}^{s,S}} \times 100\% \tag{5.17}$$

For a single sensor, the pdf of the error function can be evaluated considering all test results. Thus, the pdf of the error is given by

$$p(\epsilon^s) = \lim_{\Delta\epsilon \to 0} \frac{Prob\left[\epsilon < \epsilon(\mathbf{x}) \leq \epsilon + \Delta\epsilon\right]}{\Delta\epsilon} \tag{5.18}$$

In the above function, the random parameters are denoted by $\mathbf{x}$. From the above pdf, the cumulative

distribution function (CDF) can be estimated as

$$P(\epsilon^s) = \int_{-\infty}^{\epsilon^s} p(\xi) d\xi \tag{5.19}$$

The significance of the $P(\epsilon^s)$ is that for any acceptable level of error ϵ^s, it gives the probability of the detection of that mode from a specific sensor.

5.2 Numerical Results & Discussion

In this section, numerical examples are presented to demonstrate the performance of the proposed automated time-frequency base OMA for random eigen value problem. For this purpose, two different experimental result (i.e. beam and plate with random parameter) are used for demonstration. These test were carried out by Adhikari *et. al.* [162] and the test data are freely available in the internet [159].

5.2.1 Beam with Random Parameter

In first example, a steel beam is considered whose length is 1.2m as described in section 4.2.1. On this beam, 12 movable mass is attached and each of these have 2gm weight. These movable mass is attached to beam by magnetic force. During each experiments, these movable masses are placed randomly to introduce uncertainty in the mass matrix. The test is repeated 100 times and every time these beam is excited by impulse hammer located at 50cm from the left end. In each test, impulse hammer applies an unitary impulse force to the beam. The responses are recorded by three accelerometers as shown in Fig. 4.27 and a typical recorded accelation is shown in Fig. 4.28 where the sampling rate is 16384Hz. The synchrosqueeze transformation as given in Eq. (3.55) is applied on test data of sensor 2 with complex morlet wavelet as it described in Chapter 2. The scalograms obtained from this analysis are presented in Fig. 5.1. Using these coefficients, Algo. 5 adopted here. By this algorithm, k-means clusters are formed on the absolute values of the SST coefficients. The median of these clusters are considered as identified frequencies. This automated OMA is repeated for each sensors and the identified frequency corresponding to each mode are reported in Tablee 5.1. From this table, it can be observed that the error in mean frequency estimation lies well within 5% while the same for standard deviation is very high. The reason behind this large error for standard deviation is due to the fact that Algo. 5 uses the central tendency of the clusters in the machine learning adopted in the proposed automated OMA. This can be further improved by supervised learning where the trends of the uncertainty propagation in higher modes can be modeled. However, as the main aim of this study is found on the estimation of mean frequency,

Algorithm 5 : Uncertainty on Detection of Natural Frequencies

for $S = 1$ to 100 **do**
  record acceleration response $\ddot{\mathbf{u}}(t)$
  set frequency range f_1 and f_2
  select a basis function and associated parameters
  initialize $f_{inz} = 0$
  for $n_s = 2^8$ **do**
    evaluate $W_\psi \ddot{\mathbf{u}}^{an}(a, b)$ per Eq. (3.53)
    apply SST over WT scalogram
    find out $E_{\ddot{\mathbf{u}}^{an}}$ using SST coefficients for all scales following Eq. (3.54)
    initialize $GV_n = 0$
    for $c = 1$ **do**
      evaluate $GV_n(c)$ using Eq. (3.61) and (3.62)
      if $\{GV_n(c) - GV_n(c-1)\}/GV_n(c) < 0.1$ **then**
        $c^* = c$ [optimum cluster number]
      else
        $c = c + 1$
      end if
    end for
    apply k-means clustering over $E_{\ddot{\mathbf{u}}^{an}} \approx |W_\psi \ddot{\mathbf{u}}(a, b)|^2$
    f_{idf} = median of the cluster
    $\kappa = |f_{idf} - f_{inz}|$
    if $\kappa > tolerance$ **then**
      $n_s = int\{n_s + \gamma * n_s\}$
      $f_{inz} = f_{idf}$
    else
      `break`
    end if
  end for
  for $i = 1$ to c^* **do**
    evaluate $T(\omega_n, b)$ for each median from Eq. (3.57)
    calculate $\ddot{\mathbf{u}}^q(t)$ by inverse transform of $T(\omega_n, b)$
    evaluate θ_k^q using Eq. (3.58)
    calculate phase difference $\Delta\theta_i = \theta_k^q - \theta_k^{q-1}$
    if $\Delta\theta_i \approx 0$ or π **then**
      f_{idf_i} is mode
    else
      f_{idf_i} is not a mode
    end if
  end for
  calculate $\epsilon^{s,S}$ following Eq. (5.17)
end for
calculate $p(\epsilon^s)$ by Eq. (5.18)
calculate $P(\epsilon^s)$ for each sensor by Eq. (5.19)

the results obtained from this analysis can b considered satisfactory.

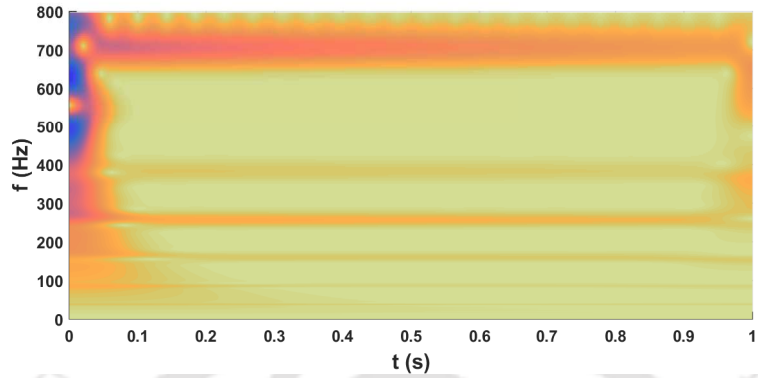

(a)

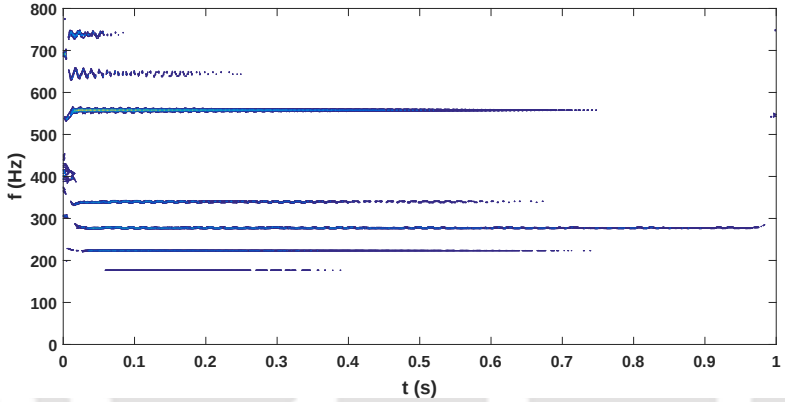

(b)

Figure 5.1: (a)Wavelet transform and (b) Synchrosqueezed Wavelet transform of beam's response recorded at sensor 2

Once the frequencies are extracted, the probability density function (pdf) of the identified modal frequency are developed numerically which can be compared with either close form expression [i.e. Eq. (5.1) to Eq. (5.16a)] or experimentally obtained from the individual test data using FFT-Analyzer. To obtain the pdf from extracted frequencies, the histograms are plotted for mode 6 and shown in Fig. 5.3. From the histogram figure, it is observed that there are very less point available to fit it to any known distribution. Thus, here, Kernel density estimator is used to generate the pdf. As per the Kernel density estimator, for any real values of x, the density estimator formula is

$$\widehat{f}_h(x) = \frac{1}{nh} \sum_{i=1}^{n} K\left(\frac{x - x_i}{h}\right) \tag{5.20}$$

where, $x_1, x_2, ..., x_n$ are random samples from unknown distribution; n is the sample size; $K(\cdot)$ is the Kernel smoothing function and h is the bandwidth. Here, fourteen dominant frequencies

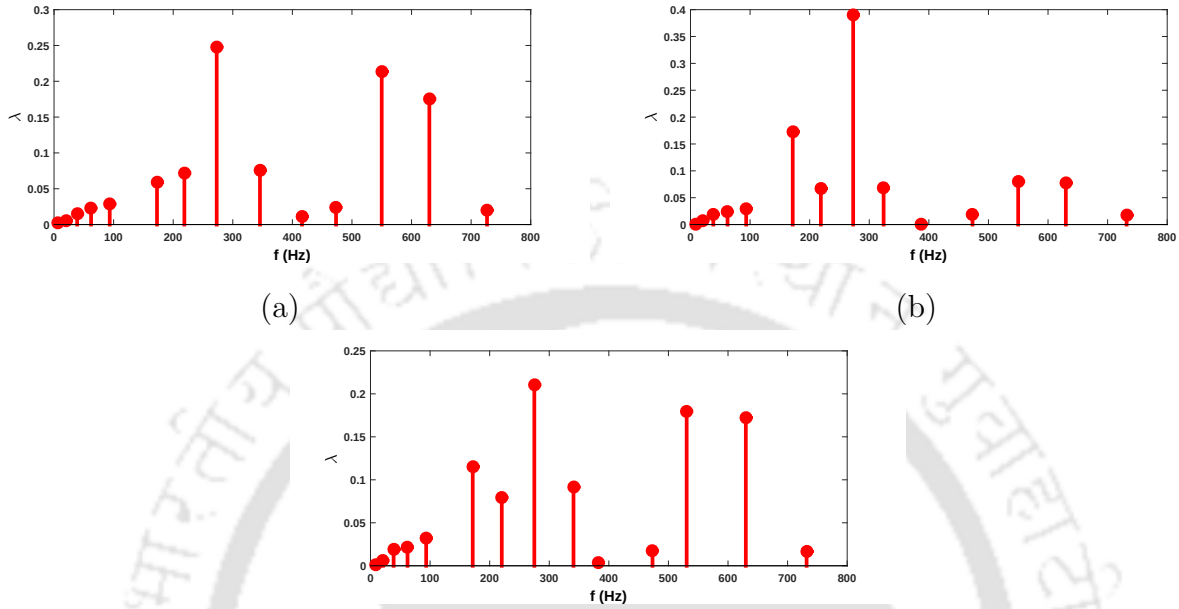

(a) (b)

(c)

Figure 5.2: Median of clusters shows location of identified frequencies of three test

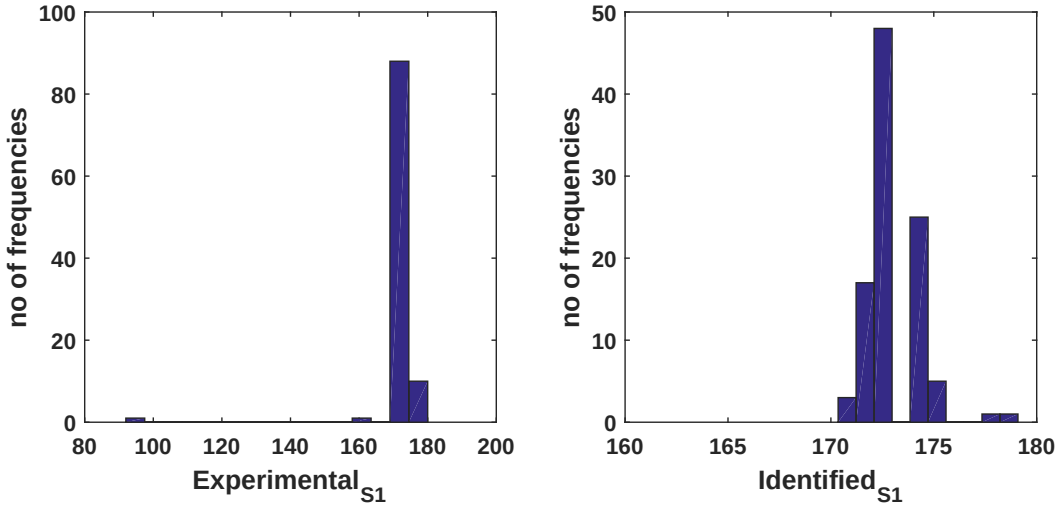

Figure 5.3: Histogram of the frequencies of mode 6

are identified from recorded responses and these are compared with the experimental results. The numerically evaluated pdf of frequencies are shown in Fig. 5.4 for few typical modes. The purpose of the comparison is to show the close match between the identified and experimental frequencies which in turn, proves the accuracy of the proposed methodology. To estimate the accuracy of the method, error is calculated as proposed in Eq. (5.17). The error pdf for 14 modes are shown in Fig. 5.6 for three sensors while their respective CDFs are shown in Fig 5.7. From this figures, the probability of detection of a particular mode from a particular sensors can be evaluated for different levels of estimation errors. Fig. 5.7 shows the 5% error mark and 85% detectibility level. From this figure, it can be concluded that the uncertainty associated with the frequencies are successfully estimated by the proposed automated OMA using combine synchrosqueeze transform and k-means clustering. Mode 1 has the highest level of estimation error as it is weak in term of energy given in Tablee 5.1. This feature is also reported by Adhikari and Phani [163] and hence should not be attributed to the shortcoming of the proposed OMA strategy. Here need to mention that standard deviations are calculated from the numerical pdfs. Histogram show in Fig. 5.3 have few discrete data point which are far away from the mean value. While the numerical pdfs are calculated, effects of these values are neglected. If standard deviations are calculated from the histogram directly then it would not be coherent with the numerical pdfs. The identification algorithm is able to detect the random frequencies in the mean sense. However, for few frequencies there are difference in higher moments. As Fig. 5.5 shows that although mean values are similar to the experimental results, there are variation in standard deviation. The importance of these results is that from this plot the detectibility of any mode for a specific sensor can be estimated. For example, from Fig. 5.7 with considering 2% error in identified value, mode 7 ($N = 7$) frequency has chance for detection near 1 from sensor-1 and sensor-2. Now if response from sensor-3 is used for identification, there are only 60% chance for detection.

5.2.2 Plate with Random Parameter

In this second example, a steel plate is considered whose length is 998mm, width is 530mm and thickness is 2.05mm. The experimental set up is shows in Fig. 5.8. On this plate, 10 mass-spring oscillator are randomly placed to perform 100 tests. To record response, 6 accelerometer are used at different locations of this plate. During each test the movable mass-spring oscillator are placed at 10 random locations to creat the uncertain mass matrix. The plate is excited by impulse hammer that applies an unit force at each time of the test. The responses are recorded by accelerometers as shown in Fig. 5.8 and one of the set of sample responses are shown in Fig. 5.9.

The sampling rate for recoding the data is is set to be as 16384Hz, as in the previous case. The acceleration data are down sampled by four times i.e. 4096Hz to use in time-frequency analysis. The synchrosqueeze transformation as given in Eq. (3.55) is applied on these acceleration data

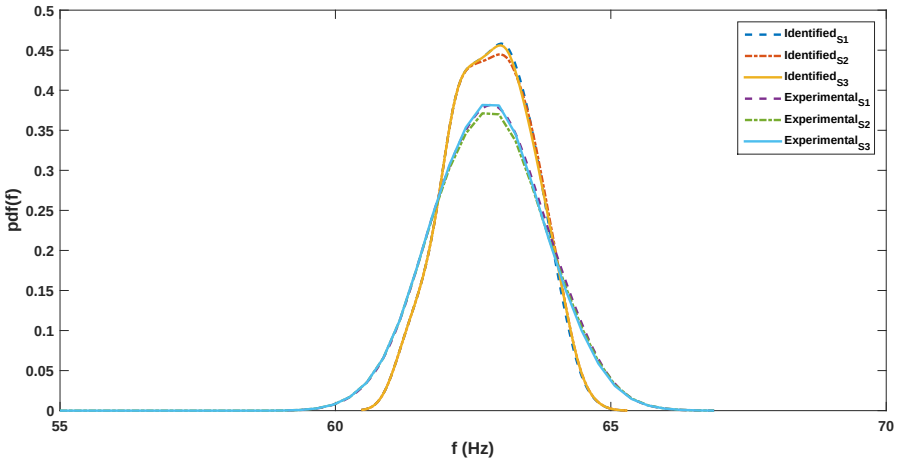

(a)

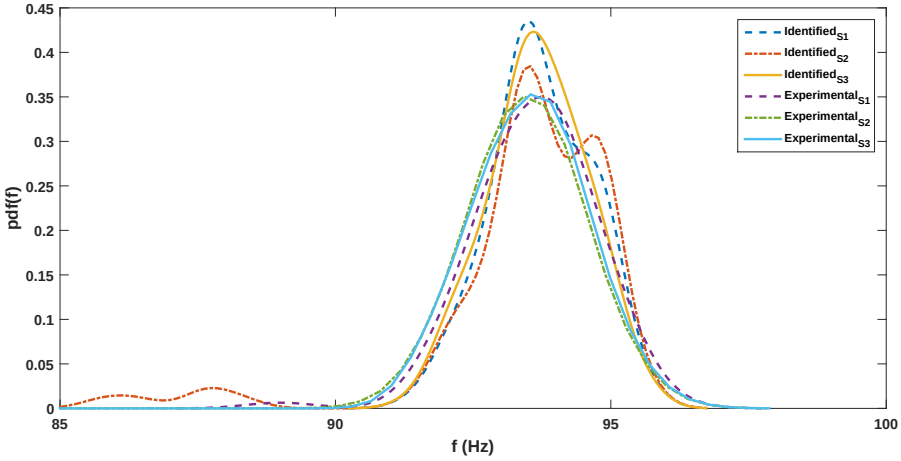

(b)

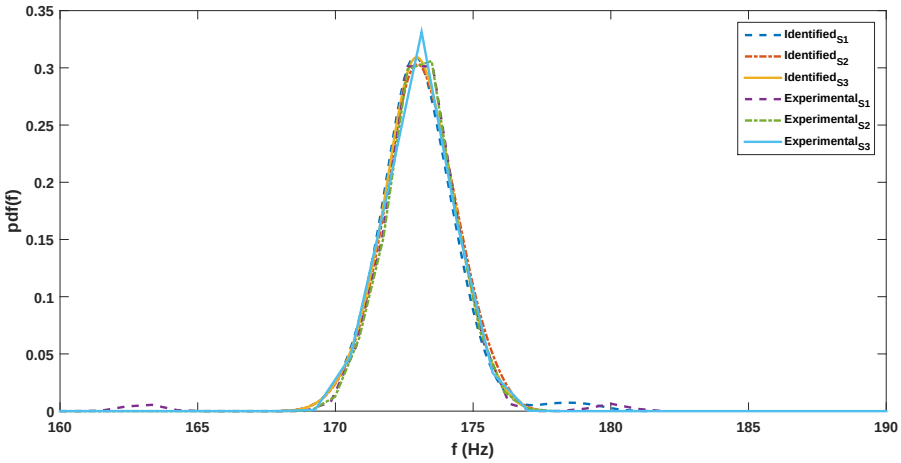

(c)

Figure 5.4: Comparison of pdf of identified and experimental cases from beam experiment for few typical modes (a) mode 4 (b) mode 5 and (c) mode 6

Table 5.1: Mean and standard deviation of identified frequencies for beam

Sensor 1				Sensor 2				Sensor 3			
μ		σ		μ		σ		μ		σ	
f_{exp}	f_{idf}	f_{exp}	f_{idf}	f_{exp}	f_{idf}	f_{exp}	f_{idf}	f_{exp}	f_{idf}	f_{exp}	f_{idf}
9.08	8.23 [9.35]	2.21	5.72	9.07	9.02 [0.59]	2.15	2.60	9.18	8.81 [4.02]	2.67	2.82
21.11	20.99 [0.57]	3.08	2.99	21.11	21.00 [0.52]	2.96	2.87	21.01	21.02 [0.07]	2.25	2.72
38.94	38.92 [0.04]	3.09	3.34	38.55	38.93 [0.98]	8.85	3.34	38.77	38.93 [0.40]	8.98	3.34
62.80	62.79 [0.01]	2.87	3.52	62.31	62.80 [0.79]	5.90	3.56	62.54	62.80 [0.41]	3.65	3.55
93.61	93.74 [0.14]	2.63	3.71	92.86	93.48 [0.66]	6.77	4.90	93.23	93.67 [0.47]	4.25	3.69
172.25	173.07 [0.47]	1.45	1.25	169.96	173.09 [1.84]	1.96	1.59	172.72	173.03 [0.18]	1.09	1.60
218.17	219.11 [0.43]	1.69	2.91	217.72	219.06 [0.61]	2.15	2.49	218.81	214.49 [1.97]	1.29	1.72
273.13	273.22 [0.03]	3.63	2.62	271.50	273.28 [0.66]	2.39	3.28	272.55	273.26 [0.26]	4.67	2.96
334.23	331.45 [0.83]	1.49	2.02	331.90	334.85 [0.89]	2.16	2.28	333.18	334.06 [0.26]	1.31	2.24
398.98	383.89 [3.78]	1.35	1.84	396.77	386.20 [2.67]	2.93	2.45	398.64	387.44 [2.81]	1.41	1.17
473.03	473.54 [0.11]	3.20	3.64	470.21	477.58 [1.57]	2.84	4.94	472.19	472.79 [0.13]	1.27	4.08
547.96	549.23 [0.23]	2.82	3.26	545.74	546.80 [0.19]	2.34	2.48	547.22	547.90 [0.12]	1.59	8.51
633.15	631.75 [0.22]	2.77	3.05	630.43	630.62 [0.03]	2.47	1.96	632.12	631.07 [0.17]	1.39	2.30
725.14	730.84 [0.79]	5.16	7.02	723.35	729.90 [0.91]	2.43	7.35	724.81	727.72 [0.40]	5.59	7.92

[% error shown in parentheses]

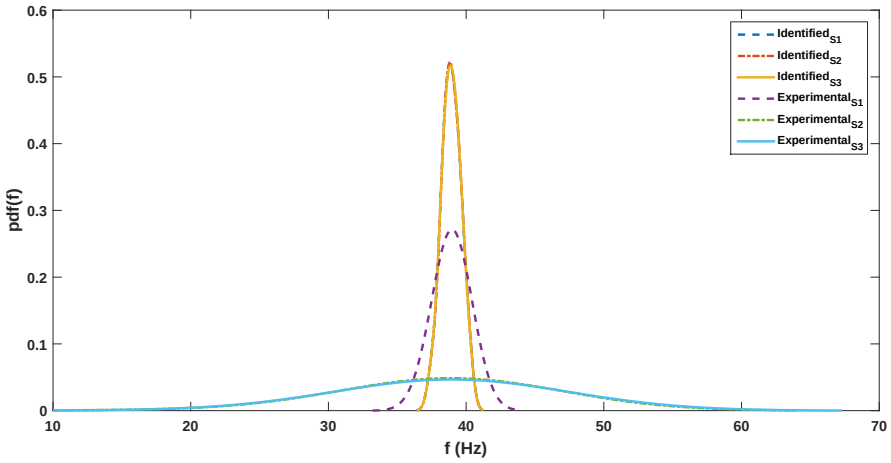

Figure 5.5: Comparison of pdf of identified and experimental cases from beam experiment for mode 3

using complex morlet wavelet basis function. The resulting scalograms from sensor 1 are presented in Fig. 5.10. On this SST coefficients, above mentioned identification algorithm is applied to extract the frequencies. By this algorithm, k-means cluster is formed on the absolute values of the SST coefficients. The median of this cluster is considered as identified frequencies and the process is repeated to identify the dominant frequencies from 100 tests recorded by 6 sensors.

After the extraction of dominant frequencies from the response, the pdfs for each case are evaluated numerically as described in the previous section. These are compared with pdfs obtained from experiment. Like previous experiments, one can correlate these pdf to the close form solution explained from Eq. (5.1) to Eq. (5.16a). Here, sixteen dominant frequencies are identified from the vibration signals and these are compared with the experimental results. The numerically evaluated pdf of frequencies are shown in Fig. 5.11 for few typical modes. The difference in mean level is very less while the difference comes in dispersion i.e. standard deviation. The major difference comes in the lower values of frequencies as contribution of these frequencies are less as observed from the experimental data [162]. Here, it may be noted that the error for each case is estimated based on the experimental data. The error pdf for sixteen frequencies are shown in Fig. 5.11 for three sensors following Eq. (5.18). In most of the cases, errors in mean modal frequencies have very less values (i.e. below 3%) as given in Table 5.2 and Table 5.3. It proves the efficiency of the proposed method. By forming the CDF of the error value, the probabilty of detection of a particular mode is estimated as in Fig. 5.11. Here, it may be noticed that for the same frequency the probability of identification varies sensor to sensor. However, with 5% allowable error, the probability of detection of the modes are very high except one or two cases which are due to modal energy contents.

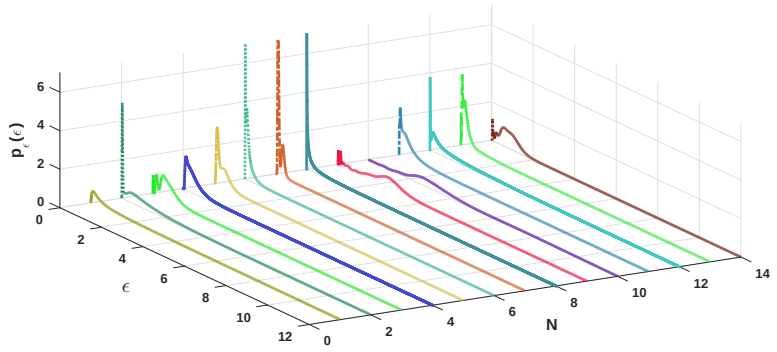

(a)

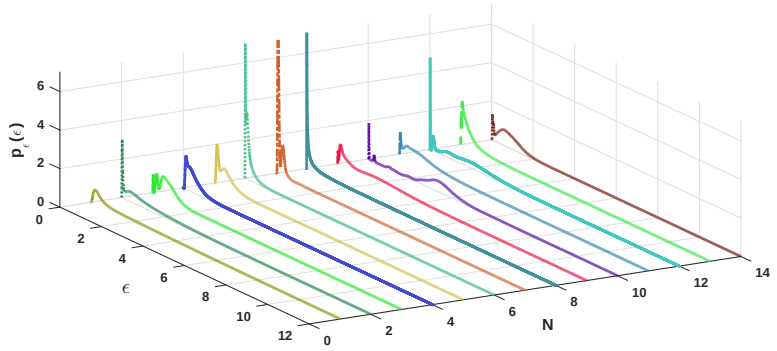

(b)

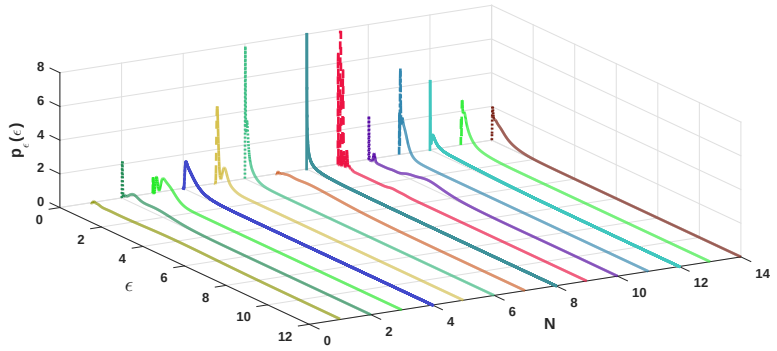

(c)

Figure 5.6: Probability distribution function of error in frequency estimation for beam

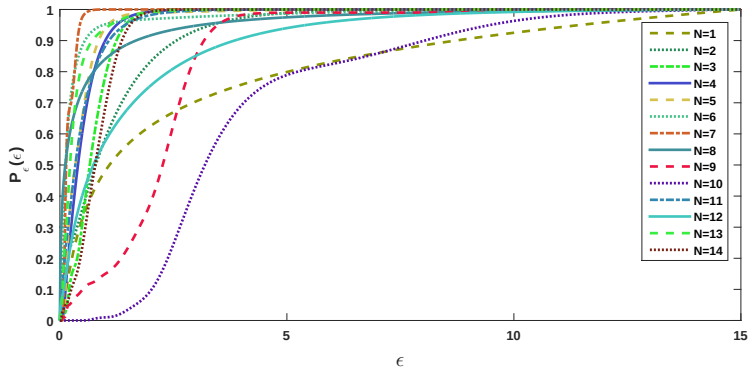

(a)

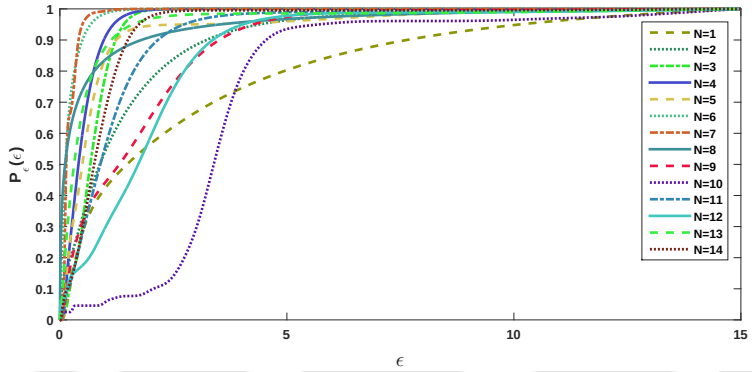

(b)

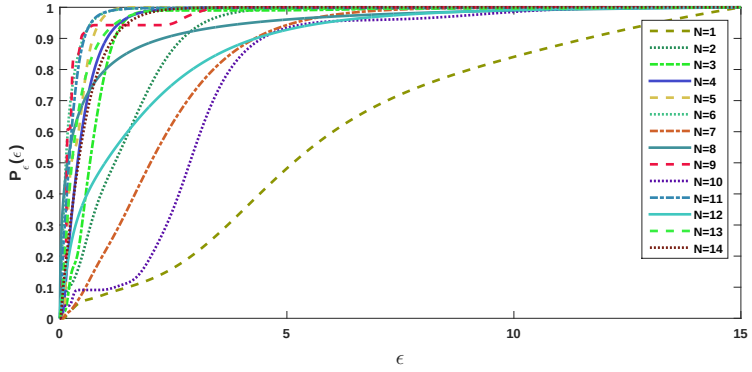

(c)

Figure 5.7: Detectability of frequencies for beam for different sensors

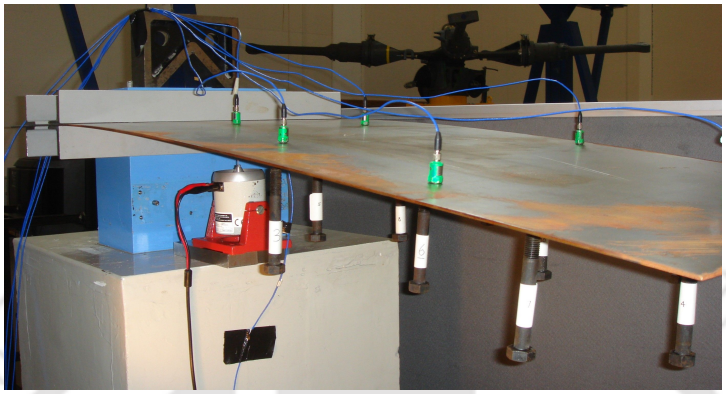

Figure 5.8: Experimental setup for laboratory test of plate

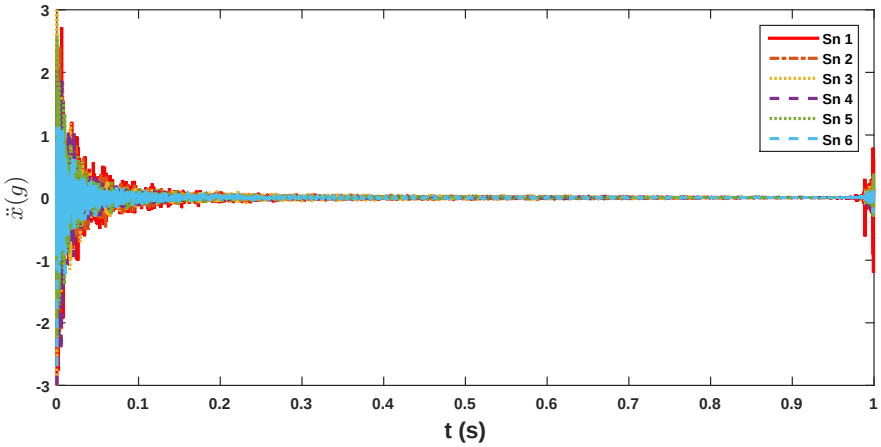

Figure 5.9: Plate vibration response of test 1

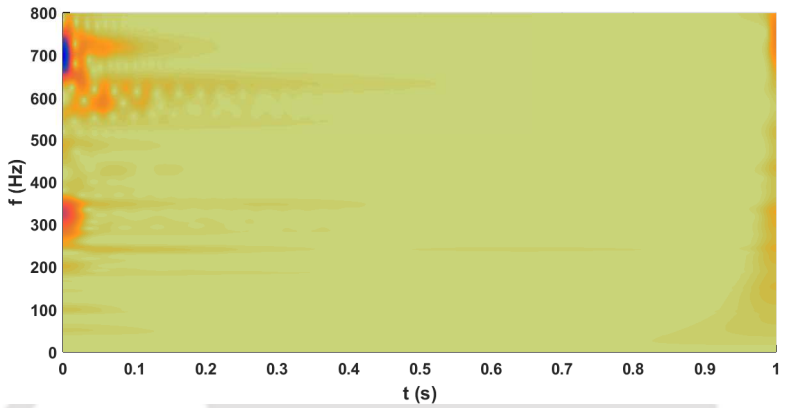

(a)

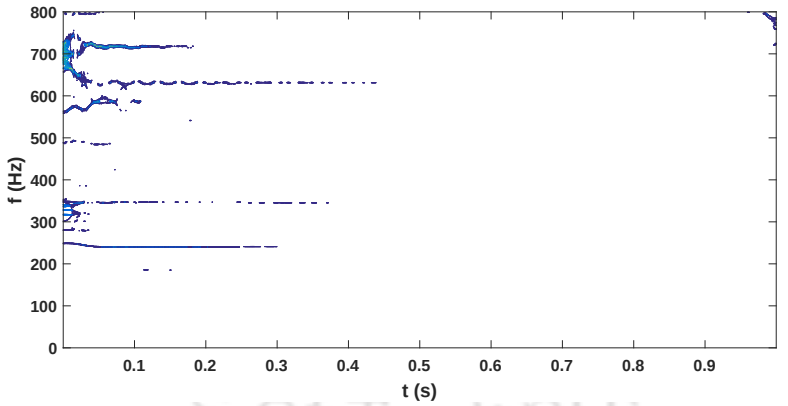

(b)

Figure 5.10: (a)Wavelet transform and (b) Synchrosqueezed Wavelet transform of plate response recorded at sensor 1

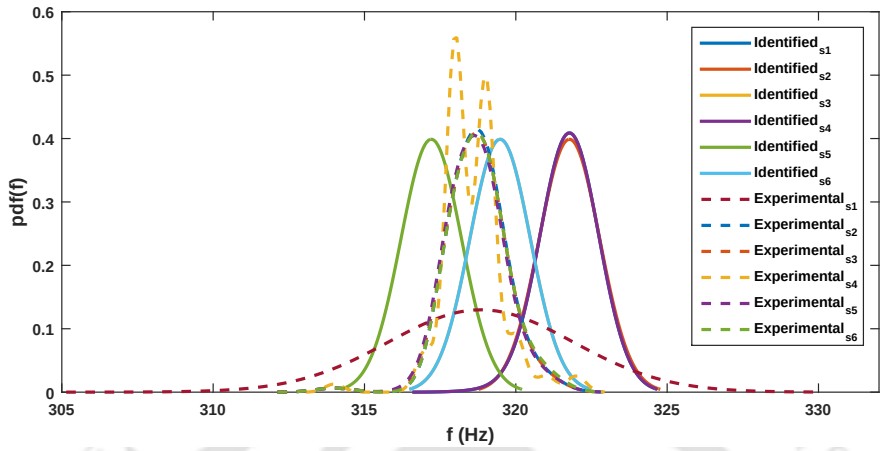

(k)

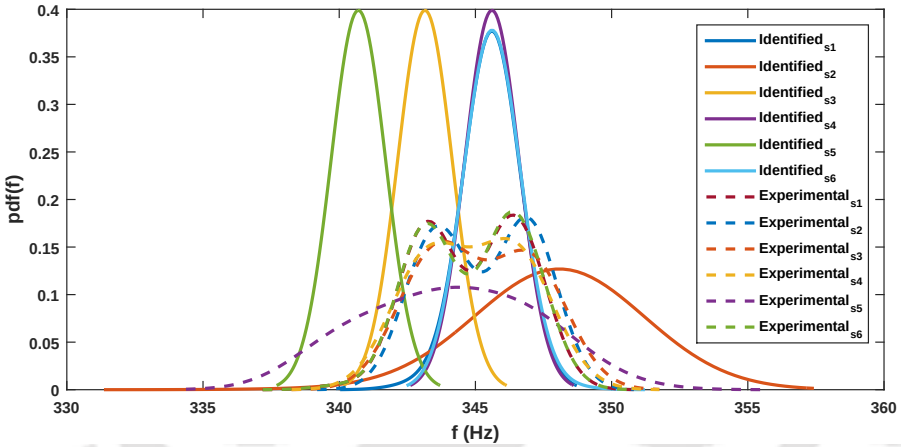

(l)

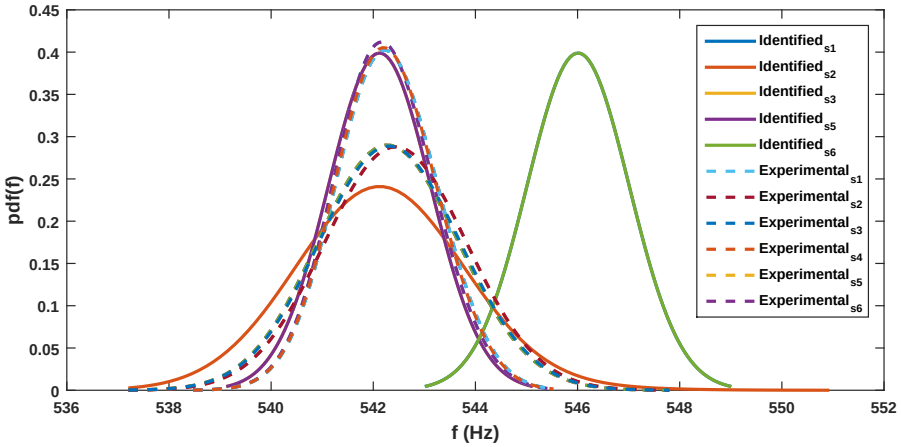

(n)

Figure 5.11: Comparison of pdf of identified and experimental cases for plate experiment for mode (a) 11 (b) 12 and (c) 14

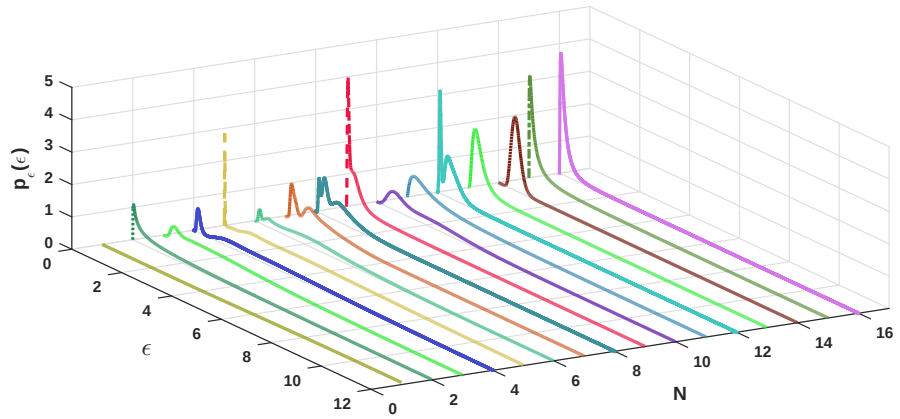

(a)

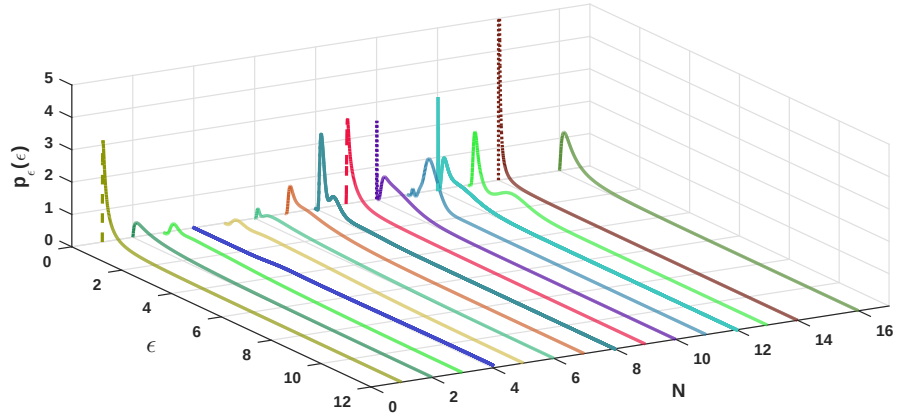

(b)

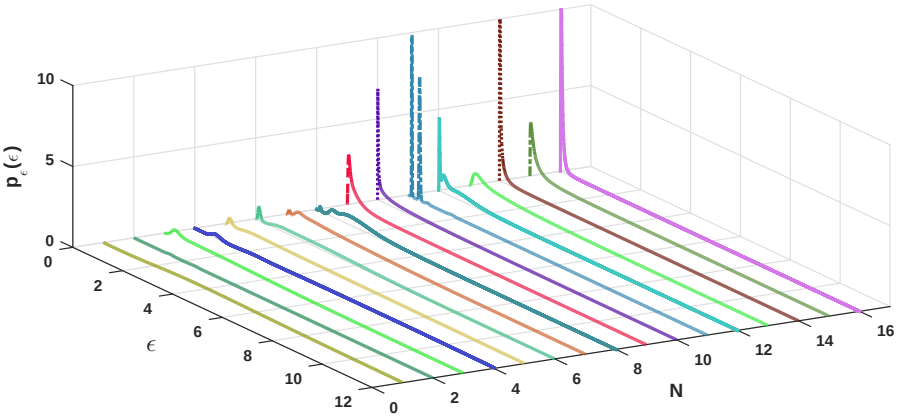

(c)

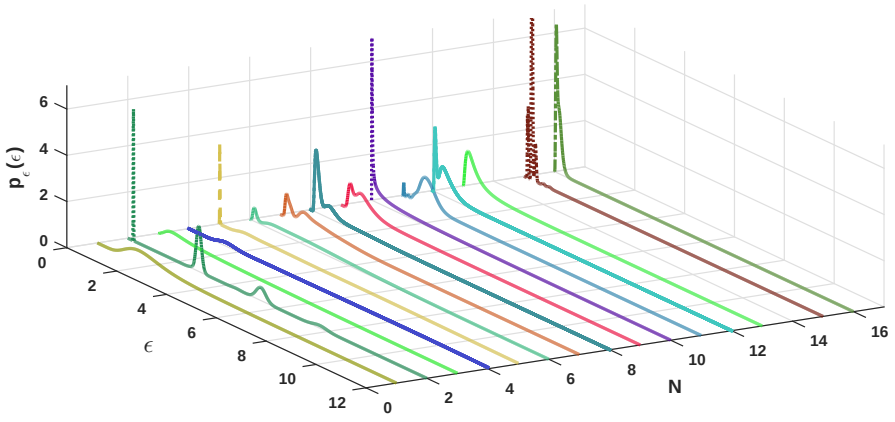

(d)

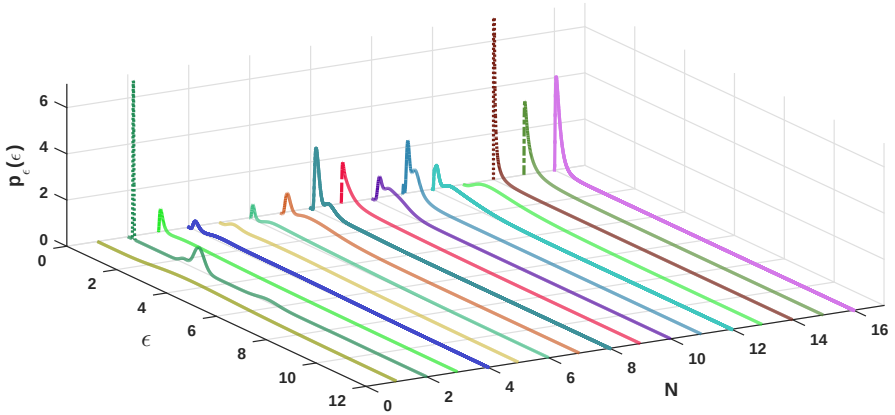

(e)

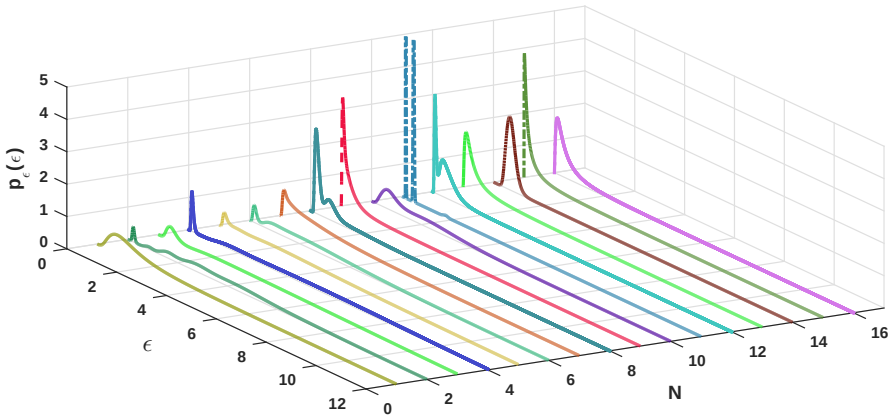

(f)

Figure 5.11: Probabilistic distribution function of error in frequency estimation for plate

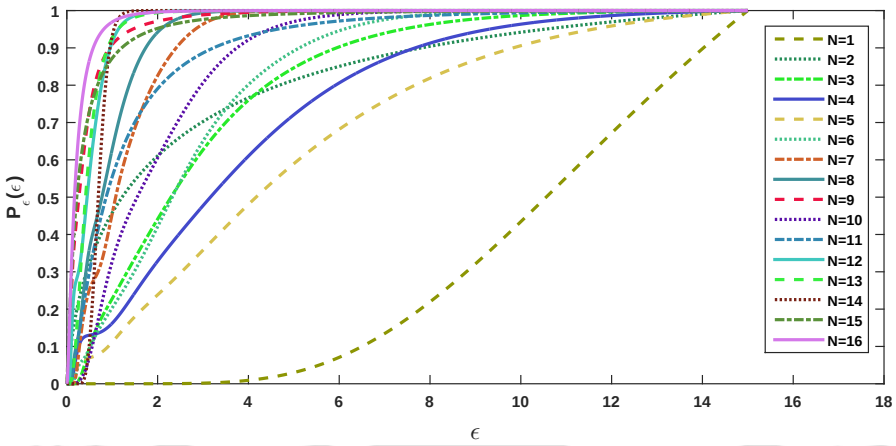

(a)

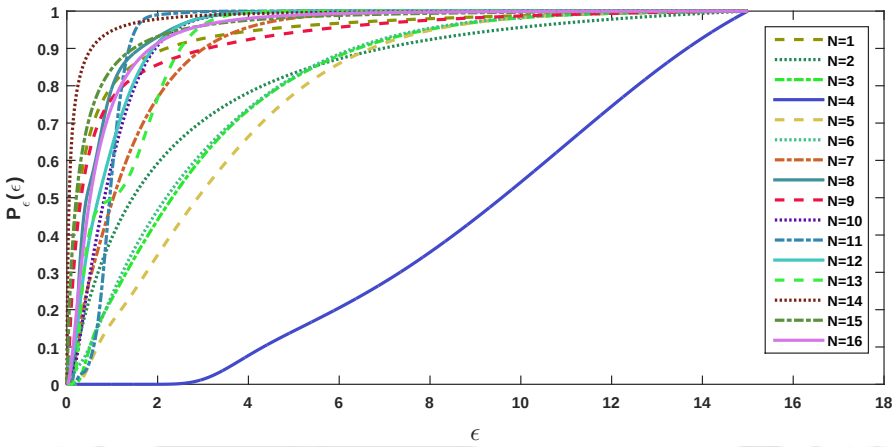

(b)

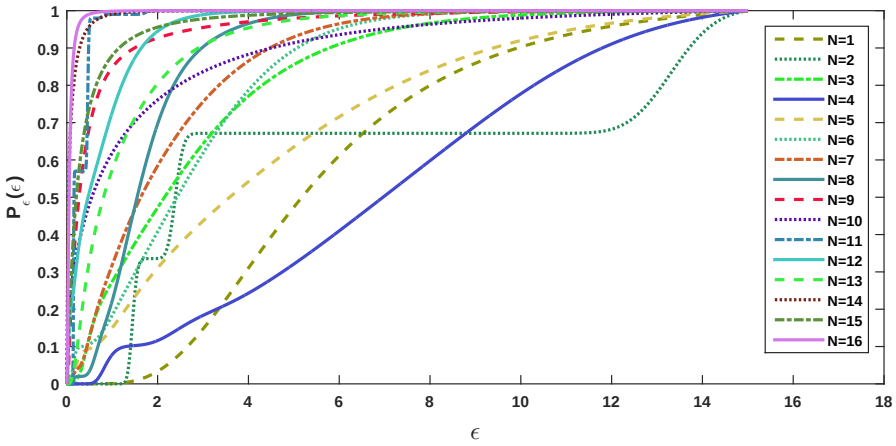

(c)

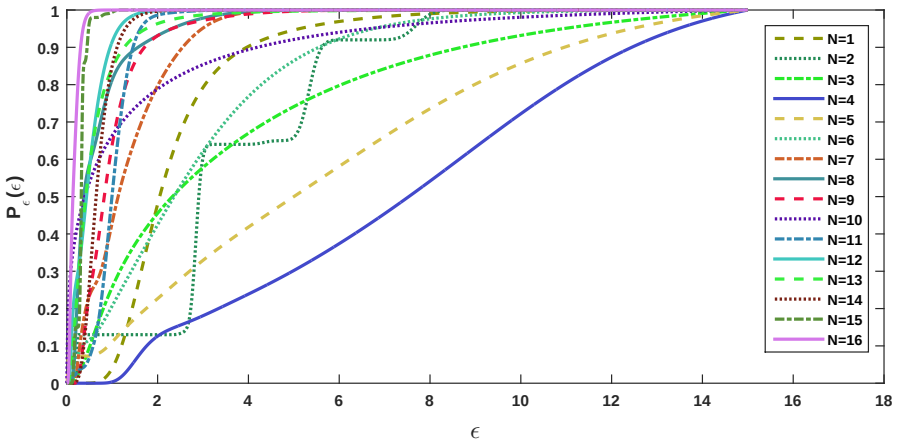

(d)

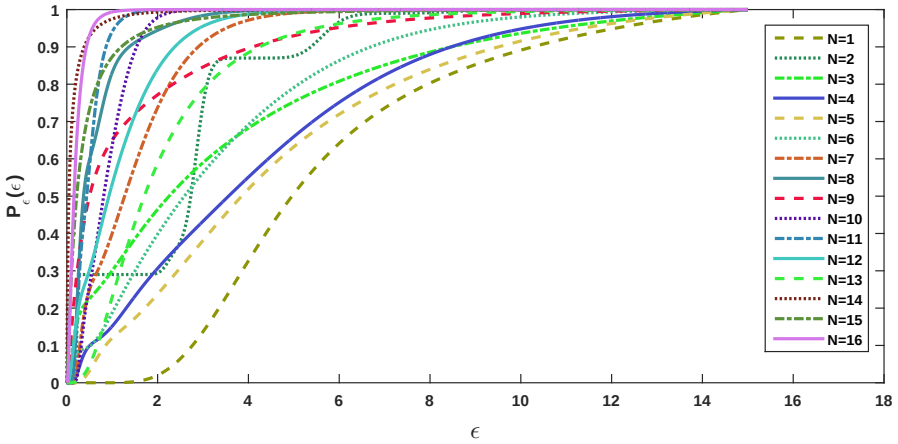

(e)

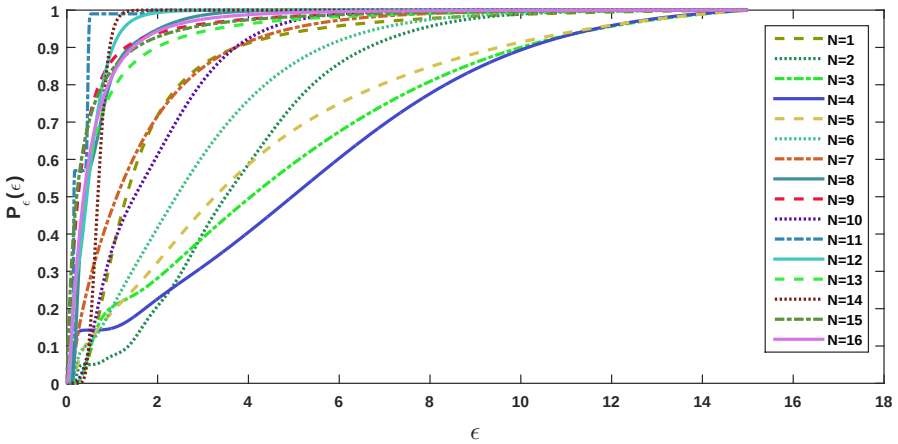

(f)

Figure 5.11: Detectability of frequencies using different sensors for plate

Table 5.2: Mean and standard deviation of identified frequencies for plate [sensor 1, 2 and 3]

Sensor 1				Sensor 2				Sensor 3			
μ		σ		μ		σ		μ		σ	
f_{exp}	f_{idf}	f_{exp}	f_{idf}	f_{exp}	f_{idf}	f_{exp}	f_{idf}	f_{exp}	f_{idf}	f_{exp}	f_{idf}
14.26	12.22 [14.29]	0.441	0.270	14.09	13.97 [0.85]	0.288	0.020	14.08	13.30 [5.55]	0.273	0.119
38.27	39.07 [2.10]	0.790	0.164	38.29	38.79 [1.30]	0.782	0.216	38.39	30.21 [21.31]	0.840	1.265
55.77	56.28 [0.91]	1.681	0.001	55.70	56.21 [0.92]	1.720	0.440	55.74	56.25 [0.92]	1.606	0.168
59.60	60.94 [2.25]	2.045	0.439	59.35	65.39 [10.17]	1.971	0.001	59.50	63.58 [6.85]	2.013	0.354
82.23	84.02 [2.17]	2.964	3.037	82.53	83.38 [1.03]	2.911	0.120	82.25	85.16 [3.54]	2.986	0.121
93.96	93.70 [0.28]	2.621	1.269	94.05	93.26 [0.84]	2.622	1.580	94.05	94.13 [0.09]	2.717	0.067
146.88	146.63 [0.17]	2.051	0.211	147.03	147.66 [0.43]	2.172	0.528	147.03	149.79 [1.88]	2.153	0.000
185.36	184.28 [0.58]	1.528	0.001	185.44	185.59 [0.08]	1.696	0.132	185.15	188.26 [1.68]	1.533	0.134
242.35	241.76 [0.24]	1.395	0.172	241.00	241.76 [0.31]	4.003	0.172	242.07	241.76 [0.13]	2.520	0.172
286.10	291.14 [1.76]	2.642	0.001	286.15	284.96 [0.41]	2.713	0.001	286.02	289.09 [1.07]	2.975	0.207
318.83	321.75 [0.92]	0.911	0.229	318.72	321.77 [0.96]	0.877	0.001	318.70	319.48 [0.25]	0.893	0.001
344.86	345.56 [0.20]	1.781	0.346	345.25	348.01 [0.80]	1.783	0.738	345.20	343.15 [0.59]	1.820	0.001
485.08	486.98 [0.39]	0.800	0.347	489.28	483.55 [1.17]	3.985	0.001	490.04	487.02 [0.62]	5.189	0.001
542.22	546.01 [0.70]	0.484	0.001	542.30	542.16 [0.03]	0.541	0.389	542.28	542.12 [0.03]	0.514	0.001
631.40	629.90 [0.24]	0.551	0.001	631.31	629.90 [0.22]	0.526	0.533	631.33	629.90 [0.23]	0.533	0.001
717.65	716.36 [0.18]	0.687	0.001	717.68	721.44 [0.52]	0.618	0.514	716.04	716.36 [0.04]	0.400	0.001

[% error shown in parentheses]

Table 5.3: Mean and standard deviation of identified frequencies for plate [sensor 4, 5 and 6]

Sensor 4				Sensor 5				Sensor 6			
μ		σ		μ		σ		μ		σ	
f_{exp}	f_{idf}	f_{exp}	f_{idf}	f_{exp}	f_{idf}	f_{exp}	f_{idf}	f_{exp}	f_{idf}	f_{exp}	f_{idf}
14.10	14.27 [1.22]	0.302	0.010	14.24	13.39 [5.94]	0.429	0.120	14.09	14.16 [0.52]	0.288	0.060
38.28	36.94 [3.49]	0.830	0.274	38.29	39.07 [2.03]	0.808	0.191	38.22	38.28 [0.16]	0.848	1.372
55.73	57.45 [3.08]	1.669	0.340	55.55	57.01 [2.64]	1.789	0.500	55.70	58.21 [4.51]	1.726	0.623
59.53	64.00 [7.51]	2.062	0.001	60.10	62.16 [3.43]	1.726	0.247	60.10	63.12 [5.02]	1.784	0.192
82.55	87.03 [5.42]	2.883	0.062	82.50	84.63 [2.59]	2.876	3.008	82.60	84.86 [2.73]	2.981	2.749
93.82	92.80 [1.09]	2.728	0.164	94.16	92.14 [2.14]	2.770	0.001	93.91	92.80 [1.18]	2.749	0.001
147.12	146.61 [0.34]	2.148	0.001	147.13	145.55 [1.07]	1.846	0.146	147.32	148.66 [0.91]	2.233	0.444
185.28	185.59 [0.17]	1.676	0.132	185.31	185.59 [0.15]	1.555	0.132	185.33	185.60 [0.15]	1.551	0.000
242.39	240.05 [0.96]	1.588	0.001	243.84	241.76 [0.85]	3.866	0.172	242.13	241.81 [0.13]	2.228	0.348
285.70	282.94 [0.97]	3.020	0.001	286.05	287.01 [0.34]	2.476	0.001	286.23	291.14 [1.72]	2.711	0.001
318.58	321.75 [0.99]	1.027	0.229	318.65	317.21 [0.45]	0.903	0.001	318.74	319.48 [0.23]	0.906	0.001
344.92	345.61 [0.20]	1.710	0.001	344.05	340.70 [0.97]	2.787	0.001	344.87	345.63 [0.22]	1.790	0.248
485.12	486.98 [0.38]	1.305	0.347	495.51	487.02 [1.71]	1.307	0.001	486.39	483.55 [0.58]	3.025	0.001
542.44	542.12 [0.06]	0.556	0.552	542.33	542.12 [0.04]	0.552	0.001	542.26	546.01 [0.69]	0.505	0.001
630.20	629.94 [0.04]	2.089	0.452	631.39	629.90 [0.24]	0.549	0.001	631.37	629.94 [0.23]	0.544	0.452
717.41	716.36 [0.15]	0.637	0.001	717.55	716.36 [0.17]	0.642	0.001	718.74	721.44 [0.38]	1.021	0.514

[% error shown in parentheses]

5.3 Summary

In this chapter, the uncertainty associated with random eigen value problems are detected and compared with experimental values. For this purpose, two different experimental results are presented here to prove the efficiency of the proposed algorithm. Results show that the mean value of the modes can be detected satisfactorily. Besides, mean modal frequency detection, probability of detection of a particular mode from a particular sensor is also studied. It shows that the probability of detection varies from sensor to sensor which can be useful for optimal sensor placement. Together these results (i.e. beam and plate) establish the fact that proposed automated identification strategy is both accurate and efficient that needs no user intervention as compared to the other time-frequency methods available in the literatures.

Chapter 6

Conclusion & Future Work

6.1 Conclusion

The final conclusions are drawn based on the numerical examples presented on the previous chapters. These are outlined section-wise below –

6.1.1 Adaptive HHT

In section 3.1.1, the study presents an adaptive filtering based HHT scheme to identify the modal parameters using the measured acceleration response due to multi-component earthquake excitations. For this purpose, an actual RC framed building is used as a test bed and the acceleration responses are measured at limited locations. From this analysis it can be concluded that –

- The proposed AHHT based time-frequency analysis can efficiently identify the modal parameters of LTI system. The band widths of the pre-filtering are adjusted in every iteration and the modal frequencies are obtained by applying HHT on the filtered signal. The iteration is stopped for a particular modal frequency if the difference in identified frequencies in two successive iteration is well within tolerance. In this context, a blind source separation is developed base on the instantaneous phase of the IMFs of signals from different sensors. The significance of the proposed AHHT is that it not only helps to avoid mode-mixing but also helps to identify the modal parameters without any prior knowledge of the input force and the system parameters.

- The identification strategy developed in Eq. (3.15) clearly shows that the mean slope represents the term $\eta_j \omega_{n_j}$ while the zero mean fluctuation at every time instant is due to the pulse train of an arbitrary input force. Thus the proposed HHT based model helps to extract modal

parameters from the response due to any arbitrary non-stationary multi-component earthquake ground motions as opposed other methods developed in the literature using impulse or ambient vibrations. Therefore, it is primarily effective for structural health monitoring immediately after any seismic event where further application of impulse or other excitation may not be permitted without knowing the status of the structure. With simple modification, the method is also applicable to check the tuning of the controller during and after any seismic event.

- From the numerical analysis, it can be revealed that the damping estimation from an arbitrary excitation is not very accurate. However, synthetic experiments show that damping can be accurately evaluated from the impulse response of the same structure. Therefore, once the other parameters are identified from the limited measurements and the status of the structural health is established, one can evaluate damping using known impulse load applied on the structure or ambient vibration.
- Although, limited measurements are used in this case, proposed AHHT based algorithm could identify all eight modal frequencies accurately from each measurement. However, the mode shape identification using the ratio of IMFs suffers a set-back due to limited measurements. To by-pass this problem, a FE model updating scheme is discussed. Here, the objective function is formulated in terms of the error between the eigen values obtained from AHHT algorithm and FE analysis. Once, the FE model is updated, complete mode shape can be obtained from the updated model.
- As the proposed method is tested using a full scale building response due to multi-component excitations, it can be easily executed for other lifeline structures. This will help in disaster management as the status of the structure can be easily established immediately after any seismic event if measurements are available. It is particularly useful to decide wether immediate occupancy of the structure is possible after earthquake as further testing on structure with known excitation involves time and cost. Hence, the proposed method is also effective from disaster management point of view when urgent decision making about the status of the structure receives paramount importance.

6.1.2 MEMD Based Method

In section 3.1.2, an adaptive multi-variate empirical mode decomposition is proposed to identify the modal parameters of linear structural systems. Although, the superiority of MEMD based time-frequency analysis has already been established in the literature, it still suffers mode-mixing in higher modes. To avoid this difficulty, the adaptive filtering scheme of the recorded response as discussed in AHHT are used to improve the performance of modal identification. The choice of band width for this purpose depends on the degree and extent of mode-mixing observed in

the decomposed IMFs. Examples considered for numerical study clearly show that the proposed adaptive MEMD scheme has excellent performance to identify the modal parameters (i.e. natural frequency, mode shape and modal damping) with significant level of accuracy.

6.1.3 WT-HT Based Technique

In section 3.2, a combined Wavelet-Hilbert transform based signal processing is implemented for modal identification. The main observations from this study are as follows –

- CWT based filters are designed to locate energy concentration in the responses which correspond to either structural mode or the frequency of the input excitation. It is shown that this filtered signal exactly matches with the IMFs obtained using modified version of HHT. This, in term, bypass the heuristic time consuming estimation of IMF evaluation using EMD. To the best of authors knowledge, nobody has reported this feature of CWT earlier.
- Once the filtered signals corresponding to each mode are obtained, Hilbert transform is used on these filtered signals to identify the instantaneous frequencies and phases. In this context, the modal frequencies are separated from the excitation frequencies, if any, by comparing the instantaneous phases obtained from different sensors. The process of the CWT based filtering and subsequent modal frequency estimation is continued iteratively using sub-band coding similar to wavelet packet transformation until the convergence in parameter estimation is achieved. The proposed identification scheme can detect closely spaced modes even when the energy content is low. Here, the compact supports of MLP basis function offer leakage free filtering which helps to accurately locate the closely spaced modal frequencies, if any. This unique feature of the MLP based filters coupled with Hilbert transform is implemented to identify modal parameters of bridge.
- It is shown that the present identification technique is superior than conventional technique like NExT-ERA in terms of the number of identified modes and accuracy. The modal damping estimated by the proposed scheme is also very accurate as shown using synthetic experiments. Finally, the large number of modal frequencies obtained from the proposed method helps to update the FE model for accurate estimation of the mode shapes.

6.1.4 SST Based Method

A combined synchrosqueezed wavelet transform and unsupervised k-means clustering is used in this study to identify modal parameters. Here, the synchrosqueezing offers better frequency resolution while k-means clustering based machine learning helps to segregate the frequency localization without any intermittency with the user. The proposed identification strategy is applied on different

engineering problems to demonstrate its efficiency and accuracy. The major observations from this study are as follows -

- Wavelet transformation has proved to be an efficient tool for modal identification. However, wavelet coefficients alone fail to pinpoint the modal frequency as shown in different scalograms and demand either user interface (which is often subjective) or additional mathematical improvisation for efficient frequency tracking. The second option is utilized in two steps here - i) improving frequency resolution by synchrosqueezing and ii) clustering based identification of energy concentration in different scales.
- Synchrosqueezing operates over the wavelet coefficients to improve the clarity of the scalogram (i.e. better resolution) and hence, it also bears the same characteristics of the wavelet scalogram except narrowing the frequency bands that contain signal energy.
- k-means clustering can efficiently identify the energy localization without any user intervention. However, this may provide frequencies that do not correspond to the modal vibration which, in the proposed technique, are detected using phase portrait. This involves inverse synchrosqueezed transformation of the coefficients in the clusters identified by the k-means algorithm. Once the modal frequencies are identified, modal damping ratio can also be traced using any standard algorithm (e.g. NExT).
- Different numerical applications demonstrated in this study prove that the proposed algorithm works efficiently for large class of linear problems. In particular, the second and third examples demonstrate that large number of modal frequencies often observed in the civil and mechanical vibrations can be effectively traced. In this context, it may be noted that different basis functions (e.g. complex morlet, lognormal, generalized morse) offer the same quality of the end result. Hence, either of them can be adopted for frequency tracking.

In general, the proposed synchrosqueezed wavelet transformation based clustering technique has proved to be an effective identification tool that can be adopted in vibration based system identification. The numerical results clearly show its accuracy in different civil and mechanical problems. This algorithm can be easily adopted for damage detection and real-time frequency tracking for control problems.

6.1.5 Modal Identification of Uncertain System

Finally in section 5.2, synchrosqueezed transformation based OMA of random dynamical systems are demonstrated to identify the probabilistic description of the modal frequencies. The efficiency and effectiveness of this method are discussed with the help of laboratory test data. Based on the numerical results presented in this section, following conclusions are drawn –

- Here, an outline is proposed to quantify the uncertainty associated with the modal frequencies from the recorded acceleration responses. The proposed method is able to measure the probability distribution function associated with a particular mode. It is shown that the sensor locations affect the detectibility of a particular mode. This is due to the proximity of the sensor to the zero crossing of the modal vibration.

- The proposed approach for random eigen value problem is efficient enough to capture small variation in the natural frequencies. Thus, it enables to evaluate the probability distribution function (pdf) of the natural frequencies without any prior knowledge of the structure and the input excitation. However, in the present study, major emphasis is given to identify the frequencies in mean sense as the actual distribution of random eigen frequencies are unknown.

- As the proposed method does not require any training data or pre-tuning for a problem, this method has wider scope for inverse parameter estimation of large class of systems. As it can effectively detect modal frequencies with very small error, it can be easily incorporated for damage identification of a dynamic system.

6.2 Future Work

In this section, possible avenues for further extension of the proposed methodologies are enumerated below –

- The proposed methodologies can be extended for optimal sensor number and their location for better observability. It needs coupling with finite element model updating for the optimization of sensor placement. This will also enable the designer also to locate the optimal actuator placement for efficient control.

- This thesis is focused on the OMA of actual structures using recorded forced response. The direct application of this study can be the health assessment or retrofitting of the civil or mechanical systems. In this process, the change in modal parameters (i.e. damage), if any, can be detected/quantified which can be utilized for further decision making for maintenance.

- The proposed modal parameter estimation combined with finite element model updating can be used for bridge rating. The accurate in-situ health assessment of the bridge can help the designer to plan for the maintenance schedule and strengthening measures, if any within its operational service.

- The proposed algorithms for tracking modal frequencies in online and/or offline can be used for vibration control. While offline tracking of frequency helps the designer to tune the

passive controller for similar future inputs, online tracking can be directly used as feedback for tuning the actuators for optimal control.

- Besides vibration control problems, these methodologies can be extended for energy harvesting where the harvester can be tuned to dominant mode (in real time). This can help to optimize the output of an energy harvester.
- The present work is focused on the modal parametric identification of linear structures. This can be extended for nonlinear parametric identification. The change in structural parameters or damage can exhibit different nonlinearities which can be identified. Besides damage induced nonlinearity, proposed methodology can be used to detect nonlinear normal modes.

Appendix A

FE Model Updating and Modal Correlation Analysis

A overview of the FE model updating is presented here. Reader may refer Friswell & Mottershed [172] for the details of this technique. Among various methods available in the literature [172, 173], direct model updating is the one which prescribes parameter updating on the basis of the modal information available from the experiment. In this approach, first the modal parameters of the structure are obtained from system identification. An objective function is then developed based on the error between the modal parameters obtained from OMA and FE model. The error function (i.e. weighted Euclidean norm between the eigen values $\mathbf{\Lambda}$) is then minimized to obtain the optimized FE model w.r.t the experimental observations. The objective function along with the constrained conditions are as follows

$$\begin{aligned} J &= \|\mathbf{W}(\mathbf{\Lambda}_{FE} - \mathbf{\Lambda}_{SI})\| \\ &= \sum_{i=1}^{l}\sum_{k=1}^{n}\left[\sum_{r=1}^{l}\mathbf{W}_{ir}\left(\mathbf{\Lambda}_{FErk} - \mathbf{\Lambda}_{SIrk}\right)\right]^2 \end{aligned} \tag{A.1}$$

subject to the constrained conditions

$$\mathbf{\Phi}^T\mathbf{M}\mathbf{\Phi} = \mathbf{I} \tag{A.2a}$$

$$\mathbf{K}^T = \mathbf{K} \tag{A.2b}$$

$$\mathbf{K}\Phi = \mathbf{M}\mathbf{\Phi}\mathbf{\Lambda} \tag{A.2c}$$

Here, l and n represent the observed mode from experiment and that in the FE model. Here, it may be noted that the accuracy of the model updating increases with the increased number of the modes observed from the experimental identification. However, optimization of FE model does not ensure unique global solution but often provides multiple local minima (i.e. different combinations of $\mathbf{M}$

and **K** matrices), all of them leading to the same observed natural frequencies from the experiment [172]. To identify the actual state of the structure, mass matrix **M** is assumed to be known as the geometry and the material property used in construction can be estimated accurately for all practical purpose. Furthermore, mass of a structure is less affected by damage and weathering as compared to stiffness and damping. Thus, using the known values **M**, optimum **K** is identified and the mode shapes for the complete structure are obtained from the eigen analysis of **M** and the updated **K** matrices. Finally, the modal assurance criteria (MAC) [174] is verified which is widely recommended in the literatures. Mathematical expression of MAC for p^{th} analytical mode (i.e. $\boldsymbol{\phi}_{Ap}$) and q^{th} experimental mode (i.e. $\boldsymbol{\phi}_{Eq}$) is as follows

$$MAC = \frac{|\boldsymbol{\phi}_{Ap}^T \boldsymbol{\phi}_{Eq}|^2}{\boldsymbol{\phi}_{Ap}^T \boldsymbol{\phi}_{Ap} \boldsymbol{\phi}_{Eq}^T \boldsymbol{\phi}_{Eq}} \tag{A.3}$$

MAC values close to unity is considered ideal. However, values ranging from 0.95 to 1.00 are assumed to be acceptable for all practical purpose [175].

Appendix B

Equivalent Strut Model for Brick Infills

Here, the description of equivalent strut model for the infill of a framed structure is presented. The BRNS building used in this study has brick infill wall. This brick infill provides significant stiffness to the framed structures [160, 176]. The stiffness of these infills can be modeled by strut members which act in compression only [refer Fig. 4.24(a)]. The stiffness of the strut is given by

$$K_i = R\frac{AE_i}{L_e} \tag{B.1}$$

where, R is reduction factor for opening in the wall. Here, for practical reason the reduction factor is considered as 0.7 [160]. A and E_i represent the cross section area of the strut and Young's modulus of the infill material respectively. The effective length of the strut is denoted by L_e. E_i can be evaluated from the material properties while the area and effective length can be calculated as below

$$A = W_i t \tag{B.2a}$$

$$L_e = \sqrt{H_i^2 + L_i^2} \tag{B.2b}$$

In the above equation, W_i and t represent the width and thickness of the equivalent strut respectively. The height and length of the infill wall is represented by H_i and L_i respectively. All the above mention parameters can be measured physically from the structural drawing except the strut width. The equivalent strut width can be obtained from the following equation

$$W_i = 0.175(\lambda_i H)^{-0.4}\sqrt{H^2 + L^2} \tag{B.3}$$

where, H and L are the height and length of the frame respectively and λ_i is parameter which given below

$$\lambda_i = \sqrt[4]{\left[E_i t \sin 2\theta\right]\left[4E_c I_c H_i\right]^{-1}} \tag{B.4}$$

Column's Young's modulus and modulus of inertia are represented by E_c and I_c respectively while θ denotes the direction of the diagonal strut and it calculated as bellow

$$\theta = \tan^{-1}\left(\frac{H}{L}\right) \tag{B.5}$$

Following the above formulations, the stiffness matrix of BRNS building is calculated as below

$$[\mathbf{K}]_{xy} = \begin{bmatrix} 360593181.6 & 0 & -230377923.7 & 0 \\ 0 & 0 & 542937172.6 & 0 \\ -230377923.7 & 0 & 460755847.5 & 0 \\ 0 & -344149171.6 & 0 & 688298343.3 \\ 0 & 0 & -230377923.7 & 0 \\ 0 & 0 & 0 & -344149171.6 \\ 0 & 0 & 0 & 0 \\ 0 & 0 & 0 & 0 \end{bmatrix}$$

$$\begin{bmatrix} 0 & 0 & 0 & 0 \\ -344149171.6 & 0 & 0 & 0 \\ -230377923.7 & 0 & 0 & 0 \\ 0 & -344149171.6 & 0 & 0 \\ 360593181.6 & 0 & -130215257.9 & 0 \\ 0 & 542937172.6 & 0 & -198788001.0 \\ -130215257.9 & 0 & 130215257.9 & 0 \\ 0 & -198788001.0 & 0 & 198788001.0 \end{bmatrix} N/m \tag{B.6}$$

Corresponding to the stiffness matrix, the mass matrix of the BRNS building is calculated from the geometry provided in Fig. 3.2 and it is given below

$$[\mathbf{M}]_{xy} = \begin{bmatrix} 27636.97 & 0 & 0 & 0 & 0 & 0 & 0 & 0 \\ 0 & 27636.97 & 0 & 0 & 0 & 0 & 0 & 0 \\ 0 & 0 & 25618.62 & 0 & 0 & 0 & 0 & 0 \\ 0 & 0 & 0 & 25618.62 & 0 & 0 & 0 & 0 \\ 0 & 0 & 0 & 0 & 25618.62 & 0 & 0 & 0 \\ 0 & 0 & 0 & 0 & 0 & 25618.62 & 0 & 0 \\ 0 & 0 & 0 & 0 & 0 & 0 & 17805.66 & 0 \\ 0 & 0 & 0 & 0 & 0 & 0 & 0 & 17805.66 \end{bmatrix} kG \tag{B.7}$$

Appendix C

Wavelet Based Non-stationary Response Characterization

Let us consider a single degree of freedom system driven by non-stationary excitation which can be modeled by amplitude modulated stationary process as follows

$$m\ddot{x}(t) + c\dot{x}(t) + kx(t) = f(t) = A(t)W_h(t) = \sum_i A_i\delta(t - t_i)W_h(t) \tag{C.1}$$

On wavelet transforming both sides of Eq. C.1 leads to the following form

$$m\frac{\partial^2}{\partial b^2}W_\psi x(a,b) + c\frac{\partial}{\partial b}W_\psi x(a,b) + kW_\psi x(a,b) = W_\psi f(a,b) = A(b)W_\psi W_h(a,b) \tag{C.2}$$

Thus, the response due to non-stationary pulse train can be expressed as

$$\begin{aligned} W_\psi x(a,b) &= \int_0^b \frac{1}{m\omega_d} e^{-\eta\omega_n(b-\tau)} sin(\omega_d(b-\tau)) \sum_i A_i\delta(\tau - b_i)W_\psi W_h(a,\tau)d\tau \\ &= \frac{1}{m\omega_d}\sum_i A_i e^{-\eta\omega_n(b-b_i)} sin(\omega_d(b-b_i))W_\psi W_h(a,b_i) \end{aligned} \tag{C.3}$$

Considering two time instances [i.e. b_1 & b_2 in wavelet domain] the second order response statistics can be expressed as

$$\begin{aligned} E[W_\psi x(a,b_1), W_\psi x(a,b_2)] = E\Bigg[&\left\{\frac{1}{m\omega_d}\sum_i A_i e^{-\eta\omega_n(b_1-b_i)} sin(\omega_d(b_1-b_i))W_\psi W_h(a,b_i)\right\}. \\ &\left\{\frac{1}{m\omega_d}\sum_j A_j e^{-\eta\omega_n(b_2-b_j)} sin(\omega_d(b_2-b_j))W_\psi W_h(a,b_j)\right\}\Bigg] \end{aligned} \tag{C.4}$$

Above equation can be simplified in the following form

$$E[W_\psi x(a,b_1), W_\psi x(a,b_2)] = \left\{\frac{1}{m\omega_d}\right\}^2 \sum_i \sum_j A_i A_j e^{-\eta\omega_n(b_1+b_2-b_i-b_j)} sin(\omega_d(b_1-b_i))sin(\omega_d(b_2-b_j))E[W_\psi W_h(a,b_i)W_\psi W_h(a,b_j)] \tag{C.5}$$

For the special case when, $b_1 = b_2$ and $i = j$, one can evaluate the instantaneous energy of the non-stationary response $x(t)$.

Bibliography

[1] H. Li, J. Ou, The state of the art in structural health monitoring of cable-stayed bridges, Journal of Civil Structural Health Monitoring 6 (1) (2016) 43–67.

[2] J. M. Ko, Y. Q. Ni, Technology developments in structural health monitoring of large-scale bridges, Engineering Structures 27 (12) (2005) 1715–1725.

[3] F. N. Catbas, M. Susoy, D. M. Frangopol, Structural health monitoring and reliability estimation: Long span truss bridge application with environmental monitoring data, Engineering Structures 30 (9) (2008) 2347–2359.

[4] T. Nishikawa, J. Yoshida, T. Sugiyama, Y. Fujino, Concrete crack detection by multiple sequential image filtering, Computer Aided Civil and Infrastructure Engineering 27 (1) (2012) 29–47.

[5] S. Park, H. Park, J. Kim, H. Adeli, 3D displacement measurement model for health monitoring of structures using a motion capture system, Measurement 59 (2015) 352–362.

[6] Q. Han, J. Xu, A. Carpinteri, G. Lacidogna, Localization of acoustic emission sources in structural health monitoring of masonry bridge, Structural Control and Health Monitoring 22 (2) (2015) 314–329.

[7] S. W. Doebling, C. R. Farrar, M. B. Prime, A summary review of vibration-based damage identification methods, Shock and Vibration Digest 30 (2) (1998) 91–105.

[8] S. Das, P. Saha, S. Patro, Vibration-based damage detection techniques used for health monitoring of structures: a review, Journal of Civil Structural Health Monitoring 1–31.

[9] S. W. Doebling, C. R. Farrar, M. B. Prime, D. W. Shevitz, Damage identification and health monitoring of structural and mechanical systems from changes in their vibration characteristics: a literature review, Los Alamos National Laboratory Report LA-13070-MS USA.

[10] B. Peeters, G. De Roeck, Reference-based stochastic subspace identification for output-only modal analysis, Mechanical systems and signal processing 13 (6) (1999) 855–878.

[11] C.-H. Loh, K. J. Loh, Y.-S. Yang, W.-Y. Hsiung, Y.-T. Huang, Vibration-based system identification of wind turbine system, Structural Control and Health Monitoring 24 (3) (2017) e1876.

[12] A. Chakraborty, B. Basu, M. Mitra, Identification of modal parameters of a mdof system by modified l–p wavelet packets, Journal of Sound and Vibration 295 (3) (2006) 827–837.

[13] A. Chakraborty, B. Basu, Analysis of frequency nonstationarity via continuous wavelet transform in the response of primary-secondary systems, Journal of structural engineering 136 (12) (2010) 1608–1612.

[14] S. Nagarajaiah, B. Basu, Output only modal identification and structural damage detection using time frequency & wavelet techniques, Earthquake Engineering and Engineering Vibration 8 (4) (2009) 583–605.

[15] N. E. Huang, Z. Shen, S. R. Long, M. C. Wu, H. H. Shih, Q. Zheng, N.-C. Yen, C. C. Tung, H. H. Liu, The empirical mode decomposition and the hilbert spectrum for nonlinear and non-stationary time series analysis, Proceedings of the Royal Society of London A: Mathematical, Physical and Engineering Sciences 454 (1971) (1998) 903–995.

[16] E. S. Carbajo, R. S. Carbajo, C. Mc Goldrick, B. Basu, Asdah: An automated structural change detection algorithm based on the hilbert–huang transform, Mechanical Systems and Signal Processing 47 (1) (2014) 78–93.

[17] S. Mahato, M. V. Teja, A. Chakraborty, Combined wavelet–hilbert transform-based modal identification of road bridge using vehicular excitation, Journal of Civil Structural Health Monitoring 7 (1) (2017) 29–44.

[18] Y. Yang, S. Nagarajaiah, Dynamic imaging: real-time detection of local structural damage with blind separation of low-rank background and sparse innovation, Journal of Structural Engineering 142 (2) (2015) 04015144.

[19] Y. Yang, C. Dorn, T. Mancini, Z. Talken, S. Nagarajaiah, G. Kenyon, C. Farrar, D. Mascareñas, Blind identification of full-field vibration modes of output-only structures from uniformly-sampled, possibly temporally-aliased (sub-nyquist), video measurements, Journal of Sound and Vibration 390 (2017) 232–256.

[20] Y. Yang, S. Nagarajaiah, Blind denoising of structural vibration responses with outliers via principal component pursuit, Structural Control and Health Monitoring 21 (6) (2014) 962–978.

[21] R. Jangid, Optimum Multiple Tuned Mass Dampers for base-excited undamped system, Earthquake engineering & structural dynamics 28 (9) (1999) 1041–1049.

[22] S. Ali, A. Ramaswamy, Optimal dynamic inversion-based semi-active control of benchmark bridge using MR dampers, Structural Control and Health Monitoring 16 (5) (2009) 564–585.

[23] S. Gur, S. K. Mishra, S. Chakraborty, Performance assessment of buildings isolated by shape-memory-alloy rubber bearing: Comparison with elastomeric bearing under near-fault earthquakes, Structural Control and Health Monitoring 21 (4) (2014) 449–465.

[24] I. Talebinejad, C. Fischer, F. Ansari, Numerical evaluation of vibration-based methods for damage assessment of cable-stayed bridges, Computer-Aided Civil and Infrastructure Engineering 26 (3) (2011) 239–251.

[25] P. F. Silva, N. J. Ereckson, G. D. Chen, Seismic retrofit of bridge joints in central us with carbon fiber-reinforced polymer composites, ACI structural journal 104 (2) (2007) 207.

[26] J. Brownjohn, K.-Y. Koo, C. Basagiannis, A. Alskif, A. Ngonda, Vibration monitoring and condition assessment of the university of sheffield arts tower during retrofit, Journal of Civil Structural Health Monitoring 3 (3) (2013) 153–168.

[27] E. Reynders, System identification methods for (operational) modal analysis: review and comparison, Archives of Computational Methods in Engineering 19 (1) (2012) 51–124.

[28] B. Peeters, G. De Roeck, Stochastic system identification for operational modal analysis: a review, Journal of Dynamic Systems, Measurement, and Control 123 (4) (2001) 659–667.

[29] G. P. Cimellaro, S. Piantà, A. De Stefano, Output-only modal identification of ancient L'Aquila city hall and civic tower, Journal of Structural Engineering 138 (4) (2011) 481–491.

[30] J. M. W. Brownjohn, F. Magalhaes, E. Caetano, A. Cunha, Ambient vibration re-testing and operational modal analysis of the Humber Bridge, Engineering Structures 32 (8) (2010) 2003–2018.

[31] J. H. Macdonald, W. E. Daniell, Variation of modal parameters of a cable-stayed bridge identified from ambient vibration measurements and fe modelling, Engineering Structures 27 (13) (2005) 1916–1930.

[32] J. C. Asmussen, Modal analysis based on the Random Decrement Technique - Application to civil enegineing structures, Ph.D. thesis, Aalborg University, Department of Building Technology and Structural Engineering (1997).

[33] J. Juang, R. Pappa, An eigensystem realization algorithm for modal parameter identification and model reduction, Journal of Guidance, Control, and Dynamics 8 (5) (1985) 620–627.

[34] P. Andersen, R. Brincker, P. H. Kirkegaard, Theory of covariance equivalent armav models of civil engineering structures, Tech. rep., Dept. of Building Technology and Structural Engineering, Aalborg University (1995).

[35] F. Ubertini, C. Gentile, A. L. Materazzi, Automated modal identification in operational conditions and its application to bridges, Engineering Structures 46 (0) (2013) 264 – 278.

[36] D. M. Siringoringo, Y. Fujino, System identification of suspension bridge from ambient vibration response, Engineering Structures 30 (2) (2008) 462–477.

[37] Y. Yang, S. Nagarajaiah, Time-frequency blind source separation using independent component analysis for output-only modal identification of highly damped structures, Journal of Structural Engineering 139 (10) (2012) 1780–1793.

[38] Y. Yang, S. Nagarajaiah, Blind modal identification of output-only structures in time-domain based on complexity pursuit, Earthquake Engineering & Structural Dynamics 42 (13) (2013) 1885–1905.

[39] Y. Yang, S. Nagarajaiah, Output-only modal identification with limited sensors using sparse component analysis, Journal of Sound and Vibration 332 (19) (2013) 4741–4765.

[40] Y. Yang, S. Nagarajaiah, Blind identification of damage in time-varying systems using independent component analysis with wavelet transform, mechanical systems and signal processing 47 (1) (2014) 3–20.

[41] F. Magalhães, Á. Cunha, E. Caetano, R. Brincker, Damping estimation using free decays and ambient vibration tests, Mechanical Systems and Signal Processing 24 (5) (2010) 1274–1290.

[42] J. T. Huffman, F. Xiao, G. Chen, J. L. Hulsey, Detection of soil-abutment interaction by monitoring bridge response using vehicle excitation, Journal of Civil Structural Health Monitoring 5 (4) (2015) 389–395.

[43] F. Benedettini, M. Dilena, A. Morassi, Vibration analysis and structural identification of a curved multi-span viaduct, Mechanical Systems and Signal Processing 54 (2015) 84–107.

[44] J. N. Juang, R. S. Pappa, An eigensystem realization algorithm for modal parameter identification and model reduction, Journal of guidance, control and dynamics 8 (5) (1985) 620–627.

[45] G. H. James, T. G. Carne, J. P. Lauffer, The natural excitation technique (next) for modal parameter extraction from operating structures, Modal Analysis 10 (4) (1995) 260–277.

[46] P. Van Overschee, B. L. R. De Moor, Subspace identification for linear systems: theory, implementation, applications, Vol. 3, Kluwer academic publishers Dordrecht, 1996.

[47] N. M. M. Maia, J. M. M. Silva, Modal analysis identification techniques, Philosophical Transactions of the Royal Society of London. Series A: Mathematical, Physical and Engineering Sciences 359 (1778) (2001) 29–40.

[48] W. J. Staszewski, A. N. Robertson, Time–frequency and time–scale analyses for structural health monitoring, Philosophical Transactions of the Royal Society of London A: Mathematical, Physical and Engineering Sciences 365 (1851) (2007) 449–477.

[49] M. Feldman, Hilbert transform applications in mechanical vibration, John Wiley & Sons, 2011.

[50] N. E. Huang, Z. Shen, S. R. Long, M. C. Wu, H. H. Shih, Q. Zheng, N. C. Yen, C. C. Tung, H. Liu, The Empirical Mode Decomposition and Hilbert spectrum for nonlinear and nonstationary time series analysis, Proceedings of the Royal Society of London 454 (1998) 903–995.

[51] J. N. Yang, Y. Lei, S. Pan, N. Huang, System identification of linear structures based on Hilbert Huang spectral analysis. part 1: normal modes, Earthquake Engng Struct. Dyn. 32 (9) (2003) 1443–1467.

[52] J. N. Yang, Y. Lei, S. Lin, N. Huang, Identification of natural frequencies and dampings of in-situ tall buildings using ambient wind vibration data, Journal of Engineering Mechanics 130 (5) (2004) 570–577.

[53] S. Nagarajaiah, N. Varadarajan, Short time Fourier transform algorithm for wind response control of buildings with variable stiffness TMD, Engineering Structures 27 (2005) 431–441.

[54] S. Narasimhan, S. Nagarajaiah, A STFT semiactive controller for base isolated buildings with variable stiffness isolation systems, Engineering Structures 27 (2005) 514–523.

[55] B. F. Yan, A. Miyamoto, E. Bruhwiler, Wavelet transform-based modal parameter identification considering uncertainty, Journal of Sound and Vibration 291 (2006) 285–301.

[56] A. Chakraborty, B. Basu, M. Mitra, Identification of modal parameters of a mdof system by modified L-P Wavelet packets, Journal of Sound and Vibration 295 (2006) 827–837.

[57] T. P. Le, P. Argoul, Continuous Wavelet transform for modal identification using free decay response, Journal of Sound and Vibration 277 (2004) 73–100.

[58] J. A. Demarchi, K. C. Craig, Comments on natural frequencies and dampings identification using Wavelet transforms: application to real data, Mechanical Systems and Signal Processing 17 (2) (2003) 483–488.

[59] N. E. Huang, Z. Shen, S. R. Long, A new view of nonlinear water waves: The Hilbert Spectrum, Annual Review of Fluid Mechanics 31 (1999) 417–457.

[60] J. N. Yang, Y. Lei, S. Pan, N. Huang, System identification of linear structures based on Hilbert-Huang spectral analysis. Part 1: normal modes, Earthquake Engineering and Structural Dynamics 32 (2003) 1443–1467.

[61] S. Nagarajaiah, N. Varadarajan, Short time Fourier transform algorithm for wind response control of buildings with variable stiffness TMD, Engineering Structures 27 (3) (2005) 431–441.

[62] S. Narasimhan, S. Nagarajaiah, A STFT semiactive controller for base isolated buildings with variable stiffness isolation systems, Engineering Structures 27 (4) (2005) 514–523.

[63] W. J. Staszewski, Identification of damping in MDOF systems using time-scale decomposition, Journal of Sound and Vibration 203 (2) (1997) 283–305.

[64] T. Kijewski, A. Kareem, Wavelet transforms for system identification in civil engineering, Computer-Aided Civil and Infrastructure Engineering 18 (5) (2003) 339–355.

[65] A. Chakraborty, B. Basu, Nonstationary response analysis of long span bridges under spatially varying differential support motions using continuous wavelet transform, Journal of Engineering Mechanics 134 (2) (2008) 155–162.

[66] Z. Wu, N. E. Huang, A study of the characteristics of white noise using the empirical mode decomposition method, Proceedings of the Royal Society of London 460 (2004) 1597–1611.

[67] Z. Min, S. Fan, Modal parameter extraction based on Hilbert transform of modal response, Asian Transactions on Engineering 2 (01) (2012) 25–33.

[68] J. N. Yang, Y. Lei, S. Lin, N. Huang, Identification of natural frquencies and dampings of in situ tall building using ambient wind vibration data, Journal of Engineering Mechanics 130 (5) (2004) 570–577.

[69] P. F. Pai, Nonlinear vibration characterization by signal decomposition, Journal of Sound and Vibration 307 (2007) 527–544.

[70] A. R. Messina, V. Vittal, Nonlinear, non-stationary analysis of interarea oscillations via Hilbert spectral analysis, IEEE Transaction on Power Systems 21 (3) (2006) 1234–1241.

[71] P. F. Pai, A. N. Palazotto, Detection and identification of nonlinearties by amplitude and frequency modulation analysis, Mechanical Systems and Signal Processing 22 (2008) 1107–1132.

[72] P. F. Pai, A. N. Palazotto, HHT-based nonlinear signal processing method for parametric and non-parametric identification of dynamical systems, International Journals of Mechanical Science 50 (2008) 1619–1635.

[73] J. N. Yang, Y. Lei, S. Lin, N. Huang, Hilbert-Huang based approach for structural damage detection, Journal of Engineering Mechanics 130 (1) (2004) 85–95.

[74] S. Lin, J. N. Yang, L. Zhou, Damage identification of a benchmark building for structural health monitoring, Smart Material and Structures 14 (2005) 162–169.

[75] Z. Y. Shi, S. S. Law, Identification of linear time-varying dynamical systems using Hilbert transform and empirical mode decomposition method, Journal of Aplied Mechanics 74 (2007) 223–230.

[76] Z. Wang, G. Chen, Recursive Hilbert-Huang transformation method for time-varying property identification of linear shear-type building under base excitation, Journal of Engineering Mechanics 138 (6) (2012) 631–639.

[77] C. Geng, F. H. Wang, Z. J. Jin, Modal parameter identification of power transformer winding based on Hilbert-Huang transform, Power and Energy Society General Meeting (PES), IEEE (2013) 1–5.

[78] H. G. Chen, Y. J. Yan, J. S. Jiang, Vibration-based damage detection in composite wingbox structures by HHT, Mechanical Systems and Signal Processing 21 (2007) 307–321.

[79] R. Yan, R. X. Gao, Hilbert-Huang transform based vibration signal analysis for mechine health monitoring, IEEE Transactions Instrumentation and Measurement 55 (6) (2006) 2320–2329.

[80] M. Datig, T. Schlurmann, Performance and limitation of the Hilbert-Huang transformation (HHT) with an application to irregular water waves, Ocean Engineering 31 (2004) 1783–1834.

[81] T. U. Wu, Y. L. Chung, C. H. Liu, Looseness diagnosis of rotating machinery via vibration analysis through Hilbert-Huang transformation approach, Journal of Vibration and Acoustics 132 (2010) 1–9.

[82] Z. K. Peng, W. T. Peter, F. L. Chu, A comparison study of improved hilbert–huang transform and wavelet transform: application to fault diagnosis for rolling bearing, Mechanical Systems and Signal Processing 19 (5) (2005) 974–988.

[83] Z. K. Peng, W. T. Peter, F. L. Chu, An improved hilbert–huang transform and its application in vibration signal analysis, Journal of Sound and Vibration 286 (1) (2005) 187–205.

[84] Z. Wu, N. E. Huang, Ensemble empirical mode decomposition: a noise-assisted data analysis method, Advances in Adaptive Data Analysis 1 (01) (2009) 1–41.

[85] J. N. Yang, Y. Lei, S. Pan, N. Huang, System identification of linear structures based on Hilbert–Huang spectral analysis. Part 1: normal modes, Earthquake Engineering and Structural Dynamics 32 (9) (2003) 1443–1467.

[86] J. Chen, Y. L. Xu, R. C. Zhang, Modal parameter identification of Tsing Ma suspension bridge under Typhoon Victor: EMD-HT method, Journal of Wind Engineering and Industrial Aerodynamics 92 (10) (2004) 805–827.

[87] X. H. He, X. G. Hua, Z. Q. Chen, F. L. Huang, Emd-based random decrement technique for modal parameter identification of an existing railway bridge, Engineering Structures 33 (4) (2011) 1348–1356.

[88] D. J. Yu, W. X. Ren, EMD-based stochastic subspace identification of structures from operational vibration measurements, Engineering Structures 27 (12) (2005) 1741–1751.

[89] B. Yan, A. Miyamoto, A comparative study of modal parameter identification based on wavelet and hilbert–huang transforms, Computer-Aided Civil and Infrastructure Engineering 21 (1) (2006) 9–23.

[90] N. E. Huang, M. L. Wu, S. R. Long, S. S. Shen, W. Qu, P. Gloersen, K. L. Fan, A confidence limit for the empirical mode decomposition and hilbert spectral analysis, Proceedings of Royal Society of London Series 459 (2003) 2317–2345.

[91] B. Hazra, A. Sadhu, A. J. Roffel, P. E. Paquet, S. Narasimhan, Underdetermined blind identification of structure by using the modified cross-correlation method, Journal of Engineering Mechanics 138 (4) (2012) 327–337.

[92] B. Hazra, A. Sadhu, A. J. Roffel, S. Narasimhan, Hybrid time-frequency blind source separation towards ambient system identification of structures, Computer Aided Civil and Infrastructure Engineering 27 (5) (2012) 314–332.

[93] X. He, X. Hua, Z. Chen, F. Huang, Emd-based random decrement technique for modal parameter identification of an existing railway bridge, Engineering Structures 33 (4) (2011) 1348 – 1356.

[94] K. C. G. Ong, Z. Wang, M. Maalej, Adaptive magnitude spectrum algorithm for hilbert–huang transform based frequency identification, Engineering Structures 30 (1) (2008) 33–41.

[95] N. Rehman, D. P. Mandic, Empirical mode decomposition for trivariate signals, IEEE Transactions On Signal Processing 58 (3) (2010) 1059–1068.

[96] N. Rehman, D. P. Mandic, Multivariate empirical mode decomposition, Proceedings of The Royal Soceity A 466 (2010) 1291–1302.

[97] N. Rehman, D. P. Mandic, Filter bank property of multivariate empirical mode decomposition, Signal Processing, IEEE Transactions on 59 (5) (2011) 2421–2426.

[98] N. Rehman, D. P. Mandic, Empirical mode decomposition for trivariate signals, Signal Processing, IEEE Transactions 58 (3) (2010) 1059–1068.

[99] J. Fleureau, A. Kachenoura, L. Albera, J.-C. Nunes, L. Senhadji, Multivariate empirical mode decomposition and application to multichannel filtering, Signal Processing 91 (12) (2011) 2783 – 2792.

[100] X. Zhao, T. H. Patel, M. J. Zuo, Multivariate emd and full spectrum based condition monitoring for rotating machinery, Mechanical Systems and Signal Processing 27 (2012) 712–728.

[101] T. Wang, M. Zhang, Q. Yu, H. Zhang, Comparing the applications of EMD and EEMD on time–frequency analysis of seismic signal, Journal of Applied Geophysics 83 (2012) 29–34.

[102] L. Yang, Z. Yang, L. Yang, P. Zhang, An improved envelope algorithm for eliminating undershoots, Digital Signal Processing 23 (1) (2013) 401–411.

[103] G. Chen, Z. Wang, A signal decomposition theorem with hilbert transform and its application to narrowband time series with closely spaced frequency components, Mechanical systems and signal processing 28 (2012) 258–279.

[104] Z. Wang, G. Chen, Analytical mode decomposition with hilbert transform for modal parameter identification of buildings under ambient vibration, Engineering Structures 59 (2014) 173–184.

[105] W.-C. Shen, Y.-H. Chen, A.-Y. A. Wu, Low-complexity sinusoidal-assisted emd (saemd) algorithms for solving mode-mixing problems in hht, Digital Signal Processing 24 (2014) 170–186.

[106] I. Daubechies, J. Lu, H.-T. Wu, Synchrosqueezed wavelet transforms: an empirical mode decomposition-like tool, Applied and computational harmonic analysis 30 (2) (2011) 243–261.

[107] H.-T. Wu, P. Flandrin, I. Daubechies, One or two frequencies? the synchrosqueezing answers, Advances in Adaptive Data Analysis 3 (01n02) (2011) 29–39.

[108] C. A. Perez-Ramirez, J. P. Amezquita-Sanchez, H. Adeli, M. Valtierra-Rodriguez, D. Camarena-Martinez, R. J. Romero-Troncoso, New methodology for modal parameters identification of smart civil structures using ambient vibrations and synchrosqueezed wavelet transform, Engineering Applications of Artificial Intelligence 48 (2016) 1–12.

[109] Z.-C. Wang, W.-X. Ren, J.-L. Liu, A synchrosqueezed wavelet transform enhanced by extended analytical mode decomposition method for dynamic signal reconstruction, Journal of Sound and Vibration 332 (22) (2013) 6016–6028.

[110] H. Yang, Synchrosqueezed wave packet transforms and diffeomorphism based spectral analysis for 1d general mode decompositions, Applied and Computational Harmonic Analysis 39 (1) (2015) 33–66.

[111] D. Iatsenko, P. V. McClintock, A. Stefanovska, Linear and synchrosqueezed time–frequency representations revisited: Overview, standards of use, resolution, reconstruction, concentration, and algorithms, Digital Signal Processing 42 (2015) 1–26.

[112] G. Thakur, E. Brevdo, N. S. Fučkar, H.-T. Wu, The synchrosqueezing algorithm for time-varying spectral analysis: Robustness properties and new paleoclimate applications, Signal Processing 93 (5) (2013) 1079–1094.

[113] Z. Li, H. S. Park, H. Adeli, New method for modal identification of super high-rise building structures using discretized synchrosqueezed wavelet and hilbert transforms, The Structural Design of Tall and Special Buildings 26 (3).

[114] C. Li, M. Liang, Time–frequency signal analysis for gearbox fault diagnosis using a generalized synchrosqueezing transform, Mechanical Systems and Signal Processing 26 (2012) 205–217.

[115] L. Wanhammar, Analog filters using MATLAB, Vol. 233, Springer, 2009.

[116] B. Boashash, Time-frequency signal analysis and processing: a comprehensive reference, Academic Press, 2015.

[117] L. Cohen, Time-frequency analysis, Vol. 778, Prentice hall, 1995.

[118] L. Debnath, F. A. Shah, Wavelet transforms and their applications, Springer, 2002.

[119] E. Saff, A. Snider, Fundamental of Complex Analysis for Mathematics Science and Engineering, Prentice-Hall, Inc., New York, 1976.

[120] D. Gabor, Theory of communication. part 1: The analysis of information, Journal of the Institution of Electrical Engineers-Part III: Radio and Communication Engineering 93 (26) (1946) 429–441.

[121] C. W. Therrien, The Lee-Wiener legacy : A history of the statistical theory of communication], IEEE Signal Processing Magazine 19 (6) (2002) 33–34.

[122] J. S. Bendat, A. G. Piersol, Random data: analysis and measurement procedures, Vol. 729, John Wiley & Sons, 2011.

[123] M. Simon, G. Tomlinson, Use of the hilbert transform in modal analysis of linear and non-linear structures, Journal of Sound and Vibration 96 (4) (1984) 421–436.

[124] G. Tomlinson, Developments in the use of the hilbert transform for detecting and quantifying non-linearity associated with frequency response functions, Mechanical Systems and Signal Processing 1 (2) (1987) 151–171.

[125] M. Feldman, Non-linear system vibration analysis using Hilbert transform - I. Free vibration analysis method 'FREEVIB', Mechanical Systems and Signal Processing 8 (2) (1994) 119–127.

[126] M. Feldman, Non-linear system vibration analysis using Hilbert transform - II. Forced vibration analysis method 'FORCEVIB', Mechanical Systems and Signal Processing 8 (3) (1994) 309–318.

[127] N. E. Huang, N. O. Attoh-Okine, The Hilbert-Huang transform in engineering, CRC Press, 2005.

[128] N. E. Huang, S. S. P. Shen, Hilbert-Huang transform and its applications, Vol. 16, World Scientific, 2014.

[129] A. Grossmann, J. Morlet, Decomposition of hardy functions into square integrable wavelets of constant shape, SIAM journal on mathematical analysis 15 (4) (1984) 723–736.

[130] J. Morlet, G. Arens, E. Fourgeau, D. Glard, Wave propagation and sampling theory part i: Complex signal and scattering in multilayered media, Geophysics 47 (2) (1982) 203–221.

[131] A. Aldroubi, M. Unser, Wavelets in medicine and biology, CRC press, 1996.

[132] M. Antonini, M. Barlaud, P. Mathieu, I. Daubechies, Image coding using wavelet transform, Image Processing, IEEE Transactions on 1 (2) (1992) 205–220.

[133] P. Boškoski, A. Debenjak, B. M. Boshkoska, Fast electrochemical impedance spectroscopy, in: Fast Electrochemical Impedance Spectroscopy, Springer, 2017, pp. 14–18.

[134] I. Daubechies, T. Paul, Time-frequency localisation operators-a geometric phase space approach: II. The use of dilations, Inverse Problems 4 (3) (1988) 661.

[135] S. C. Olhede, A. T. Walden, Generalized morse wavelets, IEEE Transactions on Signal Processing 50 (11) (2002) 2661–2670.

[136] J. M. Lilly, S. C. Olhede, Generalized Morse wavelets as a superfamily of analytic wavelets, IEEE Transactions on Signal Processing 60 (11) (2012) 6036–6041.

[137] H. Shima, T. Nakayama, Higher mathematics for physics and engineering, Springer Science & Business Media, 2010.

[138] S. Mallat, A wavelet tour of signal processing: the sparse way, Academic press, 2008.

[139] W. J. Staszewski, K. Worden, G. R. Tomlinson, Time–frequency analysis in gearbox fault detection using the wigner–ville distribution and pattern recognition, Mechanical systems and signal processing 11 (5) (1997) 673–692.

[140] J. Ville, Theory and application of the notion of complex signal, Tech. rep., RAND CORP SANTA MONICA CA (1958).

[141] A. K. Chopra, Dynamics of Structures - Theory and Application to Earthquake Engineering, 3rd Edition, Pearson, 2013.

[142] Strong-motion Virtual Data Cetnre, https://strongmotioncenter.org/vdc/scripts/event.plx?evt=88 (access on 8th Nov, 2018).

[143] L. A. Montejo, L. R. Velazquez, R. I. Ramirez, S. Jang, Wavelet and HHT based identification of different levels of inelatic action in RC structures, 15 WCEE (2012) 1–10.

[144] L. Chaparro, Signals and Systems using MATLAB, Academic Press, 2010.

[145] Z. K. Peng, P. W. Tse, F. L. Chu, A comparisson study of improved Hilbert-Huang transform and wavelet transform: application to fault diagonosis for rolling bearing, Mechanical Systems and Signal Processing 19 (2005) 974–988.

[146] Z. Wu, N. E. Huang, Ensemble empirical mode decomposition: a noise-assisted data analysis method, Advances in adaptive data analysis 1 (01) (2009) 1–41.

[147] S. Mahato, M. V. Teja, A. Chakraborty, Adaptive HHT (AHHT) based modal parameter estimation from limited measurements of an RC-framed building under multi-component earthquake excitations, Structural Control and Health Monitoring 22 (7) (2015) 984–1001.

[148] J. K. Vandiver, A. B. Dunwoody, R. B. Campbell, M. F. Cook, A mathematical basis for the random decrement vibration signature analysis technique, Journal of Mechanical Design 104 (1982) 307–313.

[149] A. Chakraborty, B. Basu, M. Mitra, Identification of modal parameters of a mdof system by modified L–P wavelet packets, Journal of Sound and Vibration 295 (3) (2006) 827–837.

[150] L. Debnath, F. A. Shah, Wavelet transforms and their applications, Springer, 2002.

[151] B. Basu, V. K. Gupta, Stochastic seismic response of single-degree-of-freedom systems through wavelets, Engineering Structures 22 (12) (2000) 1714–1722.

[152] R. Tarinejad, M. Damadipour, Modal identification of structures by a novel approach based on FDD-wavelet method, Journal of Sound and Vibration 333 (2014) 1024–1045.

[153] J. Lardies, S. Gouttebroze, Identification of modal parameters using the wavelet transform, International Journal of Mechanical Sciences 44 (11) (2002) 2263 – 2283.

[154] J. Abonyi, B. Feil, Cluster analysis for data mining and system identification, Springer Science & Business Media, 2007.

[155] R. J. Nath, System identification of prototype base isolated rc building using recorded earthquake response, Master's thesis, Dept. of Civil Engineering, IIT Guwahati (2010).

[156] B. Hazra, A. Sadhu, R. Lourenco, S. Narasimhan, Retuning tuned mass dampers using ambient vibration response, Smart Materials and Structures 19 (11) (2010) 115002.

[157] B. Basu, V. K. Gupta, Seismic response of SDOF systems by wavelet modeling of nonstationary processes, Journal of Engineering Mechanics 124 (10) (1998) 1142–1150.

[158] Z. K. Peng, P. W. Tse, F. L. Chu, A comparison study of improved Hilbert–Huang transform and wavelet transform: application to fault diagnosis for rolling bearing, Mechanical Systems and Signal Processing 19 (5) (2005) 974–988.

[159] Experimental uncertainty quantification in structural dynamics, http://engweb.swan.ac.uk/~adhikaris/uq/, accessed: 23-09-2015.

[160] G. Mondal, S. K. Jain, Lateral stiffness of masonry infilled reinforced concrete (rc) frames with central opening, Earthquake spectra 24 (3) (2008) 701–723.

[161] S. Mahato, M. V. Teja, A. Chakraborty, Adaptive HHT (AHHT) based modal parameter estimation from limited measurements of an RC-framed building under multi-component earthquake excitations, Structural Control and Health Monitoring 22 (7) (2015) 984–1001.

[162] S. Adhikari, M. Friswell, K. Lonkar, A. Sarkar, Experimental case studies for uncertainty quantification in structural dynamics, Probabilistic Engineering Mechanics 24 (4) (2009) 473–492.

[163] S. Adhikari, A. S. Phani, Random eigenvalue problems in structural dynamics: experimental investigations, AIAA Journal 48 (6) (2010) 1085–1097.

[164] S. Adhikari, M. Friswell, Random matrix eigenvalue problems in structural dynamics, International Journal for Numerical Methods in Engineering 69 (3) (2007) 562–591.

[165] H. Pradlwarter, G. Schuëller, G. Szekely, Random eigenvalue problems for large systems, Computers & Structures 80 (27-30) (2002) 2415–2424.

[166] C. Desceliers, R. Ghanem, C. Soize, Maximum likelihood estimation of stochastic chaos representations from experimental data, International Journal for Numerical Methods in Engineering 66 (6) (2006) 978–1001.

[167] S. Rahman, Probability distributions of natural frequencies of uncertain dynamic systems, AIAA journal 47 (6) (2009) 1579–1589.

[168] V. Cotoni, R. Langley, M. Kidner, Numerical and experimental validation of variance prediction in the statistical energy analysis of built-up systems, Journal of Sound and Vibration 288 (3) (2005) 701–728.

[169] D. Song, S. Chen, Z. Qiu, Stochastic sensitivity analysis of eigenvalues and eigenvectors, Computers & structures 54 (5) (1995) 891–896.

[170] P. B. Nair, A. J. Keane, R. S. Langley, Improved first-order approximation of eigenvalues and eigenvectors, AIAA journal 36 (9) (1998) 1721–1727.

[171] S. Adhikari, Calculation of derivative of complex modes using classical normal modes, Computers & Structures 77 (6) (2000) 625–633.

[172] M. I. Friswell, J. E. Mottershead, Finite Element Model Updating in Structural Dynamics, Vol. 38, Springer, 1995.

[173] T. Marwala, Finite-Element-Model Updating Using Computional Intelligence Techniques, Springer, 2010.

[174] R. J. Allemang, D. L. Brown, A correlation coefficient for modal vector analysis, in: Proc. of the 1^{st} international modal analysis conference, Vol. 1, SEM, Orlando, USA, 1982, pp. 110–116.

[175] R. J. Allemang, The modal assurance criterion–twenty years of use and abuse, Journal of Sound and Vibration 37 (8) (2003) 14–23.

[176] K. Korkmaz, F. Demir, H. Tekeli, A. Karahan, Effects of infilled masonry walls on nonlinear structural behavior of precast concrete structures in turkey, in: The 14th World Conference of Earthquake Engineering, 2008, pp. 12–17.